

Durham E-Theses

Detection of radiation in the energy range 0.1 to 10MeV by use of a nuclear gamma-ray spectrometer

Summers, William Marshall

How to cite:

Summers, William Marshall (1983) *Detection of radiation in the energy range 0.1 to 10MeV by use of a nuclear gamma-ray spectrometer*, Durham theses, Durham University. Available at Durham E-Theses Online: <http://etheses.dur.ac.uk/7158/>

Use policy

The full-text may be used and/or reproduced, and given to third parties in any format or medium, without prior permission or charge, for personal research or study, educational, or not-for-profit purposes provided that:

- a full bibliographic reference is made to the original source
- a [link](#) is made to the metadata record in Durham E-Theses
- the full-text is not changed in any way

The full-text must not be sold in any format or medium without the formal permission of the copyright holders.

Please consult the [full Durham E-Theses policy](#) for further details.

DETECTION OF RADIATION IN THE
ENERGY RANGE 0.1 TO 10MeV BY USE OF
A NUCLEAR GAMMA-RAY SPECTROMETER

by

WILLIAM MARSHALL SUMMERS, B.Sc.

The copyright of this thesis rests with the author.
No quotation from it should be published without
his prior written consent and information derived
from it should be acknowledged.

A Thesis
Submitted to the University of Durham
for the Degree of
Master of Science
February, 1983



(i)

DETECTION OF RADIATION IN THE
ENERGY RANGE 0.1 TO 10 MeV BY USE OF
A NUCLEAR GAMMA-RAY SPECTROMETER

ABSTRACT

An 86 cm³, actively shielded Ge(Hp), Nuclear Gamma-ray Spectrometer was flown from Palestine, Texas, U.S.A., in August 1979, to a residual atmospheric pressure of 4.3 g cm⁻²; by means of a high altitude balloon. The design, construction and response characteristics of the instrument, which has: (a) an energy resolution of 2.5 keV at 1.33 MeV, (b) an opening angle of 5.2° (FWHM) and (c) a measured efficiency of 23% relative to a 3" x 3" NaI(Tl) crystal, is described herein.

Also presented are measurements of the gamma-ray lines which were detected at various atmospheric depths during the ascent phase of the flight. These features originate from secondary gamma production in the shield and Ge(Hp) crystal from atmospheric radiation 'leaking' through it. The results are in accord with those obtained from independent experiments of other workers.

The minimum sensitivity of the spectrometer to cosmic, point, line sources is shown to be 3×10^{-3} and 1×10^{-2} photons cm⁻²s⁻¹ for active and passive shielding respectively, for an observation time of one hour on both source and background.

William Marshall Summers, B.Sc.

PREFACE

The work described in this thesis was carried out during the period 1977 to 1980 while the author was a member of the Experimental Gamma-ray Astronomy Group of the Department of Physics, Durham University, working under the supervision of Dr. M.G. Thompson.

During this time the author has been involved, together with his colleagues, in all stages of the work including design, construction and testing of the apparatus. In addition the author has had special responsibility for the design and construction of the Al collimator, development of minicomputer programs for celestial source location during the spectrometer's balloon flight and for the development of a Monte-Carlo based computer model for simulation of response characteristics of the spectrometer's detectors.

CHAPTER 4. RESPONSE CHARACTERISTICS OF THE DURHAM GAMMA-RAY SPECTROMETER	
4.1 Introduction	57
4.2 Interaction of Gamma-Rays with Matter	57
4.2.1 Photoelectric Absorption	58
4.2.2 Compton Scattering	59
4.2.3 Pair Production	63
4.3 Monte-Carlo Simulation and Detector Characteristics	64
4.4 Gamma-Ray Line Detectability	79
CHAPTER 5. THE DURHAM GAMMA-RAY SPECTROMETER BALLOON FLIGHT	
5.1 Introduction	82
5.2 The Flight	84
CHAPTER 6. EVALUATION OF THE FLIGHT DATA	
6.1 Introduction	87
6.2 Housekeeping and System Orientation	88
6.3 Pulse-height Spectra	90
CHAPTER 7. THE FUTURE OF EXPERIMENTAL GAMMA-RAY ASTRONOMY	94
ACKNOWLEDGEMENTS	97
REFERENCES	98

(v)

NOMENCLATURE

Unless otherwise stated the symbols used in this thesis carry the following interpretations.

A	Avogadro's constant	$6.022 \times 10^{-23} \text{ mole}^{-1}$
c	Velocity of light	$2.998 \times 10^8 \text{ ms}^{-1}$
E	Energy	
e	Charge on the electron	$1.602 \times 10^{-19} \text{ C}$
F	Flux	
H	Magnetic field strength	
h	Planck's constant	$6.626 \times 10^{-34} \text{ Js}$
I	Intensity	
k	Boltzmann's constant	$1.381 \times 10^{-23} \text{ JK}^{-1}$
M	Mass	
M_0, m_0	Rest mass	
P	Momentum	
r_0	Classical Electron Radius	$5.292 \times 10^{-11} \text{ m}$
T	Absolute Temperature	
t	Time	
v	Particle velocity	
Z	Mass number	
α	Fine structure constant	7.30×10^{-3}
β	v/c	
γ	Lorentz factor $(1 - \beta^2)^{-\frac{1}{2}}$	
λ	Wavelength	
ν	Frequency	
ρ	Density	
σ	Standard deviation	
Ω	Solid angle	

The following subscripts are also employed:

e Electron

max Maximum

min Minimum

p Proton

thresh Threshold

γ Gamma-ray photon

π Pion

μ Muon

\perp Perpendicular component

// Parallel component

CHAPTER ONE

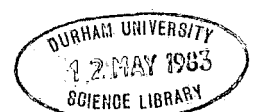
INTRODUCTION

1.1 GENERAL INTRODUCTION

Sir William Herschel's discovery, towards the close of the eighteenth century, of the existence of 'calorific' (infra-red) rays constituted the first step in a progressive realisation that the radiation which stimulates the eye forms only a minute portion of a whole spectrum of electromagnetic and cosmic radiation and that the 'picture' of the universe formed from the study of the visible region alone must consequently be a limited one. As a result the cosmos is presently being studied over a much larger spectral range in an attempt to overcome this limitation.

As a tool for the attainment of a better understanding of the universe, electromagnetic radiation has an advantage over cosmic rays in that it supplies directional information. All but the highest energy cosmic rays are significantly deviated from their original trajectories by magnetic fields, however electromagnetic radiation is not affected in this way and therefore reaches an observer, from the source, by an undeviated path. In particular, gamma-rays in the energy range $\sim 10^5$ eV to $\sim 10^7$ eV possess two lineaments which lead to their distinction as a powerful probe of the cosmos; (a) their penetrability of matter, and (b) their production at discrete energies from nuclear processes (i.e. gamma-ray lines). These two characteristics combined with the directional property mean that the following astrophysical topics may be better understood following perscrutation at these energies:

- (i) Sites of Nucleosynthesis.
- (ii) Location of discrete sources of cosmic rays.
- (iii) Nature of Quasars, Radio Galaxies, Seyfert Galaxies, Supernovae etc.
- (iv) Prevalent conditions of the early universe.
- (v) Existence and location of antimatter.



In spite of the obvious incentive of finding possible solutions to these matters, which are among the most fundamental in astrophysics, progress in practical, low energy, gamma-ray astronomy has until the present time been rather slow owing to various experimental difficulties:

- (a) Extremely low fluxes.
- (b) Presence of the terrestrial atmosphere.
- (c) Insufficiently sensitive detectors of poor angular and energy resolution.

Hence in order to perform successful observations experiments must be capable of being carried to the 'top' of the atmosphere or beyond via balloons and satellites, moreover advantage must be taken of technological developments to improve the sensitivity and resolution of experiments.

The Durham Nuclear Gamma-ray Spectrometer, described in this report, is designed for the study of the gamma-ray spectrum in the energy range 0.05 to 10 MeV from balloon altitude incorporating Germanium technology for high energy resolution and NaI(Tl) anticoincidence shielding for high sensitivity.

1.2 HISTORICAL DEVELOPMENT OF GAMMA-RAY ASTRONOMY

Experimental study of celestial gamma radiation began with apparatus designed to detect energies above 50 MeV and although the main concern here is with energies in the range 0.05 MeV to 10 MeV it is worthwhile to mention a few of the higher energy devices which were implemented prior to the development of gamma-ray line spectrometers.

The first true gamma-ray astronomy experiment was a balloon-borne ionisation chamber [Rossi and Hulsizer (1949)]. Designed for photon energies above 50 MeV it demonstrated that of the primary cosmic radiation arriving at the earth, electrons and gamma rays > 1 GeV constituted less than 1% and this finding was subsequently independently confirmed by the flight of a cloud chamber, Critchfield et al. (1952)

In the decade and a half following Rossi and Hulsizer's endeavour several experiments covering photon energies above 50 MeV were mounted. Carlson et al. (1950) and Svensson (1958), showed the secondary nature of the large proportion of gamma-rays above 100 MeV at low atmospheric depths by means of balloon-borne emulsion apparatus and an upper limit of $0.45 \text{ MeV cm}^{-2} \text{ s}^{-1} \text{ sr}^{-1}$ was placed on the photon energy flux below 100 MeV by means of Geiger-Mueller tubes used as the payload of a V-2 rocket [Perlow and Kissinger (1951)]. A scintillation counter [Cline (1961)] and a Cerenkov counter, [Duthie et al. (1963)], both designed for detection of π^0 meson decay photons (again above 50 MeV), produced conflicting data regarding the primary intensity. This clearly showed that in comparison with the charged particle flux and the secondary gamma flux generated in the atmosphere, the primary gamma-ray flux is too low to be measured accurately by such methods.

Below 50 MeV practical activity, in astronomical terms, did not begin until approximately ten years after Rossi and Hulsizer's work. Morrison (1958) produced a paper containing theoretical predictions of gamma fluxes at discrete energies, i.e. gamma-ray spectral lines, from several cosmic sources and this brought about the development of instruments capable of reasonable spectral resolution which were subsequently and are continually being, improved.

Prior to 1966 the devices used were omnidirectional counters of alkali halide scintillation crystal incorporating thin plastic scintillators in "phoswich" configuration to provide veto of charged particles. With such devices, carried by balloons, detection of the 0.511 MeV electron-positron annihilation line, [Peterson (1963)] and a study of the gamma-ray spectrum as a function of atmospheric depth [Vette (1962) and Anderson (1961)] have been achieved. The measured

count rates from these experiments extrapolated to zero atmospheric depth gave: $6.0 \text{ photons cm}^{-2} \text{ s}^{-1}$ between 0.03 MeV and 1.0 MeV, and $0.2 \text{ photons cm}^{-2} \text{ s}^{-1}$ in the 0.511 MeV line. These rates are almost entirely due to atmospheric albedo gamma-rays.

Arnold et al. (1962) and Metzger et al. (1964) report the results from two omnidirectional CsI(Tl) spectrometers enclosed in 4π phoswich charged particle shields. One of the spectrometers was carried aboard the Ranger 3 spacecraft and the other on Ranger 5. Each instrument was housed within a thin aluminium shell and supported at the end of an extendible boom. Data, including the pulse-height spectrum, were recorded at a distance from the earth which was well beyond the radiation belts. Two boom positions for data collection facilitated an evaluation of the effect of the spacecraft background.

Figure 1.1 shows the spectrum obtained from the Ranger 3 mission with the boom in the extended position. A straight line of $0.17 \text{ counts cm}^{-2} \text{ s}^{-1} \text{ MeV}^{-1}$, where E is expressed in MeV, provides a good fit to the data and after the application of a 10% correction to account for local secondaries the inferred differential flux is:

$$dn(E) = 0.012 dE/E^{2.2} \text{ photons cm}^{-2} \text{ s}^{-1} \text{ MeV}^{-1}$$

The observed flux did not change significantly upon re-orientation of the instrument, thus a celestial origin was inferred since the detector was sufficiently anisotropic to have shown an effect if as much as one quarter of the flux originated from the Sun.

Rangers 3 and 5 also provided upper limits for the primary flux in the 0.511 MeV electron-positron annihilation line and the neutron-proton capture line (2.23 MeV). The figures obtained were; $0.014 \text{ photons cm}^{-2} \text{ s}^{-1}$ for the 0.511 MeV line and $0.005 \text{ photons cm}^{-2} \text{ s}^{-1}$ for the 2.23 MeV line. These figures represent the sum flux values from all discrete

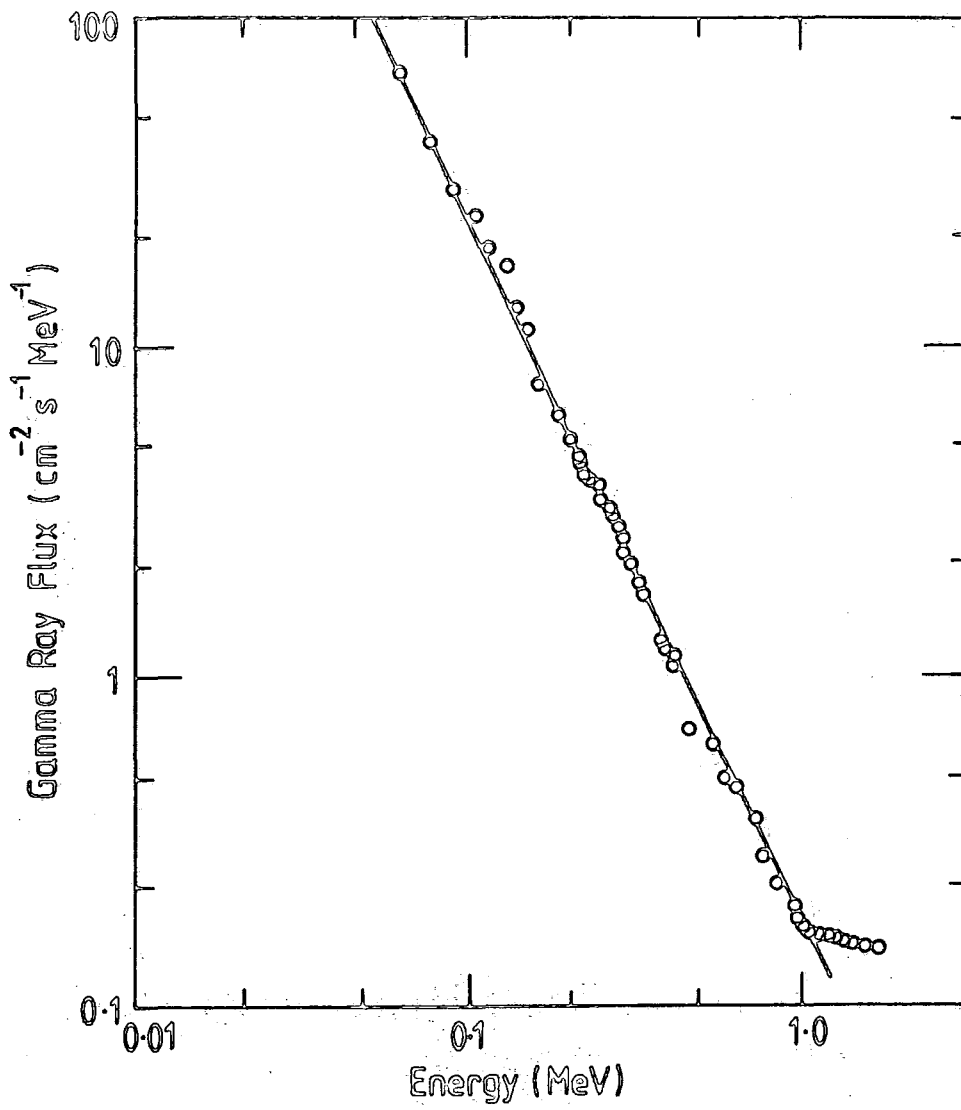


Figure 1-1 Gamma ray spectrum obtained from Ranger 3 spacecraft. [Metzger et al(1964)]

sources plus the integral of the diffuse flux over all directions. Finally concerning the Ranger missions, extrapolations of the data to higher and lower energies have been performed and good agreement is obtained with independent experimental data for these regions.

The terrestrial atmospheric 0.511 MeV line, [Peterson (1963)] has been found to be a factor of five or six times higher than the celestial counterpart as set by the Ranger craft. This fact alone indicates the enormous difficulties of overcoming background when searching for cosmic gamma-ray lines with instruments in close proximity to the earth. Kasturirangan et al. (1972), Nakagawa et al. (1971), Chupp et al. (1970), Frost et al. (1966) and Rocchia et al. (1965), have all failed to detect any variation in intensity of the atmospheric 0.511 MeV line which could be attributed to sources.

Several experimenters have since reported the existence of celestial gamma radiation from discrete sources in the nuclear transition energy range and these reports are described in Chapter 2.

1.3 MECHANISMS FOR GAMMA RADIATION

1.3.1 Thermal Radiation

Any astrophysical body which is optically thick emits radiation closely approximating that of a black body, Unsöld (1969), Eisberg and Resnick (1974). The form of this radiation is described by Planck's Law, which in its basic form is expressed as an energy density:

$$\rho_T(\lambda)d\lambda = \frac{8\pi hc}{\lambda^5} \left\{ \frac{d\lambda}{\exp[hc/\lambda kT]-1} \right\} \quad (1.1)$$

The function is plotted for various temperatures in figure 1.2 showing the shift of the peak of the spectrum to shorter wavelengths with increase of temperature of the body. This shift of the peak is described by Wien's displacement law:

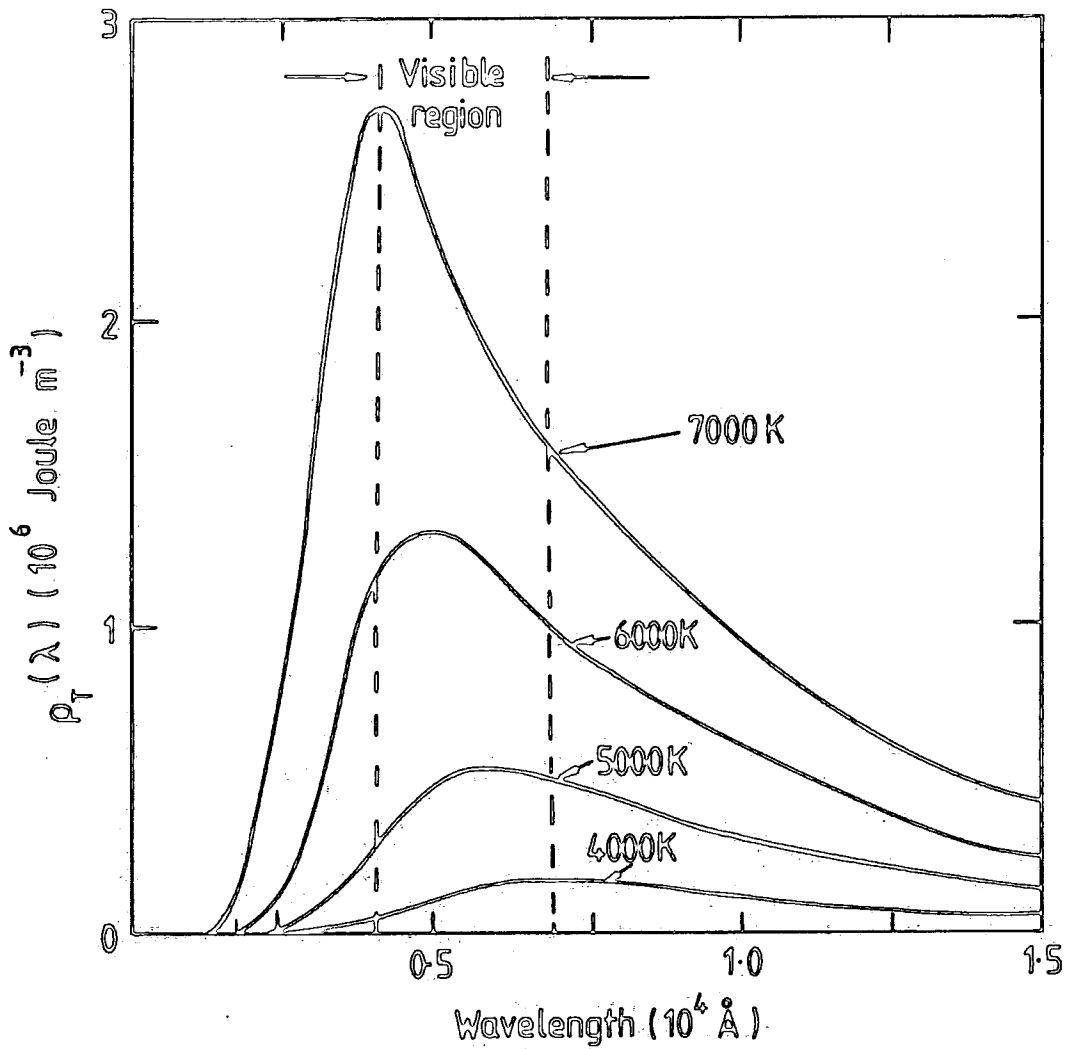


Figure 1.2 Black body energy density as a function of wavelength for various temperatures. [Eisberg and Resnick (1974)]

$$\lambda_{\max} T = 2.898 \times 10^{-3} \text{ mK}^{-1} \quad (1.2)$$

In energy units this is expressed as:

$$E_{\max} \text{ (MeV)} = 4.7 \times 10^{-10} T \text{ (K)} \quad (1.3)$$

By virtue of temperature therefore, astrophysical objects may contribute to the gamma-ray spectral region; however, temperatures of the order $10^8 \text{ K} < T < 10^{10} \text{ K}$ are required. Solar flares have been postulated as possessing temperatures sufficiently high to explain solar, hard X-ray bursts. Supernova type explosions may produce the required temperatures in the lower part of the range but towards 10^{10} K the only possible source is thought to be the creation of the universe itself i.e. the 'big bang' and any black body radiation produced during that process is expected to be extremely red-shifted at the current epoch.

In terms of photon energy the photon number spectrum expected from the black body process is, from Planck's Law:

$$N(E_{\gamma}) = 9.9 \times 10^{40} E_{\gamma}^{-2} \left\{ \exp[1.2 \times 10^{10} E_{\gamma} / T] - 1 \right\}^{-1} \text{ cm}^{-2} \text{ s}^{-1} \text{ MeV}^{-1} \quad (1.4)$$

where E_{γ} is expressed in MeV.

1.3.2 Inverse Compton Scattering

An interaction of a low energy photon and a relativistic electron which results in the scattering of the photon with increased energy and a correspondingly decreased electron energy constitutes the Inverse Compton process. Figure 1.3 (a and b) shows the interaction from two distinct inertial frames of reference, i.e. the laboratory frame(S) and the rest frame of the electron(S'). The kinematical situation represented in the S' frame is in fact the basic Compton scattering process, described in detail in Section 4.2.2, and transformation of the

post-interaction quantities to the S frame by means of the relativistic equations for the aberration of light and Doppler effect yields the result of an enhanced energy recoil photon.

$$\epsilon_1 \sim \gamma^2 \epsilon \tag{1.5}$$

where γ is the Lorentz factor: $\gamma = (1 - \beta^2)^{-\frac{1}{2}}$; $\beta = \frac{v}{c}$. This approximation applies only to the case where $\gamma \epsilon \ll m_0 c^2$ and consequently electrons in the cosmic-ray range may convert starlight or 3K microwave background photons into the gamma-ray region.

In these circumstances the scattering process reduces to the classical case of Thomson scattering and in this limit a fast electron moving through a cosmic photon distribution of energy density ρ undergoes a number of photon collisions per second N given by:

$$N = \sigma_T c \frac{\rho}{\epsilon} \tag{1.6}$$

where σ_T is the Thomson total cross section. Hence the power scattered by a single electron is

$$P_c(\gamma, \rho) \sim \sigma_T c \gamma^2 \rho \tag{1.7}$$

However, a more rigorous treatment introduces a factor of $\frac{4}{3}$ such that

$$P_c(\gamma, \rho) \sim \frac{4}{3} \sigma_T c \gamma^2 \rho \tag{1.8}$$

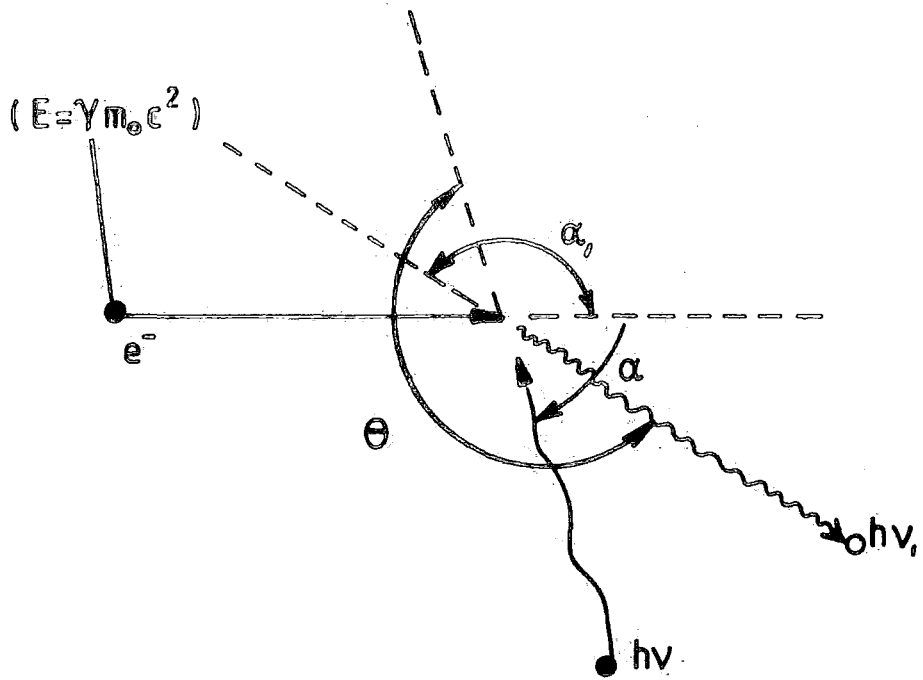
It is usually the case in cosmic-ray applications that a continuum of electron energies is encountered and typically a power-law form for this electron energy spectrum is invoked:

$$n(\gamma) d\gamma = n_0 \gamma^{-m} d\gamma \tag{1.9}$$

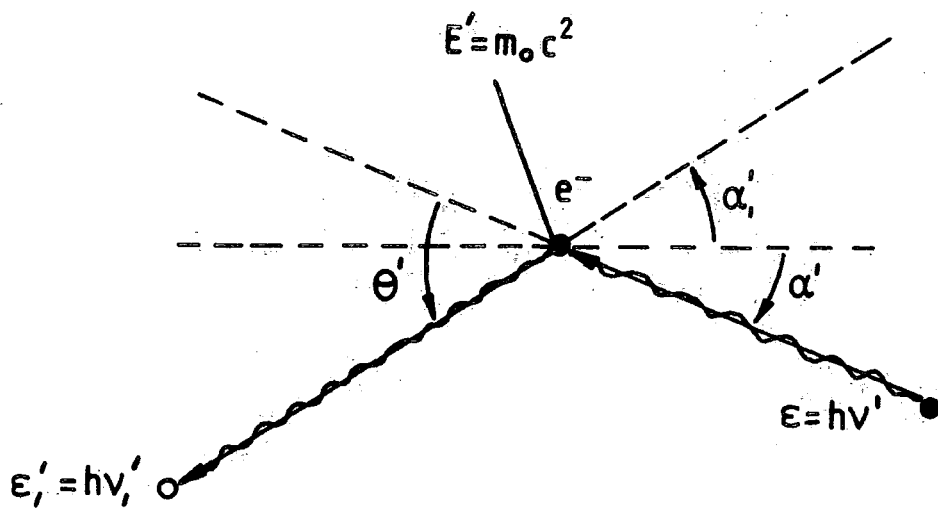
further, a black body distribution represented by:

$$\langle \epsilon \rangle = 2.7kT \tag{1.10}$$

where k is the Boltzmann constant and T is the black body temperature, is employed for the ambient photons. Now in a given direction from a



(a) Local inertial frame of fixed stars (S)



(b) Electron rest frame (S')

Figure 1-3 Inverse Compton process
[Weekes (1969)]

region of fast electrons which extends a distance $R \equiv R_1 - R_2$ along the line of sight, the specific intensity $[(I_\nu)_c]$ received at earth is:

$$(I_\nu)_c = \int_{R_1}^{R_2} \frac{1}{4\pi} \frac{dP}{d\nu d\tau} dr \quad (1.11)$$

assuming that both the ambient photon and the electron fluxes are locally isotropic.

Using these approximations Felten and Morrison (1966) produce, for the specific intensity, the expression

$$(I_\nu)_c \sim 1.06 \times 10^{-15} (3.66 \times 10^{-6})^{(3-m)} n_o R \rho T^{(m-3)/2} \nu^{(1-m)/2} \quad (1.12)$$

in c.g.s. units.

This may be re-expressed as

$$(I_\epsilon)_c \sim 10^9 (56.9)^{(3-m)} n_o R \rho T^{(m-3)/2} \epsilon^{-(m+1)/2} \text{cm}^{-2} \text{s}^{-1} \text{sr}^{-1} \text{MeV}^{-1} \quad (1.13)$$

where R is in light years, ρ is eVcm^{-3} , $h\nu$ is in eV and n_o has units cm^{-3} .

1.3.3 Magnetobremstrahlung

The Lorentz force which is exerted on a moving charged particle in a magnetic field H causes it to spiral around the field lines and the consequent acceleration results in the radiation of electromagnetic energy by the particle; this process is known as Magnetobremstrahlung.

The frequency ν_L of the spiral motion is given by the expression:

$$\nu_L = \frac{1}{2\pi} \frac{eH_\perp}{m_o c} \quad (1.14)$$

where H_\perp represents the magnetic field component perpendicular to the particle's velocity vector; and for a non-relativistic particle the 'cyclotron' radiation produced is isotropic and is of the same frequency ν_L .

Synchrotron radiation (figure 1.4) arises from a relativistic particle in a magnetic field and in this case the radiation is concentrated

in a cone having its axis centred on the instantaneous particle trajectory. Such radiation is no longer of a unique frequency, rather there is a broad and assymmetric spectral distribution with a centre of gravity lying close to the frequency ν_s where

$$\nu_s = \frac{3}{2} \gamma^2 \nu_L \approx 4.2 \times 10^{-6} \gamma^2 H_{\Delta} \text{ MHz} \quad (1.15)$$

where H_{Δ} is expressed in microgauss.

The detailed theory of synchrotron emission has been discussed by Schwinger (1949) who gives for the instantaneous synchrotron power $P_s(\gamma, H)$ from a single particle of charge Z and rest mass M :

$$P_s(\gamma, H_{\Delta}) = 9.89 \times 10^{-16} \left(\frac{E}{Mc^2}\right)^2 H_{\Delta}^2 \left(\frac{Z^2 m_o}{M}\right)^2 \text{ eVs}^{-1} \quad (1.16)$$

For an electron $Z = 1$ and $M = m_o$ this expression reduces to:

$$e P_s(\gamma, H_{\Delta}) = 9.89 \times 10^{-16} H_{\Delta}^2 \gamma^2 \text{ eVs}^{-1} \quad (1.17)$$

Equation (1.16) indicates the dependence of the particle energy loss rate on the inverse fourth power of the particle rest mass, from which it may be understood that electrons rather than protons are the primary source of synchrotron radiation. The proton synchrotron power is:

$$p P_s \approx \left(\frac{m_o}{M_p}\right)^4 e P_s \approx 10^{-13} e P_s \quad (1.18)$$

In application to the astrophysical environment it is again necessary to consider a spectrum of electron energies and as with the argument for Inverse Compton radiation the same power-law spectrum is used [equation (1.9)].

For a uniform but randomly orientated magnetic field in a region of linear dimension R (light years) the intensity (I_ν) received at earth is:

$$(I_\nu)_s \approx 4.8 \times 10^{-20} (4.9 \times 10^2)^{(3-m)} n_o R H^{(1+m)/2} \nu^{(1-m)/2} \text{ Watts m}^{-2} \text{ sr}^{-1} \text{ Hz}^{-1} \quad (1.19)$$

where ν is expressed in MHz and n_o is in c.g.s. units.

Examination of equation (1.15) reveals the necessity for strong magnetic fields or extremely energetic electrons if photons in the MeV energy range are to be produced. It therefore seems that the most likely astrophysical locations for hard X-ray and gamma radiation from Magnetobremsstrahlung would be supernova remnants or close to the surfaces of condensed objects such as neutron stars.

Comparison of equation (1.19) for synchrotron with equation (1.12) for Inverse Compton indicates that for an electron power-law spectrum the gamma-ray spectral shapes in the two cases have the same dependence upon frequency. This is due to the similarity of the two processes as discussed by Jones (1965); the synchrotron process may be regarded as the interaction of an electron with 'virtual' photons of a magnetic field having energy density $H^2/8\pi$. The two processes are competitive energy-loss mechanisms and their relative importance in various regions of the cosmos may be estimated by a comparison of equations (1.17) and (1.8). This comparison leads to the ratio $e P_s / P_c$ given by:

$$\frac{e P_s}{P_c} \approx \frac{3}{2} \left(\frac{H^2}{8\pi \rho} \right) \sin^2 \phi \quad (1.20)$$

where ϕ is the angle between the electron velocity vector and the local magnetic field H, i.e. the relative importance of the two mechanisms depends upon the ratio of the magnetic and photon field energy densities.

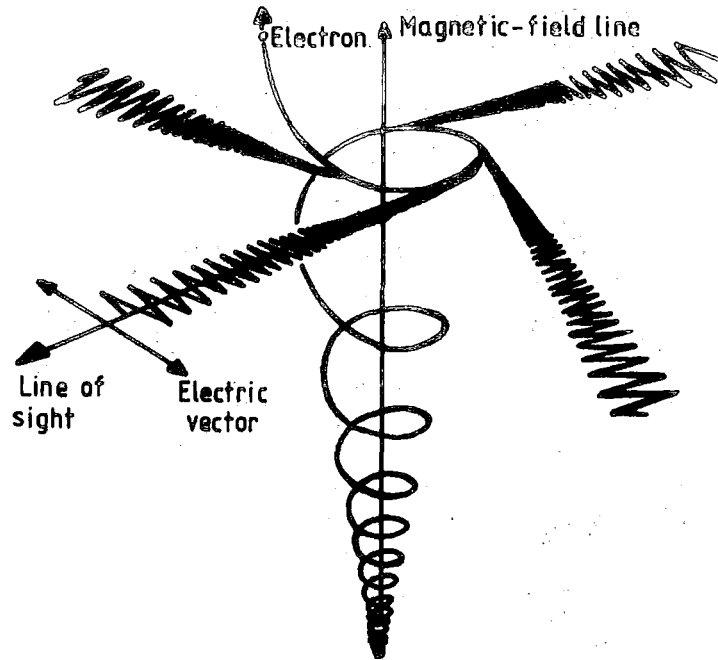


Figure 1.4 Idealized geometry, in perspective, for an electron moving in a magnetic field, emitting magnetobremstrahlung (synchrotron radiation) [Chupp (1977)]

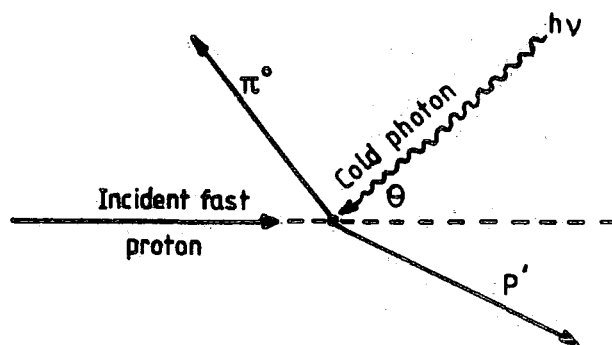


Figure 1.5 Photomeson production by a fast proton colliding with a cold photon. [Chupp (1977)]

Thus the Inverse Compton process is believed to dominate in interstellar and intergalactic space, however, in the vicinity of galactic nebulae such as the Crab nebula the synchrotron mechanism should become important and may even dominate.

1.3.4 Neutral Pi-Meson Decay

Neutral pions (π^0) are unstable particles which decay to produce, in practically 100% of cases, two gamma-rays which, in the rest frame of the meson, are of equal energy; $m_\pi c^2/2 \sim 70$ MeV: (π^0 rest frame lifetime = 10^{-16} s). In the terrestrial observer's frame of reference the two gamma photons have unequal energies which add up to the total energy of the pion E_π . In the extreme case of the two photons being emitted in the direction of motion of the pion, Stecker (1971) has shown that the maximum and minimum photon energies are:

$$\begin{aligned} E_{\max, \gamma} &= \frac{E_\pi}{2} (1 + \beta_\pi) \\ E_{\min, \gamma} &= \frac{E_\pi}{2} (1 - \beta_\pi) \end{aligned} \tag{1.21}$$

where $\beta_\pi = \frac{v_\pi}{c}$

Production of neutral pions in space may occur via any of the following mechanisms.

- (a) Photomeson production
- (b) Nucleon-Nucleon collision
- (c) Matter-Antimatter Annihilation
- (a) Photomeson production

The basic process, $\gamma + p = p + \pi^0$ (where p represents a proton), is shown schematically in figure 1.5 and involves the collision of an energetic proton with an optical or microwave photon γ . A threshold energy E_p^{th} is required of the proton for the production of a π^0 meson [Jackson (1962) and Fazio (1967)].

$$E_p^{th} = \frac{m_\pi c^2 (m_\pi c^2 + 2m_p c^2)}{2\epsilon_0 (1 + \cos \theta)} \quad (1.22)$$

where ϵ_0 is the photon energy in the laboratory frame of reference.

Consequently for a head-on collision of a proton with a thermal photon of $\epsilon_0 \sim 1$ eV, the threshold proton kinetic energy is approximately 10^{17} eV; since the rest energy of the pion ($m_\pi c^2$) is ~ 140 MeV.

(b) Nucleon-Nucleon collision

In this category the most important interaction of concern to astrophysics is the proton-proton collision, since 90% of cosmic rays are protons and 90% of the cool interstellar gas is hydrogen. From a basic p-p collision several individual combinations of secondary particles, including one or more π^0 mesons, are possible and Pollock and Fazio (1963) list the most important of these. Here also is given an expression for the threshold kinetic energy necessary to produce x mesons:

$$(K.E.)_{thresh} = x(280 + 10x) \text{ MeV} \quad (1.23)$$

Hence $(K.E.)_{thresh}$ for a single pion is 290 MeV.

Stecker (1971) gives for gamma-rays of energy E_γ , from a unit volume at distance \underline{r} from the earth, a production rate $q(E_\gamma, \underline{r})$:

$$q(E_\gamma, \underline{r}) = 4\pi n(\underline{r}) \int dE_p I(E_p, \underline{r}) \int_{E_{\pi min}}^{E_{\pi max}} dE_\pi \sigma(E_\pi, E_p) 2f(E_\gamma, E_\pi) \quad (1.24)$$

$\text{cm}^{-3} \text{s}^{-1} \Delta E_\gamma^{-1}$

where $n(\underline{r})$ is the hydrogen number density (cm^{-3}) at \underline{r} and $I(E_p, \underline{r})$ is the mean directional intensity of cosmic rays ($\text{cm}^{-2} \text{s}^{-1} \text{sr}^{-1}$) of energy E_p in the source volume, $\sigma(E_\pi, E_p) dE_\pi$ is the cross section for the production of a π^0 meson with energy E_π in the interval dE_π , and $f(E_\gamma, E_\pi)$ is the gamma-ray distribution function from π^0 decay where:

$$f(E_\gamma, E_\pi) = (E_\pi^2 - m_\pi^2)^{-\frac{1}{2}} \quad (1.25)$$

$$\text{for } \frac{E_\pi}{2} (1 - \beta_\pi) \leq E_\gamma \leq \frac{E_\pi}{2} (1 + \beta_\pi)$$

The predicted cosmic ray π^0 gamma-ray spectrum at Earth, taken from Stecker (1970), is shown in figure 1.7. The results shown are based on experimental production cross section data which are summarised by Stecker (1973) and shown in figure 1.6.

Neutral pion production from proton-alpha particle (α) (both p- α and α -p) is important since although the cosmic Helium abundance is about one tenth that of Hydrogen the multiplicity/cross section production is significantly larger at all energies for α interactions than for p-p.

(c) Matter-Antimatter annihilation.

Protons and Antiprotons may react to produce gamma radiation either by direct annihilation or through the intermediary of meson production. The latter case is the more important since the cross section for direct annihilation is smaller than that involving mesons by a factor $(\frac{1}{137})^2$. Stecker et al. (1971 a and b) have calculated the gamma-ray spectrum resulting from this mechanism for the particular case where the annihilations are at rest and this is shown in figure 1.8.

1.3.5 Bremsstrahlung

Radiation produced from the interaction of a charged particle with the nuclear coulomb field of another particle is known as Bremsstrahlung. Heitler (1954) gives for the bremsstrahlung differential cross section:

$$\sigma_B(E_o, E_\gamma) dE_\gamma = 4\sigma_o Z^2 \frac{dE_\gamma}{E_\gamma} f(E_\gamma, E_o) \quad (1.26)$$

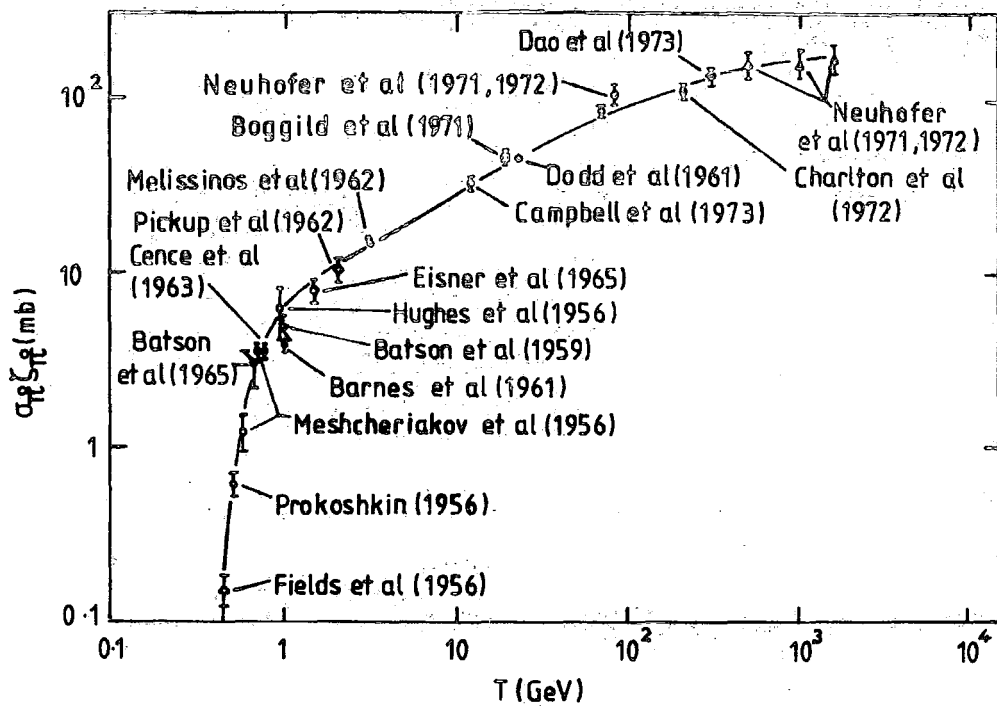


Figure 1-6 The experimental production cross section times multiplicity for π^0 meson production from p-p interactions. [Stecker (1973)]

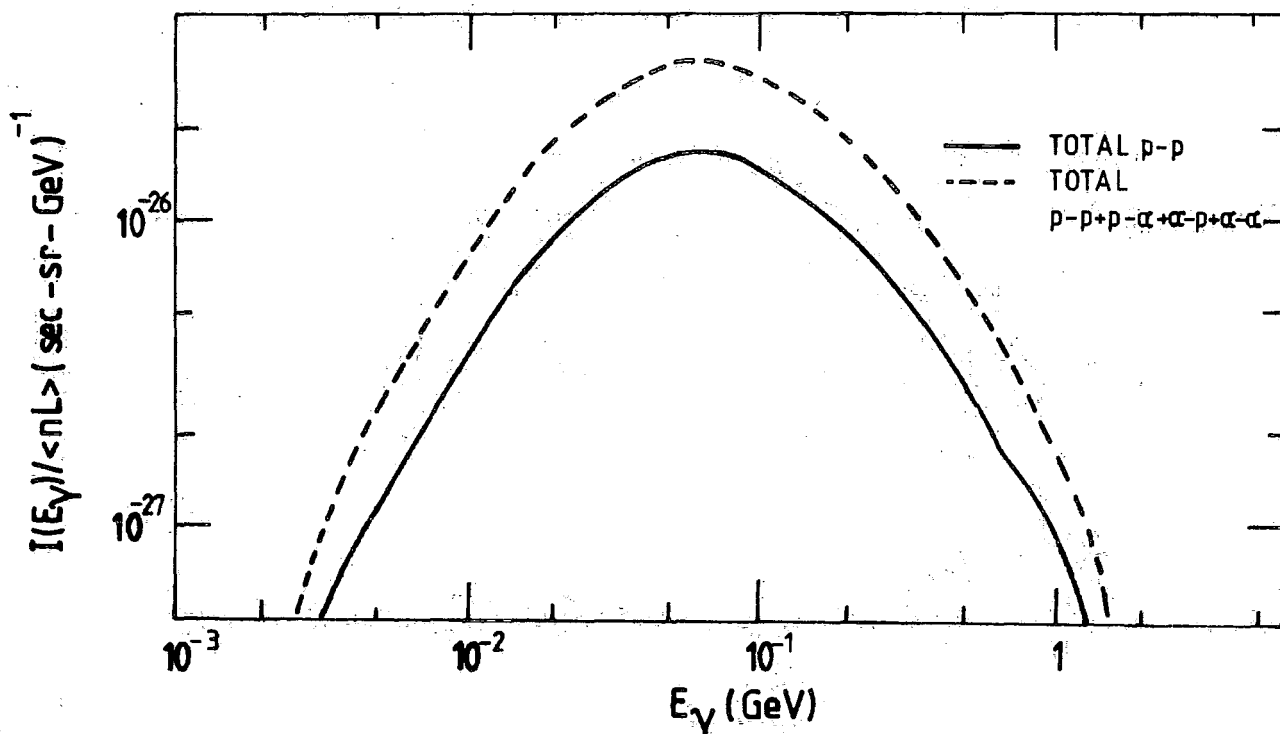


Figure 1-7 The calculated differential production spectrum of γ -rays produced in cosmic-ray interactions based on the isobar-plus-fireball model [Stecker (1970)]

where $\sigma_o = \frac{1}{137} \left(\frac{e^2}{M_o c^2} \right)^2$: (M_o is the incident particle rest mass)

and $f(E_\gamma, E_o)$ is the distribution function for gamma-ray production.

Thus the probability of emission of a bremsstrahlung photon of energy E_γ is inversely proportional to the square of the mass of the incident particle and consequently proton bremsstrahlung is negligible compared to that from electrons.

In the ultra-relativistic case the cross section may be approximated by:

$$\sigma_B(E_o, E_\gamma) dE_\gamma \sim \left(\frac{m}{X_o} \right) \frac{dE_\gamma}{E_\gamma} \text{ cm}^2 \quad (1.27)$$

where m represents the mass of the target atom and X_o is the radiation length. Applying the power-law electron spectrum $I_e(E) dE = K_e E_e^{-\alpha} dE$ Fazio (1967) has shown that the resulting differential gamma-ray spectrum is:

$$I_\gamma(E_\gamma) dE_\gamma = \frac{m N(L)}{X_o} \left(\frac{dE_\gamma}{E_\gamma} \right) \int_{E_\gamma}^{\infty} I_e(E) dE \quad (1.28)$$

where $N(L)$ is the integrated number of target nuclei in the line of sight.

This may be reduced to:

$$I_\gamma(E_\gamma) dE_\gamma = \frac{m N(L)}{X_o} \left(\frac{K_e}{\alpha-1} \right) E_\gamma^{-\alpha} dE_\gamma \quad (1.29)$$

1.3.6 Electron-Positron Annihilation

A collision involving an electron and its antiparticle the positron results in the complete annihilation of the two particles and the emission of one or more photons.

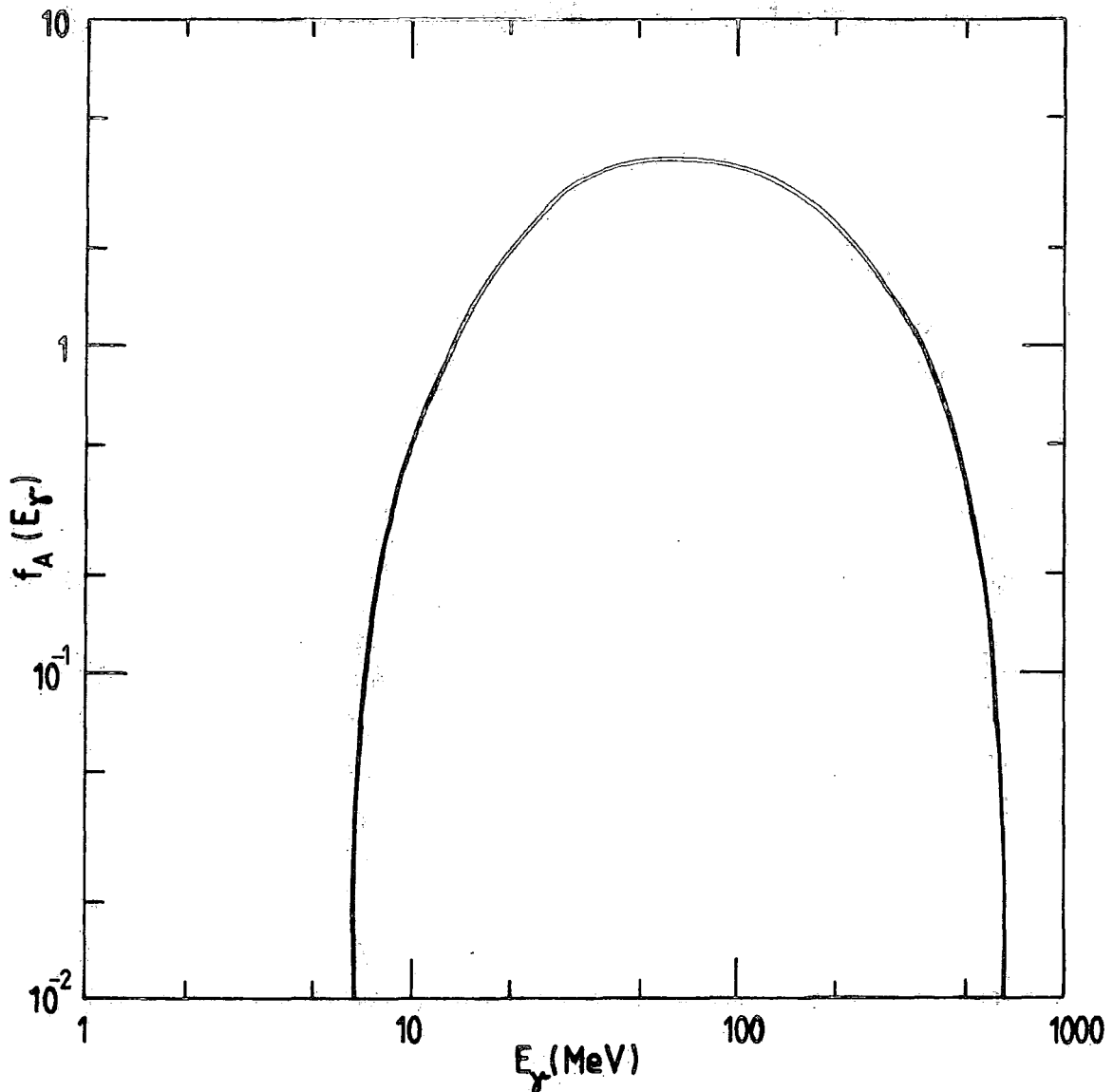


Figure 1-8 Normalised local π^0 gamma-ray spectrum from proton-antiproton annihilation at rest. [Stecker (1971)]

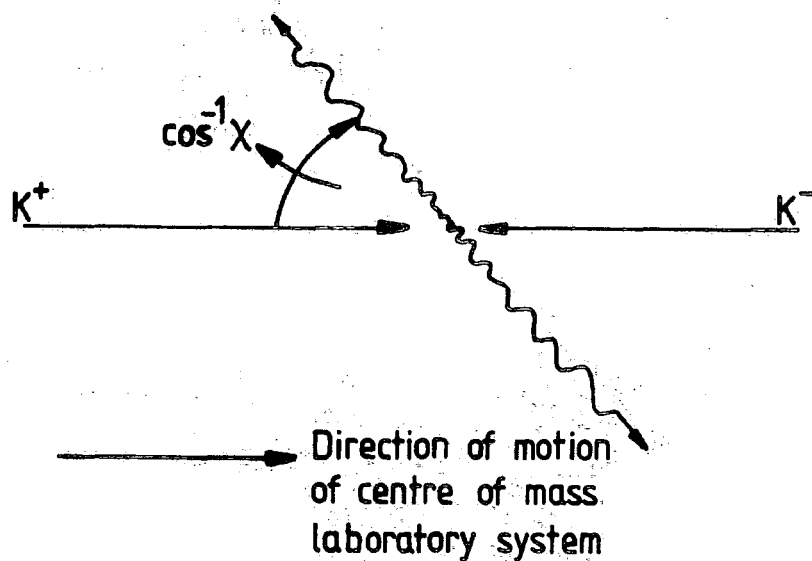


Figure 1-9 Two photon electron-positron annihilation in the centre of mass system. [Chupp (1977)]

Single photon emission is only possible where the electron is bound within an atom, since in such a case the single photon momentum may be balanced by the nucleus of the atom. It is thought that this mechanism is of little relevance to astrophysics. However, in-flight annihilation of a positron with a free electron is of greater significance. Here a plurality of photons is produced, but since the relativistic cross section for n photon annihilation ($n < 2$) is a factor $(1/137)^{(n-2)}$ less than that for the two photon process it is the latter which is normally considered [Stecker (1971)].

The differential cross section for gamma-ray production in the centre of mass frame of reference is:

$$d\sigma = \frac{\sigma_0}{2\gamma_c^2 \beta_c} \left\{ \frac{1 + \beta_c^2 (2 - \chi^2)}{(1 - \beta_c^2 \chi^2)} - \frac{2\beta_c^4 (1 - \chi)^2}{(1 - \beta_c^2 \chi^2)} \right\} d\chi \quad (1.30)$$

where $\sigma_0 = \pi r_0^2$; χ is as shown in figure 1.9; $\beta_c = \left(\frac{\gamma - 1}{\gamma + 1}\right)^{\frac{1}{2}}$ and $\gamma_c = \left(\frac{\gamma + 1}{2}\right)$ are the positron velocity and Lorentz factor in the centre of mass system for a laboratory frame Lorentz factor:

$$\gamma = \frac{E_+}{m_0 c^2} = (1 - \beta^2)^{-\frac{1}{2}}$$

where E_+ is the total energy of the positron. The energies of the emergent gamma-rays in the laboratory system are dependent on the angle χ :

$$E_\gamma = m_0 c^2 (1 + \beta_c \chi) \quad (1.31)$$

for $1 \leq \gamma < \infty$; $-1 \leq \chi \leq 1$

Hence for an annihilation at rest ($\gamma = 1$) the two photons are emitted with equal energy: $m_0 c^2 \sim 0.511$ MeV. In the ultra relativistic case the angular distribution of the emitted photons is strongly peaked at $\chi = \pm 1$, i.e. the photon emission in the laboratory system lies chiefly

along the velocity vector of the centre of mass and therefore the forward moving photon carries most of the available energy and the backward photon takes up the remainder which according to Stecker (1971) has a lower limit of 0.25 MeV.

The in-flight annihilation gamma-ray spectrum therefore has a low energy cut-off and an upper energy limit which is determined by E_+ . The actual shape of the spectrum between these energy limits depends upon the positron spectrum.

1.3.7 Nuclear De-Excitation

True gamma radiation occurs only when a nucleus in an excited state undergoes a transition to a lower energy state. A detailed treatment of radiative transitions is given by Cohen (1971). The instantaneous intensity of gamma-rays for a particular transition is:

$$N(s^{-1}) = N_i(t)A_{i \rightarrow f} \quad (1.32)$$

where N_i is the number of nuclei in a particular excited state and $A_{i \rightarrow f}(s^{-1})$ is the transition probability from the initial state i to the final state f producing a gamma-ray of energy $E_i - E_f$. $N_i(t)$ depends upon the mechanism producing the excited state and is discussed in terms of the process cross-section.

Nuclear gamma radiation is described in terms of the classical multipole description of an oscillating charge or current distribution. Cohen (1971) discusses two possibilities: (a) Electric multipole radiation $[(E-l)$ radiation] and (b) Magnetic multipole radiation $[(M-l)]$. In each of the cases the transition probability is given by:

$$(E - l) A_{i \rightarrow f} = \frac{2(l + 1)}{\hbar l [(2l + 1)!!]^2} \left(\frac{w}{c}\right)^{2l+1} Q_l^2 (s^{-1}) \quad (1.33)$$

$$(M - \ell) A_{i \rightarrow f} = \frac{2(\ell + 1)}{\hbar \ell [(2\ell + 1)!!]^2 c^2} \left(\frac{w}{c}\right)^{2\ell+1} A_\ell^2 (s^{-1}) \quad (1.34)$$

where ℓ is the angular momentum quantum number, w is angular frequency, $\hbar = \frac{h}{2\pi}$ (h is Planck's constant), Q_ℓ and A_ℓ are closely related to the electric and magnetic multipole oscillations causing the transition.

In practice experimentally determined life times of specific transitions are used as given by Lederer et al. (1968) or alternatively gamma-ray line production cross sections may be used which implicitly include the transition probability.

Excited states can be produced in several ways, e.g. by charged particle interactions: $(p, p'\gamma)$; $(\alpha, \alpha'\gamma)$; (p, γ) ; (α, γ) and by neutron interactions: $(n, n'\gamma)$; (n, γ) . Spallation reactions or fission can leave nuclei in excited states and also radioactive by-products which decay by particle emission (β^+ , β^- , $p, \alpha \dots$) can populate levels in daughter nuclei.

1.4 EXPECTED COSMIC SOURCES OF GAMMA-RAY LINE EMISSION

Supernovae are expected to contain radioactivity and Table 1.1 lists the lines which should be observable together with the relevant mean lives, yield of radioactive nuclei per Supernova, photon energy and number of photons per disintegration [Clayton et al. (1969), Lingenfelter and Ramaty (1978), Arnett (1978)]. The half lives of the isotopes are very important from the aspect of detectability since the gamma-rays cannot escape from the dense region of nucleosynthesis and if the decay of the nuclei occurs prior to significant expansion the lines will not be seen. This is particularly applicable to the ^{56}Ni decay chain. It is calculated that for an average Galactic Supernova rate of one in 25 years there should exist several remnants with ^{44}Ti radioactivity and possibly one with ^{22}Na emission observable by a detector of sensitivity 5×10^{-5} photons $\text{cm}^{-2} \text{s}^{-1}$. Cassiopeia A at a

Table 1.1 Gamma-ray producing chains from Supernovae and Novae
Ramaty (1978).

Decay Chain	Mean Life (yr)	Nuclei per Supernova	Photon Energy (MeV)	Photons or positrons per disintegration
$^{56}\text{Ni} \rightarrow ^{56}\text{Co} \rightarrow ^{56}\text{Fe}$	0.31	3×10^{54}	0.847	1
			1.238	0.70
			2.598	0.17
			1.771	0.16
			1.038	0.13
			e^+	0.2
$^{57}\text{Co} \rightarrow ^{57}\text{Fe}$	1.1	7×10^{52}	0.122	0.88
			0.014	0.88
			0.136	0.12
$^{22}\text{Na} \rightarrow ^{22}\text{Ne}$	3.8	$3 \times 10^{52} (10^{48}/\text{nova})$	1.275	1
			e^+	0.9
$^{44}\text{Ti} \rightarrow ^{44}\text{Sc} \rightarrow ^{44}\text{Ca}$	68	6×10^{51}	1.156	1
			0.078	1
			0.068	1
			e^+	0.94
$^{60}\text{Fe} \rightarrow ^{60}\text{Co} \rightarrow ^{60}\text{Ni}$	4.3×10^5	5×10^{50}	1.332	1
			1.173	1
			0.059	1
$^{26}\text{Al} \rightarrow ^{26}\text{Mg}$	1.1×10^6	4×10^{50}	1.809	1
			1.130	0.04
			e^+	0.85

distance of 2.8 kpc, having occurred only 300 years ago is a candidate for observation of the ^{44}Ti decay chain since the predicted flux is $\sim 4 \times 10^{-5}$ photons $\text{cm}^{-2}\text{s}^{-1}$. At 10 Mpc distance the Virgo cluster could present a steady source of 0.847 and 1.238 MeV lines from ^{56}Ni decay provided that the cluster Supernova rate exceeds $\sim 10 \text{ year}^{-1}$.

Doppler broadening determines the line widths owing to the velocity (10^4 kms^{-1}) of the expanding medium and this is expected to be $\sim 6\%$ except for ^{60}Fe and ^{26}Al where the broadening should be only $\sim 0.2\%$ since these isotopes essentially come to rest before decay due to their long mean lives.

Novae are currently believed to be caused by thermonuclear runaway in the CNO cycle resulting from accretion onto a white dwarf from a large, cool companion. Radio nuclei are synthesised during this process and therefore gamma-ray line emission is expected [Clayton and Hoyle (1974)]. The line which should be most easily detectable is that at 1.275 MeV from ^{22}Na decay. According to Truran (1978) the flux from a nova at 1 kpc is $\sim [8 \times 10^{-5} \exp(-t/3.8 \text{ years})]$ photons $\text{cm}^{-2}\text{s}^{-1}$, it is expected therefore, that for the estimated nova rate of $\sim 40 \text{ year}^{-1}$ a diffuse emission at 1.275 MeV should be detectable by an instrument of broad field of view while observing the Galactic plane.

Cosmic-ray interaction with the interstellar medium also should be a source of line emission [Meneguzzi and Reeves (1975)]. Prime candidates for detection are lines from ^{12}C , ^{14}N , ^{16}O , ^{20}Ne , ^{24}Mg , ^{28}Si , and ^{56}Fe (table 1.2) of which the strongest are predicted to be from $^{12}\text{C}^*$ and $^{16}\text{O}^*$ at 4.4 and 6.1 MeV respectively. The line widths for the collisional interactions depend upon whether the target nucleus lies (i) in the cosmic-ray beam (ii) in the stationary interstellar gas,

Table 1.2 Principal Gamma-Ray Lines from De-excitation
Ramaty (1978).

Production Process	Photon Energy (MeV)	Mean Lifetime (seconds)
${}^4\text{He}(\alpha, n){}^7\text{Be}^*$	0.431	2.7×10^{-13}
${}^4\text{He}(\alpha, p){}^7\text{Li}^*$	0.478	10^{-16}
${}^{56}\text{Fe}(p, p'){}^{56}\text{Fe}^*$	0.847	9.7×10^{-12}
${}^{56}\text{Fe}(p, n){}^{56}\text{Co}(e^+, e){}^{56}\text{Fe}^*$ (100%)		9.6×10^6
${}^{56}\text{Fe}(p, n'){}^{56}\text{Fe}^*$	1.238	1.0×10^{-12}
${}^{56}\text{Fe}(p, n){}^{56}\text{Co}(e^+, e){}^{56}\text{Fe}^*$ (67%)		9.6×10^6
${}^{24}\text{Mg}(p, p'){}^{24}\text{Mg}^*$	1.369	1.75×10^{-12}
${}^{20}\text{Ne}(p, p'){}^{20}\text{Ne}^*$	1.634	1.2×10^{-12}
${}^{28}\text{Si}(p, p'){}^{28}\text{Si}^*$	1.779	6.8×10^{-13}
${}^{14}\text{N}(p, p'){}^{14}\text{N}^*$	2.313	8.5×10^{-14}
${}^{14}\text{N}(p, n){}^{14}\text{O}(e^+){}^{14}\text{N}^*$ (100%)		102
${}^{12}\text{C}(p, p'){}^{12}\text{C}^*$	4.438	5.62×10^{-14}
${}^{16}\text{O}(p, x){}^{12}\text{C}^*$		5.62×10^{-14}
${}^{14}\text{N}(p, p'){}^{14}\text{N}^*$	5.105	1.2×10^{-11}
${}^{16}\text{O}(p, p'){}^{16}\text{O}^*$	6.129	2.4×10^{-11}
${}^{28}\text{Si}(p, p'){}^{28}\text{Si}^*$	6.878	2.5×10^{-12}

Table 1.3 Approximate local interstellar Emissivities and Diffuse Galactic fluxes from the direction of the Galactic Centre.
Ramaty (1978).

Mechanism	Photon Energy (MeV)	FWHM (keV)	Local Emissivity (photon/H atom) sec	Flux (Photon $\text{cm}^{-2}\text{s}^{-1}$ rad)
Inelastic	4.44	100	3×10^{-26}	6×10^{-5}
Collisions	6.129(grain)	8	5×10^{-27}	1×10^{-5}
($w = 1\text{eV cm}^{-3}$)	6.129(gas)	150	1×10^{-26}	2×10^{-5}
	0.847(total)	2	6×10^{-27}	1×10^{-5}
e^+ annihilation	0.511	5	2×10^{-25}	1×10^{-4}
${}^{26}\text{Al} \rightarrow {}^{26}\text{Mg}$	1.809	3	1×10^{-25}	7×10^{-5}
${}^{60}\text{Fe} \rightarrow {}^{60}\text{Co} \rightarrow {}^{60}\text{Ni}$	1.332	2	1×10^{-25}	7×10^{-5}
	1.173	2	1×10^{-25}	7×10^{-5}
	0.059	0.1	1×10^{-25}	7×10^{-5}
${}^{22}\text{Na} \rightarrow {}^{22}\text{Ne}$	1.275	10	2×10^{-25}	1×10^{-4}
π^0 Decay + Bremsstrahlung	>100	-	1.5×10^{-25}	1×10^{-4}

(iii) in interstellar dust grains. In the first and second cases the widths should be ~ 1 MeV, due to the high velocity of the targets, and ~ 100 keV from recoiling nuclei emission, respectively. For case (iii) the width depends on the target nucleus excitation lifetime and the size and composition of the containing grain.

Intensities for the 0.511 MeV line from nucleosynthesis processes and lines from ^{26}Al , ^{60}Fe and ^{21}Na decay can be estimated from the emissivities per hydrogen atom in the solar system and the fluxes are given in Table 1.3.

Matter accreting onto neutron stars may produce line radiation from inelastic collisions induced by the accreting particles [Ramaty et al. (1973)]. Electron pairs created on pulsars and the resultant positron annihilation can produce a line at 0.511 MeV [Sturrock (1971)]. Gravitation would produce red shifts of these lines of $\sim 20\%$ if the emission originated from the star's surface and Brecher (1971) suggests that from identification of the line, the degree of red shift and a mass determination then the neutron star's internal composition may be revealed.

Extragalactic line emission is expected from objects in which non-thermal processes are dominant and nucleosynthesis in extragalactic Supernovae may in the past have significantly contributed to the Universal background around 0.5 to 0.8 MeV from the decay of ^{61}Ni [Clayton and Silk (1969)]. It is believed that despite cosmological red-shift broadening these lines could be discernible in the background and so provide information on the nucleosynthesis rate at earlier epochs.

CHAPTER 2METHODS AND OBSERVATIONAL STATUSOF GAMMA-RAY ASTRONOMY2.1 DETECTION METHODS

The crucial fact of concern to the design of instruments for gamma-ray astronomy is that at the energies in question the photons cannot be reflected or directly focussed as those of lower energy can, rather, they penetrate matter and tend to lose energy in interactions with electrons, as described in Chapter 4, Sections 4.1 and 4.2. Thus at photon energies in the gamma-ray region less than ~ 10 MeV all of the instruments currently in use or proposed for astronomical research utilise those electrons by employing scintillation and/or solid-state detectors arranged in various configurations to produce pulses which may then be processed using pulse-height analysis.

There are principally two sorts of device:

- (i) the so called Compton Telescope.
- (ii) actively shielded devices.

Figure 2.1 helps to illustrate the operational principle of the Compton telescope. S1 and S2 are arrays of scintillation elements, where each element is optically isolated from the rest. A gamma photon γ_0 compton scatters in scintillator S1 and the secondary photon γ_1 undergoes a further interaction in S2. The recoil electron e_1 produces a start pulse in S1 for a delayed coincidence with the pulse in S2 from e_2 and the direction of γ_0 is determined from the kinematics of the Compton scattering using the pulse-heights from the electrons e_1 and e_2 . Knowledge of the specific cells which record the delayed coincidence approximately defines the direction of scattered photon γ_1 . The figure shows that a neutron can produce a similar response if it inelastically scatters in S1, however, the transit time from S1 to S2 for the neutron is typically

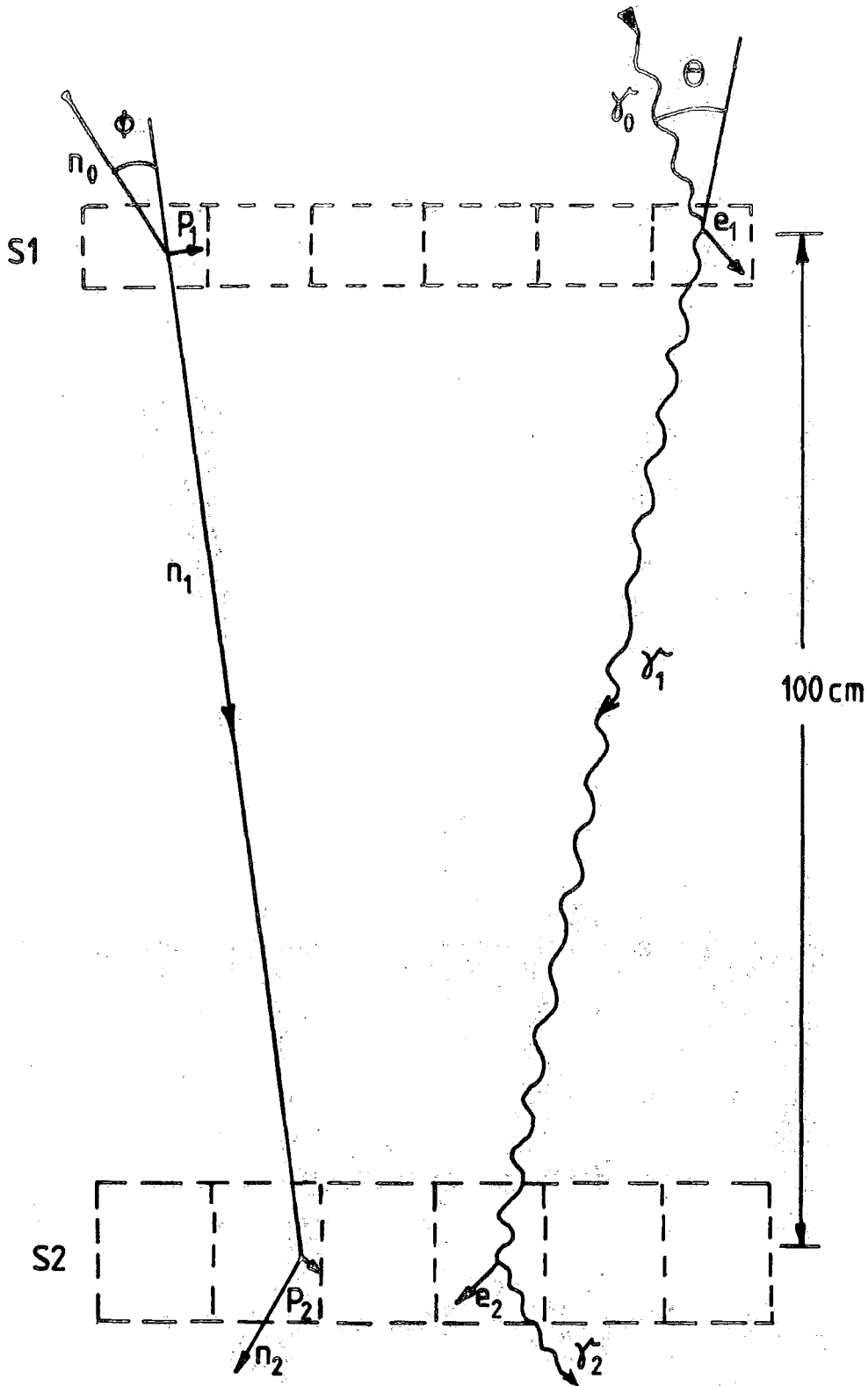


Figure 2.1 Illustration of the basic principle of the Compton telescope.

much greater than that for the gamma-ray so the two types of event can be separated. Upward moving gamma-rays are eliminated by the coincidence arrangement. Accepted incident gamma-rays may, however, only be defined to lie on the surface of a cone of half angle θ since there is no information concerning the direction of e_1 . The projection of the cone onto the sky is called the event circle. The energy of γ_0 is:

$$E_{\gamma_0} = E_{e_1} + E_{\gamma_1} \quad (2.1)$$

and from equation (4.7)

$$\cos \theta = 1 + m_0 c^2 \left(\frac{1}{E_{\gamma_0}} - \frac{1}{E_{\gamma_1}} \right) \quad (2.2)$$

where:

$$E_{\gamma_1} = E_{e_2} + E_{\gamma_2} \quad (2.3)$$

E_{e_1} and E_{e_2} are the measured pulse heights in S1 and S2. If γ_1 is totally absorbed in S2 then $E_{\gamma_1} = E_{e_2}$ and hence:

$$E_{\gamma_0} = E_{e_1} + E_{e_2} \quad (2.4)$$

and:

$$\cos \bar{\theta} = 1 + m_0 c^2 \left(\frac{1}{E_{e_1} + E_{e_2}} - \frac{1}{E_{e_2}} \right) \quad (2.5)$$

where $\bar{\theta}$ is an approximation to the true value θ and since E_{e_2} is usually less than E_{γ_1} then $\bar{\theta}$ must be an upper limit to the scattering angle. From $\bar{\theta}$ an approximation to E_{γ_0} is obtained.

The telescope has an imaging property for celestial point sources in the field of view. For the scattered gamma-rays that are totally absorbed in S2 then the various values of $\bar{\theta}$ represent the true scattering angles and the event circles of the gamma-rays from the point source will intersect at one point. Because only totally absorbed events

from a point source are accepted the energy resolution is good and there is almost complete suppression of the gamma-ray line Compton tails.

Originally the Compton telescope approach is due to Schönfelder et al. (1973) and several telescopes of this sort are now in use [Herzo et al. 1975; Graml et al., 1977, 1978; White et al. 1978] which uses a combination of liquid scintillation elements for the S1 array and NaI(Tl) for S2, has an angular resolution of $\sim 10^\circ$ (FWHM) within a 40° (FWHM) field of view and an energy resolution of slightly better than 10% (FWHM) at energies above ~ 1 MeV. During a three hour balloon flight the 3σ detection sensitivity for a 1 MeV gamma-ray line is reported as being 1.4×10^{-3} photons $\text{cm}^{-2}\text{s}^{-1}$.

Actively shielded devices are, however, the most commonly used systems for nuclear line region gamma-ray astronomy. These instruments comprise one or more central alkali-halide scintillation or solid-state detectors, usually thallium activated sodium iodide [NaI(Tl)] or germanium {either lithium drifted germanium [Ge(Li)] or high purity germanium (Ge)}, surrounded by an alkali-halide scintillation anti-coincidence shield. Such shielding typically restricts the field of view of the central detector to $\sim 10^\circ$ to 30° (FWHM) and is effective in suppressing most components of the radiation background. There are effectively two elements to the shielding in this arrangement: (a) the passive element, where the scintillator simply acts as an absorber and (b) the active element, where the scintillation property of the material is put to use by the detection of photons which Compton scatter within it and subsequently interact in the central detector therefore allowing such an event to be vetoed. This active aspect of the shielding has been found in practice to reduce background by a factor of ~ 40 at around 1 MeV over that using passive shielding alone.

Solid-state Ge and Ge(Li) crystals produce much higher energy resolution than NaI(Tl) scintillation crystals, typically $\sim 0.25\%$ as compared to $\sim 7\%$ respectively; and therefore the germanium devices may seem to be the better choice. However, other factors must be considered, for in addition to resolution, the full energy peak efficiency and detector area are directly involved in gamma-ray line sensitivity. In the 0.1 to 10 MeV energy range NaI(Tl) has a much higher detection efficiency, for the size of detectors currently available, than Ge, as shown in table 2.1. From a practical viewpoint the poorer energy resolution of scintillators is offset by the larger detection areas and higher efficiencies. Kurfess (1978) gives the case for the future role of scintillation detectors in gamma-ray spectroscopy.

An example of a spectrometer using NaI(Tl) as its central detector is an instrument developed at Rice University; shown in cross sectional diagrammatic form in figure 2.2. The device has a 15° (FWHM) aperture provided by an NaI(Tl) anticoincidence shield, an energy resolution of 11% at 662 keV and a 511 keV gamma-ray line sensitivity at the 3σ level of 1.5×10^{-3} photons $\text{cm}^{-2} \text{s}^{-1}$. Observations of the galactic centre and N.G.C. 4151 have been performed with this spectrometer and a similar device; [Haymes et al. (1969), Johnson et al. (1972), Johnson and Haymes (1973), Haymes et al. (1975), Meegan and Haymes (1979)].

Figure 2.3 shows in cross section the design of an actively shielded Ge(Li) instrument used by Leventhal et al. (1980) of the Bell/Sandia laboratories. Note the accompanying vacuum cryostat and dewar containing liquid nitrogen which are essential requisites for Ge and Ge(Li) detectors. Apart from Ge(Li) detectors needing a low temperature ($\sim -80^\circ\text{C}$) to freeze the drifted Li profile, both types of crystal also require cooling to liquid nitrogen temperatures to eliminate noise due to thermally generated leakage currents which adversely affect energy resolution.

Table 2.1 Comparison of full energy peak efficiency and energy resolution between typical sizes of NaI and Ge crystals.
Kurfess (1978).

Energy (MeV)	Full Energy Peak Efficiency		Energy Resolution (MeV)	
	NaI 20cmx10cm	Ge 5cmx5cm	NaI 20cmx10cm	Ge 5cmx5cm
0.1	0.95	0.70	20	2
0.5	0.85	0.30	45	2
1.0	0.65	0.15	65	3
2.0	0.47	0.08	95	4
5.0	0.30	0.05*	150	5

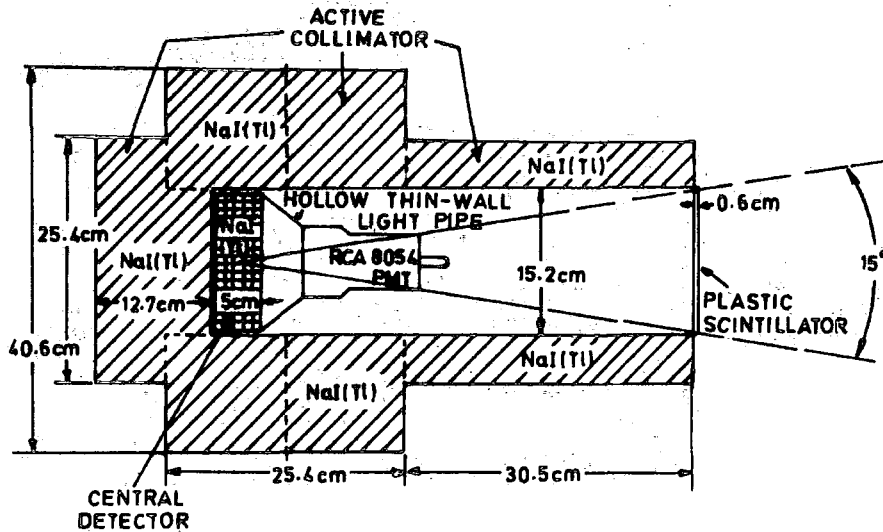


Figure 2.2 A cross sectional view of the Rice University gamma-ray spectrometer.
[Meegan (1978)]

The reported aperture and energy resolution of the Bell/Sandia spectrometer are $\sim 13^\circ$ (FWHM) at 1.33 MeV and $\sim 1\%$ at 511 keV respectively and the 3σ level 511 keV line sensitivity is 1.9×10^{-3} photons $\text{cm}^{-2}\text{s}^{-1}$.

In an attempt to compensate for the limitation in volume of germanium detectors the Jet Propulsion Laboratory produced a spectrometer which operates a matrix of four Ge(Li) crystals each of 40 cm^3 volume. A diagram of this device, which was the first to produce a celestial gamma-ray line observation [Jacobson et al. (1975)], is given in figure 2.4. The system resolution is 2.5 keV at 1 MeV and the collimation, which in this case is provided by an alternative alkali-halide scintillator, sodium activated Cesium iodide [(CsI(Na))], defines a solid angle of 0.095 sr. Over the energy range 0.05 to 10 MeV the sensitivity is 10^{-4} to 10^{-3} photons $\text{cm}^{-2}\text{s}^{-1}$.

Though it may be argued that there is still potential for actively shielded alkali-halide spectrometers there is no doubt that the advent of Ge(Li) and Ge detectors has revolutionised astronomical gamma-ray spectroscopy with their ability to pick out fine structure in the spectra from celestial sources. The Durham spectrometer, described in Chapter 3, is an actively shielded instrument using a Ge crystal rather than Ge(Li) because of the relative ease with which it can be handled.

2.2 DETECTOR BACKGROUND

From a gamma-ray source in a direction θ and ϕ the limiting measurable line flux for a detector in a balloon or satellite environment is:

$$F_{\min} \leq \frac{n}{S(E, \theta, \phi)} \sqrt{\frac{2[dB(E)/dE]\Delta E}{T_{\text{obs}}}} \quad (2.6)$$

assuming a null source count rate; where n is the number of standard deviations σ above the background, that corresponds to a detectable signal (commonly taken as 2 or 3); ΔE is the energy resolution of the instrument

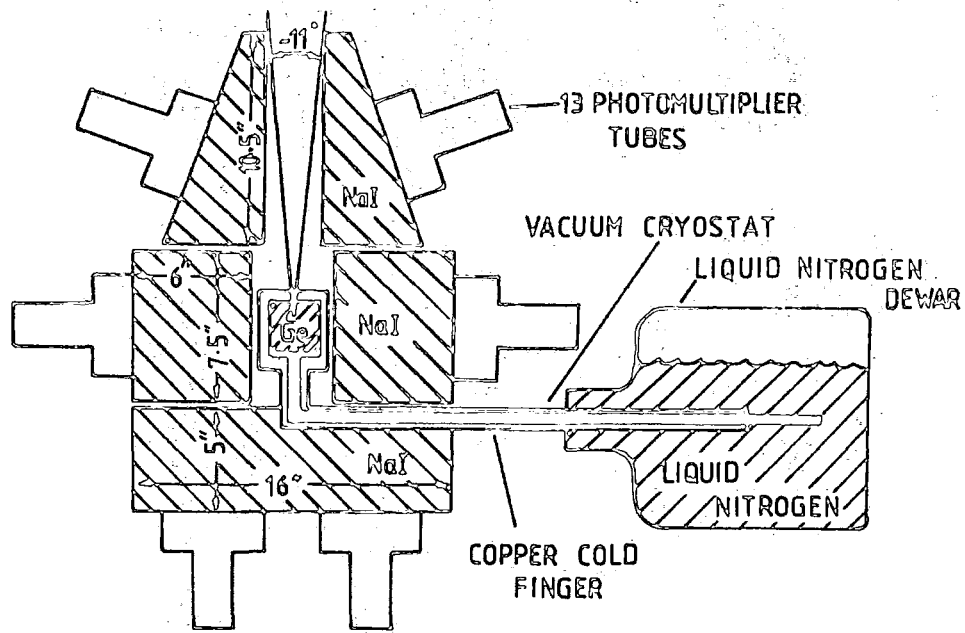


Figure 2.3 A cross sectional view of Bell-Sandia apparatus. [Leventhal et al (1977)]

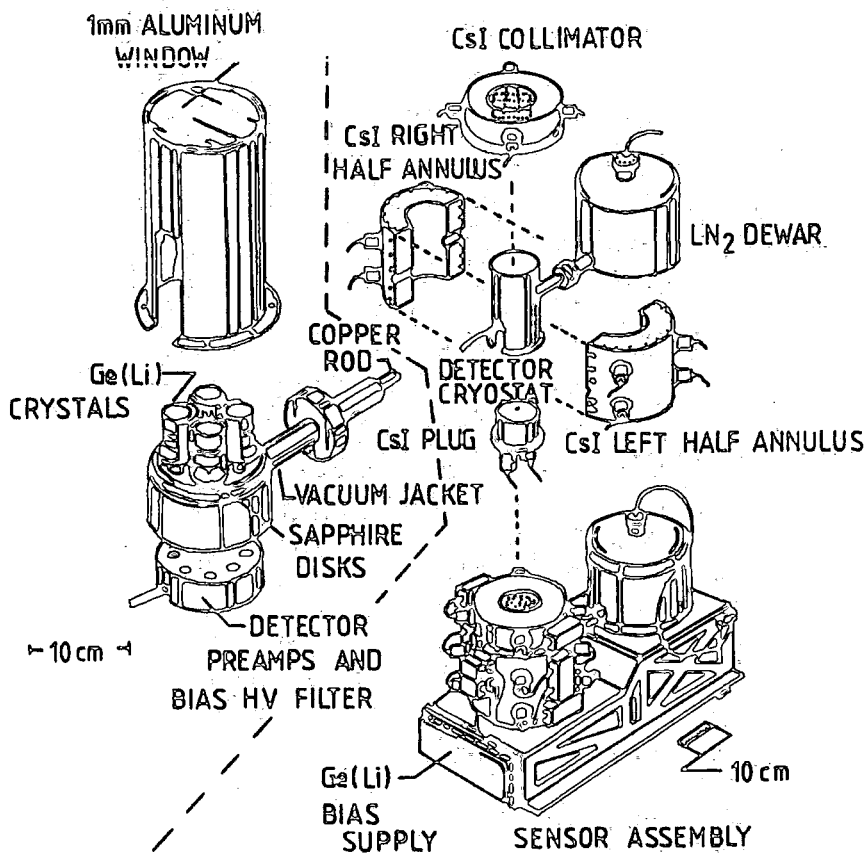


Figure 2.4 The Jet Propulsion Laboratory four-headed gamma-ray spectrometer. [Jacobson et al (1978)]

at energy E ; T_{obs} is the length of time for which the source (and background) is measured; $S(E, \theta, \phi)$ is the sensitivity of the detector to a photon of energy E which enters it from the direction (θ, ϕ) ; $dB(E)/dE$ is the net differential background count rate [in counts (unit energy interval)⁻¹ (unit time)⁻¹].

Consequently it is very important in any balloon or satellite work to achieve as low a background as possible and this may only be done from a good understanding of the various sources of background, of which there are basically three: (i) Atmospheric (ii) Intrinsic activity (iii) Local production. Ling (1974) has produced a means by which to quantify $dB(E)/dE$. Consider a detector of acceptance solid angle $\Delta\Omega$ and full energy sensitivity $S(E, \alpha) \text{cm}^2$ to photons of energy E incident at angle α to the axis from a volume element which emits $A_o(E, h')$ photons of energy E (unit energy)⁻¹ (g air)⁻¹ s⁻¹ at a distance r . Then at atmospheric depth $h(\text{g cm}^{-2})$ the detector counting rate, when viewing at zenith angle θ so that $\alpha = 0$, due to total background in a band width ΔE at E is given by:

$$\begin{aligned} \frac{dB(E)}{dE} \Delta E &= \int_{\Delta\Omega} \int_{\Delta E} \int_0^{h \sec \theta} S(E, 0) \frac{A_o(E, h') \rho(h')}{4\pi} \exp[-r'/\lambda(E)] dr dE d\Omega \\ &+ \int_{\Delta\Omega} \int_{\Delta E} S(E, 0) F_D(E) \exp[-h \sec \theta / \lambda(E)] dE d\Omega \quad (2.7) \\ &+ (\text{Background rate from activation etc.}) \end{aligned}$$

where $\rho(h')$ is the atmospheric density at the depth of the source element; $r' = \int_0^r \rho(r) dr$ (g cm^{-2}), and $\lambda(E)$ is the absorption mean free path for photons of energy E in g cm^{-2} .

The first term is the atmospheric gamma-ray flux in the form of a source function $A_o(E, h')$ expressed as the number of photons of energy E in ΔE emitted per second from a gramme of air at a particular latitude. This source function is determined empirically from balloon flight

measurements [Ling (1974)]. Term two represents the diffuse cosmic gamma-ray flux which reaches the detector through the atmosphere.

Equation (2.6) gives the flux sensitivity once the relation in equation (2.7) is determined for the particular detector system. Beuermann (1971) has developed a model for atmospheric gamma radiation around 10 MeV which consists of two components: (i) π^0 meson decay; having a broad peak around 70 MeV (ii) Primary, secondary and re-entrant albedo electron bremsstrahlung, and this work, which is limited to a cut off rigidity of 4.5 GV has subsequently been extended to a range of rigidity values by Daniel and Stephens (1974). The predicted spectra from this model and that of Ling (1975) are shown in figure 2.5 in comparison with experimental data. A shoulder at ~ 70 MeV is evident in the figure which gives support to Beuermann's model.

Figure 2.6 illustrates the results of measurements [Schönfelder et al. (1975)] of the vertical atmospheric gamma-ray energy spectrum for various depths in the atmosphere, together with the theoretical predictions. Study of the figure reveals the flux as being a function of the depth; rising to a maximum at $\sim 100 \text{ g cm}^{-2}$ (the Pfozter maximum). The models mentioned all produce flux predictions which are equal to or smaller than the measurements.

In addition the atmospheric gamma-ray flux is also dependent upon Zenith Angle. Increasing the Zenith Angle results in an increased source volume contribution to the counting rate. This dependence is expected to be less than $\sec \theta$ at small atmospheric depths owing to the curvature of the atmosphere. The work of Ling (1975) is in agreement with Compton telescope measurements of Schönfelder et al. (1977) for $0^\circ \leq \text{Z.A.} \leq 120^\circ$ where a steady increase is observed, however there is disagreement at angles $> 120^\circ$; an observed maximum is not predicted on

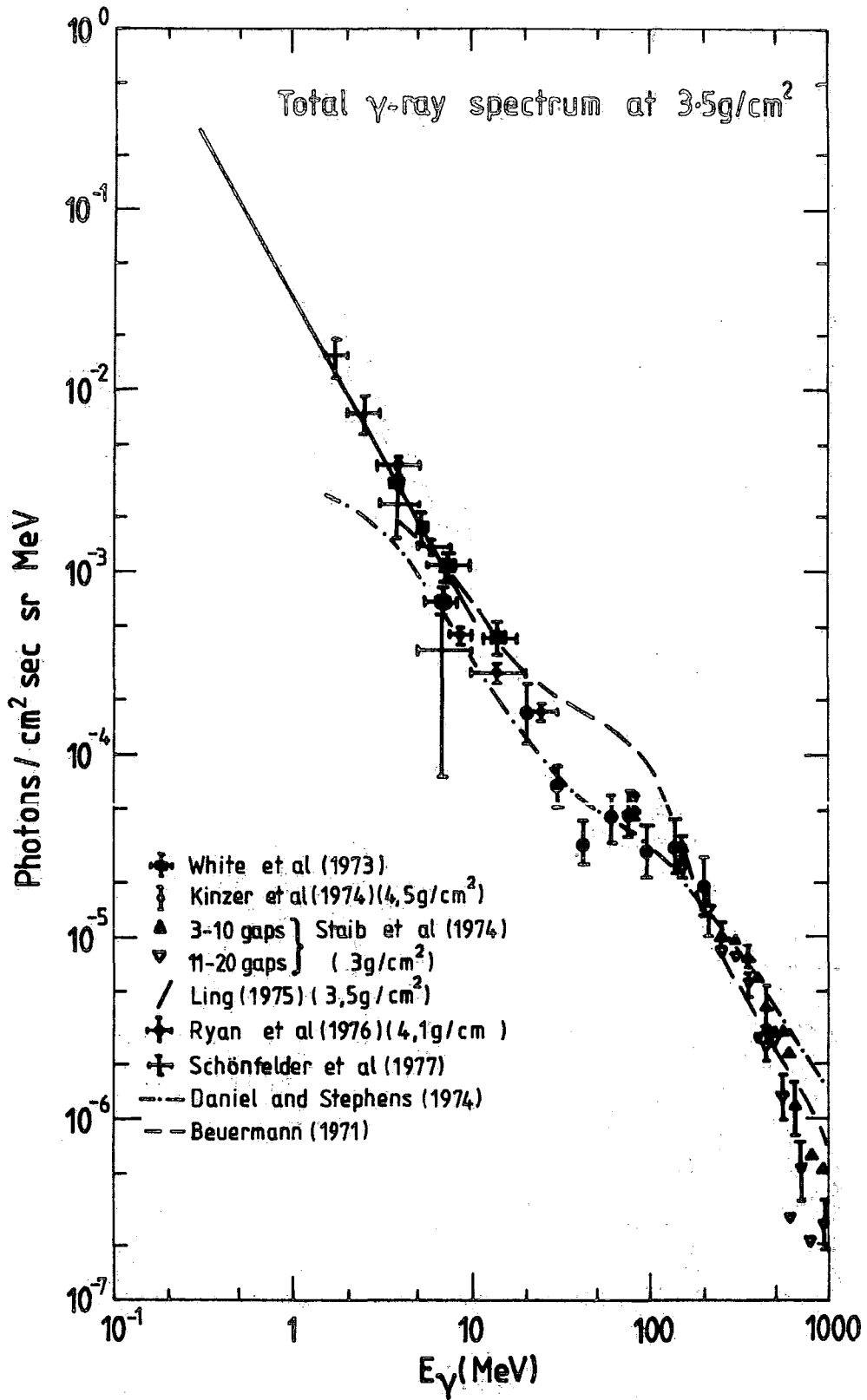


Figure 2-5 Total gamma-ray spectrum at an atmospheric depth of $3.5\text{g}/\text{cm}^2$.

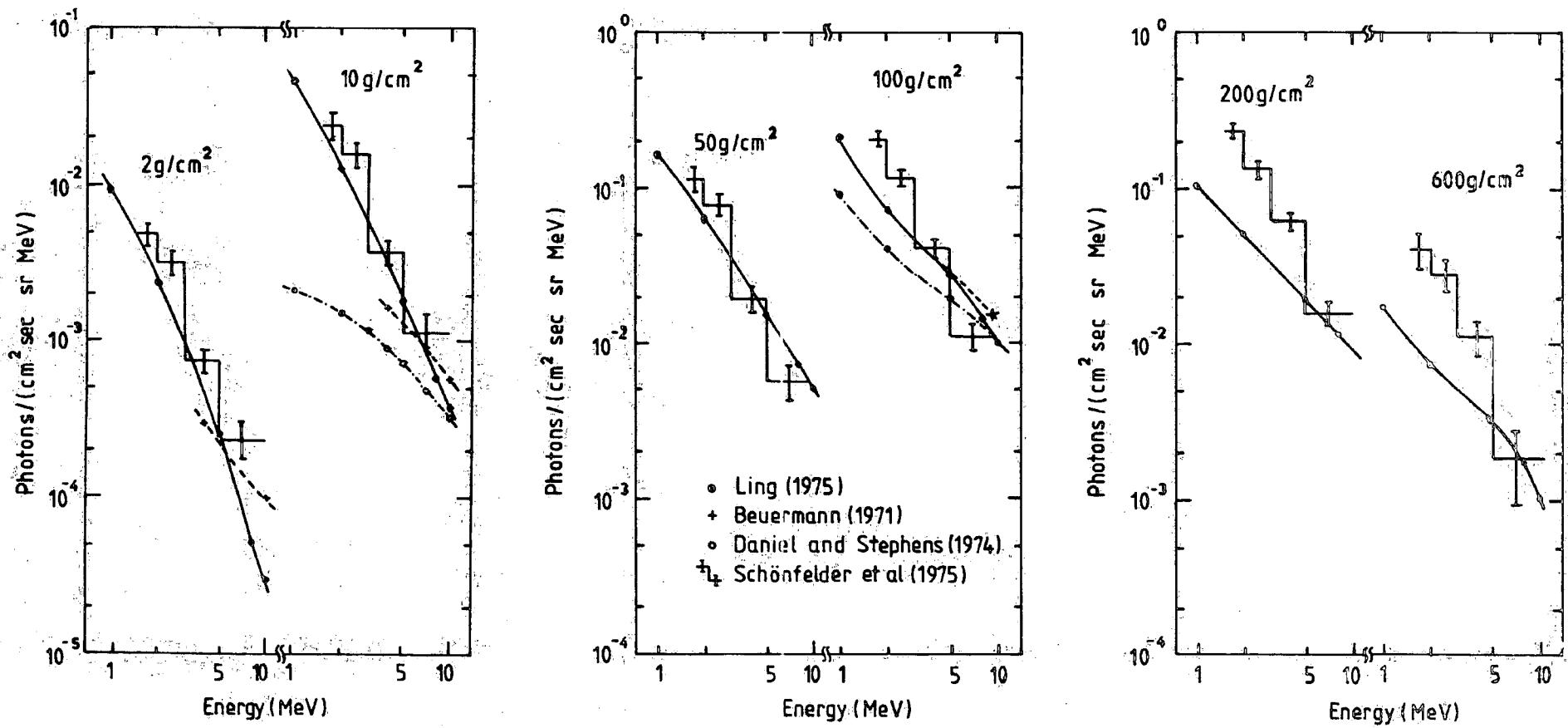


Figure 2.6 The vertical atmospheric gamma ray spectrum at various atmospheric depths.

Ling's model, however, Graser and Schönfelder (1977) have produced a maximum exhibiting model at the required Z.A.

Line radiation is also produced in the atmosphere, principally at 0.511 MeV by positron annihilation and de-excitation radiation is found from neutron capture or inelastic scattering on ^{14}N and ^{16}O nuclei.

Atmospheric 0.511 MeV radiation has been measured as a function of depth by several workers [Peterson (1963), Rocchia et al. (1965), Chupp et al. (1970) and Kasturirangan et al. (1972)] and the results are consistent with calculation. Typical values for the 0.511 MeV line flux are: (0.09 ± 0.01) and (0.2 ± 0.02) photons $\text{cm}^{-2}\text{s}^{-1}$ at 6 and 3.9 g cm^{-2} depth respectively.

Predicted and measured fluxes for other atmospheric lines are given in Table 2.2.

The materials used in the construction of a spectrometer can themselves produce radiation which contributes to the background. Such contribution arises in two ways: (i) local production; arising as a result of neutron and proton interaction with the spectrometer materials (ii) natural radioactivity contained in the materials. [Kreger and Mather (1967), Van Lieshout et al. (1966)].

In the case of local production, neutron interactions dominate for balloon based systems because of the high ratio of atmospheric neutron to proton background. Quantitative estimates of the neutron effect have been made by Ling (1974) and Ling and Gruber (1977). The net effect of atmospheric neutron interaction is more important in a shielded system than an unshielded one as although the shield reduces the atmospheric photon component, the neutron contribution is not so affected, hence the shields should not be made too thick otherwise local production dominates the background [Bhat and Thompson (1981)]. In NaI(Tl) and CsI(Na) the neutron interaction background spectrum has three parts: (i) Around 439 keV there are line features superimposed on a continuum arising from

Table 2.2 Measured and predicted atmospheric gamma-ray line fluxes

- (a) Orwig (1972) Private communication to J.C. Ling.
 (b) Kurfess (1972) Private communication to J.C. Ling.
 (c) Willett et al. (1979)
 (d) Albernhe and Vedrenne (1976)
 (e) Peterson et al. (1973)

Energy (MeV)	Process	Measured flux at $\lambda = 40^\circ$ (photons $\text{cm}^{-2}\text{s}^{-1}$)	Predicted Flux at 3.5 g cm^{-2} $\lambda = 40^\circ$ (photons $\text{cm}^{-2}\text{s}^{-1}$)
	$^{14}\text{N}(n, n' r) ^{19}\text{N}$	1×10^{-2} (b)	1.19×10^{-2}
4.44	$^{14}\text{N}(n, \alpha) ^{11}\text{B}$	1.5×10^{-2} (a) 1.36×10^{-2} (b)	3.21×10^{-3}
4.49	$^{14}\text{N}(n, \gamma) ^{15}\text{N}$	$< 8.7 \times 10^{-5}$ (e)	9.68×10^{-5}
6.087	$^{14}\text{N}(n, p) ^{14}\text{C}$	2.5×10^{-2} (a) 6.0×10^{-3} (b)	3.94×10^{-4}
6.129	$^{16}\text{O}(n, n\gamma) ^{16}\text{O}$	7.7×10^{-3} (c) 7.3×10^{-3} (d)	7.33×10^{-3}
6.32	$^{14}\text{N}(N, \gamma) ^{15}\text{N}$	$< 7.3 \times 10^{-5}$	1.31×10^{-4}
6.44	$^{14}\text{N}(n, n', \gamma) ^{14}\text{N}$		1.36×10^{-3}
6.92	$^{16}\text{O}(n, \lambda', \gamma) ^{16}\text{O}$		1.69×10^{-3}

fast neutrons, (ii) Below 2.2 MeV beta decay of I^{128} produces a flat spectrum, (iii) around 6.8 MeV there is a peak arising from slow neutron capture.

Most materials contain the natural activities ^{40}K , Ra and Th which produce numerous emissions, both continuum and discrete, at gamma-ray energies. For example: (a) ^{40}K decays by β^- emission to ^{40}Ca or alternatively to ^{40}Ar by β^+/EC decay which results in gamma emission at 1.46 MeV, (b) Thorium may be identified by the detection of a gamma-ray line at 2.62 MeV from the first excited state of ^{208}Pb (ThD) which is populated by β^- decays of ^{208}Tl (ThC"). Manufacturers of detector crystals and photomultiplier tubes attempt to keep all naturally occurring activities as low as possible in their raw materials. This source of background could become important in the future as the sensitivity of gamma-ray experiments is increased.

2.3 OBSERVATIONS OF EXTRATERRESTRIAL GAMMA RADIATION

2.3.1 The Cosmic Gamma-ray Background

Since the existence of a cosmic gamma-ray flux was established by the Ranger 3 and 5 spacecraft observations discussed in Section 1.2 several further attempts have been made to measure it using balloon and satellite borne detectors. These have identified two components, a Galactic part which exhibits a peak in the direction of the plane of the Galaxy and an isotropic part, the diffuse background.

Observationally there appears to be agreement about the shape of the diffuse radiation energy spectrum, as shown in figure 2.7. However, the origin of the flux and in particular that of a shoulder around 3 MeV is still uncertain owing to (a) the lack of observational evidence concerning the gamma-ray luminosities of galaxies etc. and (b) an excess of free parameters in all of the suggested models of truly diffuse production in intergalactic space. Stecker (1969) and Stecker

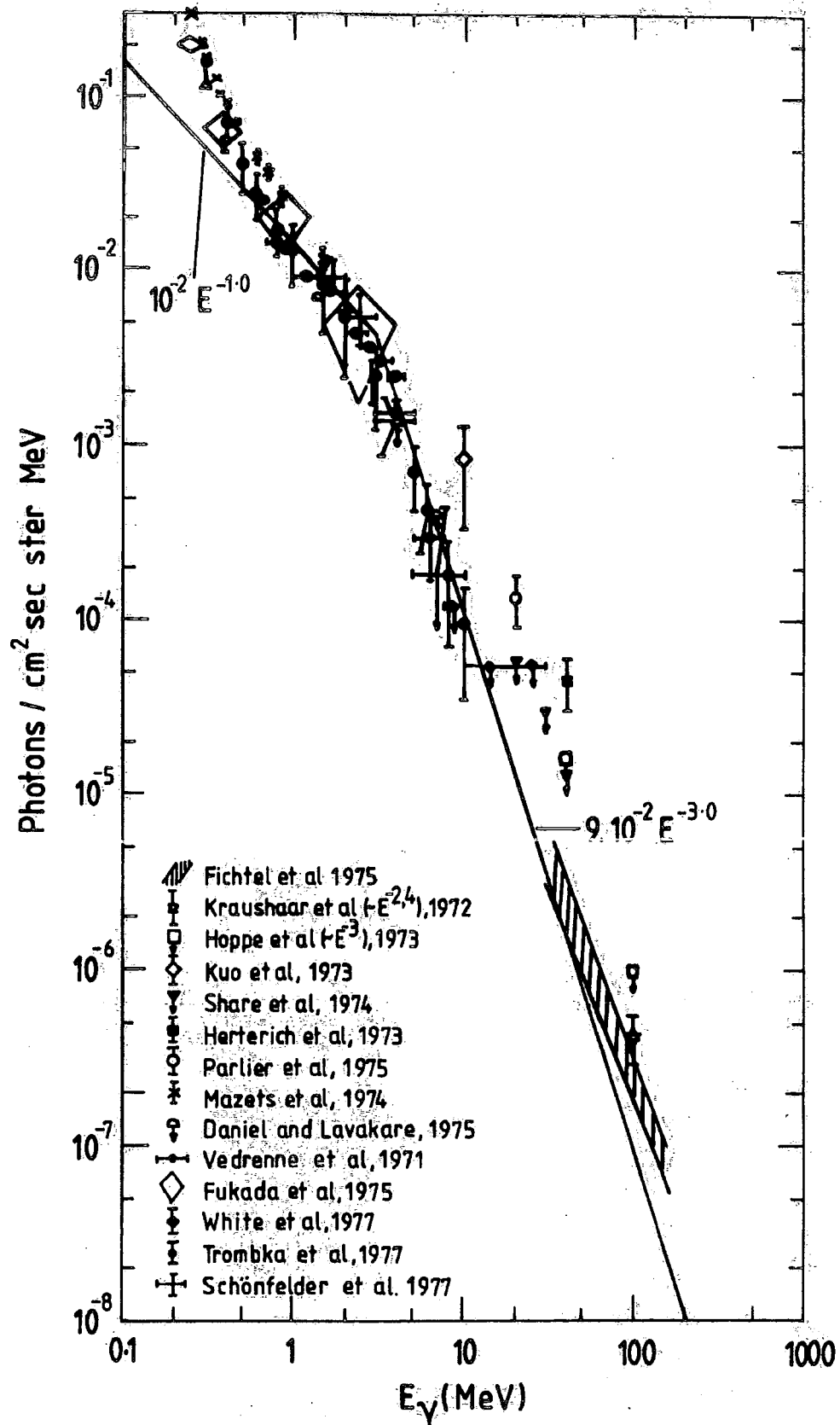


Figure 2-7 The Diffuse Cosmic γ -ray Spectrum.
 [Graml et al (1978)]

et al. (1971) have proposed two models for the cause of the 3 MeV shoulder based on the fact that the differential gamma-ray energy spectrum from π^0 meson decay peaks at ~ 70 MeV and this may easily be displaced to the 3 MeV region if the production occurs largely at red shifts around $Z = 100$. The π^0 mesons themselves would be produced from a copious supply of cosmic rays from the big bang or by simultaneous baryon-anti baryon annihilation. More recently, Rocchia et al. (1976) have indicated that the feature could result from Compton interactions of gamma-rays with low energy electrons around discrete sources, for example, Seyfert galaxies [Grindlay (1978)] and this has been given observational support by the detection of radiation > 1 MeV from N.G.C. 4151 [Schönfelder (1978)]. Isotropy and temporal constancy conditions, which have been verified at energies < 100 keV by Schwartz (1970) and Fabian and Sanford (1971) and above 2 MeV by Schönfelder et al. (1977) and White et al. (1977), are satisfied by the theories mentioned.

Information concerning the Galactic component of the gamma-ray background comes mainly from the surveys carried out by the satellites SAS II and COS B which operate in the energy range 50 MeV to 5 GeV and there is a sparsity of practical results from energies around 10 MeV.

At energies > 50 MeV then, the Galaxy appears as a narrow line source. At Galactic longitude (l^{II}) = 0° , i.e. towards the Galactic centre, its width at half maximum, in Galactic latitude (b^{II}), is: $+ 3^\circ \geq b^{II} \geq -2.5^\circ$ as shown in figure 2.8 and at $l^{II} = 120^\circ$ it is: $+ 7^\circ \geq b^{II} \geq -3^\circ$. The longitude distribution, figure 2.9, shows a broad maximum towards the Galactic centre and localised excesses in the Galactic plane which seem to occur when the line of sight tangentially intersects spiral arms [Bignami et al. (1975)]. In addition, gamma-ray point sources are embedded in the Galactic plane and some of the localised enhancements

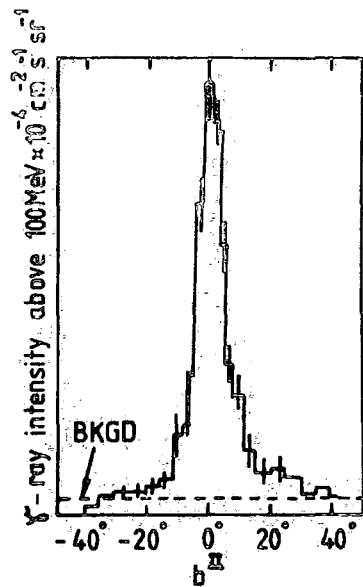


Figure 2-8 Gamma-ray intensity as a function of galactic latitude towards the Galactic centre. (Results from SAS II) [Wolfendale (1982)]

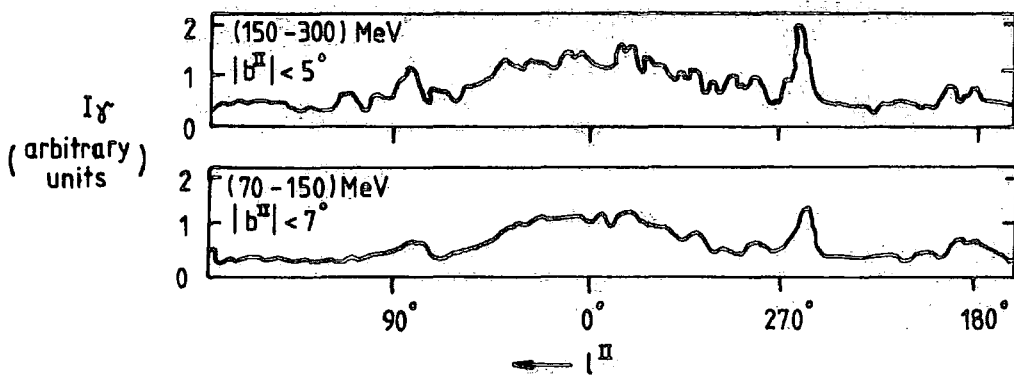


Figure 2-9 COSB: Gamma-rays as a function of Galactic longitude 'I_γ' is the approximate gamma ray density within the energy range and latitude range indicated. [Wolfendale (1982)]

have been identified with these. In particular four pulsars have been identified: PSR 1822-09, PSR 0531+21, PSR 0740+28 and PSR 0833-45.

2.3.2 Solar Gamma-Rays

Prior to 1972 several claims had been made for observations of a solar gamma-ray flux. [Apparao et al. (1966), Daniel et al. (1967), Kondo and Nagase (1969), Hirasima et al. (1969)], however these have all been highly disputed and none coincided with any optical flare activity.

The first accepted observations of solar gamma radiation are those from the University of New Hampshire's gamma-ray spectrometer, on board the OSO-7 satellite, of continuum and line radiation during the solar activity of August 2nd to August 11th, 1972, [Chupp et al. (1973)]. The instrument responsible for the observations is described by Forrest et al. (1972), and Higbie et al. (1972). Observations of line radiation were obtained from the solar flares of 0621 U.T., August 4th, 1972 and 1500 U.T., August 7th, 1972. The time integrated solar and background counting-rate spectra for the first of these two events, accumulated during the time interval 0624 to 0633 U.T., corresponding to the rising phase of the flare, is shown in figure 2.10; line emission is evident at energies: 0.51, 2.23, 4.44 and 6.13 MeV and the corresponding flux levels are: $(6.3 \pm 2.0) \times 10^{-2}$, $(2.80 \pm 0.22) \times 10^{-1}$, $(3 \pm 1) \times 10^{-2}$, $(3 \pm 1) \times 10^{-2}$, photons $\text{cm}^{-2} \text{s}^{-1}$, respectively. However, during the observations of the August 7th, 1972 flare, which were made approximately 40 minutes after the onset, only the first two of these lines were detected and these at respective flux levels, $(3.0 \pm 1.5) \times 10^{-2}$ and $(6.9 \pm 1.1) \times 10^{-2}$ photons $\text{cm}^{-2} \text{s}^{-1}$.

Chambon et al. (1978) report the detection of the 2.23 MeV line and a possible detection of that at 4.4 MeV during a flare which erupted on 22nd November 1977. Their preliminary estimates of the 2.2 MeV line

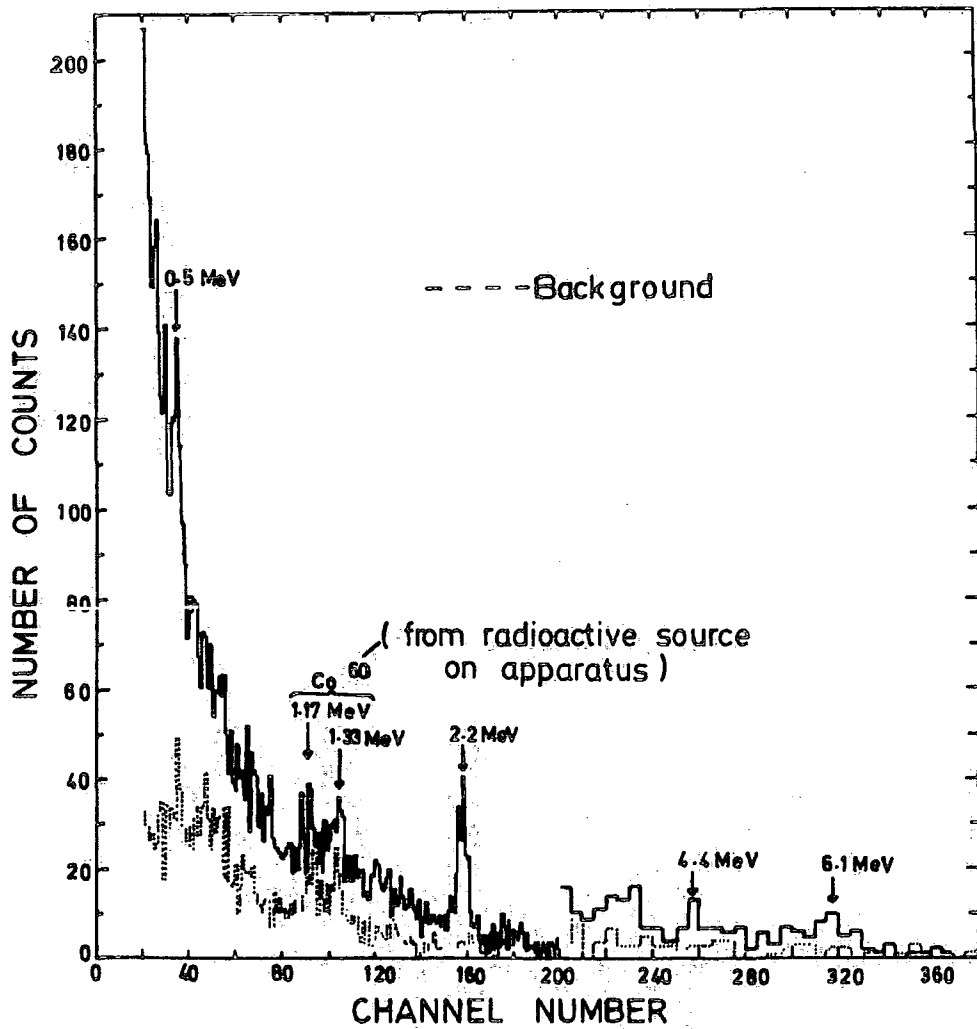


Figure 2-10 The Solar quadrant γ -ray spectrum (solid histogram) during the rising phase of the 1972 August 4th flare (0624 to 0633 U.T.) and simultaneous background spectrum (dotted histogram). [Chupp et al (1975)]

flux is compatible with Chupp's 4th August, 1972 observation. The 0.51 MeV line was not seen on this occasion though it is argued that such would be expected since if the 4.4 MeV excess is indeed due to a line then its intensity is a factor of 3 lower than the 2.2 MeV feature, which would in turn mean that the 0.51 MeV line should be a factor of 2 lower in intensity than the 2.2 MeV line, [Ramaty and Lingenfelter (1973)].

Both the 2.2 MeV and the 4.4 MeV lines were detected again during a flare which erupted on 11th July 1978 and lasted from 1035 to 1415 U.T. [Hudson et al. (1980)]. This observation comes from the A4 experiment of the HEAO-1 satellite which is described in detail by Matteson (1978) and the strengths of the lines were (1.00 ± 0.29) and (0.18 ± 0.07) photons $\text{cm}^{-2}\text{s}^{-1}$, respectively.

At 0312 U.T. June 7th, 1980, another flare was observed at gamma-ray energies and a line of energy (2.232 ± 0.012) MeV was recorded at a flux level of $(7.1 \pm 1.2) \times 10^{-2}$ photons $\text{cm}^{-2}\text{s}^{-1}$. Chupp et al. (1981) report this observation which was obtained from the Solar Maximum Mission (SMM) satellite's gamma-ray spectrometer.

Prior to the first observations calculations by Lingenfelter and Ramaty, (1967) had shown that the strongest lines from solar flares in decreasing order, should be:-

- (i) 2.223 MeV - Thermalised neutron capture on hydrogen in the solar photosphere.
- (ii) 0.511 MeV - Positron annihilation.
- (iii) 4.438 MeV - ^{12}C de-excitation.
- (iv) 6.129 MeV - ^{16}O de-excitation.

The subsequent observations have provided substantial support for the calculations not only because the predicted lines are precisely those detected but also because in the individual cases of a plurality of lines being measured their observed flux ratios agree with the calculations

within experimental error. In addition the neutron capture and positron annihilation times are finite and therefore the 2.223 MeV and 0.51 MeV lines would be expected to lag behind the flare onset. Supporting this are the time profiles from the HEAO-1 and SMM observations of the respective flares in several energy bands ranging from microwaves to gamma-rays of ~ 8 MeV; these are shown in figures 2.11 and 2.12. The HEAO-1 profile shows that the 2.223 MeV line lagged (94 ± 30) seconds behind the hard X-ray flux and this is consistent with the slowing down time required for neutron capture. Also the time history from SSM shows that the emission from the band covering the 2.223 MeV line continues beyond the end of the impulsive phase of the flare. Similar evidence comes from the 1972 observations; although four lines were detected from the August 4th flare, seen during its rising phase, only the 0.51 and 2.223 MeV lines were detected during the August 7th event which was observed at a later stage of the flare.

2.3.3 Discrete Cosmic Sources

2.3.3.1 The Galactic Centre. Table 2.3 summarises the main experiments to have viewed the Galactic centre to date. The Bell/Sandia Laboratories' apparatus and the 1974 Rice University device, which have been described briefly and referenced in Section 2.1, together with the 1970/71 Rice instrument [Johnson and Haymes (1973)] and that of the Centre d'Etudes Spatiale des Rayonnements (C.E.S.R.) [Alberne et al. (1978)] were all balloon borne, while the Jet Propulsion Laboratory (JPL) device is the HEAO-3 satellite gamma-ray spectrometer [Mahoney et al. (1980)].

In both Rice University flights of 1970 and 1971 from Parana, Argentina a bright, power-law continuum of spectral index ~ 2.4 was detected from the Galactic centre, however the absolute flux levels reported [Johnson and Haymes (1973)] differ by ~ 30 per cent. This

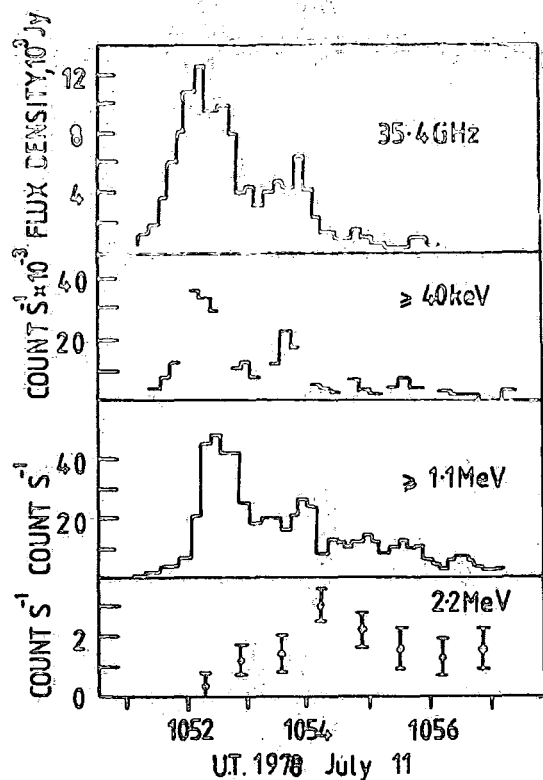


Figure 2-11 Time profile of flux variations during solar flare of 1978 July 11 (HEAO-1). [Hudson et al (1980)]

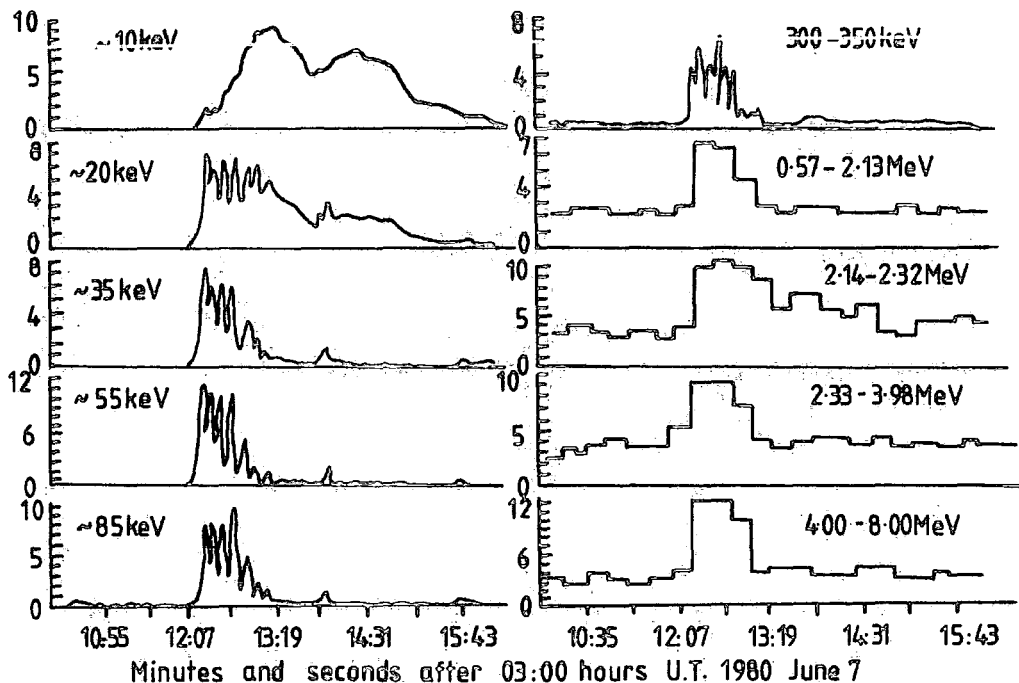


Figure 2-12 Time history of energetic photon emissions for several energy intervals from 10 keV to 8 MeV. [Chupp et al (1981)]

Table 2.3 Observations of the Galactic Centre positron annihilation line emission.

(a) Chupp (1977), (b) Alberne et al. (1981), (c) Leventhal (1978), (d) Leventhal et al. (1980), (e) Mahoney et al. (1980).

Line Energy (keV)	Line Flux 10^{-3} Photons $\text{cm}^{-2}\text{s}^{-1}$	Date of Observation	Instrument Description
(a) 476 ± 24	1.8 ± 0.5	1970 Nov. 25 and 1971 Nov. 20	75cm ² NaI(Tl) crystal. NaI(Tl) Anticoincidence shield. Aperture: 24° FWHM. Energy resolution: 15% at 511 keV
(a) 530 ± 11	0.8 ± 0.23	1974 April 2	182cm ² NaI(Tl) crystal NaI(Tl). Anticoincidence shield. Aperture 15° FWHM. Energy resolution: 12% at 511 keV.
(b) 511	4.18 ± 1.56	1977 Feb. 14 and 17	140cm ³ Ge(Li) crystal. NaI(Tl) anticoincidence shield. Aperture 50° FWHM. Energy resolution: 18 keV at 1.33 MeV.
(c) 510.7±0.5	1.22 ± 0.22	1977 Nov. 11	130cm ³ Ge crystal. NaI(Tl) Anticoincidence shield. Aperture: 15° FWHM. Energy resolution: 3.2 keV at 511 keV.
(d) 511	2.35 ± 0.71 or 1.24 ± 0.43	1979 April 15	1979 flight added ⁶ LiF/plastic neutron shield.
(e) 510.9±0.25	1.85 ± 0.21	1979 Oct.	4 Ge crystals: effective area 26.4cm ² . CsI(Na) anticoincidence shield. Aperture: 35° FWHM.
(e) 510.1	0.65 ± 0.27	1980 March	Energy resolution: 2.72 keV at 511 keV.

difference is attributed to either source variability or a variation in the systematic errors in the apparatus, which for both experiments was essentially the same. A combined result from both occasions suggests that the best representation of the flux is:

$$N(E) = (14.7 \pm 3.3)E^{(-2.42 \pm 0.05)} \text{ photons cm}^{-2}\text{s}^{-1}\text{keV}^{-1} \quad (2.8)$$

and this is shown in figure 2.13 as a solid line. Figure 2.13 also shows the data from a previous flight [Haymes et al. (1969)] together with that from the 1977 Bell/Sandia observations to be discussed shortly.

Both of the Rice flights produced evidence for a spectral feature at ~ 500 keV superimposed on the continuum. Although least-squares Gaussian fits to each data set produced different line centre energy values they agree within experimental error and therefore the features have been assumed to be due to a single gamma-ray emission line. The combined 1970/71 data for the feature yields a 5.3 σ excess above the continuum fit, lying at (476 ± 24) keV.

In 1974 the Rice University group re-observed the Galactic centre [Haymes et al. (1975)] with a new instrument (Section 2.1) flown from Parana as previously and on this occasion several spectral lines were recorded including, to a 3.5 σ confidence, one at (530 ± 11) keV which they believe to be the same feature as observed in 1970 and 71 in spite of a quantitative difference in average energy of $\sim 3.4\sigma$ (which practically excludes the possibility of statistical fluctuation). Haymes et al. (1975) suggest that the average energy of the excess is a function of the Galactic longitude coordinates observed which in 1970 were $l^{\text{II}} = 354^{\circ}$ to 17° , in 1971 $l^{\text{II}} = 351^{\circ}$ to 15° and in 1974 $l^{\text{II}} = 353^{\circ}$ to 8° .

The results for the other spectral lines detected in 1974 are displayed in Table 2.4. In the 1.2 to 2.0 MeV range the feature is too

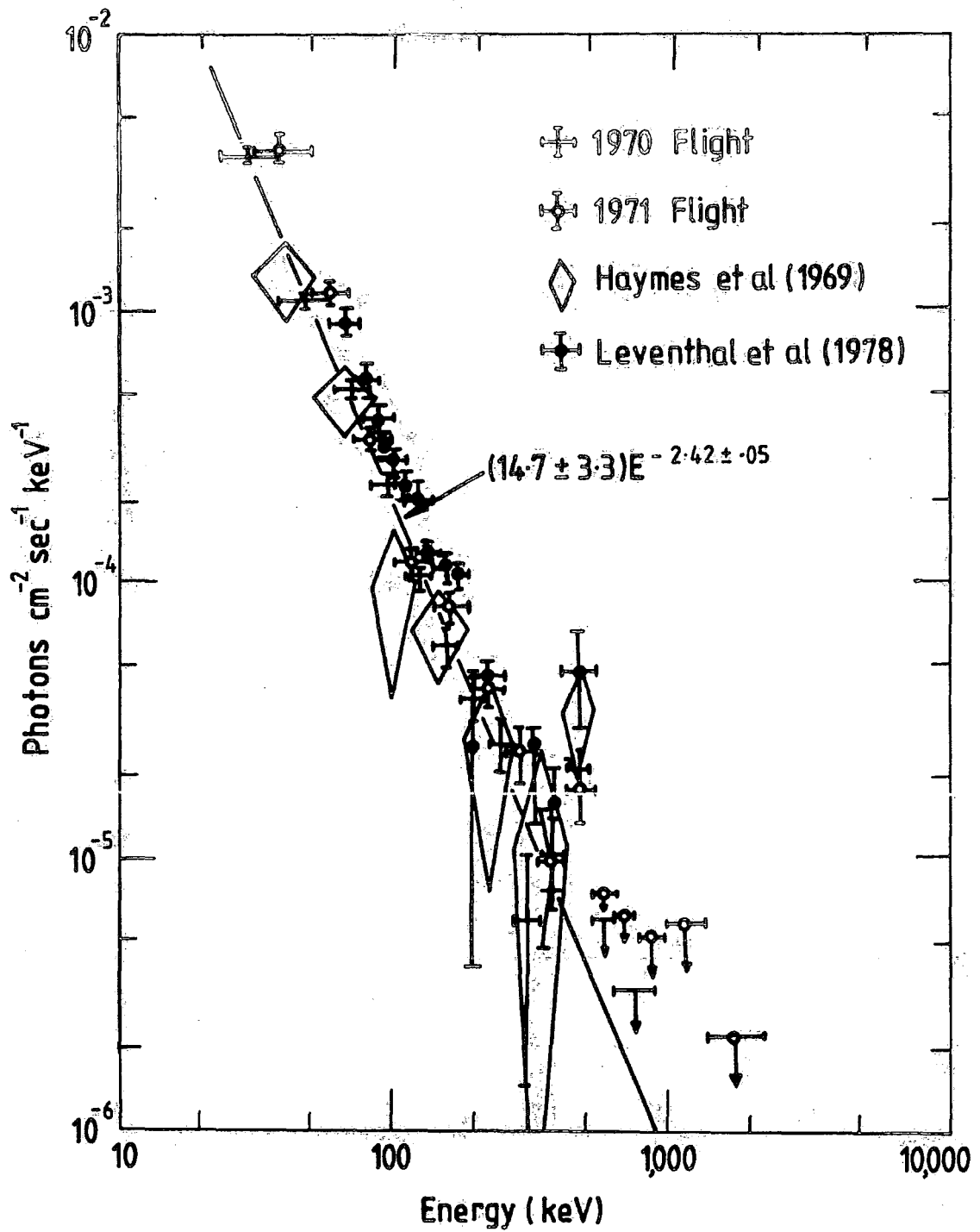


Figure 2-13 Differential photon spectrum from the galactic centre. The solid line represents the best fit spectrum of the weighted average of the Rice University 1970 and 71 observations. [Haymes (1973)]

broad to be a single spectral line and it is therefore thought to be Doppler broadened emission from several nuclides. All of the reported lines are expected, since the detected energies are close to the lines radiated by universally abundant nuclei.

The continuum detected on this occasion is satisfied by a power-law fit:

$$N(E) = (40.7 \pm 12.5)E^{(-2.78 \pm 0.06)} \text{ photons cm}^{-2} \text{ s}^{-1} \text{ keV}^{-1} \quad (2.9)$$

over the energy range 0.05 to 0.8 MeV excluding the contribution from the energy band covering 0.5 MeV.

Leventhal et al. (1978) and (1980) report the detection of a 511 keV spectral line at the 3.5σ level from the Galactic centre during two balloon flights launched from Alice Springs, Australia, using the Bell/Sandia Laboratories' instrument. During the 1979 April 15 flight a system malfunction occurred which has given rise to an uncertainty in the line flux (indicated in Table 2.3), however the result obtained from analysis of the complete data set ignoring the instrumental malfunction is in close agreement with their previous result from the 1977 November 11-12 observation.

It is believed that the fault did not affect their study of continuum radiation and a best fit power-law for this is given as:

$$N(E) = 1.8 \times 10^{-4} (E/100)^{-2.31} \text{ photons cm}^{-2} \text{ s}^{-1} \text{ keV}^{-1} \quad (2.10)$$

for the 1979 data as compared with:

$$N(E) = 2.65 \times 10^{-4} (E/100)^{-2.51} \text{ photons cm}^{-2} \text{ s}^{-1} \text{ keV}^{-1} \quad (2.11)$$

from the 1977 flight. The data for the April 1979 flight are shown in figure 2.14 together with the best fit power-law of equation (2.10) and those from the 1977 observation (equation 2.11) and the 1974 Rice result (equation 2.9). Consideration of these three results has led Leventhal et al. (1980) to the conclusion that the evidence points to an intensity

Table 2.4 Spectral Lines detected from the Galactic centre during observation of 1974 April 2nd.
Haymes et al. (1975).

	Measured Energy (MeV)		
	0.9 ± 0.1	1.2 - 2.0	4.6 ± 0.1
Flux (10 ⁻⁴ photons cm ⁻² s ⁻¹)	(3.7 ± 3.1)	26 ± 6	9.5 ± 2.7
Instrumental FWHM (MeV)	0.080	0.130	0.206
Measured FWHM (MeV)	0.1	-	0.7
Possible Origin	⁵⁶ Fe *	²⁴ Mg, * ²⁰ Ne *	¹² C *
Predicted Energy (MeV)	0.847	1.37, 1.63 1.78	4.43
Detection Confidence (σ)	1.2	4.1	3.5

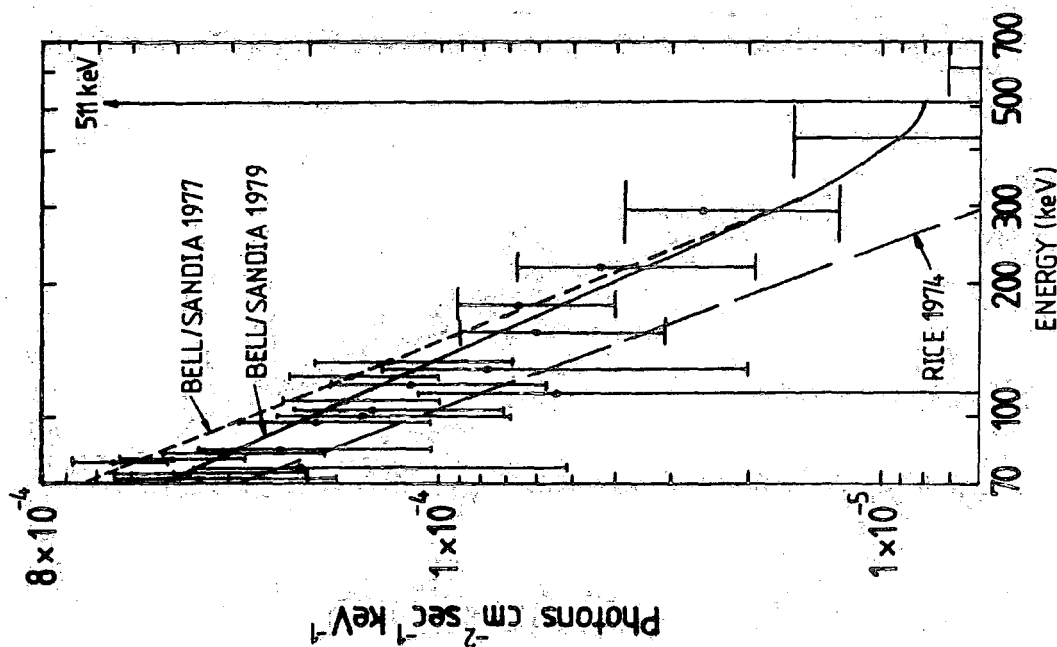


Figure 2.14 Galactic centre differential photon spectrum from the 1979 April 15 flight of the Bell/Sandia spectrometer. [Leventhal et al (1980)]

fluctuation of the Galactic centre continuum of ~ 50 per cent, on a time scale of years.

Meegan (1978) in re-assessing the Rice University results of 1971 and 1974 concludes that the discrepancy concerning the ~ 500 keV feature is resolved in view of the Bell/Sandia result at 511 keV.

Further evidence for a galactic centre emission at 511 keV has come from the HEAO-3 satellite during observations performed in the fall of 1979 and spring of 1980. A 3.5 σ decrease in the line flux is apparent between these observations and this is considered to be evidence for source variability, since the statistical likelihood of a flux change of such degree is 5.0×10^{-4} for the normal distribution fit to the feature. Taking the earlier observations, including that reported by Alberne et al. (1981) from the C.E.S.R. work, in the light of the HEAO-3 results they may also be suggestive of source flux variation. It is difficult to make a legitimate comparison of the results since each of the instruments used define different fields of view and the precise Galactic coordinates observed in each case are not the same. Thus if the emitting region were an extended source then the detected fluxes would not be the same even from a constant emission. The suggestion of source variability in the HEAO-3 case is made since the data is consistent with a point source or one of narrow spatial extent $\sim 10^{18}$ cm. However the C.E.S.R. group favour a constant intensity source extending in galactic longitude between $-30^\circ < \ell^{II} < +30^\circ$.

Overall, the 511 keV line is interpreted as being due to electron-positron annihilation though the source of the positrons is unclear. Suggestions include supernova and nova explosions, radio pulsars and cosmic-ray interactions, though calculations by Ramaty et al. (1979) indicate that cosmic-ray positron production should account for only a few per cent of the observed flux. In a more speculative vein a

massive stellar singularity at the Galactic centre may be the source of the $\sim 10^{43}$ positron electron pairs s^{-1} required by the current observations [Ramaty and Lingenfelter (1981)]. This suggestion has been put forward to explain recent Infra-Red data from the Galactic centre.

2.3.3.2 The Crab Nebula. Several measurements of low energy gamma radiation from the Crab Nebula up to 10 MeV have been reported and figure 2.15 represents the collective differential photon spectrum for the Crab up to 1 MeV. In the energy range from 1 to 10 MeV the results to date are conflicting and the spectral shape in this region has yet to be resolved. Walraven et al. (1975) have produced results which agree with a simple power-law extrapolation from the X-ray region, however, Baker et al. (1973) and Gruber and Ling (1977) give evidence for a flattening of the spectrum in this region which produces a flux excess of a factor of ~ 7 to 30 above such extrapolations.

Only two reports of line radiation from the Crab have been made; those of Leventhal et al. (1977) and Ling et al. (1979), for line features at ~ 400 keV and ~ 73 keV respectively. The former observation was performed on the 10th May 1976 from a balloon-based platform launched from Alamogordo, New Mexico and the instrument used was an NaI(Tl) anticoincidence shielded, 92 cm^3 Ge(Li) spectrometer, of aperture 12° FWHM and energy resolution 3.4 keV at 1.33 MeV. In the detected line at (400 ± 1) keV a flux of $(2.24 \pm 0.65) \times 10^{-3}$ photons $\text{cm}^{-2} \text{s}^{-1}$ was recorded corresponding to a 3.5 σ excess. Leventhal et al. (1977) interpret the line as gravitationally red-shifted 0.511 MeV positron annihilation radiation from the surface of a neutron star.

This line was not seen however by Ling et al. (1977) in observing the Crab during their balloon flight of 10th June 1974. Launched from Palestine, Texas the instrument used in this case was an actively shielded, 4 headed Ge(Li) spectrometer from the Jet Propulsion Laboratory,

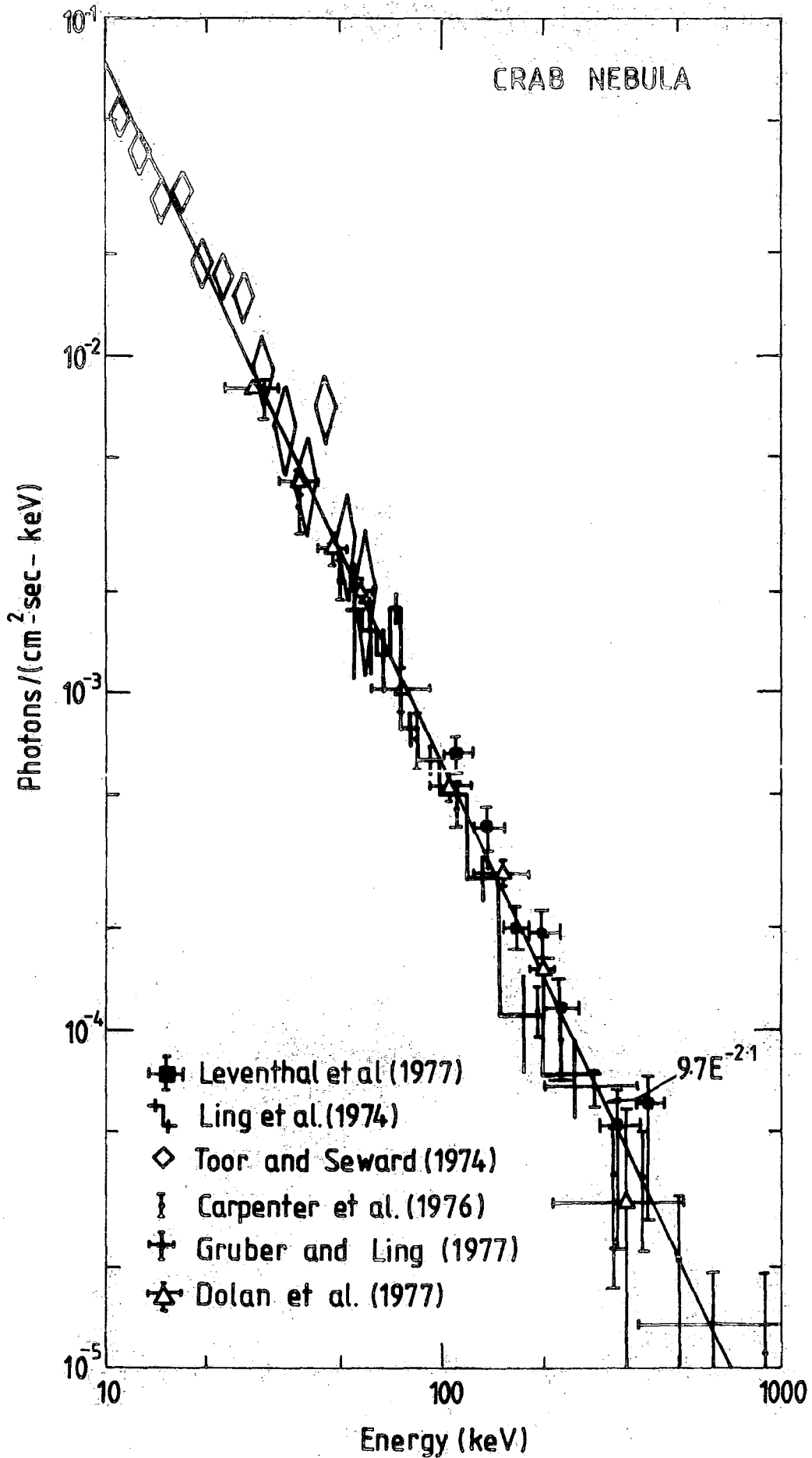


Figure 2-15 Differential photon spectrum from the Crab Nebula

Pasadena, California (shown in figure 2.4) and briefly described and referenced in Section 2.1. At the flux level stated above the 400 keV line should have produced an increase of 3.9σ statistical significance in this instrument's data, however no increase was seen. Ling et al. (1977) are careful not to rule out the possibility that the reported feature could vary with time, as the two observations were separated by 2 years.

Although the 400 keV line was not seen during the JPL flight a feature at (73.3 ± 1.0) keV was detected at 3.8σ confidence, corresponding to a flux of $(3.8 \pm 0.9) \times 10^{-3}$ photons $\text{cm}^{-2}\text{s}^{-1}$ [Ling et al. (1979)]. Possible origins for a line at this energy are (i) the two lead (Pb) $K \alpha$ X-ray emissions (74.9694 and 72.8042 keV) or, (ii) Cyclotron emission in the Crab pulsar's magnetic field.

2.3.3.3 Hercules X-1. Her X-1 is a highly variable, binary X-ray source exhibiting periodicities of (a) 1.24 second pulsations, (b) 1.70 days, due to binary eclipse and (c) 34.9 days, of currently unknown origin. Many observations of its spectrum in the keV region have been made and a summary of the results prior to 1976 is given by Manchanda (1977). Below ~ 20 keV the spectrum appears to fit a power-law of index ~ 1.5 , however, at energies above 25 keV it steepens and its shape seems to vary significantly from one 35 day cycle to another. Becker et al. (1977) confirm the break in the spectrum and their data for the 25 to 60 keV region, from the cosmic X-ray spectrometer on board the OSO-8 satellite, fits a power-law of spectral index ~ 5.3 . Trümper et al. (1978) report very good agreement with the OSO-8 data concerning the slope of the spectrum between 20 and 45 keV. However Manchanda's mean value of ~ 2.7 derived from the pre-1976 observations is at variance with these later results.

During the balloon flight reported by Trümper et al. (1978), which

was performed on 1976 May 3rd and launched from Palestine, Texas, spectral lines were observed in the 1.24s pulsed spectrum at energies (58 ± 5) keV and 110 keV. At the time of observation Her X-1 was at binary phase 0.72 to 0.82 and 5 days into cycle 45 [Davison and Fabian (1977)] of the 35 day period. Figure 2.16 shows the Her X-1 pulsed spectrum derived from the flight and the reported lines, which are clearly visible, correspond to fluxes of $(2.9 \pm 3.0 - 1.0) \times 10^{-3}$ photons $\text{cm}^{-2} \text{s}^{-1}$ for the 58 keV line and $(1.1 \pm 0.1) \times 10^{-3}$ photons $\text{cm}^{-2} \text{s}^{-1}$ for that at 110 keV and the statistical significance of the lines are 4.5σ and 3.3σ above the continuum respectively.

Quantised electron cyclotron emission in the intense magnetic field of a rotating neutron star is the suggested origin for the lines since the observed energies are those predicted from this model [Gnedin and Sunyaev (1974)] for a magnetic field strength of 5.3×10^{12} Gauss.

Trümper (1978) reports a further observation of Her X-1 performed during September/October 1977 using a much larger detector than that of their 1976 flight. In this case the recorded fluxes from the continuum and the ~ 58 keV line showed a decrease of a factor ~ 2 over those obtained previously and the 110 keV was not detected. A flux of $(1.1 \pm 0.1) \times 10^{-3}$ photons $\text{cm}^{-2} \text{s}^{-1}$ was obtained for the detected line which appeared at 55.4 keV, and a 3σ upper limit of $< 10^{-3}$ photons $\text{cm}^{-2} \text{s}^{-1}$ for the 110 keV is estimated.

In February 1977 the X-ray detector on board the Ariel V satellite observed Her X-1 and Coe et al. (1977) report a time averaged spectral feature at (64 ± 6) keV, yielding a flux of $(1.7 \pm 0.7) \times 10^{-2}$ photons $\text{cm}^{-2} \text{s}^{-1}$. Though the flux is somewhat higher than that of Trümper et al. the recorded energy is consistent, however, no confirmation of the pulsed nature of the emission could be presented.

Dennis et al. (1978) discuss the detection of pulsed emission at

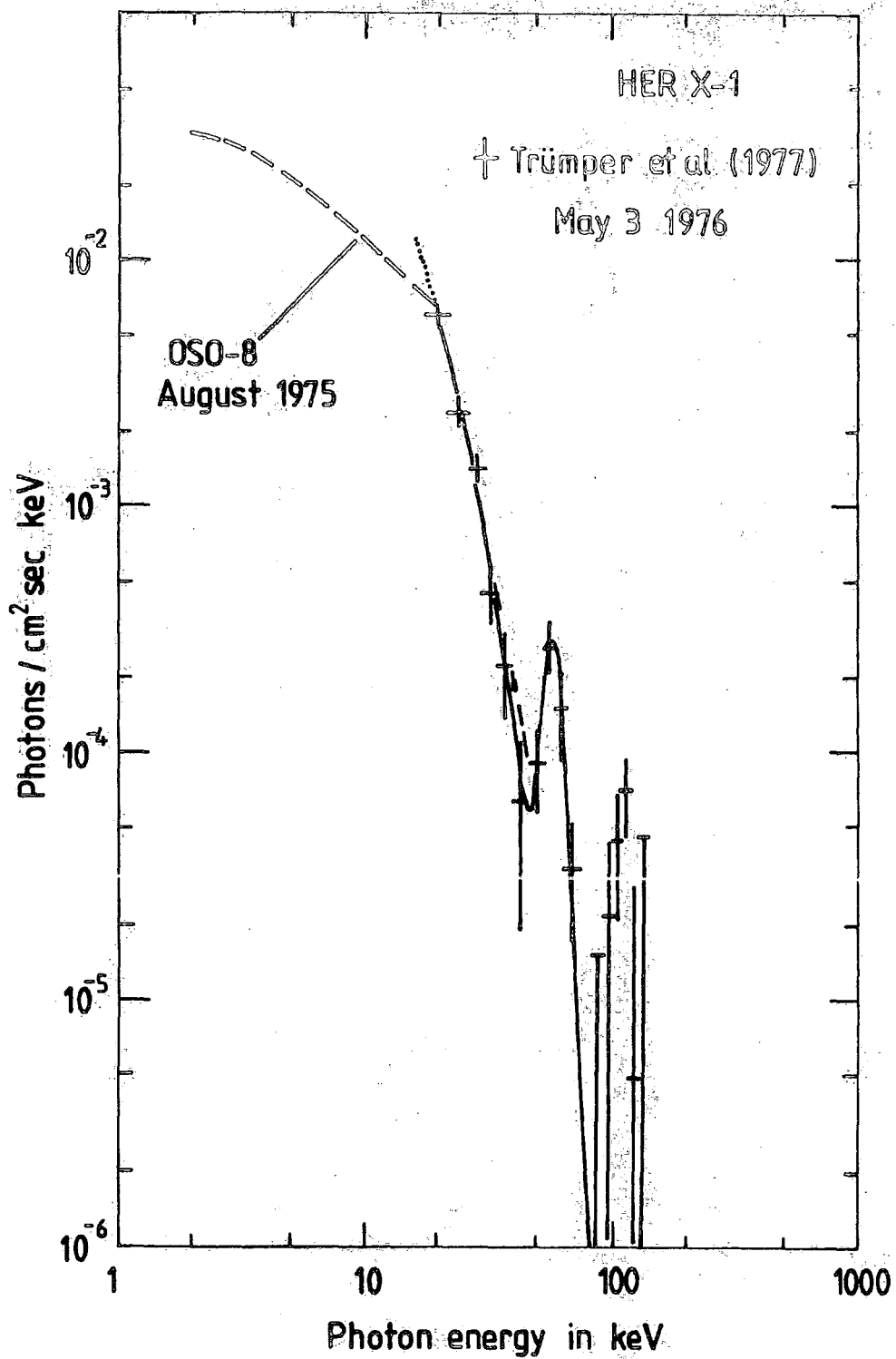


Figure 2-16 Pulsed spectrum derived from the May 3, 1976 flight, (Trümper et al, 1977)

~ 60 keV and ~ 135 keV in OSO-8 data for which 3σ upper limits of $< 2 \times 10^{-3}$ and $< 1 \times 10^{-3}$ photons $\text{cm}^{-2}\text{s}^{-1}$ respectively were obtained.

2.3.3.4 Other Discrete Sources. Radiogalaxy Centaurus-A and the optical galaxy N.G.C. 5128 which it surrounds are known to be the source of intense emission in all regions of the electromagnetic spectrum from radio to hard X-rays [Kellermann (1974)], and the consequent inference of the presence of energetic electrons in turn suggests that excited nuclei are also contained therein which should give rise to gamma-ray line radiation.

These two objects have been observed in the energy range 0.033 to 12.25 MeV by the Rice University group using the spectrometer described in Section 2.1 and evidence was found for both continuum and line emission in this range. The continuum, represented by:

$$N(E) = (0.86 \pm 0.17)E^{-(1.90 \pm 0.04)} \text{ photons cm}^{-2}\text{s}^{-1}\text{keV}^{-1} \quad (2.12)$$

is shown in figure 2.17 and the line emissions at 1.6 MeV and 4.5 MeV, which constitute the first spectral line detection from an extragalactic source, are depicted more clearly in figure 2.18. Flux levels recorded for these lines are $(3.4 \pm 1.0) \times 10^{-3}$ and $(9.9 \pm 3.0) \times 10^{-4}$ photons $\text{cm}^{-2}\text{s}^{-1}$, corresponding to a 3.3σ statistical significance in both cases.

Two models are consistent with the rather broad feature at 1.6 MeV: (a) Doppler broadening of $^{20}\text{Ne}^*$ de-excitation radiation and (b) Blending of several narrow lines from cosmic ray and excited interstellar nuclei. Model (b) has been suggested for a similar feature in the Galactic centre spectrum at 1 to 2 MeV, (section 2.3.3.1). Carbon-12 emits de-excitation radiation at 4.43 MeV and this is thought to be the likely explanation of the observed Cen-A/N.G.C. 5128 4.5 MeV feature.

Gamma-ray emission in the 1 to 20 MeV region has also been reported

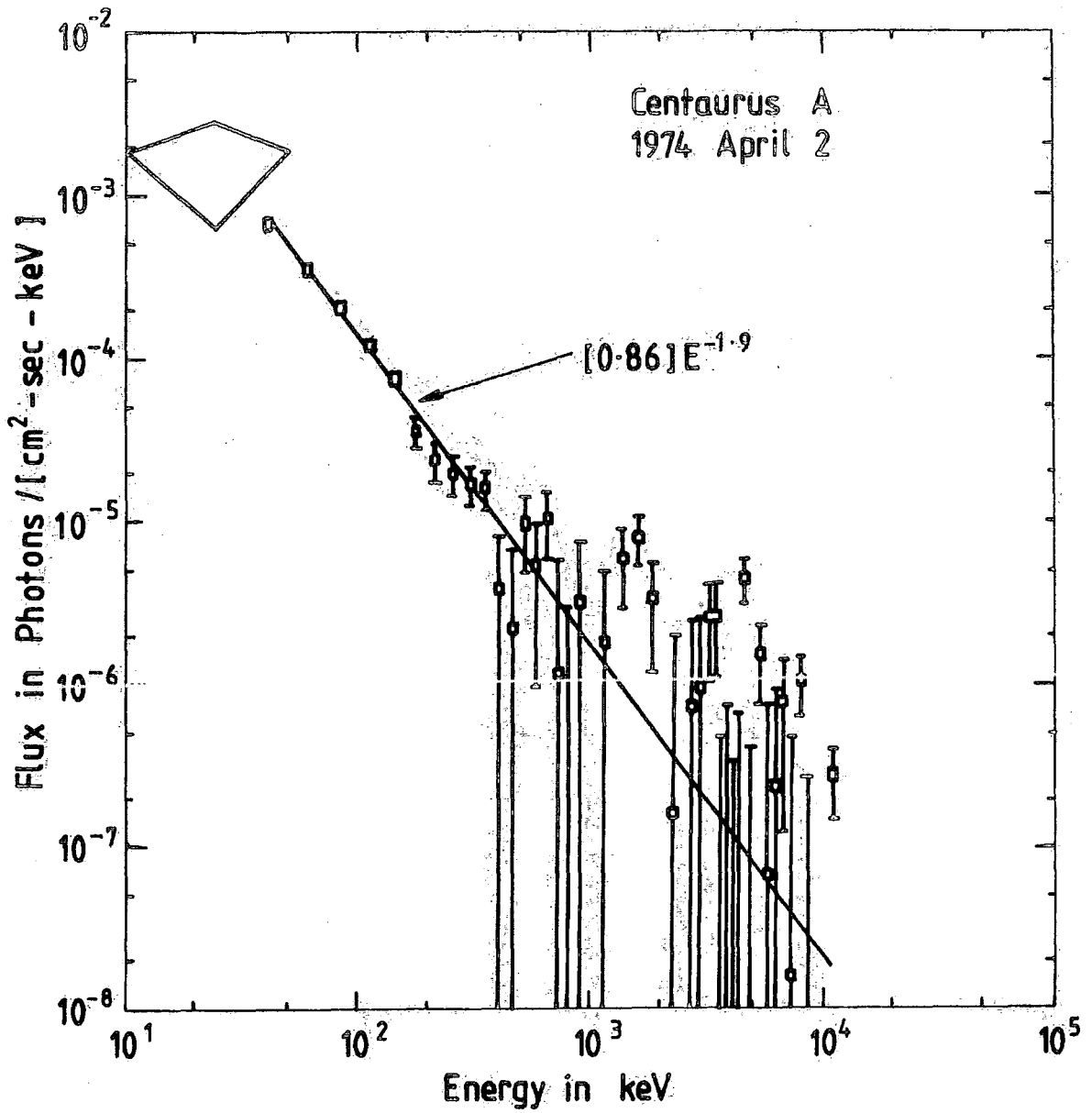


Figure 2-17 Differential photon spectrum of Centaurus A [Hall et al (1976)]

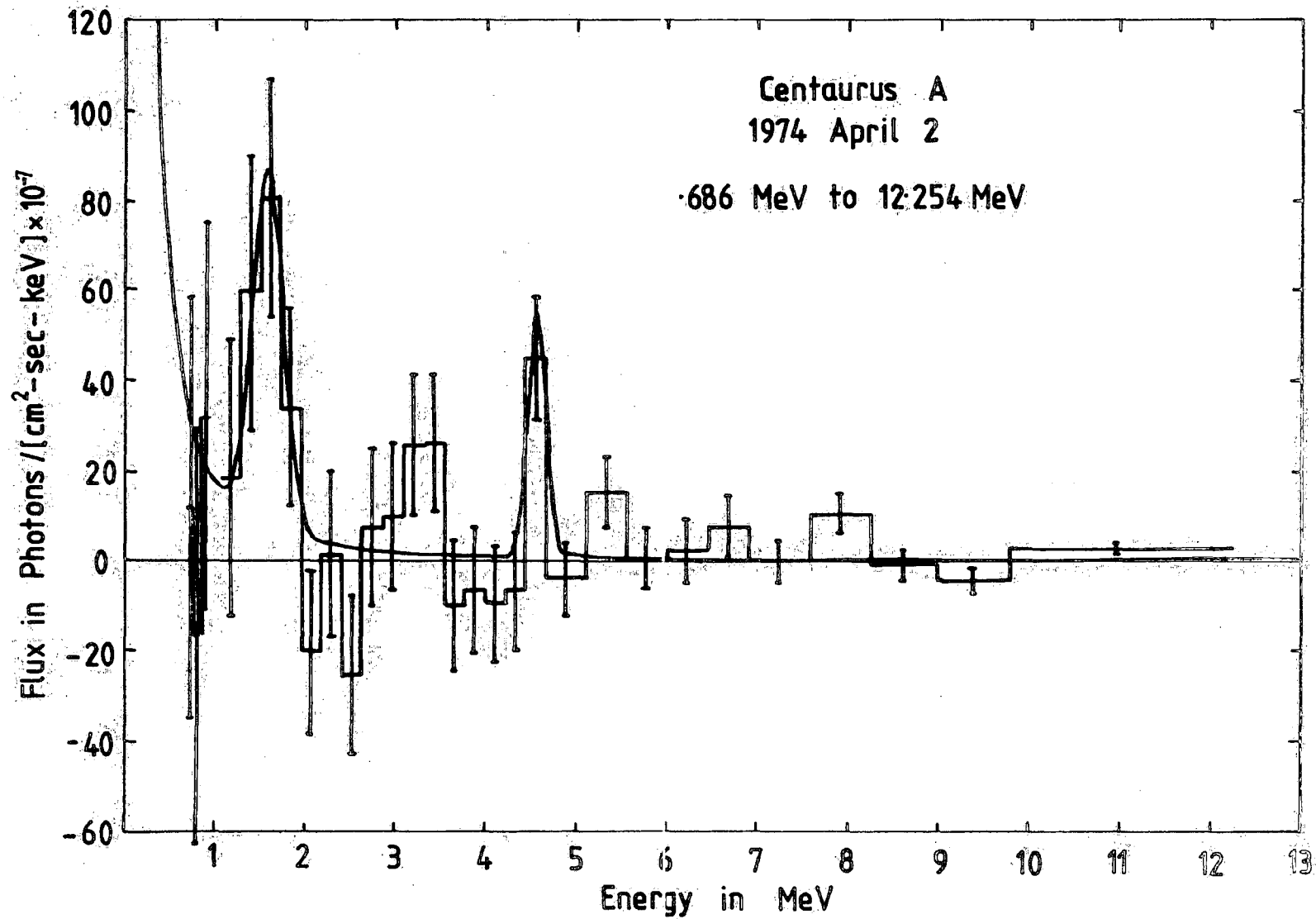


Figure 218: The Centaurus A spectrum at energies above 0.686 MeV. [Hall et al (1976)]

from the Seyfert galaxy N.G.C. 4151 by Graml et al. (1978), however the energy resolution of the Compton telescope used in this case was insufficient to resolve possible line emission. The observed flux had a significance of 7σ above background and fitted a power-law believed to be in good agreement with extrapolations from X-ray energies up to ~ 3 MeV. Meegan and Haymes (1979) have obtained upper limits for N.G.C. 4151 which are not inconsistent with those of Graml et al., however White et al. (1980) have derived 2σ upper limits to the flux from data collected during their balloon-based observation of N.G.C. 4151 of 1978 September 29th and these are factors of 5 to 10 below those of Graml et al.

In the lower energy region 100 to 200 keV Meegan and Haymes find that their data is in disagreement with observations by Di Cocco et al. (1977) and Auremma et al. (1978) and since Di Cocco's work took place in 1977 May, less than five months before that of Meegan and Haymes' the latter interpret this as an indication of variability of the hard X-ray flux.

CHAPTER 3

THE DURHAM NUCLEAR GAMMA-RAY SPECTROMETER

3.1 INTRODUCTION AND SPECTROMETER DELINEATION

The Durham Nuclear Gamma-Ray Spectrometer has been designed and built with the specific intention of observing and providing data on gamma-ray line emission from discrete celestial sources and background. As discussed in previous chapters candidate sources have been detected with greater or lesser degrees of certainty and even ambiguity by several independent workers and possible mechanisms for the emissions have been postulated, e.g. nuclear de-excitation, cyclotron radiation, positron annihilation etc. It is clear that any instrument which is to substantiate successfully the existence of such sources, possibly add to their number, and which could also give sufficient information to permit classification of the source emission mechanism, would require the following features:

- (i) As small an angular field of view as is practicable.
- (ii) High pointing accuracy.
- (iii) Good sensitivity.
- (iv) Efficient background suppression.
- (v) High energy resolution.
- (vi) Low local production of gamma radiation.

Furthermore, if the device were to be deployed at a high terrestrial altitude by means of a balloon flight then owing to the extreme forces, temperatures and pressures experienced by such a system during launch, float and landing, a sturdy and resilient structure is necessitated in both mechanical and electronic aspects of its construction.

The Durham spectrometer, shown in cross section in Figure 3.1 was designed and built incorporating as many of the features needed to

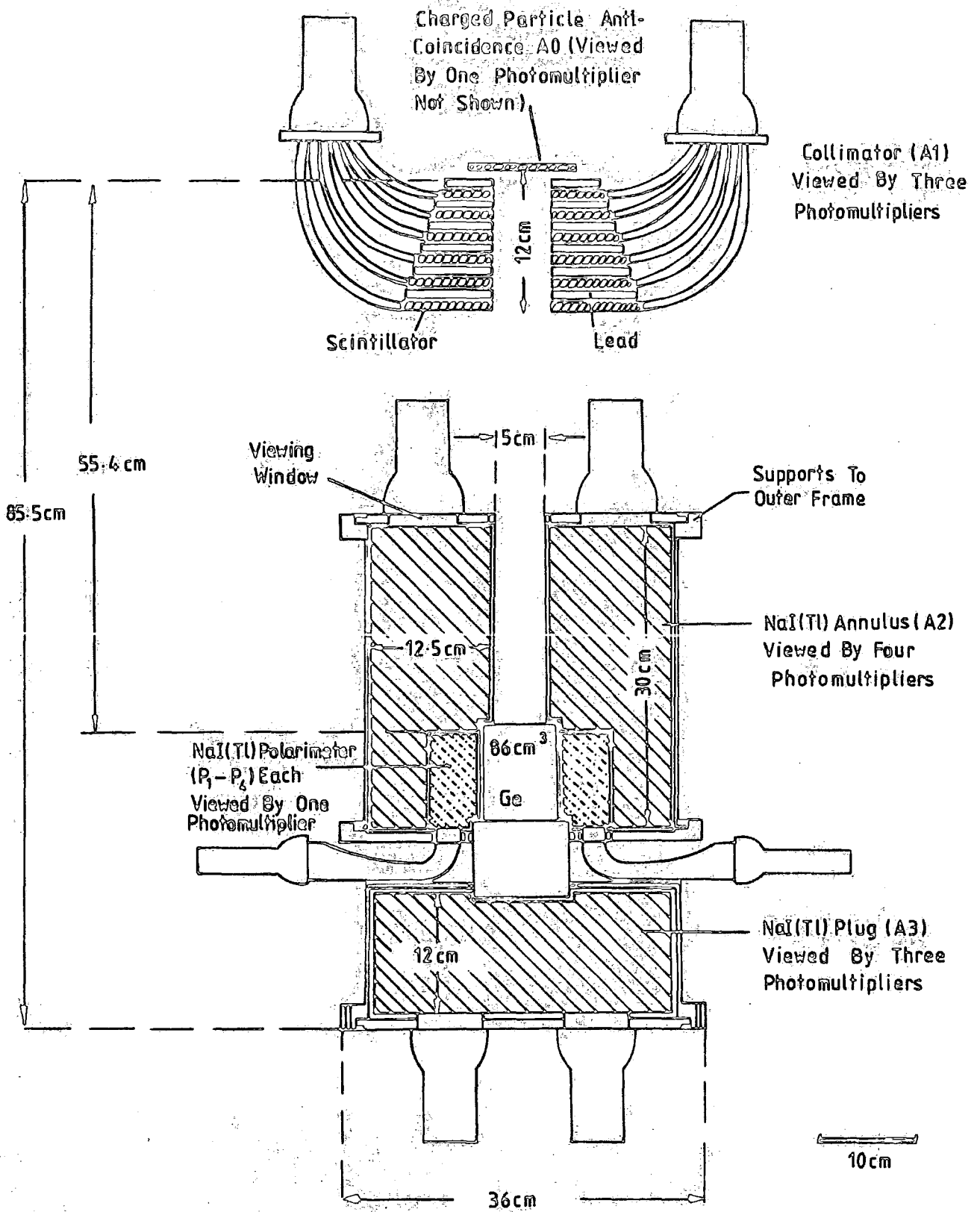


Figure 3.1 Cross-sectional representation of the Durham Gamma-Ray Spectrometer.

satisfy these criteria as was possible. The spectrometer is a cylindrically symmetric system comprising one intrinsic germanium (Ge) detector, for high energy resolution, and several scintillation detectors (A0 to A3), physically arranged to utilise the latter as (a) an anticoincidence shield, against background radiation, and (b) a collimator for the main Ge device, giving a 6° (FWHM) angular field of view. Immediately surrounding the Ge crystal is an array of four scintillation detectors (P1 to P4) designed to detect gamma photons which Compton scatter from the Ge device thus providing information concerning polarisation of the source radiation.

Housed adjacent to the A1 and A2 crystals (figure 3.2) are two Nuclear Instrumentation Module (NIM) crates containing the analogue and digital electronics. A 16383 channel pulse-height analyser (PHA) is used to analyse the pulses, from the γ -ray detector, which arise from radiation energy depositions in the range 0.05 MeV to 10 MeV. For any acceptable event in Ge or the shield two coincident pulses are analysed, e.g. the Ge pulse and any coincident pulse from the shield, and 'flag' indication of precisely which shield element produced the coincident pulse is also given. Associated 'housekeeping' information, i.e. detector count rates, system temperatures, pressure and voltages, are also handled by the electronics contained within these modules.

The spectrometer is contained within an airtight, insulated, aluminium pressure vessel and the whole unit is supported in an aluminium 'gondola'. Directional orientation, to an accuracy of $\pm \frac{1}{2}^\circ$ is achieved via an alt-azimuth steering system which can be commanded to point the spectrometer at any azimuthal angle and zenith angles in the range 0° to 50° . Information concerning the attitude of the system is derived from a number of pendulums, magnetometer elements and a sun sensor which are mounted at various locations as shown in figure 3.2.

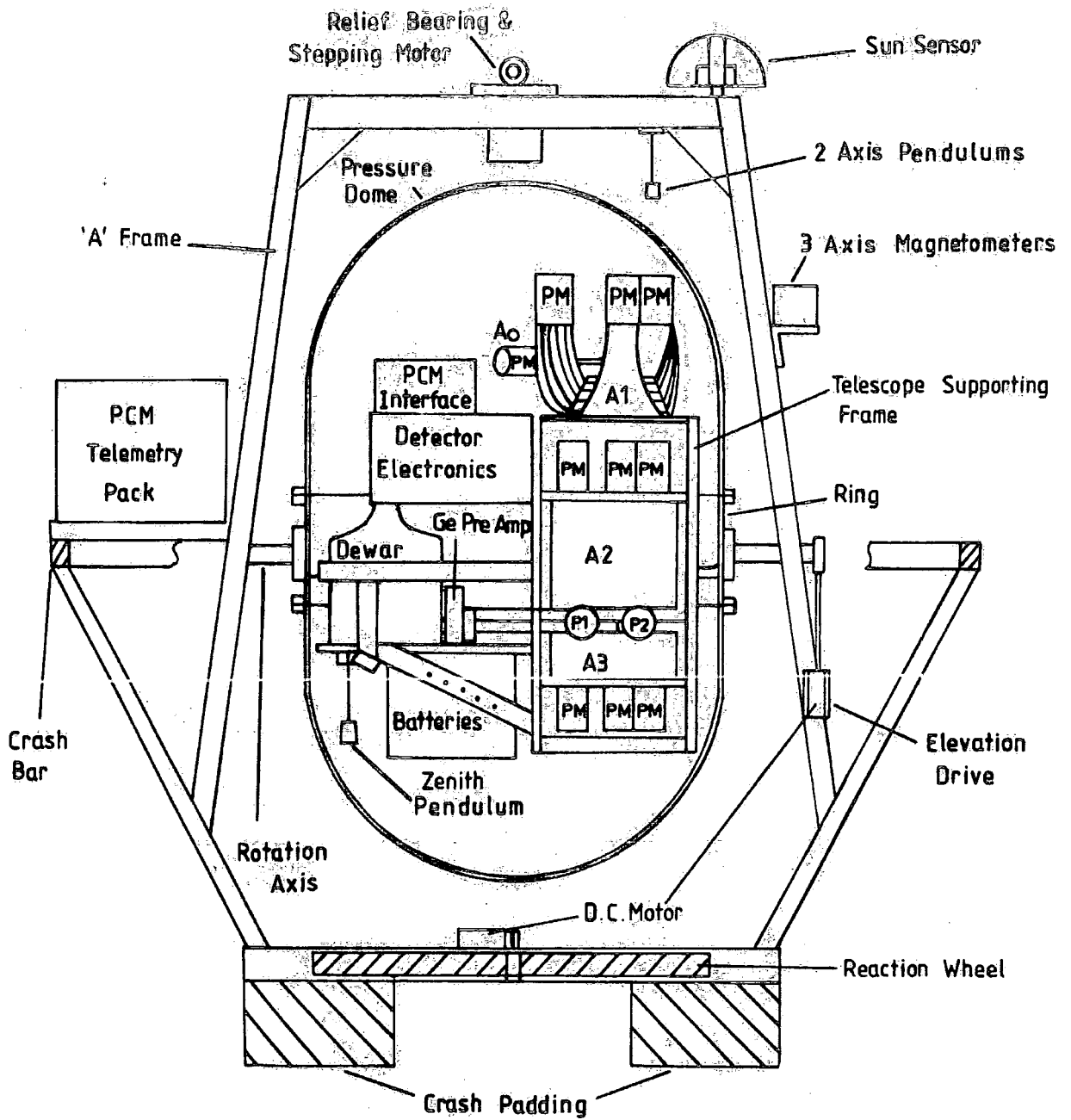


Figure 3:2 The Durham Gamma-Ray Spectrometer integrated with Gondola and Telemetry pack.

A further electronics module (of Cinch plug-in cards) contains the steering system and the interface for a pulse coded modulation (PCM) telemetry system which relays all of the data to ground during balloon flight and also allows the payload to be commanded from ground. Received data is recorded in real time on magnetic tapes for subsequent computer aided analysis. As has been mentioned two pulse-heights are recorded for coincident events, this is done to facilitate the vetoing of the Ge spectra during the computer analysis.

The telemetry system is provided by the National Centre for Atmospheric Research, National Scientific Balloon Facility, at Palestine, Texas, U.S.A.

3.2 DESIGN PHILOSOPHY

It is the application of a Ge crystal as the main detector which is chiefly responsible for the system's excellent spectrometric property; germanium having a typical energy resolution well below 1%. Although both intrinsically pure germanium and the apparently more commonly used lithium drift germanium [Ge(Li)] crystals must be operated at cryostatic temperatures the former type was preferred for the current apparatus since, unlike Ge(Li), it does not suffer irreparable damage if allowed to warm up to room temperatures when not in use. Present technology does not permit the fabrication of large volume Ge crystals and at 86 cm³ the crystal used is close to the maximum size available.

Thallium activated sodium iodide, [NaI(Tl)], was chosen as the main substance for the anticoincidence shields as this inorganic scintillation phosphor gives the optimum combination of properties relevant to the present purpose. Large volume crystals were required and therefore it was important that the material used should show little or no self-absorption of its scintillation photons. NaI(Tl) exhibits the highest

light output of currently available phosphors and figure 3.3 shows that this is the case over a wide range of temperatures; this could be important in high altitude balloon environments. Owing to the hygroscopic nature of sodium iodide, hermetically sealed aluminium containers are required to prevent contact of the material with atmospheric water which would otherwise cause the crystals to cloud and hence reduce the optical transmission property.

NaI(Tl) is used for units A2, A3 and P1 to P4 and it was originally intended that the same should be used for A1, unfortunately this was not possible from a financial aspect and consequently the A1 shield/collimator was constructed, as a multi-layered sandwich arrangement, from NE102a plastic scintillator and lead, which were ready to hand in Durham. The configuration is useful because: (a) lead is an excellent absorber; being of high atomic number (Z) and since the photoelectric absorption and pair production processes are proportional to Z^n ($n = 4$ to 5) and Z^2 respectively, and (b) although the gamma-ray detection efficiency of plastic scintillator is low it is highly efficient at charged particle detection; these charged particles are produced by the absorption and scattering processes in the lead. Al is tapered from bottom to top; primarily to facilitate a trade-off between maximum gamma photon shield traversal and minimum weight considerations, but it also effectively reduces the quantity of material above the detector and therefore local production of gamma radiation is kept to a minimum.

The same type of plastic scintillator is used for the A0 detector as its function, in covering the system's 'viewing' aperture, is to permit transmission of the gamma-rays along the aperture to the Ge whilst indicating the charged particles which reach the detector by the same route.

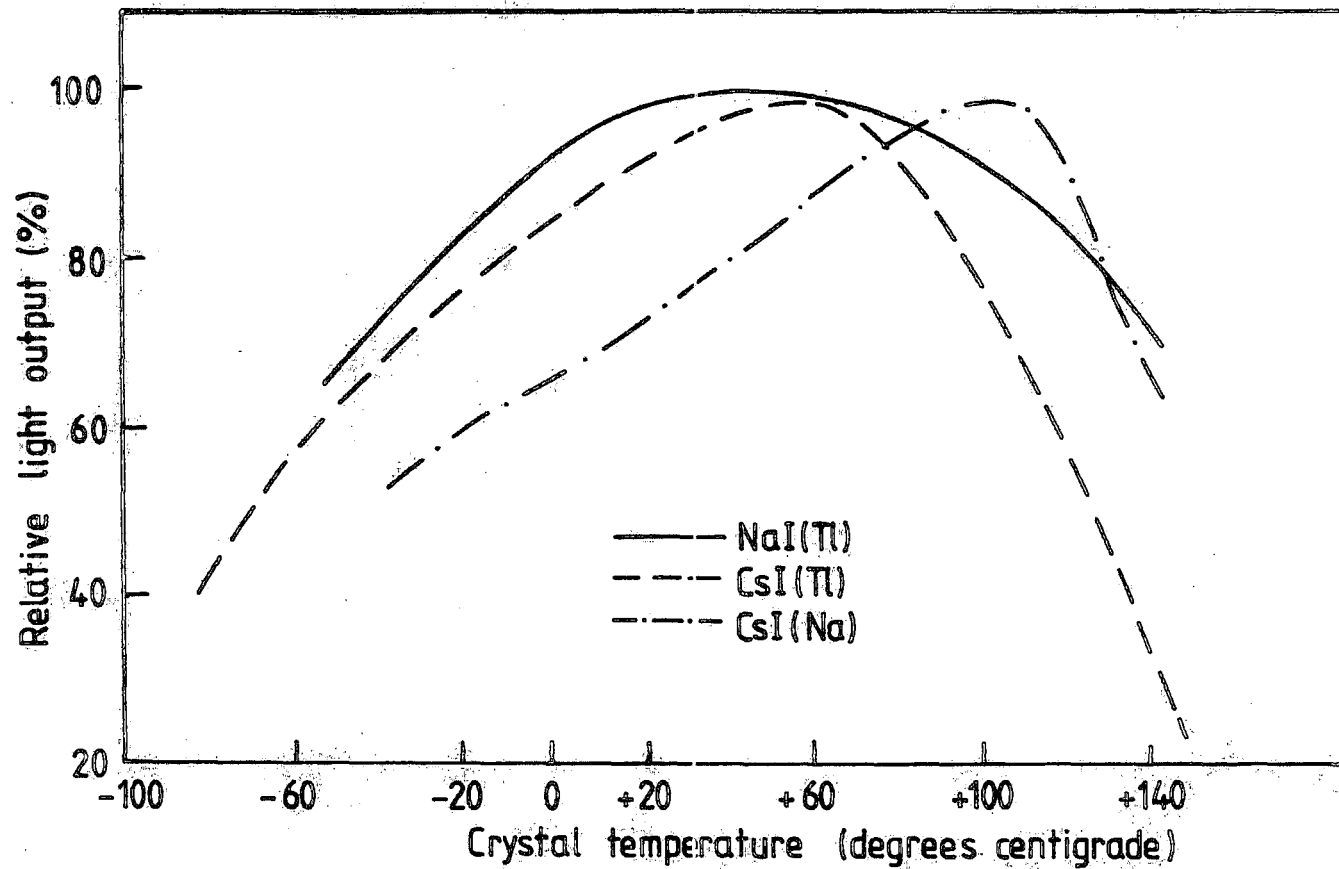


Figure 3-3 Temperature response of some scintillation materials.

Shield elements P1 to P4, which together with the Ge detector function as a polarimeter, have been included in the spectrometer design since there is reason to suggest that at least some of the cosmic γ -radiation is polarised. The device is designed to make use of the non isotropic, azimuthal distribution of Compton scattered, polarised source photons which interact within the Ge crystal. For any Compton event in Ge which scatters a photon into one of the four quadrants of the polarimeter where it subsequently interacts, a record is kept of (a) the energy deposition in both Ge and the P element and (b) precisely which P quadrant the secondary photon entered. If polarisation of the source radiation is present then two diametrically opposite P quadrants will record a higher count rate than their complementary pair. The degree of polarisation in the source radiation, at a particular energy, determines the asymmetry of the count rate between the two pairs and precisely which pair experiences the higher rate is defined by the orientation of the source radiation's electric vector with respect to the polarimeter; see section 4.2.2.

During the balloon flight electrical power for the apparatus is supplied from lithium organic batteries which are of relatively high but limited capacity and therefore the electronics are designed for low power consumption utilising low power military specification CMOS and TTL integrated circuits. Discrete components are used in the analogue circuits and the designs fulfill the requirements: (i) low power consumption (ii) high bandwidth (iii) fast rise time (iv) high linearity and (v) high stability.

Nine independent voltage rails are required for the electronics and these are obtained by series and parallel combinations of batteries, earthed at the appropriate point and regulated via monolithic voltage regulators. The detector and data handling system power consumption is ~ 50 Watts.

A pulse-height voltage range of 0 to 10 Volts is chosen to correspond to crystal energy depositions 0 to 10 MeV and the pulse-height analyser has 16383 channels over this range, yielding an energy resolution of 0.61 keV per channel which complements the resolution of the Ge crystal.

In designing the platform or 'gondola' minimum weight, rigidity and the non use of magnetic materials were the main criteria. Minimum payload weight maximises the float altitude during flight, rigidity increases the accuracy to which the spectrometer may be steered and the application of a magnetometer in the directional orientation system precludes the use of magnetic materials. Thus, aluminium alloy (HE 30TF) is employed throughout, it having the required characteristics and being easily available.

An airtight pressure vessel was chosen to enclose the instrument as the maintenance of a ground level atmospheric pressure working environment should prevent the occurrence of Corona discharge in the EHT supplies. A 10 cm thick jacket of polystyrene foam, with an outer coating of aluminium foil, was built around the pressure vessel to provide thermal insulation and a white paint coating was added to counteract the possibility of solar heating.

The spectrometer's centre of gravity was located on the horizontal axis of rotation thus minimising the couple required to alter the zenith angle of the instrument.

3.3 THE GERMANIUM DETECTOR

An intrinsic, high purity, germanium (Ge) crystal together with its necessary cryostat and dewar assembly, figure 3.4, was manufactured by P.G.T. International according to specification. The dewar may contain a maximum of 20 litres of the required liquid nitrogen coolant, thus permitting the Ge crystal to be held at working temperature ($< 135\text{K}$), by means of a 'cold finger', for a period of 10 days. Also attached to the cold finger is a signal preamplifier which is so placed in order to

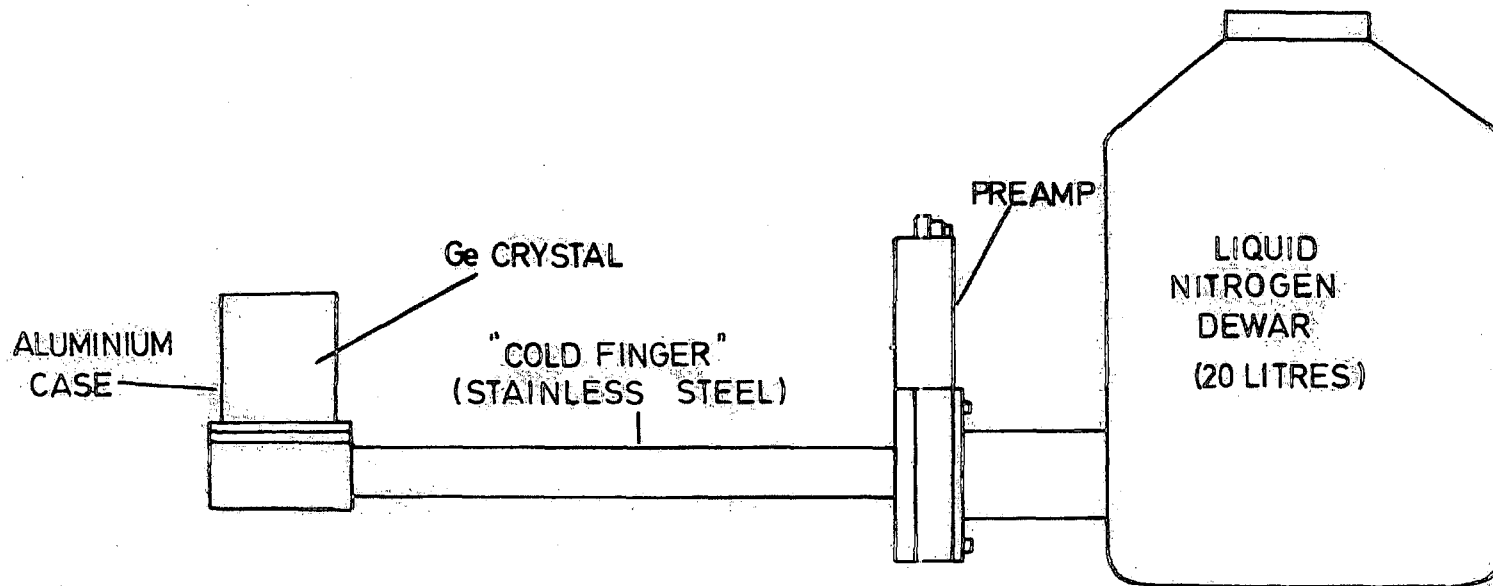


Figure 3-4 The layout of the Ge crystal, Preamp and Liquid Nitrogen Dewar.

reduce its equivalent noise charge. Power is delivered to the preamplifier from a TENNELEC spectroscopy amplifier.

The Ge crystal assembly itself is shown in cross section in figure 3.5. Within an aluminium vacuum cryostat is a right circular, cylindrical, closed end, co-axial, Ge crystal of 86 cm^3 volume, housed in an aluminium can, which is thermally coupled to the copper cold finger and a central electrode is electrically dc coupled through the can to the FET input stage of the preamplifier.

Optimum detector performance was determined at an operating bias voltage of 3.8 kV i.e. (i) a detection efficiency of 23% relative to a (7.62×7.62) cm right circular cylindrical NaI(Tl) detector irradiated by an axial, point source at 25 cm distance from its top surface, and (ii) an energy resolution at 1.33 MeV of 2.26 keV (FWHM).

3.4 THE ANTICOINCIDENCE SHIELD ARRAY

A0 is a circular disc of NE102a plastic scintillator measuring 7.5 cm in diameter and 0.3 cm in depth, mounted above the collimator A1, figure 3.1, covering the spectrometer aperture in order to complete 4π steradian charged particle rejection. A polished and appropriately machined, perspex, light-pipe optically connects the edge of the scintillator disc to one EMI 9757B, 5 cm (2 inch) diameter photomultiplier tube.

Shield and collimator A1 is a 15 cm thick lead/scintillator sandwich comprising six discs of NE102a scintillator alternately spaced with an equal number of lead discs, beginning at the top with a lead layer; both lead and scintillator having a thickness of 1.25 cm and a central hole of radius 2.8 cm. As a whole the collimator is tapered in regular steps from a radius of 11.4 cm for the bottom layer to radius 7.4 cm for the top layer. Three sets of six polished, perspex, light-pipes are positioned at 120° intervals around A1, figure 3.6, each set

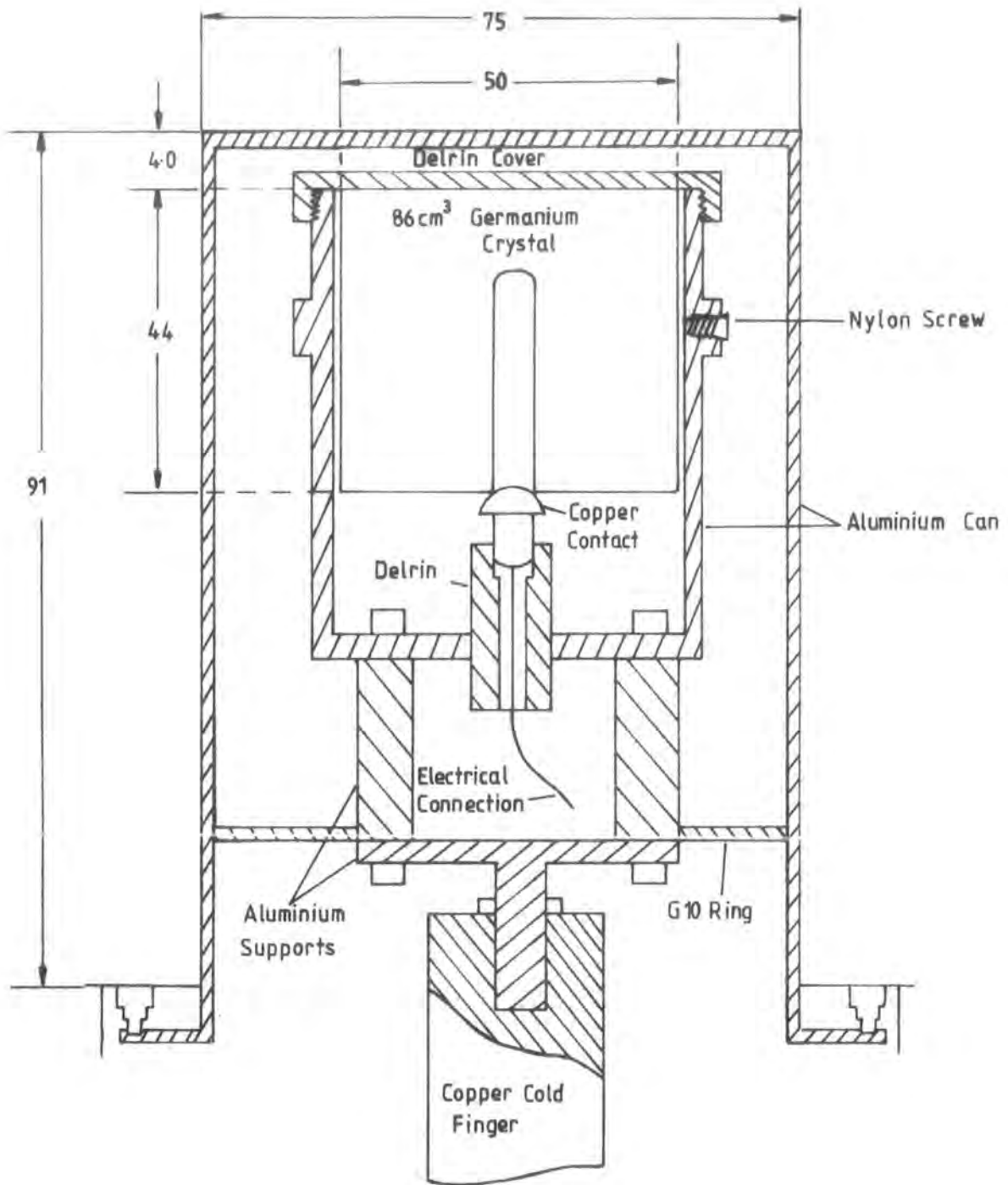


Figure 3-5 The germanium crystal assembly.

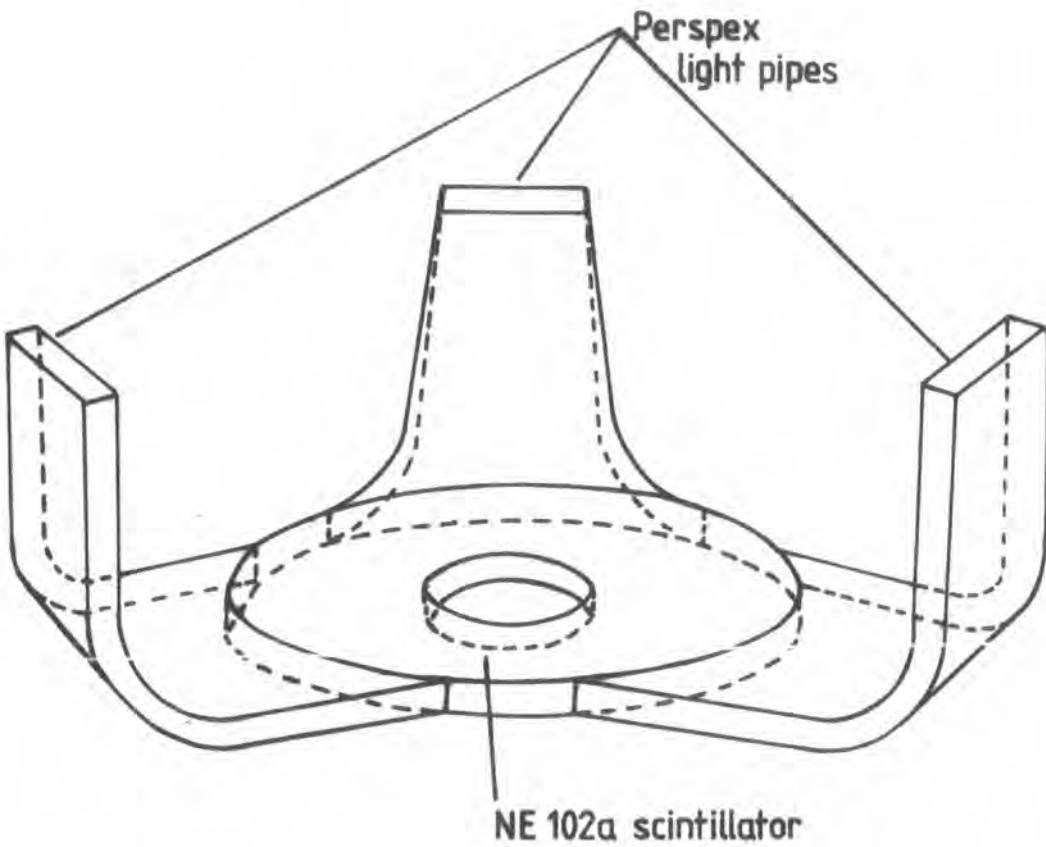


Figure 3-6 An arbitrary scintillator layer from the A1 shield/collimator showing the perspex light pipes at 120° intervals which carry the scintillations to the photomultiplier tubes.

appropriately shaped and bent to match: (i) the edges of the scintillator discs at one end and (ii) a portion of the window of one of three EMI 9758B, 7.6 cm (3 inch) diameter, photomultiplier tubes, figure 3.1.

In all cases where scintillation light-pipes are employed optical cement, type NE581, is used for joining the scintillation and photomultiplier tube windows.

Detector assembly A0 was entirely wrapped with aluminium foil, covered with black adhesive tape and given several coats of black paint to ensure the exclusion of external optical photons. In the case of A1 each layer of scintillator together with its light pipes was individually wrapped in aluminium foil and black adhesive tape and the assembly as a whole was immersed several times in a bath of paint.

NaI(Tl) shields A2, A3 and the four NaI(Tl) polarimeter quadrants (P1 → P4) were manufactured by HARSHAW CHEMIE BV. Polarimeter segments P1 to P4 and the A2 crystal which are all optically isolated from each other are hermetically sealed within one aluminium housing, figure 3.7, and A3 forms a separate unit, hermetically sealed within its own aluminium container. The A2/Polarimeter unit which surrounds the Ge detector is a right, circular, cylindrical, annulus of diameter and depth 30 cm and the axial, central aperture hole of 2.5 cm radius is bored to a depth of 24.5 cm whereupon it widens for the remaining crystal depth to a radius of 4.8 cm allowing the insertion of the Ge detector, figure 3.7.

Unit A3 is a right, circular, cylinder of 30 cm diameter and 12.5 cm depth, containing a shallow concavity in its top face again to accommodate the housing of the Ge detector, figure 3.8.

Windows of 6.7 cm diameter, for transmission of scintillation photons to photomultiplier tubes, are incorporated in the aluminium casings of each of the A2/Polarimeter and A3 units. A2 has four windows, arranged on the top face of the crystal, as shown in figure 3.7 and A3 has

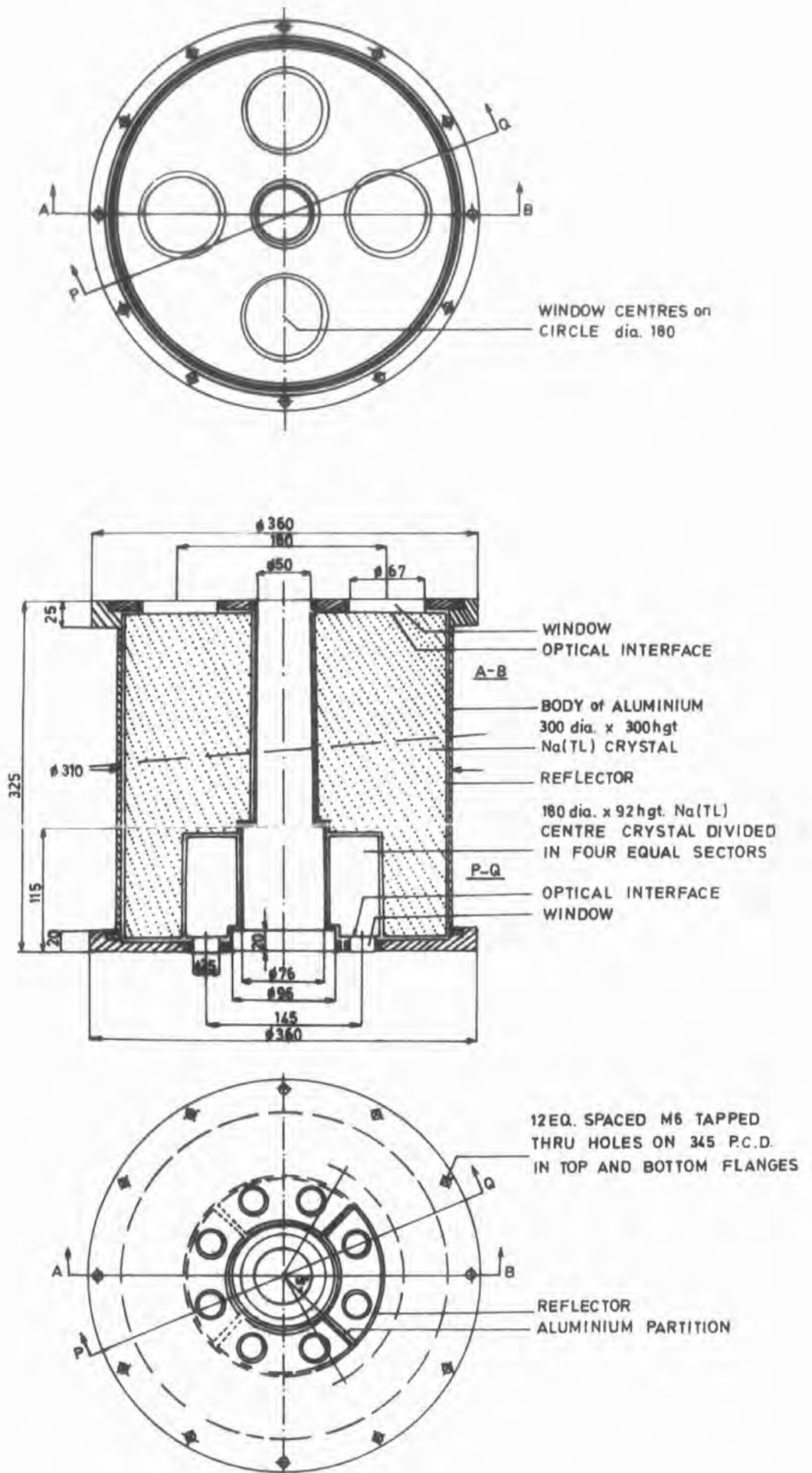


Figure 3-7 The A2 annular crystal assembly.

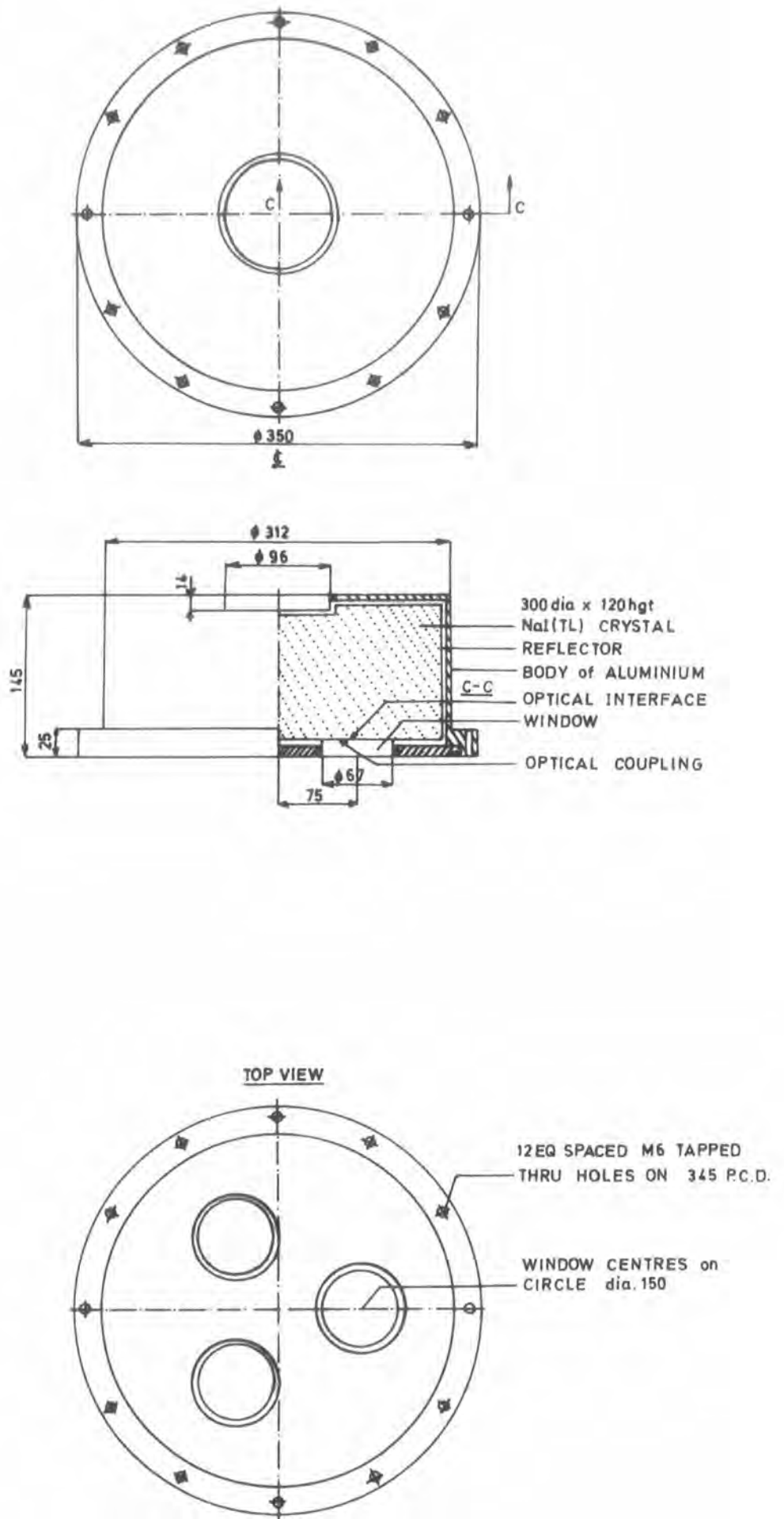


Figure 3-8 The A3 crystal assembly.

three windows, figure 3.8, in its bottom face. Each polarimeter quadrant has two windows of diameter 2.5 cm placed in the bottom face of the annulus. Crystals A2 and A3 are viewed by four and three EMI 9758B 7.6 cm (3 inch) diameter photomultiplier tubes respectively, which are directly bonded onto the windows and each polarimeter crystal is viewed by one EMI 9757B 5 cm (2 inch) photomultiplier via a two pronged, shaped and polished, perspex light-pipe. The pipe is wrapped in aluminium foil and black adhesive tape and several coats of black paint cover the pipe and photomultiplier assembly.

In the process of figuring the light-pipes for A₀, A₁ and P₁ to P₄ the following rules were applied as far as possible:

- (i) The pipe material should produce little attenuation of short wavelength optical photons.
- (ii) Highly reflective surfaces are required to minimise light losses.
- (iii) The scintillator and light-pipe should be of equal thickness at the optical coupling.
- (iv) The radius of curvature of a bend in a pipe should exceed eight times the pipe thickness.
- (v) The total area of the end of a pipe should equal the area of the viewing photomultiplier tube window.

All photo multiplier tubes have: (a) screening from magnetic fields by mu-metal shields in order to minimise gain variation and (b) a base assembly, comprising the dynode resistor chain and a head amplifier, mounted directly onto the tube. Dow Corning Silastic 9161, silicone rubber compound is used to encapsulate the base assembly of each tube to prevent high voltage discharge at low pressure. Figure 3.9 shows a tube assembly.

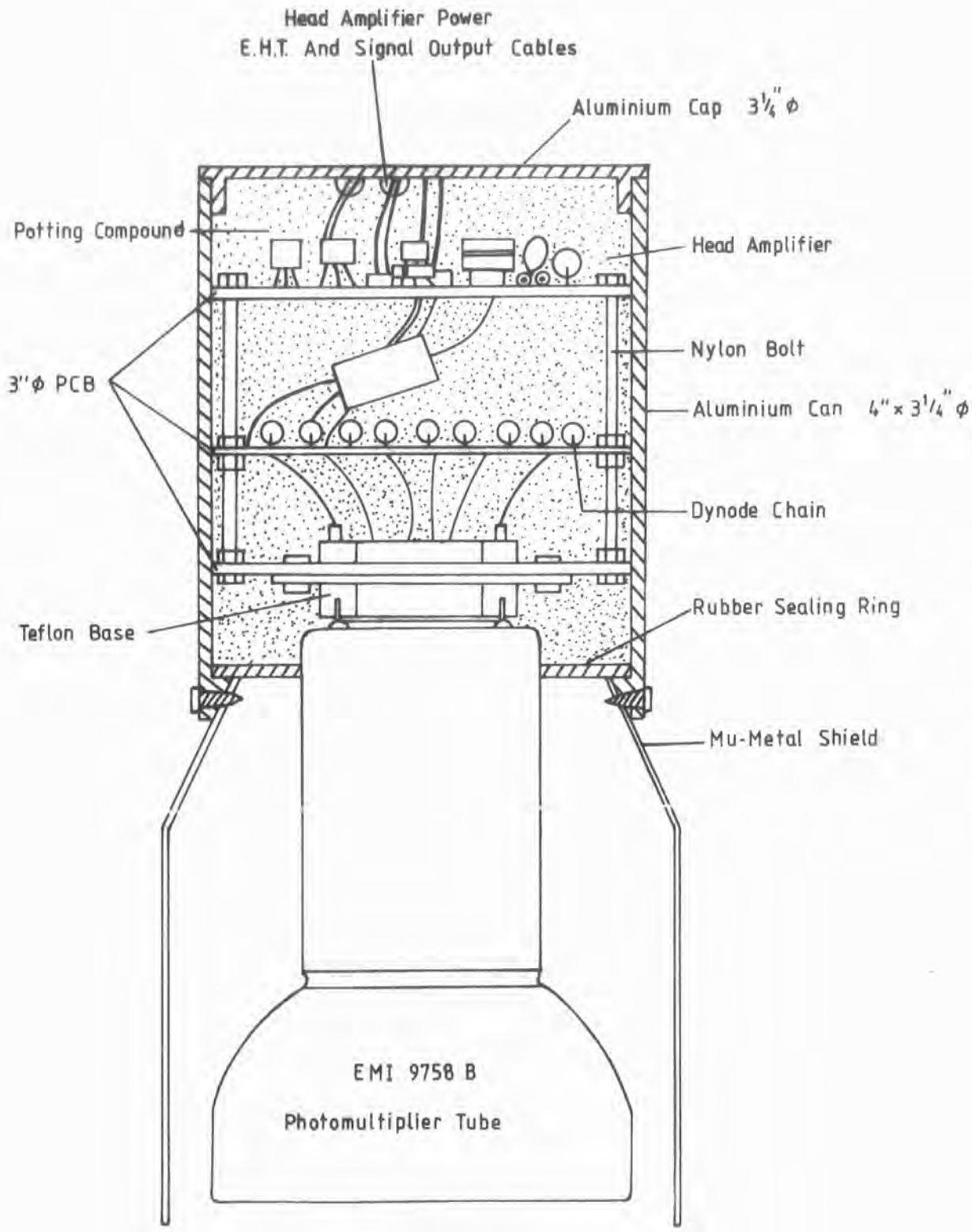


Figure 3-9 A typical photomultiplier tube and base assembly.

3.5 DATA HANDLING ELECTRONICS

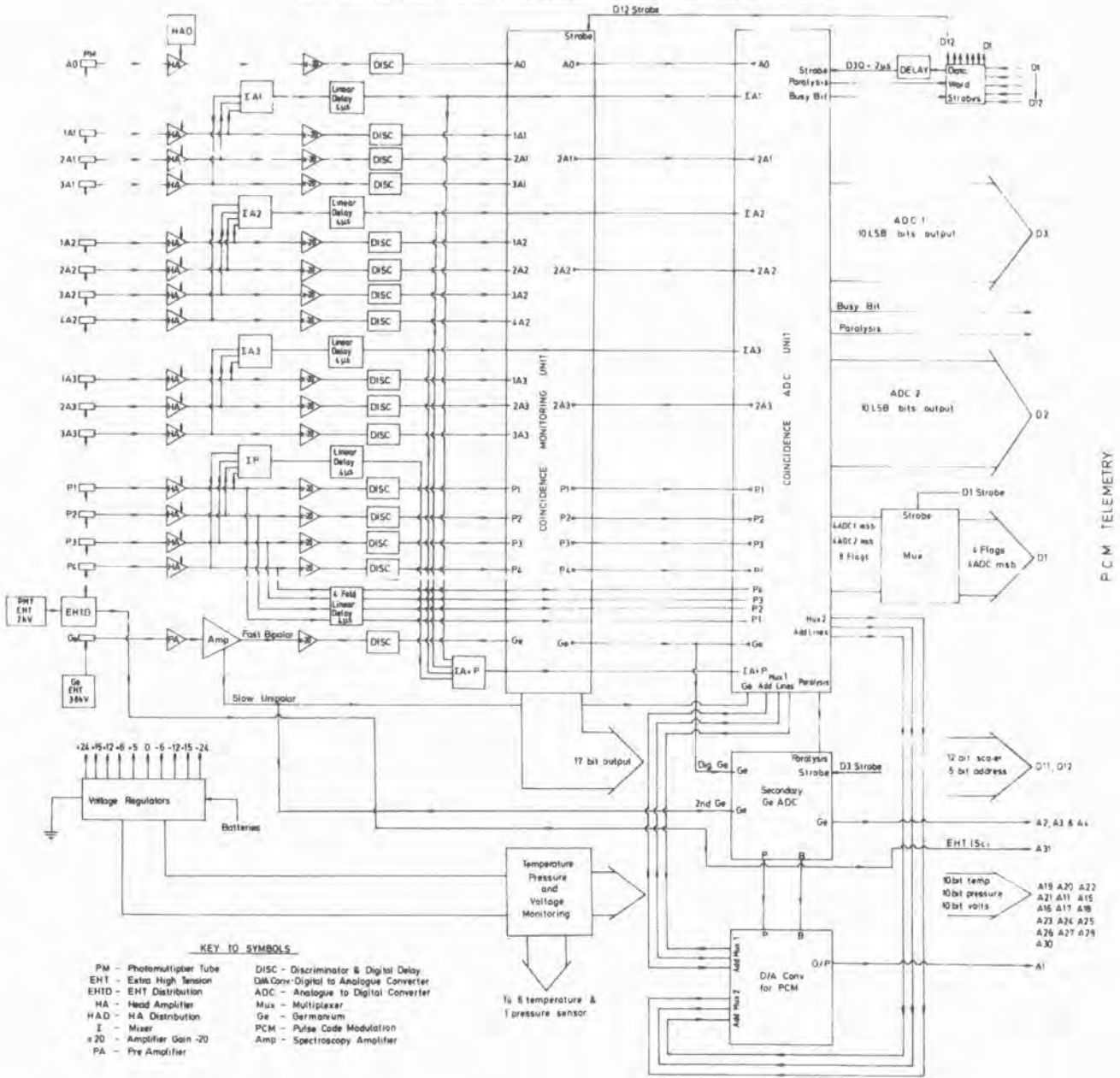
An overall schematic representation of the detector, data handling and auxiliary sensor systems' electronics is given in figure 3.10.

The heart of the data handling system is the Analogue to Digital Converter (ADC) board of the Coincidence/ADC unit. Shown in figure 3.11 this unit forms a 16383 channel PHA by means of a 14 bit ADC, type MP8014 from Analogic Ltd. Analogue pulses from the photomultipliers of each of the detectors and from Ge, which in all cases except for Ge and A0 are first averaged by mixer circuits (Σ), are input to the ADC board which then records, in a digital form, two of these pulses as specified by address information received from the coincidence board of the Coincidence/ADC unit, figure 3.12. This address information is formed, on a priority basis, by the logic contained on the coincidence board as a result of the combinations of signals at its inputs which are from the eight elements of the detector system. The combinations for the various coincidences with the pulses analysed correspondingly, are given in table 3.1 and the pulse analysis priority arrangement is:-

(1) Ge (2) P: [(i) P1 (ii) P2 (iii) P3 (iv) P4] (3) A: [(i) A2 (ii) A3 (iii) A1]. In order to prevent the A and P signals dominating the trigger pulses from the board the logic only allows every 32nd A or P event to trigger; this is done by the use of 5 bit binary scalars in the design. After the analysis the 14 bit ADC outputs from each of the two pulses are held in flip flops until the next analysis is triggered from the coincidence board. The stored information is then telemetered to ground together with 'flag' information from the coincidence board, also recorded in flip flops, which signifies which coincidences among Ge, P and A took place.

The signals input to the coincidence board of the Coincidence/ADC unit are in fact, those output from another coincidence board,

DETECTOR ELECTRONICS, DATA HANDLING AND AUXILIARY SENSOR SYSTEMS



P.C.M. TELEMETRY

Figure 3-10 The detector electronics, data handling and auxiliary sensor systems.

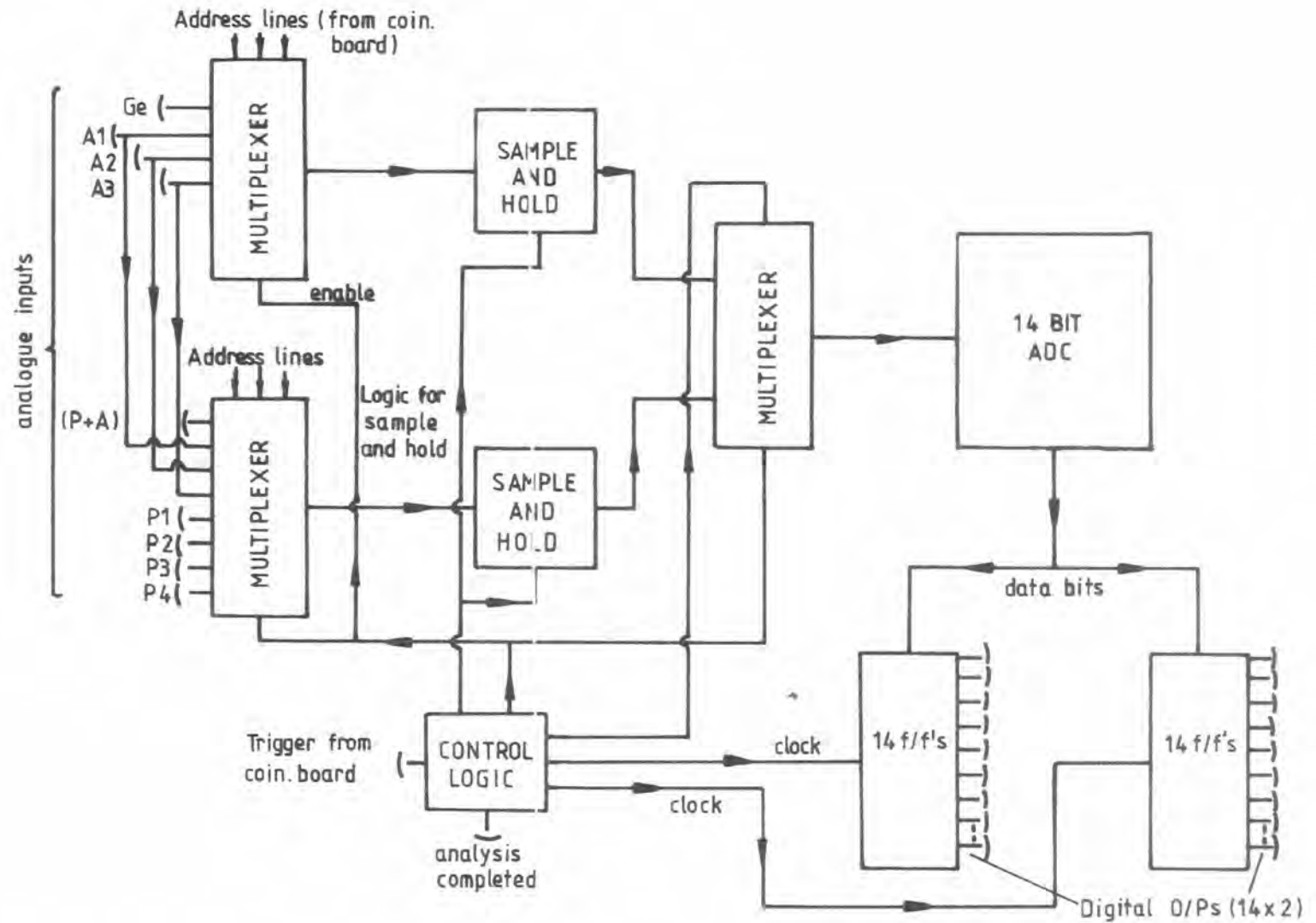


Figure 3.11 The ADC board of the Coincidence / ADC unit.

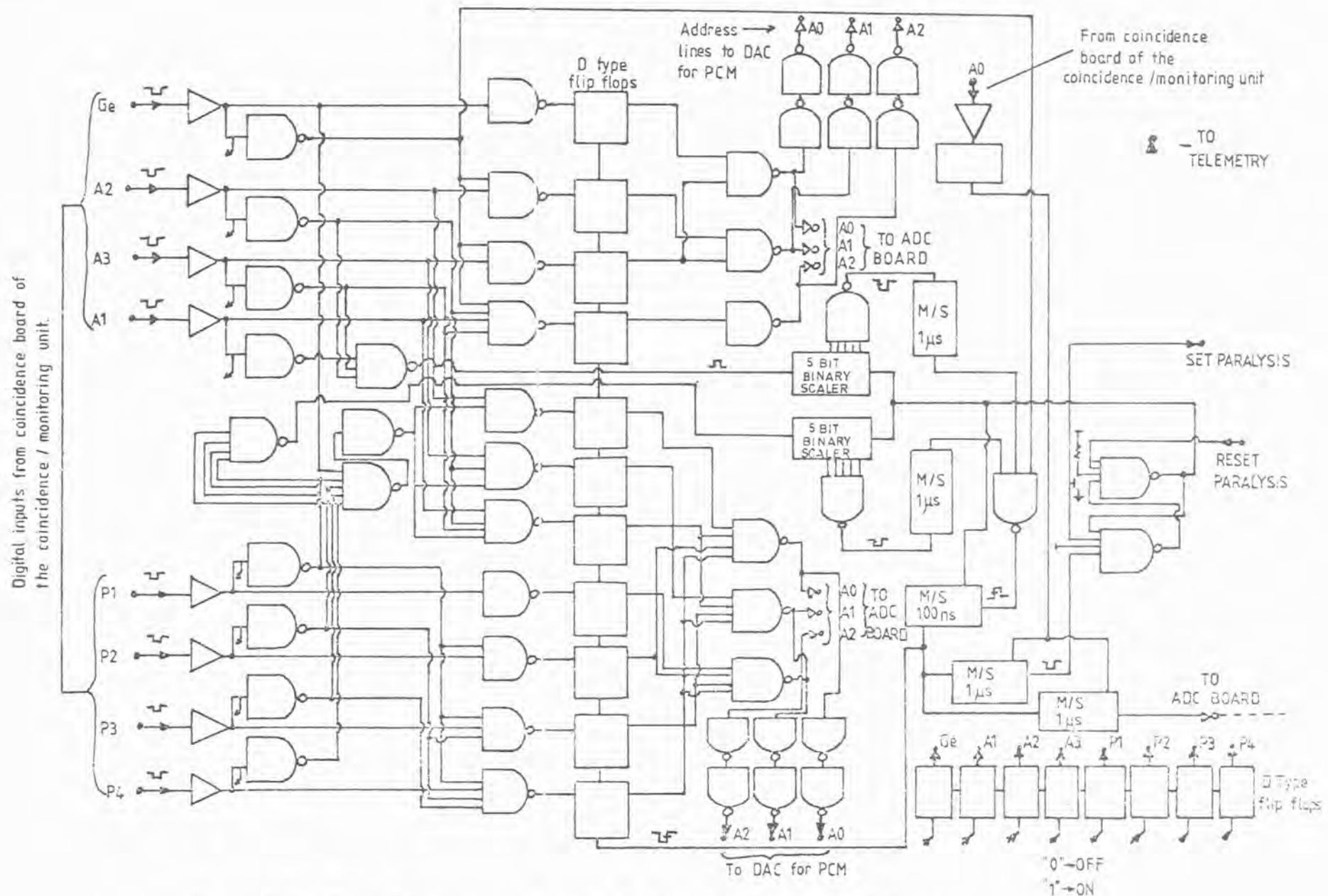


Figure 3-12 The Coincidence board of the Coincidence / ADC unit.

TABLE 3.1 The analogue signals recorded for various combinations of detector pulses

'Coincidence'	Interpretation	Analogue Pulses Analysed		Flags
G.P.A	Background	G	P	P ₁₋₄ A ₁₋₃
G.P. \bar{A}	Polarisation	G	P	P ₁₋₄ -
G. \bar{P} .A	Background	G	A	- A ₁₋₃
G. \bar{P} . \bar{A}	Source	G $\Sigma(P + A)$		- -
\bar{G} .P.A	Background	A	P	P ₁₋₄ A ₁₋₃
\bar{G} .P. \bar{A}	Background	-	P	P ₁₋₄ -
\bar{G} . \bar{P} .A	Background	A $\Sigma(P + A)$		- A ₁₋₃
\bar{G} . \bar{P} . \bar{A}	No event	-	-	- -

G = Germanium signal

P = Polarimeter Signal = P1, P2, P3, P4

A = Anticoincidence Shield Signal = A2, A3, A1

)
)
) In priority order

illustrated in figure 3.13, that of the Coincidence/Monitoring unit. This coincidence board takes as its input the original pulse from each photomultiplier tube but which has first been processed by an amplifier and discriminator (denoted as X-20 and DISC in figure 3.10) and the board produces an output for each detector A1, A2 and A3 if 2 or more signals are input from that detector. In the case of the Polarimeters an output is produced for each input quadrant signal. The following logic statements clarify the boards' function:

$$A1 = 1A1.2A1 + 1A1.3A1 + 2A1.3A1$$

$$A2 = 1A2.2A2 + 1A2.3A2 + 1A2.4A2 + 2A2.3A2 + 2A2.4A2 + 3A2.4A2$$

$$A3 = 1A3.2A3 + 1A3.3A3 + 2A3.3A3$$

$$P = P1 + P2 + P3 + P4$$

where symbols '+' and '.' carry their Boolean algebraic interpretation and the prefixes on A1, A2 and A3 denote a particular photomultiplier tube from that detector. Thus the outputs from the coincidence board of the Coincidence/Monitoring unit represent 'true' events from the particular detector.

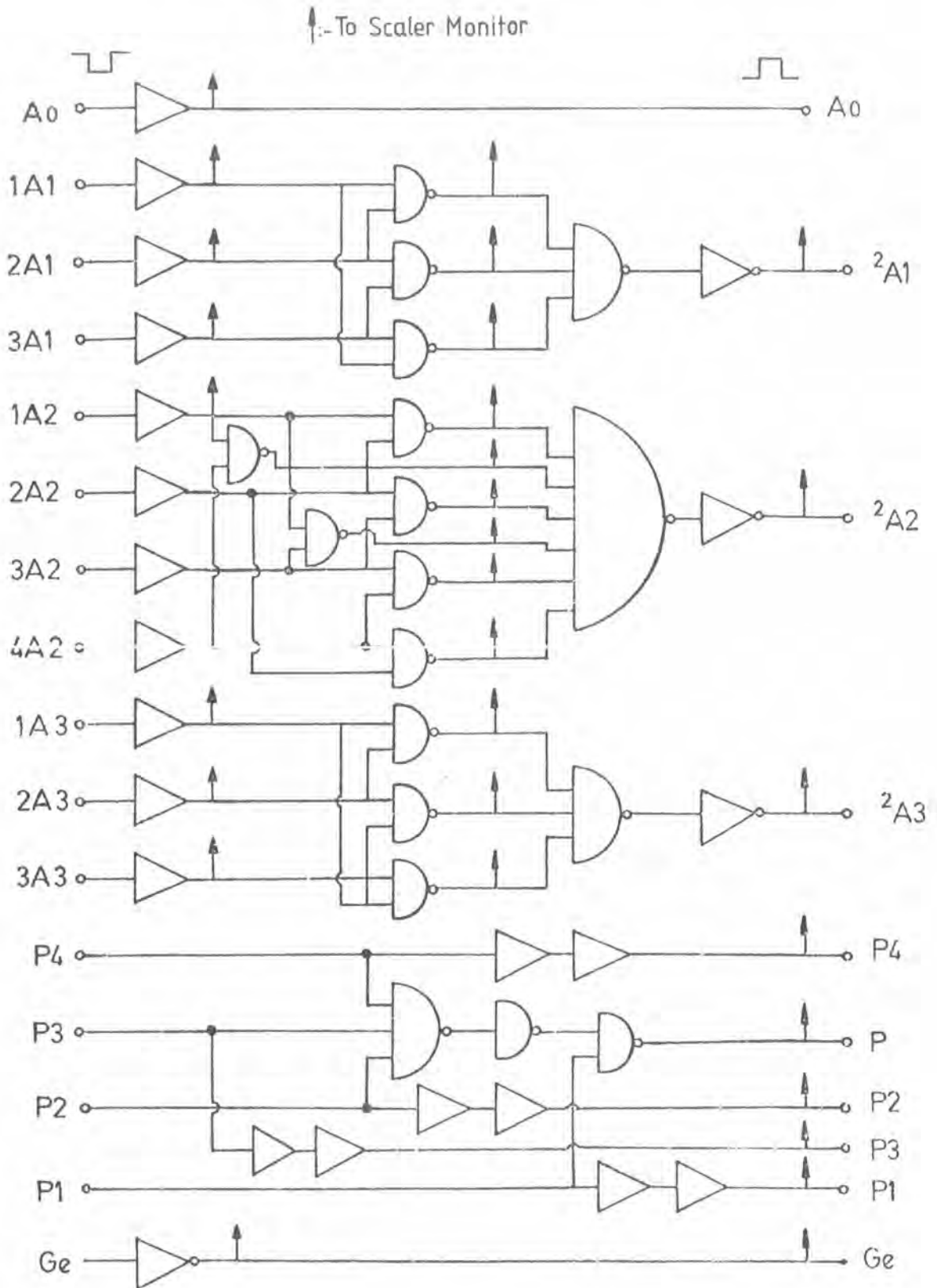
The purpose of the discriminators is to set a minimum threshold of 50 keV (\approx 50 mV) for acceptable detector energy deposition and the amplifiers (X-20) ensure that the pulse corresponding to this energy is of a reasonable voltage, i.e. 1 Volt, for the discriminator operation. Output pulses from the discriminators are standard TTL logic levels.

Analogue and digital delays are incorporated in the mixers and discriminators respectively to ensure correct timing of pulse arrival at the ADC unit. Conversion time for the ADC analysis is 8.4 μ s for each pulse.

3.6 HOUSEKEEPING ELECTRONICS

A Scaler monitor board forms the complementary part to the Coincidence/Monitoring unit, figure 3.14, and this monitors the scaler

Figure 3-13 The coincidence board of the coincidence / monitoring unit.



rates of all sixteen individual photomultiplier tube rates and the coincidence rates between the individual tubes of each shield detector. Thirty-one rates are monitored in all, over a repeated 8 second period, each for a duration of 250 ms. The scaler digital outputs are held in flip flops together with 5 address bits for subsequent telemetry to ground.

As a back up to the main ADC a secondary one of 10 bit resolution is incorporated which is dedicated solely to the Ge detector output.

Systems' voltages, temperatures and the pressure inside the airtight container are also constantly monitored by a separate systems' monitoring unit. Four thermistors are used as temperature sensors and these are placed at various locations within the airtight container. Pressure is measured by a commercial transducer (Bell and Howell type 4-393-L101) and the 9 power rail voltages are measured by means of potential dividers. These parameters are measured in the form of analogue voltages (0 to 5 Volts) and are telemetered to ground via separate analogue channels in the telemetry system.

3.7 THE SYSTEM ORIENTATION SENSORS

Information concerning orientation of the spectrometer in Zenith Angle and Azimuth is obtained from a system of pendulums and fluxgate magnetometer elements respectively. In addition a solar sensing device is incorporated to provide back up azimuthal information to that from the magnetometer.

Each magnetometer element produces an output in the range 0 to +5 Volts for field strengths of -0.5 gauss to + 0.5 gauss and for use with the azimuth drive system each output is converted to a 10 bit digital word. The signals from the horizontal elements Hx and Hy are proportional to the component of the earth's magnetic field in the direction of the elements, i.e.

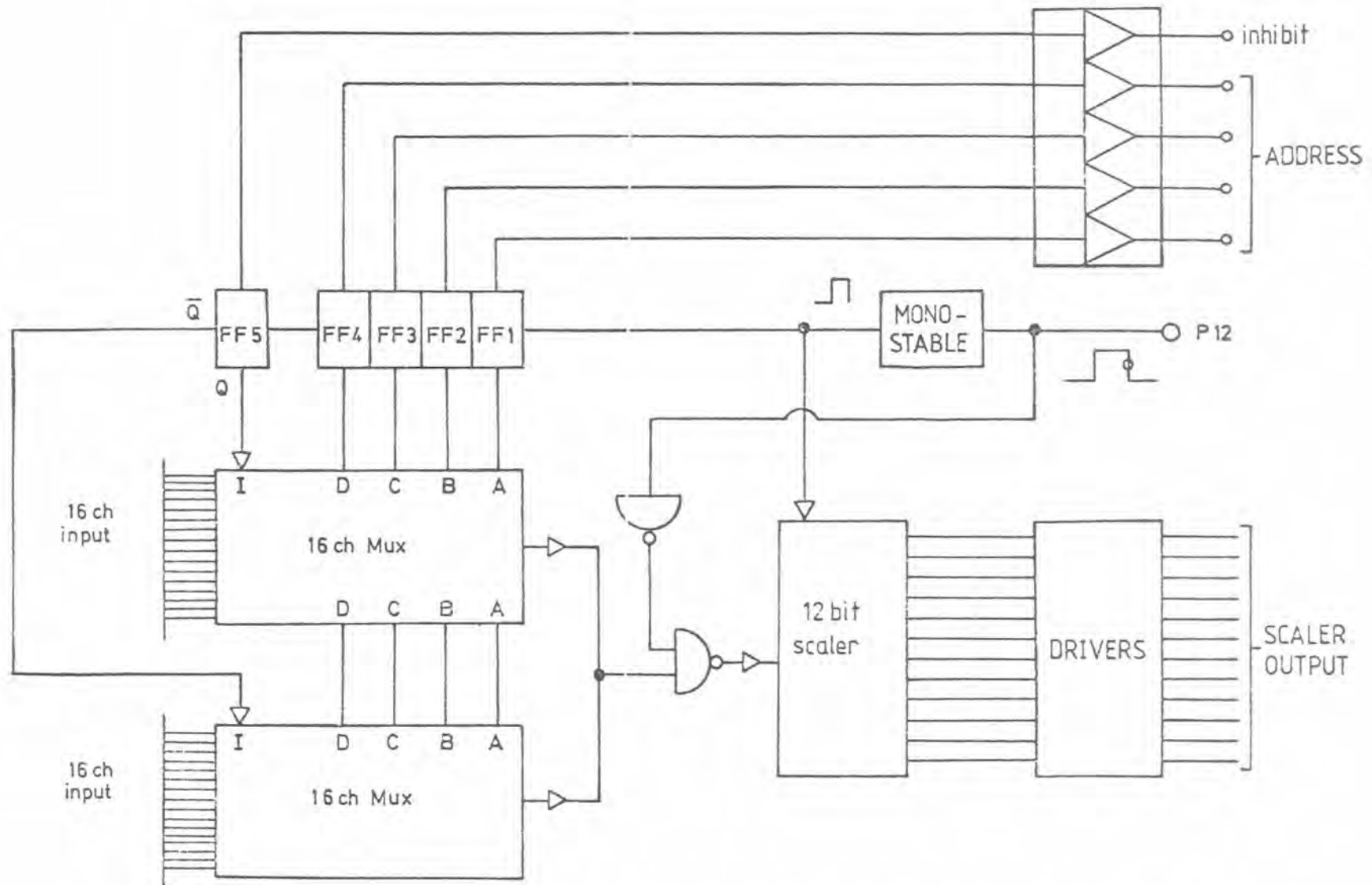


Figure 3-14 Block diagram of the scaler monitor board of the coincidence / monitoring unit.

$$V_x = k \sin \theta \cos \phi \quad (3.1)$$

$$V_y = k \sin \theta \sin \phi \quad (3.2)$$

where ϕ is the azimuthal angle, k is a constant and θ is the angle between the vertical and the field direction.

The solar sensor, shown in figure 3.15, employs two solar cells, one on each side of a metallic vane, which produce outputs proportional to the amount of light falling on them. Thus only when the cells are directly face on to the sun are their outputs equal and hence by means of a servo-positioning motor the cells are maintained in that position. A linear potentiometer on the axis of the instrument produces an output voltage representing the angle between the zenithal swing plane of the spectrometer and the direction of the sun and therefore from a knowledge of the sun's azimuth at the time of observation the spectrometer azimuth can be quickly calculated.

Zenith Angle information is provided from the outputs of three linear potentiometers, each of which is attached by a 1:2 pulley arrangement, to the fulcrum of an 11 inch long, solid pendulum which continues to hang vertically as the gondola changes its orientation. Two of the pendulums are mounted, one on the spectrometer itself and the other on the gondola, so that their swing planes correspond to the zenithal rotation plane of the spectrometer. The third pendulum is mounted on the gondola with its swing plane at right angles to that of the other two. Three pendulums are required since the gondola is expected to undergo a varying tilt during flight and therefore no single pendulum could reproduce the true Zenith Angle.

The true Zenith Angle is given by:

$$Z.A. = \text{Arc sin} \left\{ \frac{\sin^2(\theta_T - \theta') + \tan^2 \theta''}{1 + \tan^2 \theta''} \right\}^{\frac{1}{2}} \quad (3.3)$$

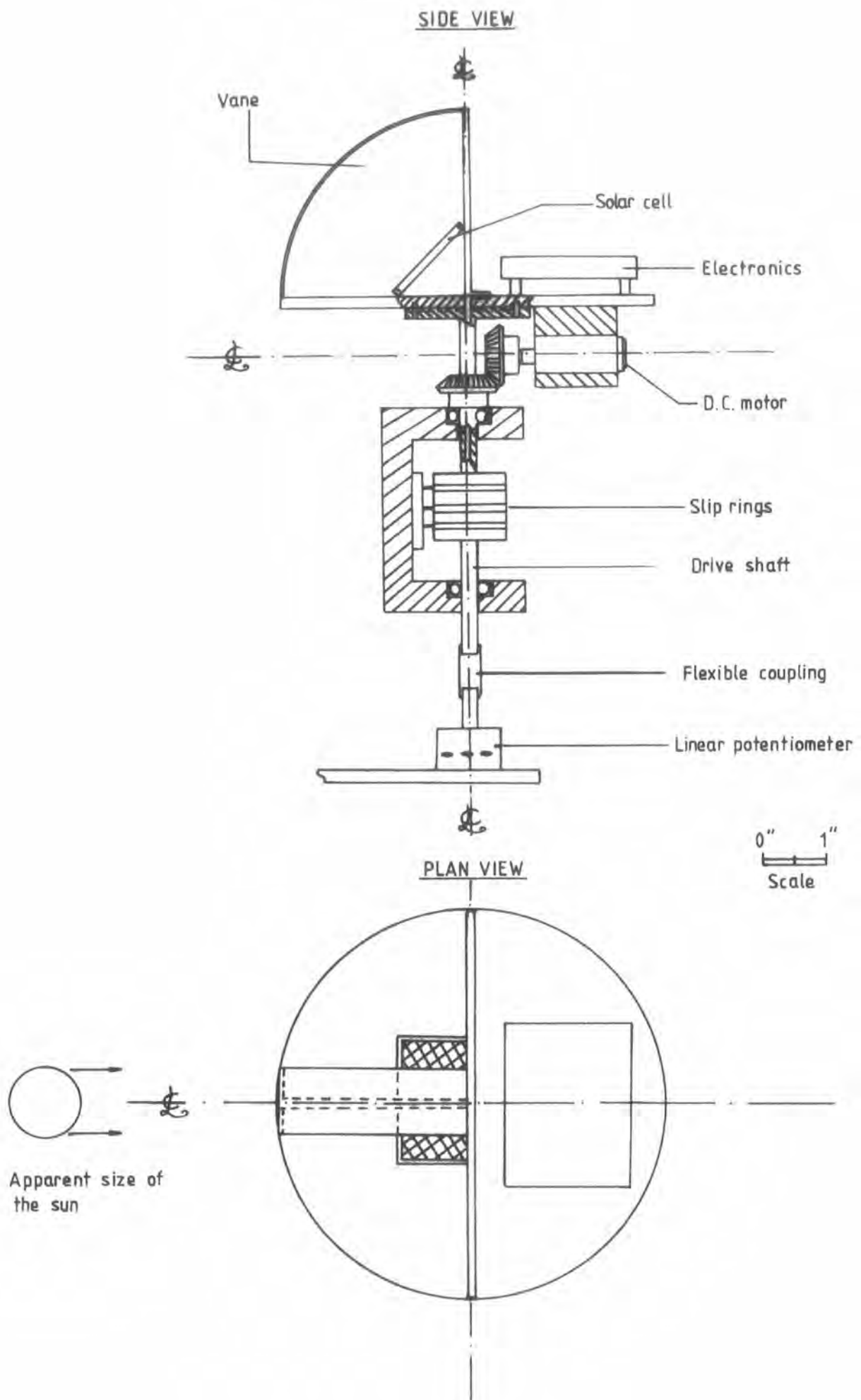


Figure 3-15 The Solar Sensor

where θ_T is the angle between the spectrometer and frame, θ' and θ'' are the tilt angles of the gondola in planes parallel and perpendicular to the spectrometer zenithal rotation plane respectively.

3.8 THE STEERING SYSTEM

Figure 3.16 illustrates the physical means by which the spectrometer is orientated in Zenith Angle. A pivoted d.c. motor turns a $\frac{1}{2}$ " diameter, threaded rod through a threaded block which is also pivoted and attached via a lever to the spectrometer central rotation axis. The electronics controlling the zenith drive is depicted in figure 3.17. Two modes of operation, i.e. manual and automatic, are available and a particular mode is chosen by the use of 'Auto' or 'Manual' telemetry commands to address an analogue switch which routes either the Auto or Manual directional information to the power amplifier driving the zenith motor.

In Manual mode 'Increase' and 'Decrease' telemetry commands, which cannot be in simultaneous operation, are sent to the differential inputs of an operational amplifier and this device produces an analogue voltage output to drive the zenith motor in the appropriate direction.

The Automatic mode functions from a telemetered 12 bit digital word, representing the required Zenith Angle, which is converted, by a Digital to Analogue converter (DAC), to an analogue signal and this is then compared, by an operational amplifier, to an analogue signal from a potentiometer which provides information on the current Zenith Angle by being attached to a pendulum. The pendulum arrangement is described in section 3.7. An error signal is output from the op amp which drives the zenith motor until a null condition obtains. This system produces a zenith drive rate of 0.25°s^{-1} in both operation modes.

Azimuthal orientation is physically achieved by a spinning reaction wheel, mounted at the bottom of the gondola (figure 3.2), consisting of

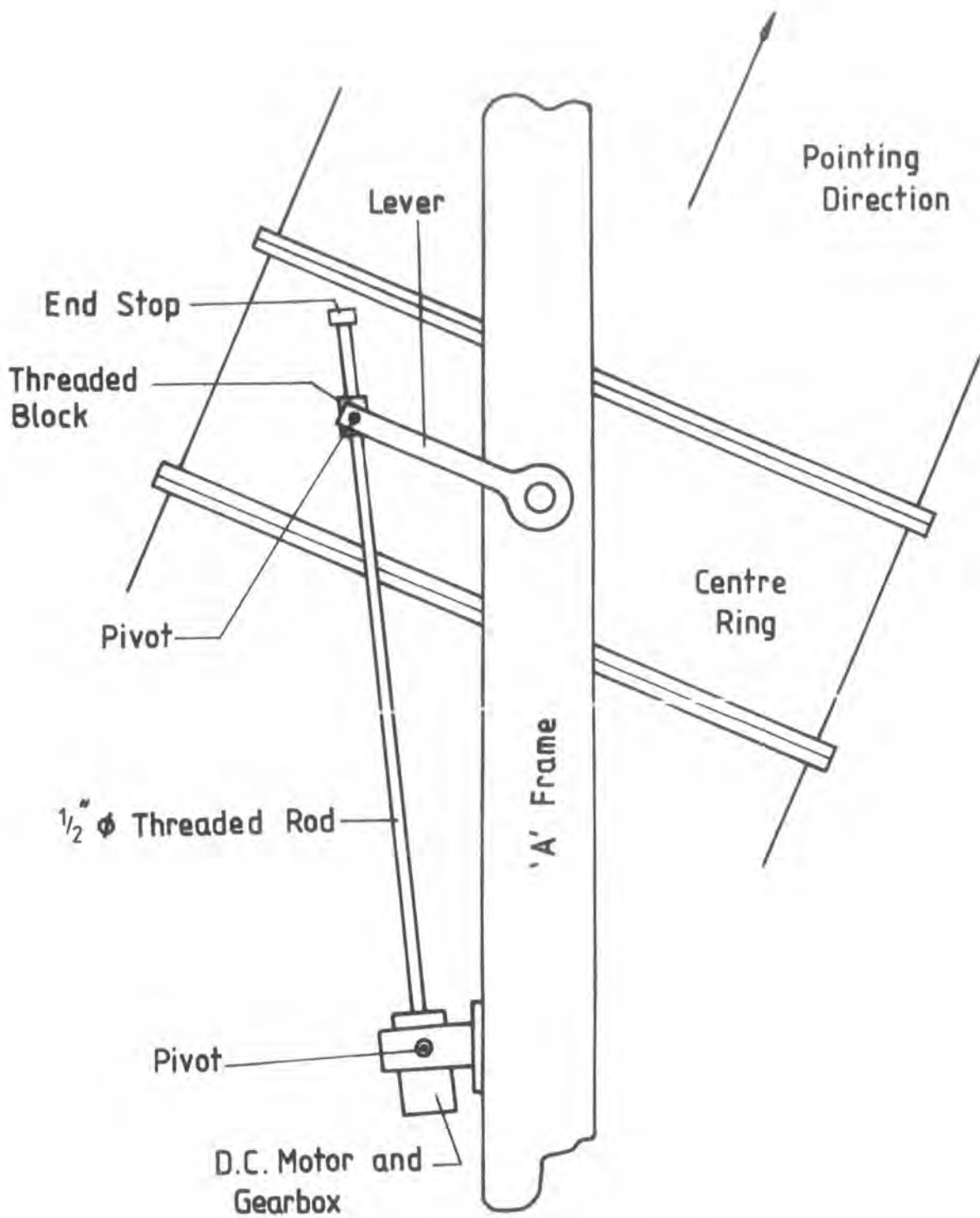


Figure 3-16 The Zenith Drive.

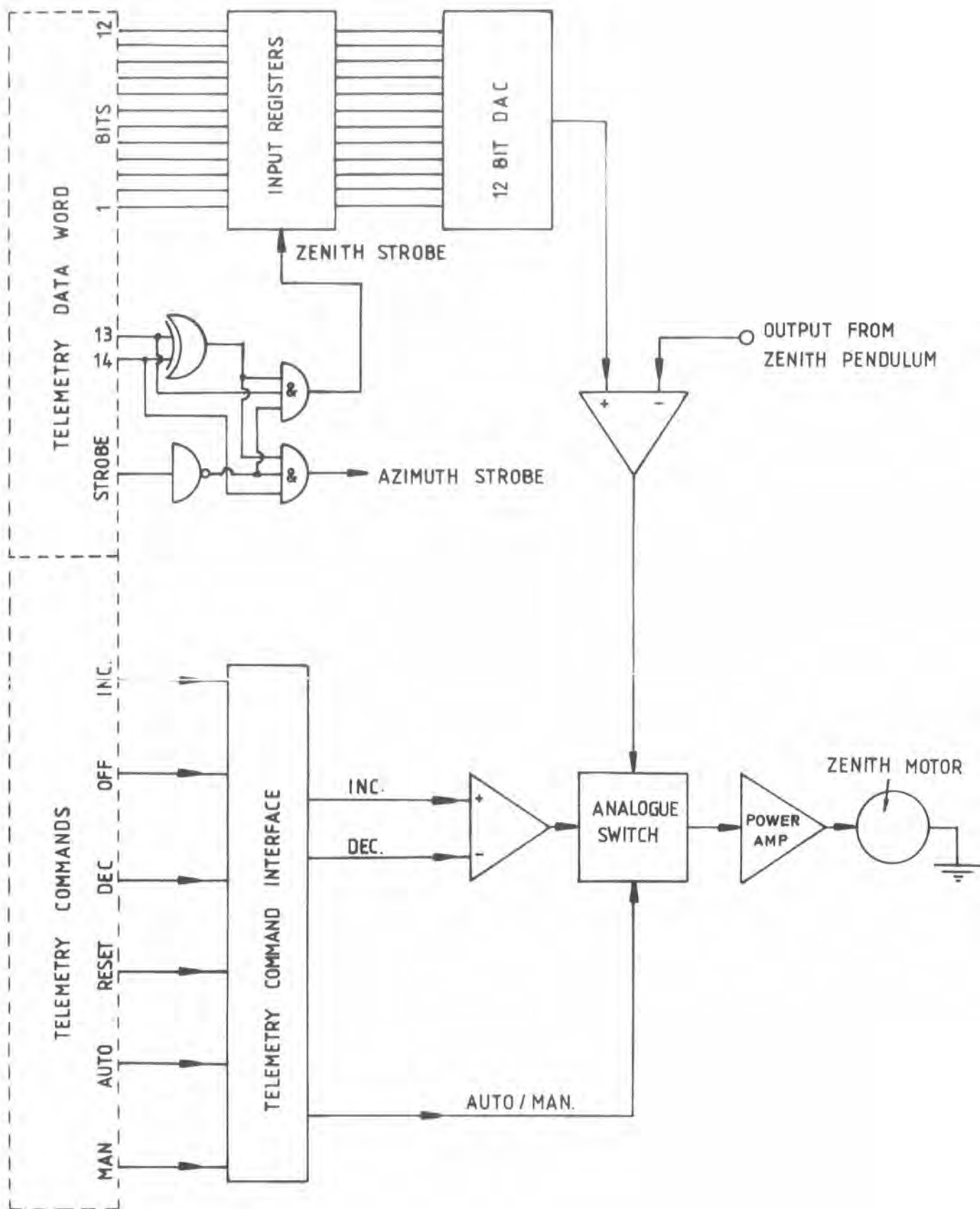


Figure 3-17 The Zenith Drive Electronics.

8 spokes, each having a lead block attached to its outer end. Figure 3.18 shows the electronic controlling arrangement for the azimuth drive and like the zenith system a facility exists for both manual and automatic control. The manual mode is the same arrangement as for the zenith system.

For automatic control a 12 bit digital word representing the required azimuthal setting is telemetered to the instrument and is transferred to a digital adder which optionally allows adjustment of $\pm 11.25^\circ$ for off source background measurement when required. The trigonometrical sine and cosine of α are then multiplied by magnetometer signals V_x and V_y respectively producing voltages $V_1 = k \sin \theta \cos \phi \sin \alpha$ and $V_2 = k \sin \theta \sin \phi \cos \alpha$, where k , θ and ϕ are as specified in section 3.7, which are subsequently employed by an operational amplifier to produce an error signal $V_e = k \sin \theta \sin (\phi - \alpha)$. Summed with a velocity signal from a tachometer on the reaction wheel this combined signal drives the wheel until a null condition is reached.

A torsion relief system is necessarily incorporated as without this the suspension cables from the balloon would become twisted. Consequently the combined signal is also fed to a voltage to frequency converter for the torsion relief stepping motor.

3.9 THE TELEMETRY SYSTEM

For each balloon flight NSBF provides a Consolidated Instrumentation Package (CIP) for telemetry purposes. The package comprises:

- L band telemetry transmitter
- Command receiver
- Omega Navigation system
- Rosemount altimeter
- F_m/F_m telemetry system
- PCM telemetry encoder
- Command decoder

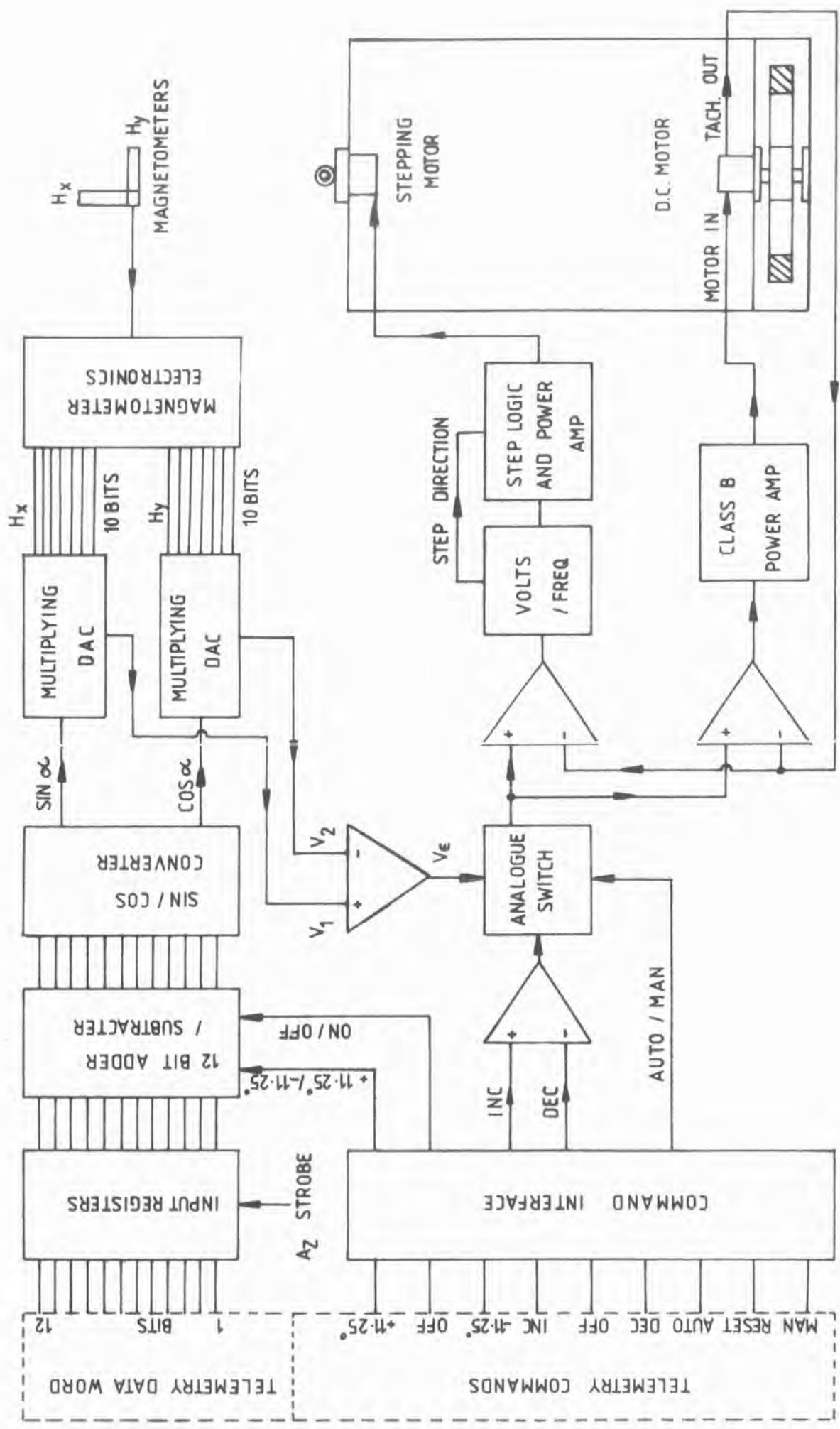


Figure 3-18 The Azimuth Steering Electronics.

The Pulse Code Modulation (PCM) encoder is a Spacetac model 2100 having a PROM programmeable format and providing forty-eight analogue and twelve 10-bit digital input channels. All twelve of the available digital channels and thirty-two of the analogue channels were used for the Durham spectrometer flight. The chosen PROM routes a 32 x 32 ten-bit word matrix cyclicly to the ground station at a rate of 40.96 k. bits s⁻¹. Figure 3.19 shows the arrangement of the Durham experiment's data within the matrix. As can be seen the two pulse heights from the spectrometer's 14-bit ADC are sampled four times in each telemetry frame using words D1, D2 and D3 and the Ge analogue pulse is also sampled four times per frame using analogue channels A2, A3 and A4. Housekeeping data and system orientation data are routed to the S7 and S8 sub-commutated words as shown in figure 3.19.

The telemetred data is received at NSBF, Palestine ground station where it is recorded via a PDP11/20 minicomputer onto industry standard computer tape together with "ground" frame time and position information in the format given in figure 3.20. Latitude and longitude is obtained by desk computer calculation from the Omega navigation system which locates the balloon to within a one mile square box. The Rosemount altimeter incorporates a displacement/frequency transducer of sufficient sensitivity to be capable of an altitude change of less than 0.1% at 120,000 feet.

Facilities are also available for payload command on the PCM system and 16 channels were used to fulfill the steering requirements. The ground station also provides for display of a limited amount of experiment data in real-time during a flight.

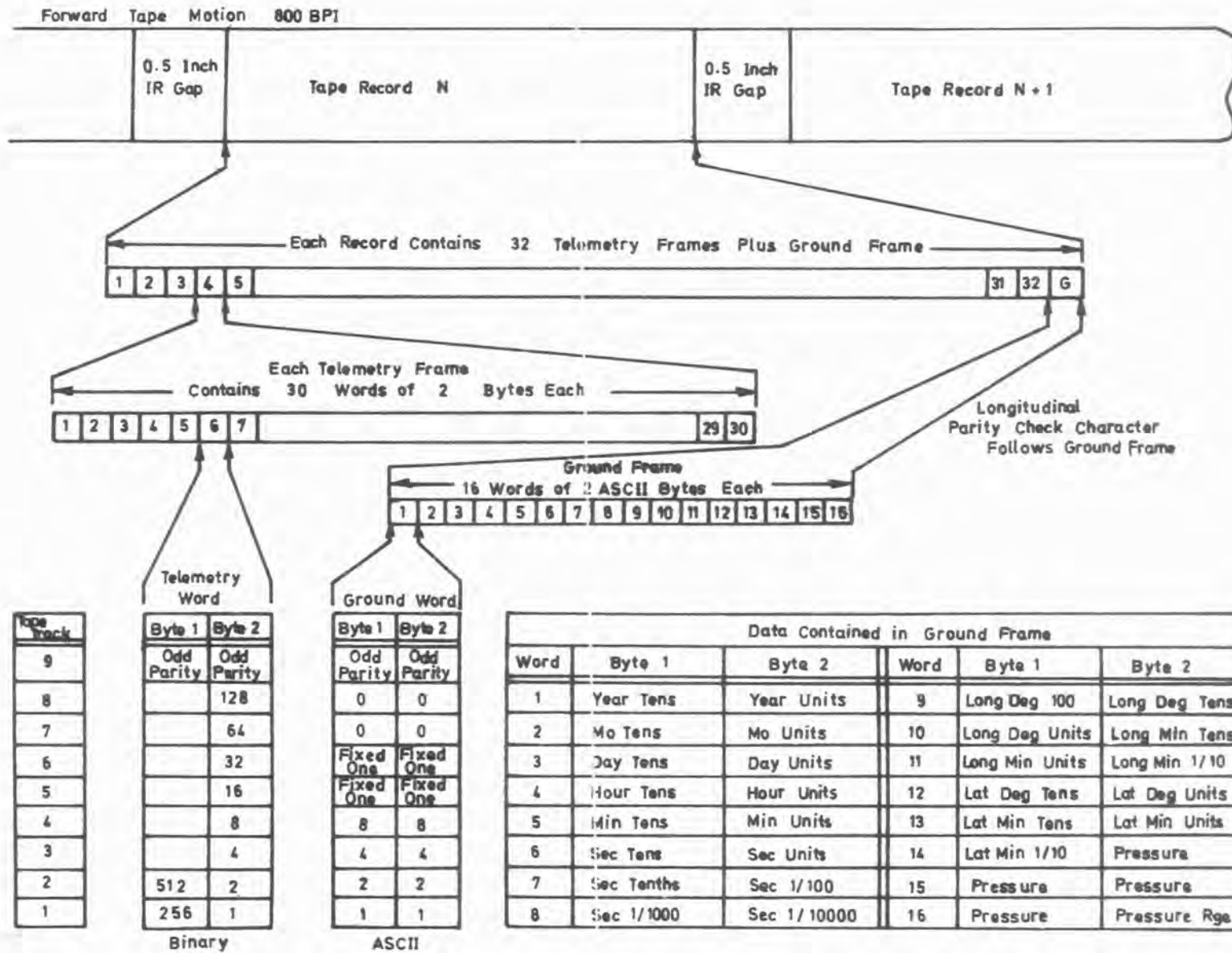


Figure 3-20 The format for each tape record.

CHAPTER FOUR
RESPONSE CHARACTERISTICS OF THE
DURHAM GAMMA-RAY SPECTROMETER

4.1 INTRODUCTION

It is presently standard practice in gamma-ray astronomy to carry out calculations of various detector response characteristics, e.g. detection efficiency. The determination of these characteristics is an endeavour which is ideally suited to the application of the Monte-Carlo technique and use of high speed digital computers owing to the statistical nature of the problem and also because numerical methods for the solution of the coupled transport equations which would otherwise be necessary (if secondary radiation is included) are impractical as they are too time consuming.

A Monte-Carlo computer simulation of some of the Durham gamma-ray spectrometer's detectors, which has been constructed in FORTRAN for use with the Northumbrian Universities Multiple Access (IBM) computer, is described in the current chapter subsequent to a discussion of the types of interaction which gamma radiation experiences during its penetration of detector materials. In addition laboratory measurements of efficiency and energy resolution for the spectrometer detectors are given and the system's response to diffuse and point sources is discussed.

4.2 INTERACTION OF GAMMA-RAYS WITH MATTER

Mono-energetic photons in penetrating matter obey an exponential law of attenuation:

$$I = I_0 e^{-\mu x} \quad (4.1)$$

where I and I_0 are the transmitted and incident intensities respectively, x is the linear thickness and μ is the total linear attenuation coefficient. This latter is a measure of the number of photons in a beam which

undergo interaction in passing through matter. Note that μ is the total of the linear scattering and absorption coefficients from all of the possible interactions; the scattering and absorption coefficients themselves are related to cross section. Table 4.1 shows the various interactions which gamma photons may undergo with matter, however, in the nuclear transition energy region the following three processes dominate: (a) Photoelectric effect, (b) Compton effect with bound electrons and (c) Pair production. These processes are described below.

4.2.1 Photoelectric Absorption

Figure 4.1 shows that the photoelectric effect dominates for medium to high atomic number (Z) materials at energies $\lesssim 0.1$ MeV. The kinematics of the process are illustrated in figure 4.2 which shows it to be one of total photon absorption with the subsequent ejection of an electron. In approximately 80% of cases the photoelectron is produced from the K-shell of the atom provided that the incident photon energy is well in excess of the K-shell binding energy. For a photon of energy $h\nu$ and a binding energy B the kinetic energy of the emergent photo-electron is given by:-

$$E_{K.E.} = h\nu - B \quad (4.2)$$

Note that a free electron cannot become a photoelectron since a third body is required to satisfy the conservation of momentum principle, also the kinetic energy of the recoiling atom is negligible. In addition either a characteristic X-ray of the atom is emitted, or the atom relaxes via emission of an Auger electron owing to the vacancy left by the ejected photo-electron. This latter phenomenon is important in detectors of small physical size since the K X-ray is likely to escape giving rise to a K-electron escape peak in the detector's spectrum.

Concerning the design of detectors it is important to consider:

(a) the Z^5 dependence of the photoelectric cross section (b) the energy

TABLE 4.1 Gamma-ray modes of interaction with matter

<u>PROCESS</u>	<u>TYPE OF INTERACTION</u>	<u>APPROXIMATE ENERGY RANGE OF MAXIMUM IMPORTANCE</u>
1. Photoelectric Effect	(a) With bound atomic electron	Dominates at Low Energy (1KeV to 500KeV)
2. Scattering from Electrons Coherent Incoherent	(a) With bound atomic electrons	< 1MeV and greatest at small scattering angles
	(b) With free electrons	independent of energy
	(c) With bound atomic electrons	< 1MeV; least at small scattering angles
	(d) With free electrons	Dominates in region of 1MeV
3. Photonuclear Absorption Nuclear Photoeffect	With nucleus as a whole	Above threshold has broad maximum in range of 10-30 MeV
4. Nuclear Scattering Coherent Incoherent	(a) With material as a whole, dependent on nuclear energy levels	Important only in very narrow resonance range
	(b) With nucleus as a whole dependent on nuclear energy levels	Narrow resonance maxima at low energies, broad maxima in range 10-30 MeV
	(c) With nucleus as a whole independent of nuclear energy levels	$\lambda >$ Nuclear radius independent of energy
	(d) With individual nucleons	$\lambda <$ Nuclear radius i.e. $>$ 100 MeV
5. Interaction with a Coulomb field	(a) In Coulomb field of nucleus	Threshold about 1 MeV dominates at $E >$ 5 or 10 MeV
Pair Production	(b) In Coulomb field of electron	Threshold at 2 MeV
Delbruck	(c) In Coulomb Field of nucleus	Real part $>$ imaginary below 3 MeV, $<$ imaginary above 15 MeV.

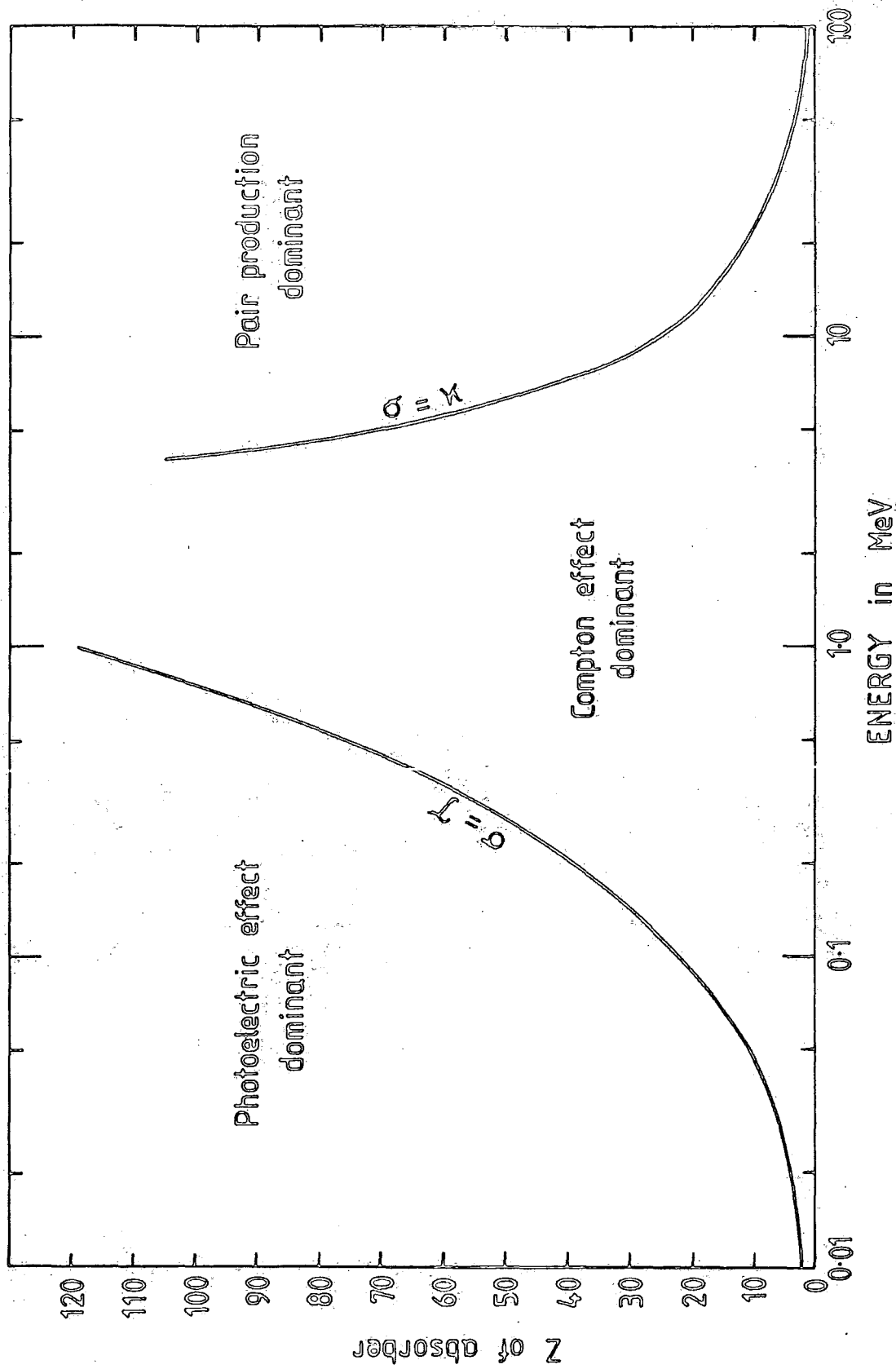


Figure 4.1 The Z-dependent boundaries where the photoelectric and Compton cross sections are equal ($\sigma = \tau$) and where the pair production and Compton cross sections are equal ($\sigma = \kappa$) vs the photon energy. (From R.D. Evans, 'The Atomic Nucleus', McGraw-Hill book company)

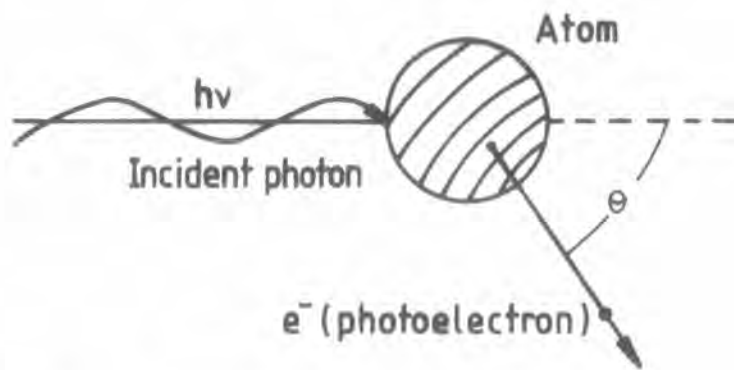


Figure 4.2 The Photoelectric effect.

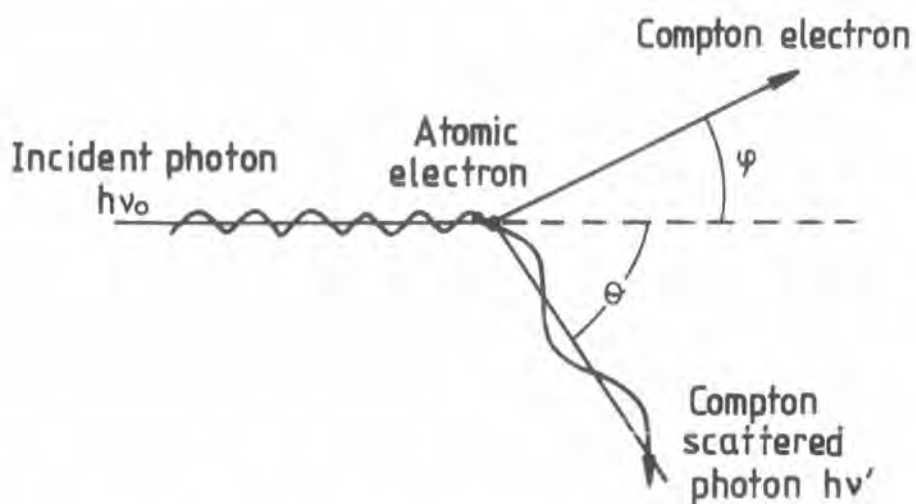


Figure 4.3 The Compton scattering process.

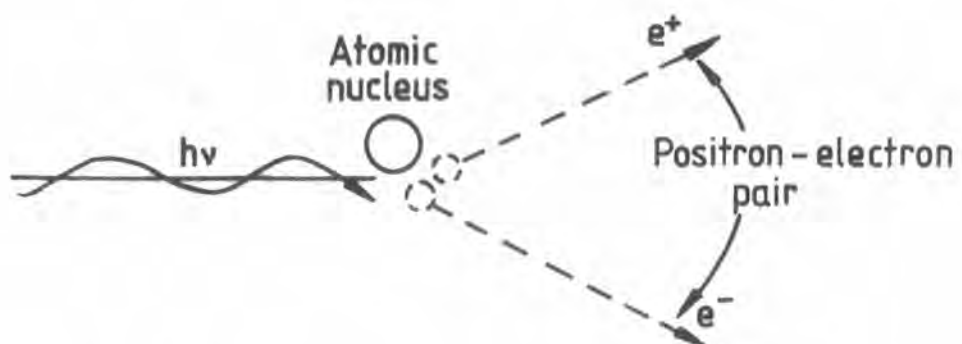


Figure 4.4 The Pair-production process

dependence of the cross-section and (c) the angular distribution of the photoelectrons. For incident photons $h\nu \gg m_0 c^2$, the photoelectric cross-section is:

$$\tau_{\alpha K} = \phi_0 Z^5 \alpha^4 \frac{5}{2} (m_0 c^2 / h\nu)^{7/2} \text{ cm}^2 (\text{atom})^{-1} \quad (4.3)$$

according to Heitler 1954; where:- $\phi_0 = \frac{8}{3} \pi r_0^2$ is the Thomson cross section; $r_0 = e^2 / m_0 c^2$ is the classical electron radius; $\alpha = 2\pi e^2 / hc = (137)^{-1}$ is the fine structure constant.

For incident photons $h\nu \sim m_0 c^2$ the dependence of cross section upon photon energy is $(h\nu)^{-1}$ as given by Davisson (1966).

Figure 4.5 shows that for low energy photons the photoelectrons are ejected at approximately right angles to the photon direction, however the angle of emission tends towards zero for higher energy photons.

4.2.2 Compton Scattering

Figure 4.1 shows that for photons of energy $0.1 \text{ MeV} \lesssim E_\gamma \lesssim 10 \text{ MeV}$ incident upon an absorber of medium to high atomic number the process of Compton scattering is the dominant interaction. The Compton effect is a photon scattering process involving free electrons, or bound electrons having a binding energy which is very much less than the impinging photon energy. A schematic representation of Compton scattering is depicted in Figure 4.3; an incident photon of energy E_{γ_0} causes the electron to recoil at angle ϕ with momentum p and kinetic energy $E_{K.E.}$ and the scattered photon is emitted at angle θ with energy E'_γ . The trajectories of the incident and scattered photons and that of the recoiling electron are coplanar, since the momentum normal to the scattering plane defining the paths of the incident and scattered photons is zero.

For Compton scattering:

$$E_{\gamma_0} = E'_\gamma + E_{K.E.} \quad (4.4)$$

Using these basic conservation equations and certain relativistic

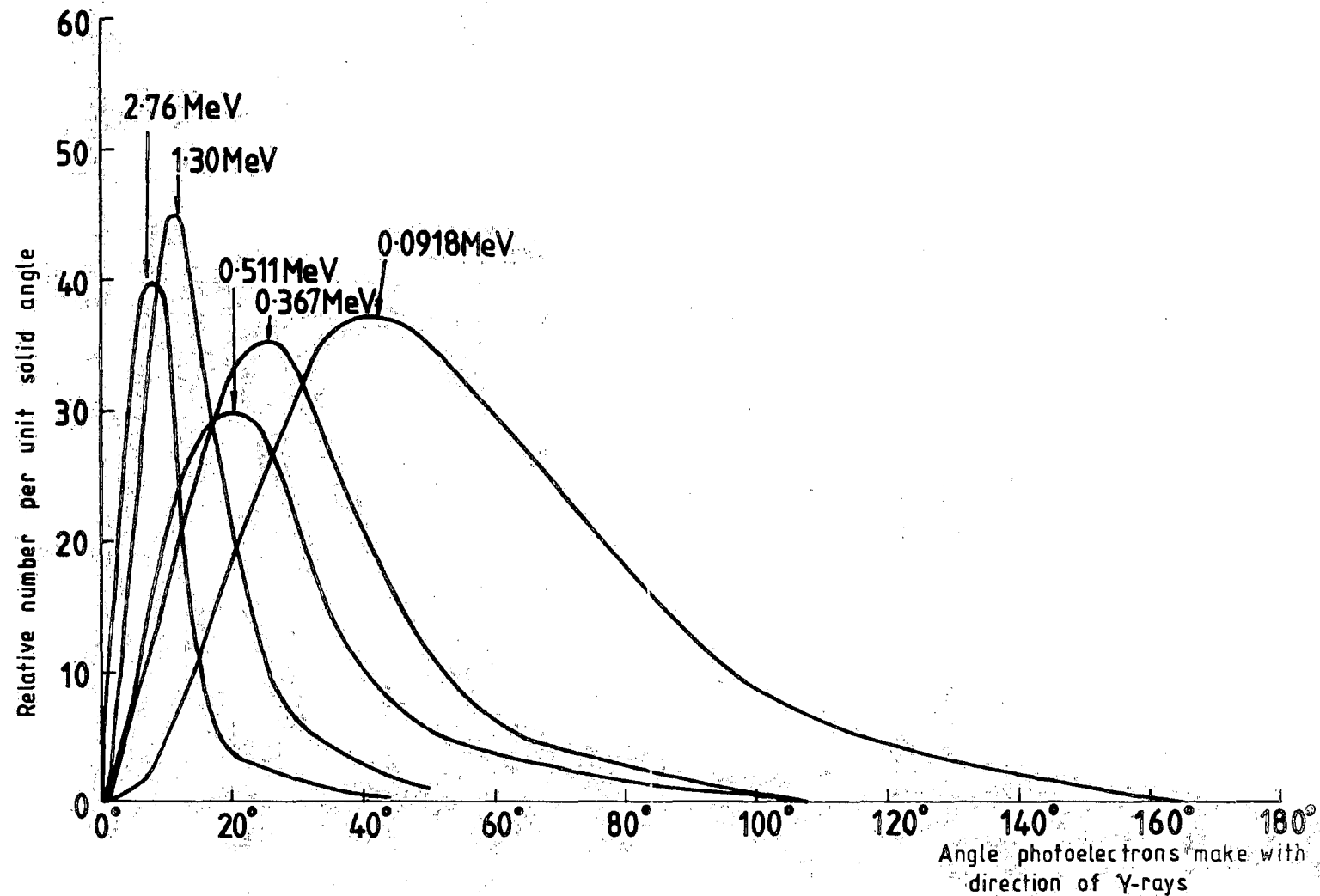


Figure 4.5 The angular distribution of photoelectrons for various incident photon energies. (From R.D. Evans, 'The Atomic Nucleus', McGraw-Hill book company)

equations the expression for the scattered photon energy is:

$$E_{\gamma}' = \frac{m_0 c^2}{1 - \cos\theta + \left(\frac{1}{\alpha}\right)} \quad (4.5)$$

where $\alpha = E_{\gamma_0}/m_0 c^2$; and $m_0 c^2$ is the rest energy of the electron. The struck electron carries away the remaining energy and this produces the result:

$$E_{K.E.} = E_{\gamma_0} \frac{\alpha (1 - \cos\theta)}{1 + \alpha(1 - \cos\theta)} \quad (4.6)$$

This expression yields a maximum kinetic energy for the electron which is, in all practical cases, less than the incident photon energy.

$(E_{K.E.})_{\max}$ is produced for $\theta = 180^\circ$ and is given by:

$$(E_{K.E.})_{\max} = \frac{E_{\gamma_0}}{1 + \left(\frac{1}{2\alpha}\right)} \quad (4.7)$$

whereupon the scattered photon has a minimum energy. However at $\theta = 0^\circ$ the scattered photon carries away the incident photon energy.

The relation between the scattering angles of the secondary photon and the electron is:

$$\cot \phi = (1 + \alpha) \tan \left(\frac{\theta}{2}\right) \quad (4.8)$$

It can be shown that for plane polarised incident radiation the differential collision cross section, (Heitler 1954), is given by:

$$d(\epsilon_\sigma) = \frac{r_0^2}{4} d\Omega \left(\frac{\nu'}{\nu_0}\right)^2 \left(\frac{\nu_0}{\nu'} + \frac{\nu'}{\nu_0} - 2 + 4 \cos^2 \alpha\right) \text{cm}^2 \text{ (electron}^{-1}\text{)} \quad (4.9)$$

where ν_0 and ν' are the frequencies of the incident and scattered radiations, α is the angle between the electric vectors of the incident and scattered radiations ϵ_0 and ϵ' respectively (figure 4.7) and $d\Omega$ is the element of solid angle through which the scattered photon emerges

after the collision. The physical interpretation of $d(\sigma_e)$ is: the absolute value of probability that, while passing through an absorber which contains one electron cm^{-2} , a photon of energy E_{γ_0} will undergo a collision from which the scattered photon emerges, with energy $E_{\gamma'}$, within solid angle $d\Omega$ and is so polarised that its electric vector is orientated at angle α to the direction of the incident electric vector.

Since the polarisation of the scattered photon is unimportant in practical cases equation (4.9) can be summed over all possible scattered photon polarisation directions and this yields, for a Compton scattering of angle θ :

$$d(\sigma_e) = \frac{r_0^2}{2} d\Omega \left(\frac{\nu'}{\nu_0}\right) \left(\frac{\nu_0}{\nu'} + \frac{\nu'}{\nu_0} - 2 \sin^2 \theta \cos^2 \eta\right) \text{cm}^2 (\text{electron})^{-1} \quad (4.10)$$

where η is the projection of ξ (figure 4.6) onto the plane normal to the incident photon direction. This expression yields a maximum value at $\eta = 90^\circ$, therefore the scattered photon and electron tend to be ejected at right angles to the electric vector of the incident radiation. This fact, emerging from equation (4.10), forms the operational basis for practical γ -ray polarimeters.

For the more common case of unpolarised radiation it is convenient to resolve the incident radiation into two orthogonally polarised components, each possessing half of the incident intensity, such that one component lies at angle $\eta = 90^\circ$ and the other at $\eta = 0^\circ$, the unpolarised differential cross section is then the sum of two components from equation 4.10:

$$d(\sigma_e) = \frac{r_0^2}{2} d\Omega \left(\frac{\nu'}{\nu_0}\right)^2 \left(\frac{\nu_0}{\nu'} + \frac{\nu'}{\nu_0} - \sin^2 \theta\right) \text{cm}^2 \text{electron}^{-1} \quad (4.11)$$

where the scattered photon enters solid angle $d\Omega = 2\pi \sin\theta d\theta$. Figure 4.8 is a polar plot of equation 4.11 and indicates a strong increase in the fraction of forward scattered photons with increasing α . Integrating

equation 4.11 over all possible values of θ yields the total collision cross-section (σ_e) which represents the probability of removal of the photon from a collimated beam while passing through an absorber containing one electron cm^{-2} :

$$\sigma_e = 2\pi r_0^2 \left\{ \frac{1+\alpha}{\alpha^2} \left[\frac{2(1+\alpha)}{1+2\alpha} - \frac{1}{\alpha} \ln(1+2\alpha) \right] + \frac{1}{2\alpha} \ln(1+2\alpha) \frac{1+3\alpha}{(1+2\alpha)^2} \right\} \text{cm}^2 \text{electron}^{-1} \quad (4.12)$$

This expression is of course the same for both polarised and unpolarised incident radiation.

The photon scattering per unit scattering angle θ is markedly different from that per unit solid angle, the former being given by:

$$\frac{d(\sigma_e)}{d\theta} = \frac{d(\sigma_e)}{d\Omega} 2\pi \sin\theta \text{cm}^2 \text{electron}^{-1} \quad (4.13)$$

A polar plot of the number versus angle distribution of scattered photons represented by equation 4.13 is shown in figure 4.9.

The directional distribution of Compton electrons is derived as follows. Each photon scattered into the solid angle between θ and $(\theta + d\theta)$ has a corresponding electron projected at an angle between ϕ and $(\phi + d\phi)$ i.e. into a solid angle $d\Omega' = 2\pi \sin\phi d\phi$. Therefore there exists the equality:

$$\frac{d(\sigma_e)}{d\Omega} 2\pi \sin\theta d\theta = \frac{d(\sigma_e)}{d\Omega'} 2\pi \sin\phi d\phi \quad (4.14)$$

Hence:
$$\frac{d(\sigma_e)}{d\Omega'} = \frac{d(\sigma_e)}{d\Omega} \frac{\sin\theta}{\sin\phi} \frac{d\theta}{d\phi} \quad (4.15)$$

and from equation (4.10) this gives:

$$\frac{d\Omega'}{d\Omega} = - \frac{1}{(1+\alpha)} \frac{(1+\cos\theta)\sin\theta}{\sin^3\phi} \quad (4.16)$$

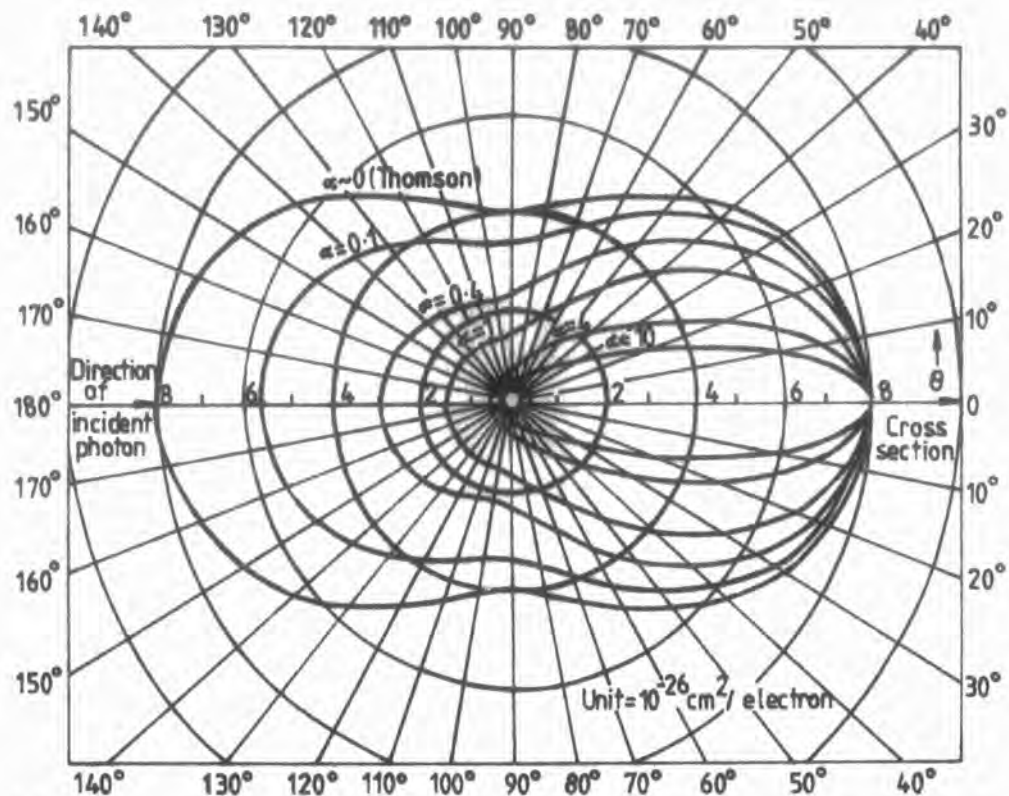


Figure 4.8 The number of photons scattered into unit solid angle $d(e\sigma)/d\Omega$, at a mean scattering angle θ . (From R.D. Evans, 'The Atomic Nucleus,' McGraw-Hill book company)

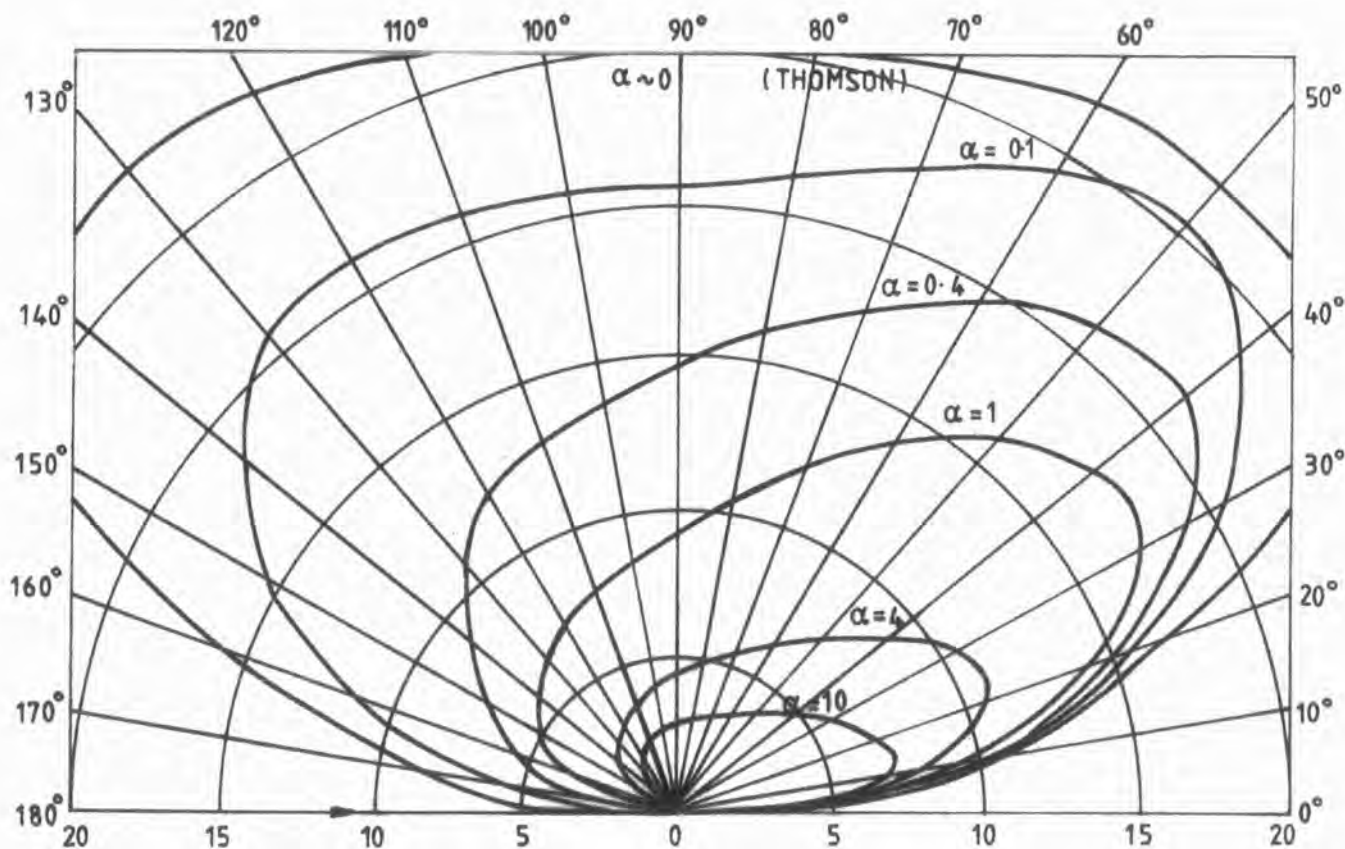


Figure 4.9 Number vs angle distribution of Compton scattered photons, $d(e\sigma)/d\theta$. (From R.D. Evans, 'The Atomic Nucleus,' McGraw-Hill book company.)

Thus in terms of equations 4.15 and 4.16 the number versus angle Compton electron distribution is:

$$\frac{d(\sigma_e)}{d\phi} = \frac{d(\sigma_e)}{d\Omega'} 2\pi \sin\phi \quad (4.17)$$

This distribution is shown in figure 4.11.

The Compton electron energy spectrum or number-energy distribution is shown in figure 4.10 and this is represented by:

$$\frac{d(\sigma_e)}{dT} = \frac{d(\sigma_e)}{d\phi} \frac{d\phi}{dT} \quad (4.18)$$

and this yields:

$$\frac{d(\sigma_e)}{dT} = \frac{d(\sigma_e)}{d\Omega} \frac{2\pi}{\alpha^2 m_o c^2} \left\{ \frac{(1+\alpha)^2 - \alpha^2 \cos^2\phi}{(1+\alpha)^2 - \alpha(2+\alpha) \cos^2\phi} \right\}^2 \quad (4.19)$$

4.2.3 Pair Production

In the coulomb field of a particle, usually a nucleus, a photon of energy, E_γ , greater than twice the electron rest energy, (i.e. $> 2 m_o c^2$), may be converted into an electron and a positron of respective kinetic energy E_- and E_+ such that :

$$E_\gamma = (E_- + m_o c^2) + (E_+ + m_o c^2) \quad (4.20)$$

This is shown schematically in figure 4.4. In general the threshold energy for the process is given by:

$$E_{th} = 2m_o c^2 \left(1 + \frac{m_o}{M} \right) \quad (4.21)$$

where M is the mass of the particle necessary to absorb the excess momentum.

For the case of no screening when $1 \ll E_\gamma \ll 1/\alpha Z^{\frac{1}{3}}$ the total cross section may be expressed as:

$$a_{p\sigma} = \alpha r_o^2 Z^2 \left(\frac{28}{9} \log \frac{2E_\gamma}{m_o c^2} - \frac{218}{27} \right) \text{cm}^2 (\text{atom})^{-1} \quad (4.22)$$

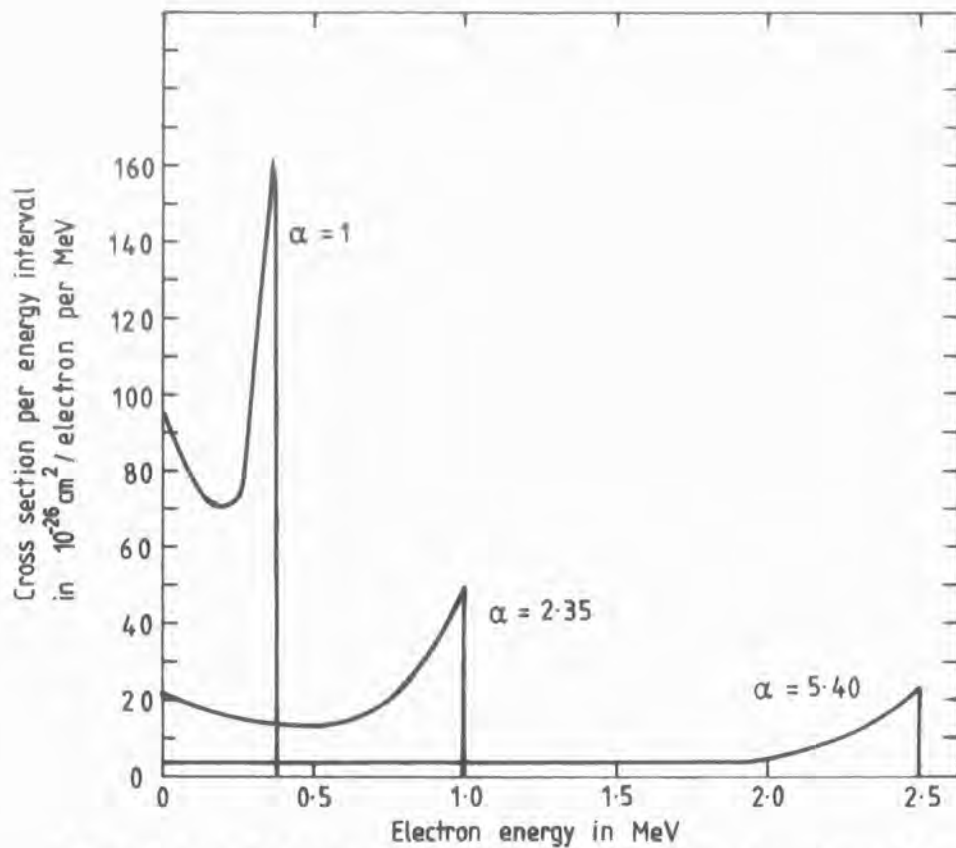


Figure 4.10 Compton electron energy distribution. (From R.D.Evans, 'The Atomic Nucleus,' McGraw-Hill book company.)

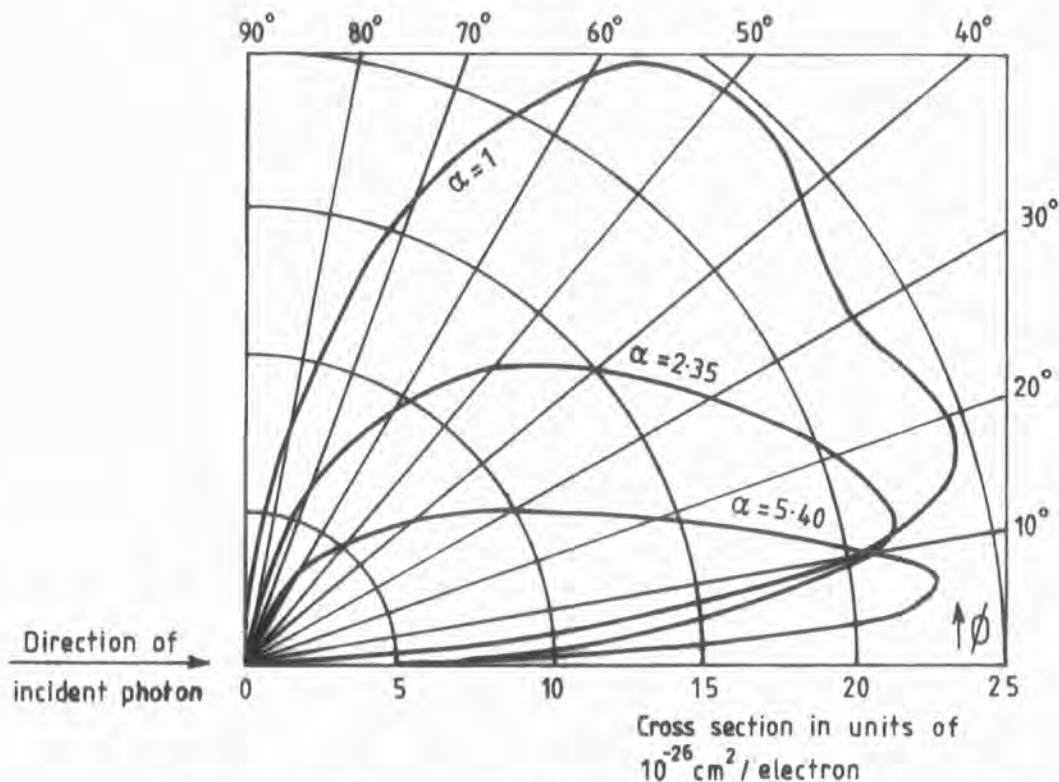


Figure 4.11 The number vs angle distribution of Compton electrons, $d(e^-)d\phi$. (From R.D.Evans, 'The Atomic Nucleus,' McGraw Hill book company.)

and for complete screening when $E_{\gamma}/m_0c^2 \gg 1/\alpha Z^{1/3}$ the cross section is:

$$a_{\sigma p}^{\sigma} = \alpha r_0^2 Z^2 \left(\frac{28}{9} \log \frac{183}{Z^{1/3}} - \frac{2}{27} \right) \text{cm}^2 (\text{atom})^{-1} \quad (4.23)$$

and in intermediate energy regions an approximate form is:

$$a_{\sigma p}^{\sigma} = \alpha r_0^2 Z^2 \left(\frac{28}{9} \log \frac{2E_{\gamma}}{m_0c^2} - \frac{218}{27} - 1.027 \right) \text{cm}^2 (\text{atom})^{-1} \quad (4.24)$$

4.3 MONTE-CARLO SIMULATION AND DETECTOR CHARACTERISTICS

When a gamma photon enters a detector it can either escape from it or undergo interaction thereby depositing a fraction or the whole of its energy in the detector material. As has been discussed in Section 4.2 there are principally three processes by which interaction and subsequent energy deposition may occur, i.e. Photoelectric absorption, Compton scattering and Pair production. Each process leads to secondary photon and/or electron creation which may generate further radiation, e.g. Bremsstrahlung or annihilation radiation and this can in turn undergo further interaction (and therefore energy deposition) in the detector. The Monte-Carlo procedure provides a method of simulating the history of primary source photons through a detector, taking into account all secondary radiations and particles.

For simulation of statistical processes a sampling technique is used based on the generation of uniformly distributed pseudo-random numbers η in the range $0 \leq \eta \leq 1$. In the current simulation, the multiplicative congruential method of generation is used:

$$\eta_{K+1} = \eta_K \lambda \text{ mod } m \quad (4.25)$$

where $m = 2^{59}$, $\lambda = 13^{13}$ and $\eta_0 = 123456789 (2^{32} + 1)$. The pseudo-random numbers are used to obtain a random variable \bar{x} from a probability distribution $f(x)$ according to equation 4.26:

$$\eta = \frac{\int_{-\infty}^{\bar{x}} f(x) dx}{\int_{-\infty}^{\infty} f(x) dx} \quad (4.26)$$

A flow chart of the Monte-Carlo simulation created for calculation of the response characteristics up to ~ 1 MeV of the detectors used in the Durham gamma-ray spectrometer is shown in figure 4.12. Since the pair production process has a threshold energy of 1.02 MeV it is not included in the simulation. The programme is designed for simulation of monoenergetic, isotropic point sources on the central axis of a circular, cylindrical detector and a rectangular Cartesian coordinate system is employed, where the z-axis is aligned with the detector's central axis and the origin lies on the detector end-face which is closest to the source.

A primary source photon is chosen for direction in terms of polar and azimuthal angles θ and ψ respectively as follows. From equation 4.13:

$$\eta = \frac{\int_0^{\theta} \sin\theta \, d\theta}{\int_0^{\theta_{\max}} \sin\theta \, d\theta} \quad (4.27)$$

which yields for the polar angle:

$$\theta = \arccos \{1 + \eta(\cos \theta_{\max} - 1)\} \quad (4.28)$$

where $\theta_{\max} = \arctan (R/d)$ for a detector of radius R and source distance d. The azimuthal angle is uniformly distributed between 0 and 2π and hence may be derived from:

$$\psi = 2\pi\eta \quad (4.29)$$

Direction cosines α, β, γ , (with respect to the x,y,z axes respectively) are calculated for the photon from θ and ψ and trajectories of all

subsequent particles and secondary radiations are described by this method.

The coordinates of the source photon's point of entry into the detector (x_0, y_0, z_0) are calculated and the distance L to the first interaction point is determined, using equation 4.26, from the intensity distribution of a gamma photon in the depth r of the detector material:

$$\eta = \frac{\int_0^L I_0 \exp [-(\mu/\rho)_{\text{tot}} \rho r] dr}{\int_0^{\infty} I_0 \exp [-(\mu/\rho)_{\text{tot}} \rho r] dr} \quad (4.30)$$

where $(\mu/\rho)_{\text{tot}}$ is the total mass attenuation coefficient for the detector material at the photon energy. Thus the average distance L a photon travels without interaction is:

$$L = - (1/\mu_{\text{tot}}) \ln (1 - \eta) \quad (4.31)$$

where μ_{tot} is the total linear attenuation coefficient. Hence the coordinates (x_1, y_1, z_1) of the point of primary interaction are calculated and a test is made for the containment of this point within the defined boundaries of the detector. If the interaction is deemed to have occurred outside of the detector the photon is judged to have survived, a new photon is selected from the source and the above procedure repeated until a primary interaction is found within the detector. The type of interaction is sampled according to the condition:

$$\eta \leq \frac{(\mu/\rho)_{\text{photo}}}{(\mu/\rho)_{\text{tot}}} \quad (4.32)$$

whereby the interaction is a photo electric event, otherwise a Compton event is chosen.

In the case of a photoelectric event the photoelectron energy is approximated as being equal to that of the originating photon. The

polar and azimuthal angles θ and ψ of photo-electron emission with respect to the photon trajectory are calculated from a table of θ as a function of pseudo-random number, by linear interpolation and from a uniform distribution between 0 and 2π respectively. For a Compton scatter the parameters are obtained as follows. Applying equations 4.4 and 4.6 to equation 4.12 gives:

$$\frac{d(\frac{\sigma}{e})}{d\theta} = \pi r_0^2 \sin\theta \left\{ \frac{1}{1+\alpha(1-\cos\theta)} \right\}^2 \left\{ [1+\alpha(1-\cos\theta)] + \left[\frac{1}{1+\alpha(1-\cos\theta)} \right] - \sin^2\theta \right\} \quad (4.33)$$

At selected energies over the required range the maximum values of $\frac{d(\frac{\sigma}{e})}{d\theta}$ had been obtained in advance and a polynomial least-squares fit made to these points. This fit is incorporated into the computer programme so that the maximum value for $\frac{d(\frac{\sigma}{e})}{d\theta}$ may be easily calculated for the current photon energy. Consequently a pseudo-random number η can be generated in the range $0 \leq \eta \leq \left[\frac{d(\frac{\sigma}{e})}{d\theta} \right]_{\max}$ for comparison with a value X of $\frac{d(\frac{\sigma}{e})}{d\theta}$ obtained by substitution of a randomly selected polar angle θ into equation 4.33. Then if $X \leq \eta$ the polar angle θ is accepted for the scattering interaction otherwise the random selection of θ and calculation of the corresponding X is repeated until an acceptable value for θ is encountered. The above sampling procedure produces a good fit to the Compton electron energy distribution and was used in preference to an expression for E'_γ , given by Carlson (1953), as reported by De Castro Faria and Levesque (1967) which was found only to reproduce the required distribution at source energies greater than ~ 1.5 MeV. Energies for the scattered photon and recoil electron are subsequently obtained from equations 4.5 and 4.6 respectively, using the accepted polar angle θ . Equation 4.8 gives the recoil electron polar angle ϕ . The azimuthal angle for the scattered photon is sampled according to

equation 4.29 and that for the recoil electron according to momentum considerations varies from ψ by π .

After interaction the trajectories of the secondary radiation and particles are found in terms of the rectangular Cartesian coordinate system by performing a rotation of coordinates. Assuming that the cosine of the polar angle of scattering is λ then for azimuthal angle ϕ and initial direction cosines, α, β, γ the direction cosines for the scattered photon and/or electron are α', β', γ' and are given in figure 4.13.

The computational procedure is organised so as to evaluate the energy loss of the electron to the detector by ionisation and bremsstrahlung, based on calculation of the electron path length R , along its trajectory, from the empirical energy-range relation:

$$R = \left\{ \frac{412 E^n}{(\rho \times 10^3)} \right\} \text{ cm} \quad (4.34)$$

where $n = (1.265 - 0.0954 \ln E)$. From Heitler (1954) the electron energy losses due to collision and bremsstrahlung are:

Collision:

$$-\left(\frac{dE}{ds}\right)_{\text{coll}} = NZ\phi_0 m_0 c^2 \frac{e^2}{\beta^2} (B + B'_{el}) \quad (4.35)$$

where N is the number of atoms cm^{-3} for the detector material; $\phi_0 = (8\pi/3)\rho^2$. B is defined by:

$$B = \left\{ \ln \left[\frac{m_0 c^2 \beta^2 (E - m_0 c^2)}{I^2 Z^2 (1 - \beta^2)} \right] - 2\beta^2 \right\} \quad (4.36)$$

where I is some average ionisation energy and E is the total electron energy. Bethe's correction term for electrons is:

$$B'_{el} = -[\beta^2 + 2\sqrt{(1 - \beta^2)}] \ln 2 + 1 + \beta^2 \quad (4.37)$$

Bremsstrahlung:

$$-\left(\frac{dE}{ds}\right)_{\text{Brem}} = \frac{16N}{3} E \left(\frac{\rho Z^2}{137}\right)^2 \quad (4.38)$$

where N is as defined above.

Up to a photon energy of ~ 1 MeV bremsstrahlung loss is small compared to that due to inelastic collision and therefore a simplified treatment of bremsstrahlung is used here; the energy is treated as a single photon emitted from the point of electron scattering in the forward direction. In calculation of the energy losses, account is taken of a diminished path length should the distance R, obtained from equation 4.34, taken along the prescribed trajectory for the electron, result in the electron leaving the detector.

All Compton secondary and bremsstrahlung photons are treated in the same manner as primary source photons unless their energy is below a threshold of 0.01 MeV in which case they are assumed to be absorbed directly. In the case of a bremsstrahlung photon and a Compton secondary both requiring treatment, the latter is stored in terms of energy, point of production and direction and analysed subsequent to the completion of bremsstrahlung handling and prior to the commencement of a new source photon history.

During the simulation, explicit records are kept of the following quantities:

- (a) Source photon history number.
- (b) Number of source photons which undergo:
 - (i) Either of the possible types of interaction.
 - (ii) Photo electric absorption.
 - (iii) Compton scattering.
 - (iv) Initial Compton scattering followed by photo-electric absorption (i.e. Indirect Photo-electric effect).

- (c) Number of source photons which deposit their full energy within the detector.

Upon completion of a pre-specified number of photon histories these records facilitate the calculation of the following detector parameters:

- (i) Total intrinsic efficiency (F); the probability of detection of a source gamma-ray which is incident upon the crystal.
- (ii) Intrinsic full-energy-peak efficiency (ϵ_p); the probability that any source gamma-ray which is incident on the crystal will deposit its full energy therein. (Also known as the Total Absorption probability).
- (iii) Peak to total ratio (γ); the probability that a detected source gamma-ray will deposit its full energy within the crystal.

The above parameters are related according to the simple expression:

$$\epsilon_p = F\gamma \quad (4.39)$$

Intrinsic full-energy peak efficiency is of great importance since it determines the minimum source strength required to give sufficient statistical result in a reasonable time. The relevance of the peak to total ratio is manifest from an appreciation that in general the error in the process of unfolding complex response spectra, to obtain the incident gamma-ray spectra, decreases as the ratio of the area under the full-energy-peak to the total area of the spectrum increases. It should be noted that specification of these parameters is useless unless the source-detector geometry and the gamma-ray energy used are stated in every case.

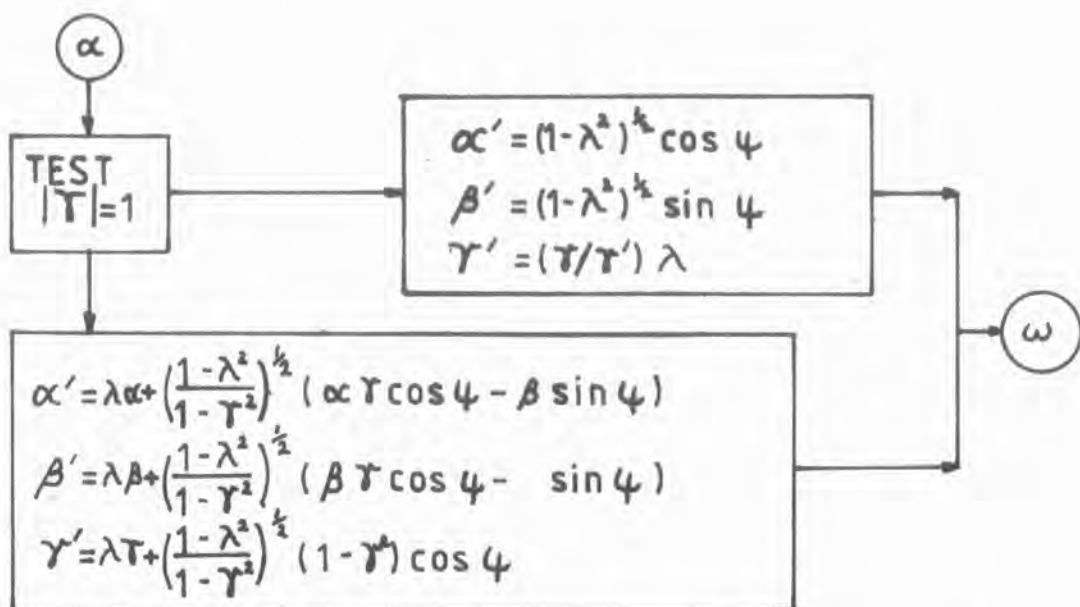


Figure 4.13 Rotation of coordinates to obtain the direction cosines of the secondary radiation and/or particle.

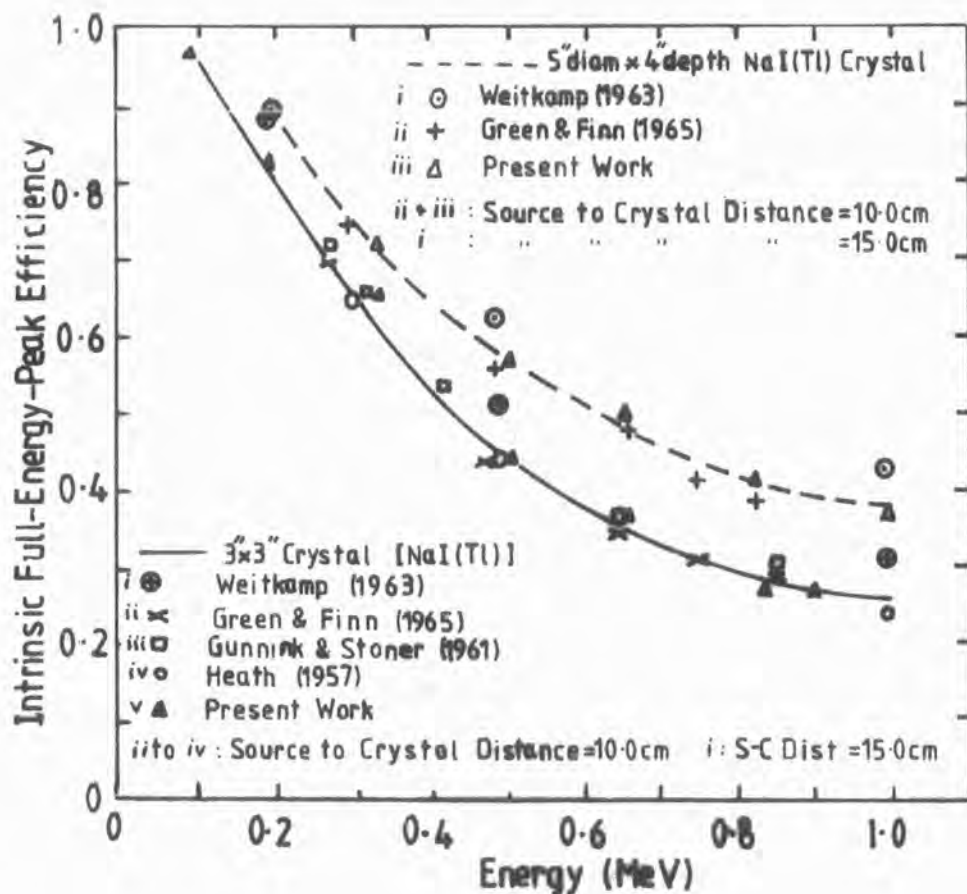


Figure 4.14 Full energy peak efficiency vs energy for two NaI(Tl) crystals.

The computer programme is constructed in a modular form and therefore, the detector type and size may be easily changed. Thus the simulation was initially applied to detectors which have been studied previously, either experimentally or using Monte-Carlo techniques, by other workers. All results quoted are in reference to monoenergetic, isotropic, point sources, placed on the central axis of the particular detector. In the current Monte-Carlo calculations 50,000 source photon histories have been simulated in each case.

Figures 4.14 and 4.15 compare the Intrinsic full-energy-peak efficiency and total intrinsic efficiency respectively (also peak to total ratio in figure 4.16), versus source energy for a 3 inch (diameter) by 3 inch (depth) NaI(Tl) crystal, derived from the current calculation, with those obtained, (a) experimentally by Gunnink and Stoner (1961) and Green and Finn (1965) and (b) from Monte-Carlo simulations of Heath (1957), Weitkamp (1963) and Zerby and Moran (1961). Also shown in figure 4.14 are the results from the same workers for the full-energy-peak efficiency of a 5 inch (diameter) x 4 inch (depth) NaI(Tl) crystal. Results from the present study agree reasonably well in all cases except for that of Weitkamp though here a source distance of 15 cm has been used as opposed to the 10 cm of the others.

Two germanium crystals were also simulated for comparison with the results of Wainio and Knoll (1966). The same three characteristics as previously are given in figures 4.16, 4.17 and 4.18 and again the agreement is favourable over the energy range considered.

The simulation has been applied to the A2 and A3 NaI(Tl) shield crystals and to the central Ge crystal of the Durham gamma-ray spectrometer. Figures 4.19 and 4.20 are plots of the usual three parameters as a function of source energy for the two shield crystals and Ge respectively. For a broad beam which is vertically incident

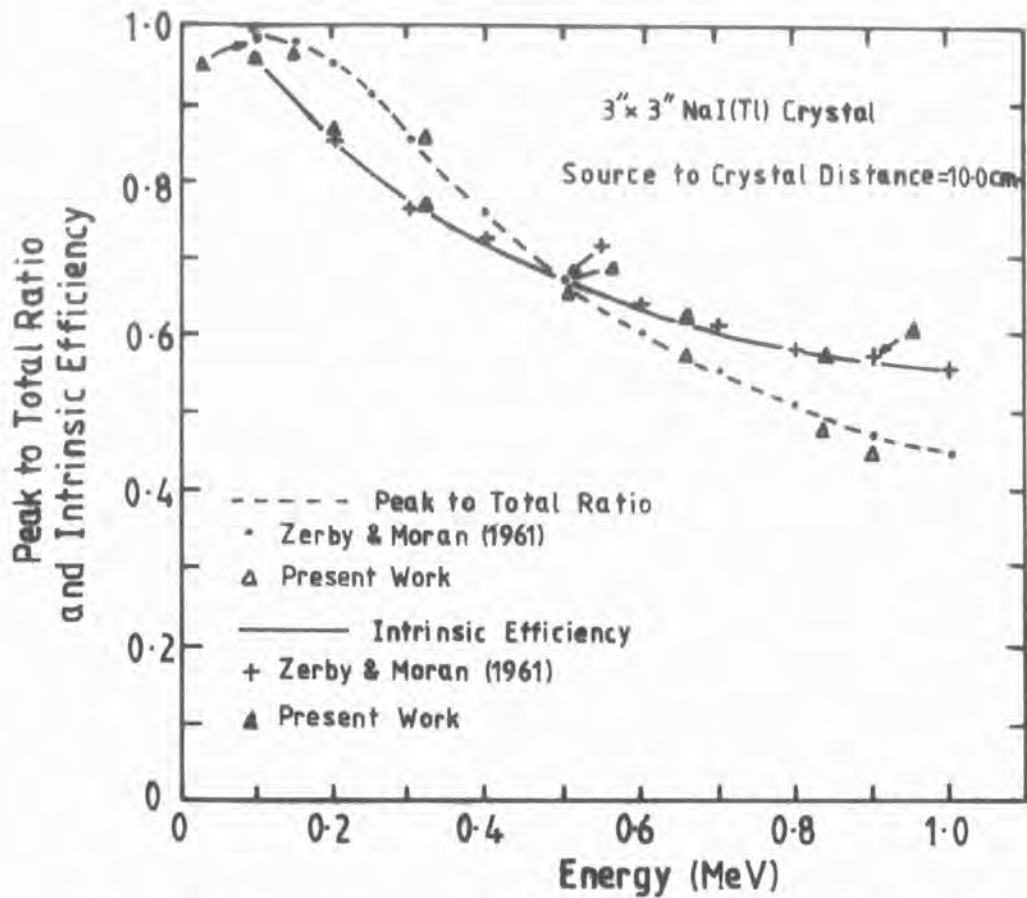


Figure 4.15 Intrinsic efficiency and peak to total ratio vs energy for a 3" x 3" NaI (Tl) crystal.

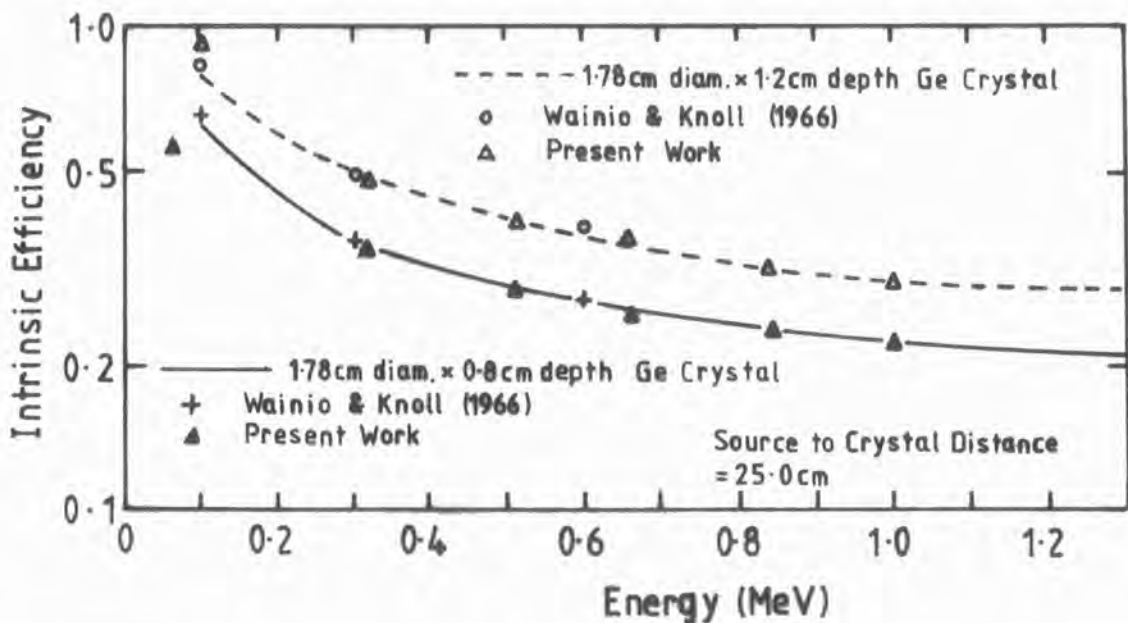


Figure 4.16 Intrinsic efficiency vs energy for two Germanium crystals.

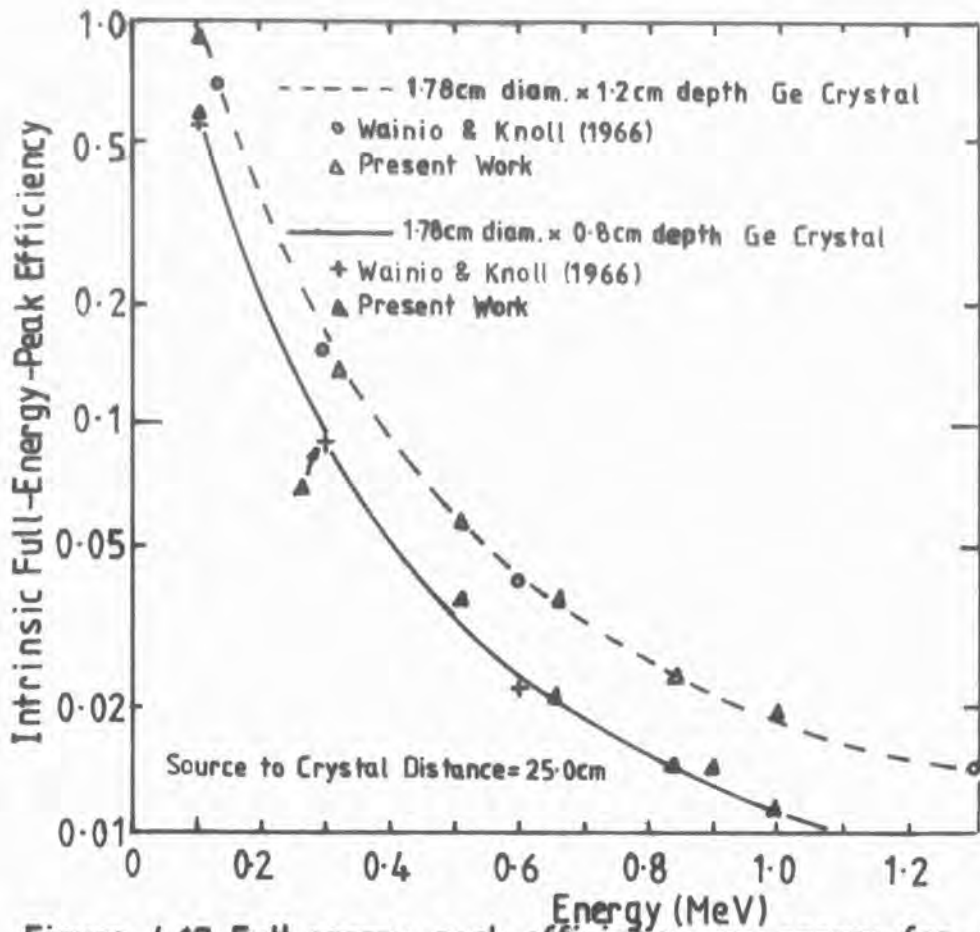


Figure 4.17 Full energy peak efficiency vs energy for two Germanium crystals.

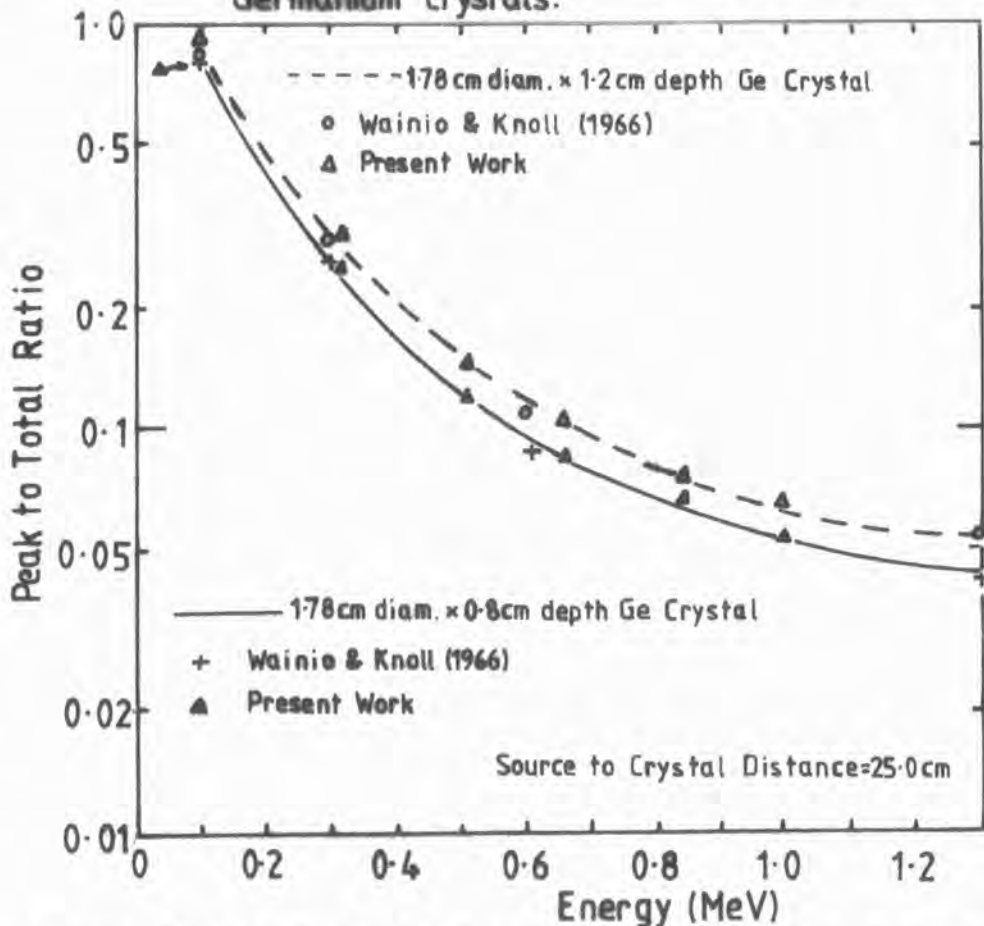


Figure 4.18 Peak to total ratio vs energy for two Germanium crystals.

on A2 and A3 the corresponding intrinsic efficiency figures at 1 MeV are ~ 1 and ~ 0.9 , however the values in response to irradiation by an isotropic point source may be seen from figure 4.19 to be much lower. This arises since the mean path length through each crystal is appreciably reduced from the case of normal incidence as the majority of the photons are produced along trajectories which pass through the curved face of the crystal and are therefore much shorter than the crystal depth. The magnitude of the overall effect is less pronounced for A2 than A3 owing to its factor 2.5 greater depth, however A2 contains a central hole of diameter 5 cm which has been taken into account in the calculations and this obviously contributes to the reduced efficiency of A2. At progressively lower energies the point source efficiency values approach those for normal incidence since the mean photon interaction distance reduces according to the attenuation equation 4.1.

Practical measurements of the same parameters for A2, A3 and Ge have been obtained from the study of energy loss spectra collected via a Canberra pulse-height analyser from standard laboratory radioactive sources which were placed in turn on the central axis of each crystal. The intrinsic efficiency, intrinsic full-energy-peak efficiency and peak to total ratio are given by:-

$$F = \frac{\Sigma S - \Sigma B_s}{NGft} \quad (4.40)$$

$$\epsilon_p = \frac{\Sigma P - \Sigma B_p}{NGft} \quad (4.41)$$

$$\gamma = \frac{\Sigma P - \Sigma B}{\Sigma S - \Sigma B} \quad (4.42)$$

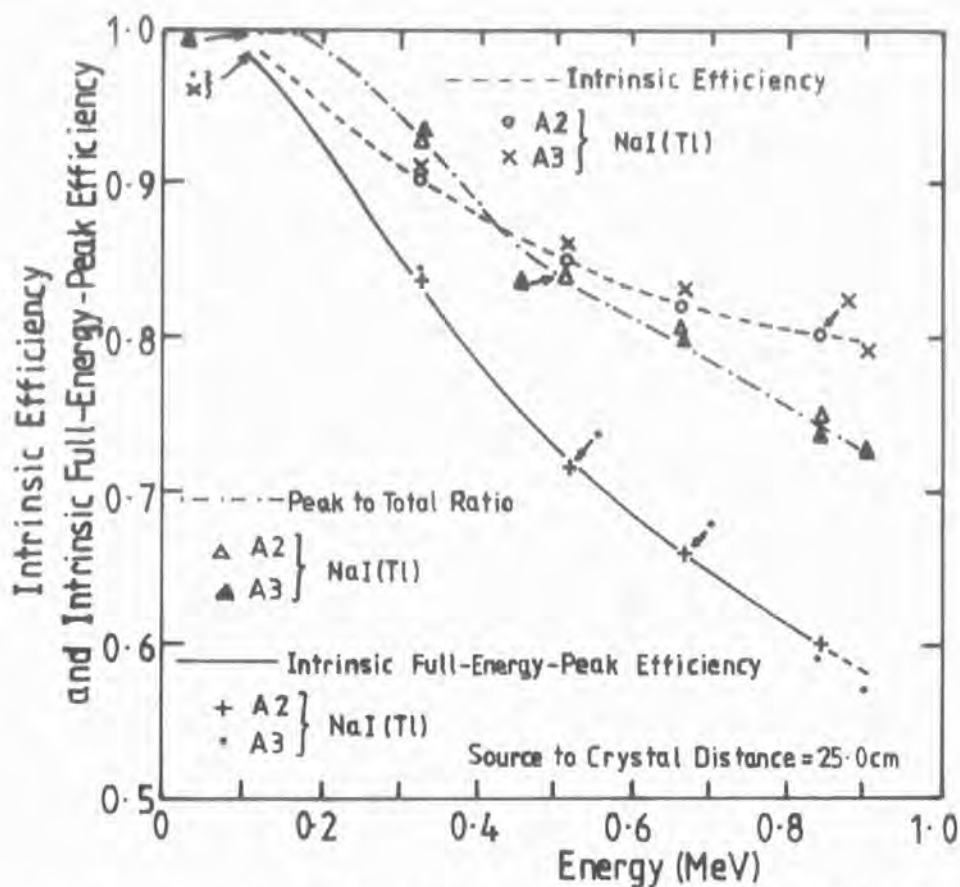


Figure 4.19 Intrinsic efficiency and intrinsic full-energy-peak efficiency vs energy for the A2 and A3 NaI(Tl) shield crystals of the Durham gamma-ray spectrometer.

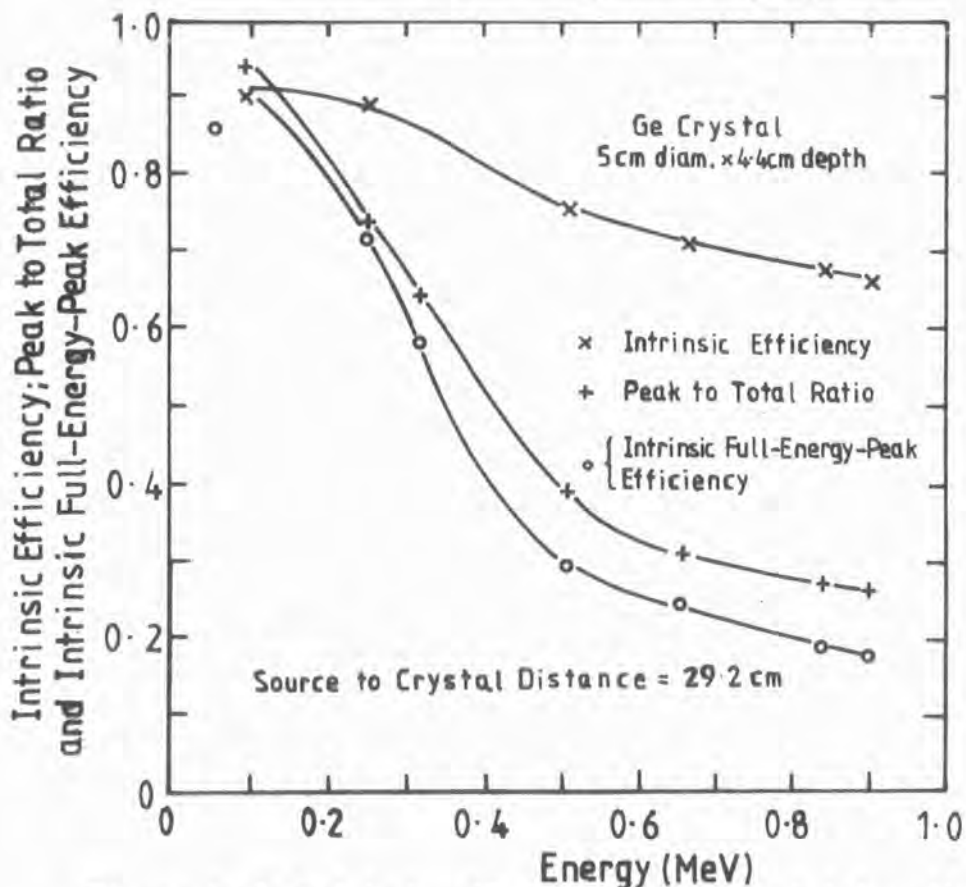


Figure 4.20 Intrinsic efficiency, peak to total ratio, and full-energy-peak efficiency vs energy for the central Ge crystal of the Durham gamma-ray spectrometer.

where: ΣP is the counts under the peak summed over the peak channels.

ΣS is the counts in the spectrum summed over the spectrum channels.

ΣB_p and ΣB_s are the background counts summed over the peak and spectrum channels respectively.

t is the exposure time.

G is the Geometric factor given by $\pi r^2 / 4\pi s^2$ where r is the radius of the crystal and s is the source distance from the crystal face.

f is the fractional yield of gamma-rays of given energy.

N is the source activity (disintegrations s^{-1}) at the time of the measurement $N = N_0 \exp \{-t/0.693 T_{\frac{1}{2}}\}$: t is the age of the source in seconds; $T_{\frac{1}{2}}$ is the source half life in seconds.

Note, however, that before a legitimate comparison of the practical data can be made with the predicted values an adjustment of the latter is required to take account of the casing which surrounds a crystal since the Monte-Carlo values plotted in figures 4.19 and 4.20 represent properties of the crystals themselves whereas the measurements are characteristic of the whole crystal assembly. A source photon which interacts in the casing layer between the source and crystal cannot subsequently contribute to the peak of the energy loss spectrum hence the full-energy-peak efficiency of a crystal assembly $\epsilon_p(As)$ is simply given by:

$$\epsilon_p(As) = \epsilon_p(c) e^{-\mu x} \quad (4.43)$$

where $\epsilon_p(c)$ represents the intrinsic full-energy-peak efficiency of the crystal itself and $e^{-\mu x}$ is the probability that a source photon survives traversal through the intervening casing layer of linear

thickness x . The precise values of x for the A2, A3 and Ge assemblies are not known since (a) each assembly is a commercial, sealed unit, and (b) the manufacturers' diagrams (upon which figures 3.5, 3.7 and 3.8 are based) do not explicitly specify the values. Figures 4.21, 4.22 and 4.25 show the predicted values of $\epsilon_p(As)$, obtained via equation 4.43 having substituted the Monte-Carlo figures for $\epsilon_p(c)$ and having applied Aluminium casing thicknesses of 0.5 cm, 1.0 cm, and 0.15 cm to the A3, A2 and Ge assemblies respectively. The different thickness values for A2 and A3 arise since the practical measurements were performed by irradiating A2 from the face supporting the photomultiplier tubes and A3 from the opposite face. In the case of Ge the apparent discrepancy between the predicted and measured values must be due to a further intervening layer of Delrin (see figure 3.5) which could be up to 3 mm thick.

Also plotted in figures 4.21 and 4.22 are the predicted and measured values of intrinsic efficiency $F(As)$ for the A2 and A3 assemblies. However, it is only possible to give a range of values for the predicted assembly intrinsic efficiency since this parameter constitutes the sum of two components: (a) the product of the intrinsic efficiency of the crystal itself [$F(c)$] and the casing survival probability [$e^{-\mu x}$]; (b) An unknown fraction of these source photons which Compton scatter from the casing into the crystal and subsequently interact. The range of values given in the figures represent the sum of components (a) and (b) where the fraction in (b) is taken as zero and unity.

Figures 4.23 and 4.24 show the peak to total ratios for the A2 and A3 assemblies [$\gamma(As)$] and as the predicted values are obtained using $F(As)$ according to the relationship of equation 4.39 the same uncertainty is manifest.

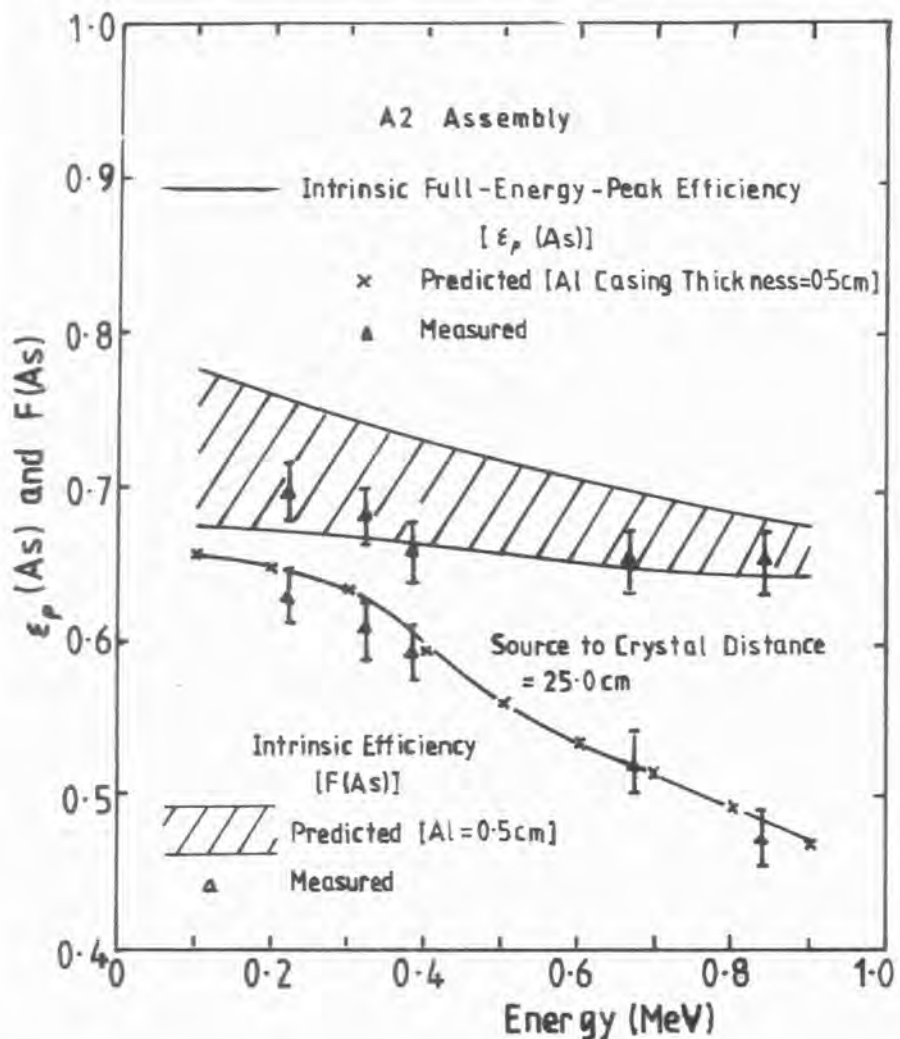


Figure 4.21 Predicted and measured values of intrinsic efficiency and intrinsic full-energy-peak efficiency for the A2 shield assembly as a function of source energy.

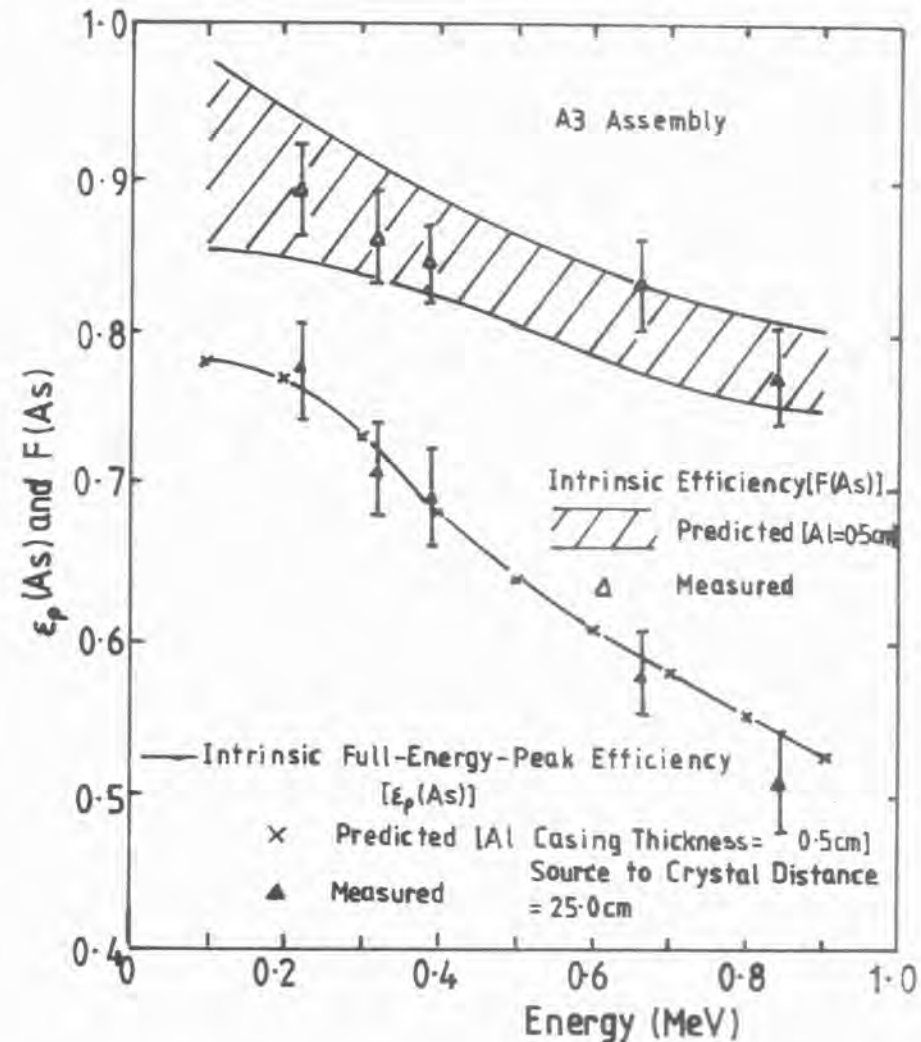


Figure 4.22 Predicted and measured values of intrinsic efficiency and intrinsic full-energy-peak efficiency for the A3 shield assembly as a function of source energy.

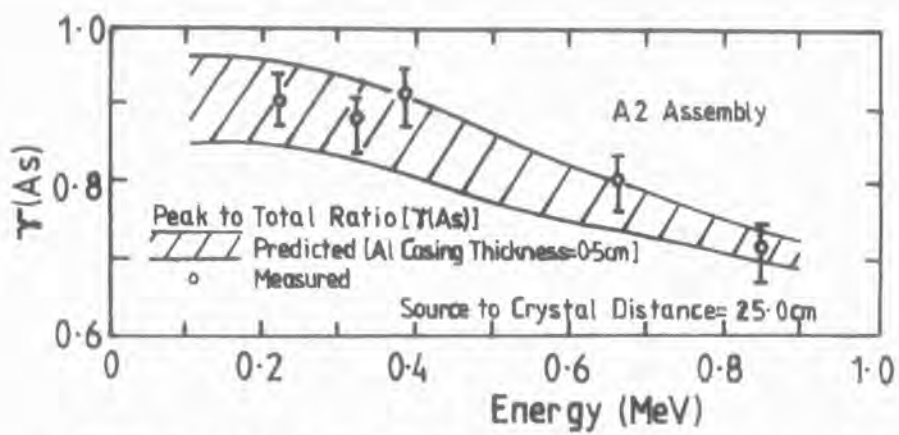


Figure 4.23 Predicted and measured values of peak to total ratio for the A2 shield assembly as a function of source energy.

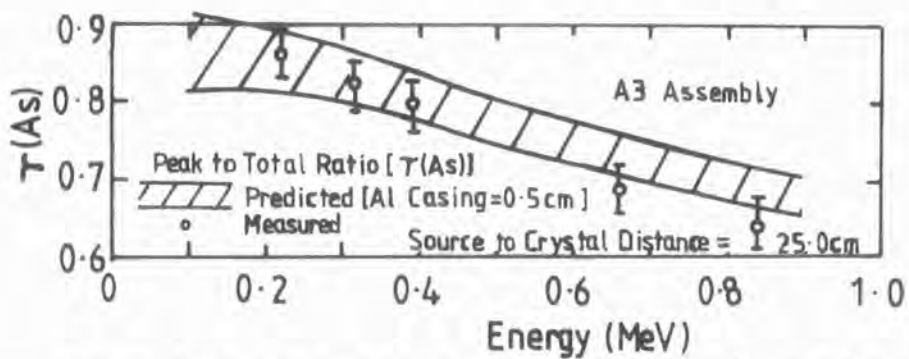


Figure 4.24 Predicted and measured values of peak to total ratio for the A3 shield assembly as a function of source energy.

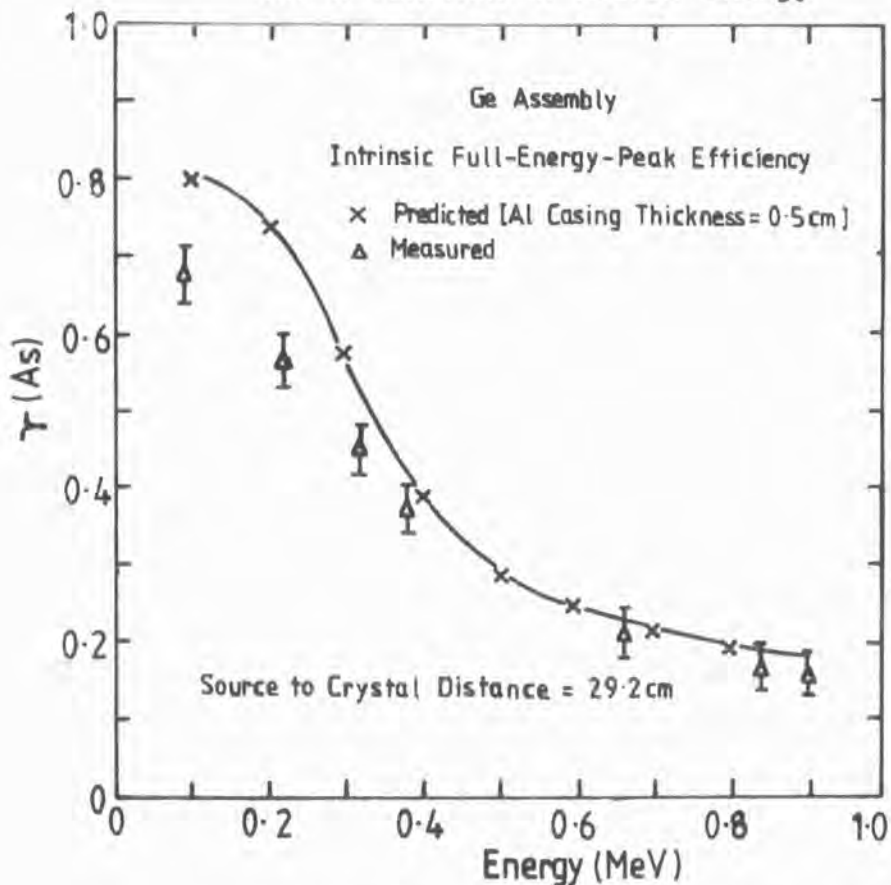


Figure 4.25 Predicted and measured values of intrinsic full-energy-peak efficiency for the Ge assembly as a function of source energy.

The spectrum produced by scintillation and solid-state devices in response to monoenergetic gamma-ray sources consists of two distinct parts; (a) the full-energy-peak, centred at the source energy and (b) a continuous distribution, stretching from the maximum Compton electron energy (i.e. the Compton edge) to zero. From the records kept in the Monte-Carlo calculations the structure of these two portions of the spectra are capable of being determined. Figures 4.26, 4.28 and 4.30 show the compositions of the full-energy-peaks of the Ge, A2 and A3 crystals respectively. The contributions from the two types of interaction are shown and the Compton contribution is further broken down into two components: (i) the contribution from a single Compton scattering in which the secondary photon is photoelectrically absorbed (Indirect photo electric effect) and (ii) the contribution from multiple Compton scattering. As would be expected from the form of variation of attenuation coefficients as a function of energy the photoelectric component dominates the peak at low energies but as the source energy increases the Compton scattering mechanism becomes dominant.

The continuous distribution component of the detector spectrum is the result of Compton scattering in which the secondary photon leaves the detector causing an energy deposition which is lower than the source energy. Deposition is from the recoil electron and therefore since the electron has a maximum energy given by equation 4.7 the continuous distribution has an upper limit at this energy (the Compton edge). Figures 4.27, 4.29 and 4.31 show the fractions of primary Compton events which contribute to the full-energy-peaks of Ge, A2 and A3 respectively as a function of source energy and the complements of the figures therefore represent the fraction of primary Compton events which leave the crystals. Thus, for example at 0.511 MeV

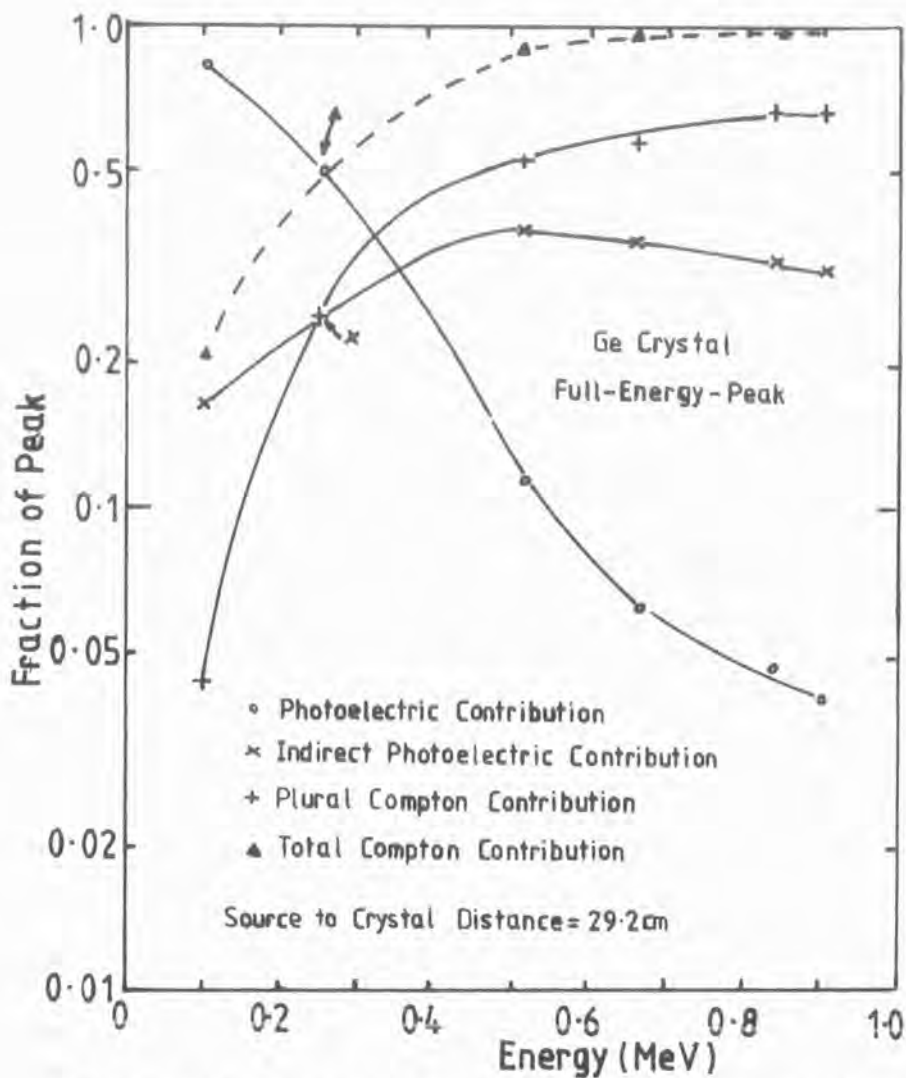


Figure 4.26 Composition of the full-energy-peak as a function of energy from monoenergetic, isotropic, point sources for the central Ge crystal of the Durham gamma-ray spectrometer.

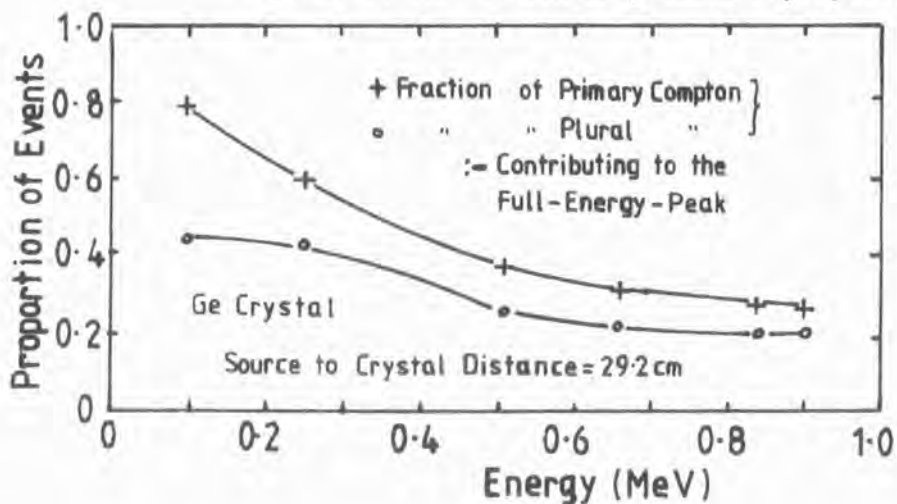


Figure 4.27 Fraction of photon histories which undergo (a) primary Compton scattering and (b) multiple (i.e. >1) Compton scattering, that contributes to the full-energy-peak, as a function of energy for the central Ge crystal of the Durham gamma-ray spectrometer.

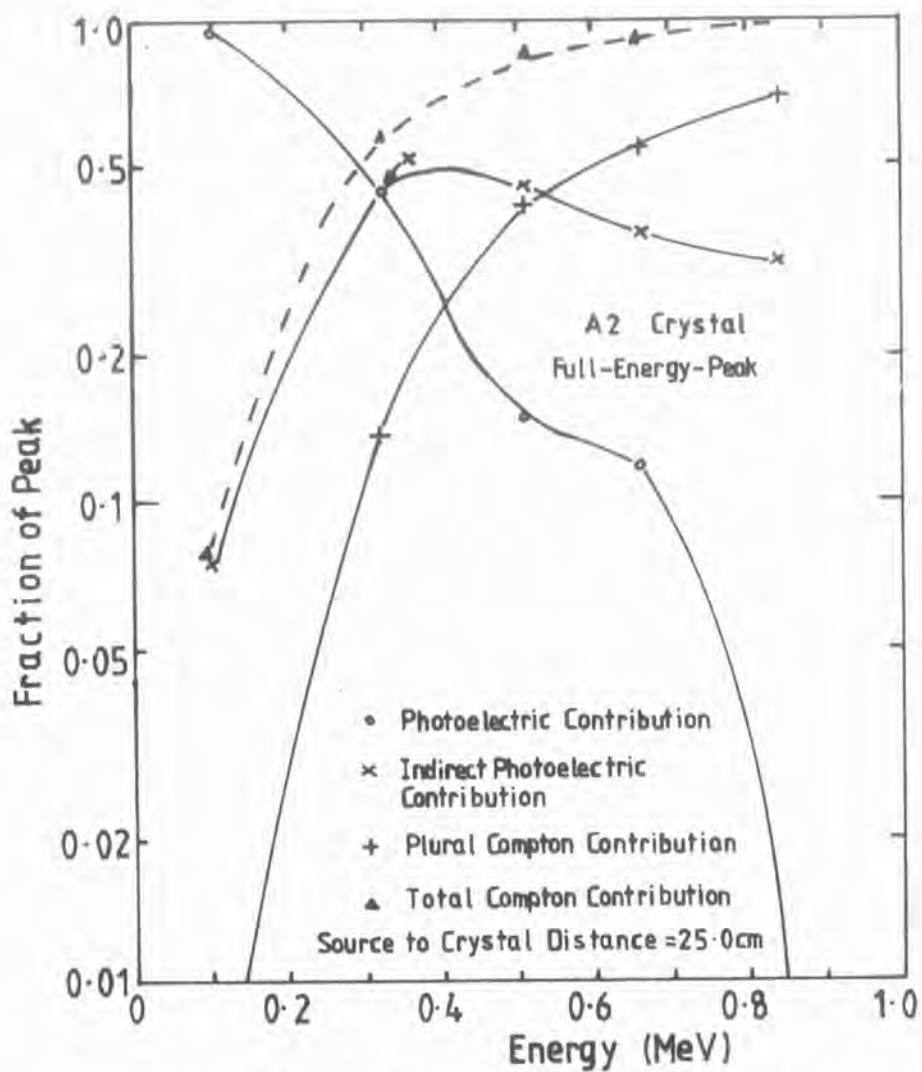


Figure 4.28 Composition of the full-energy-peak as a function of energy (monoenergetic, isotropic, point sources) for the A2 shield crystal.

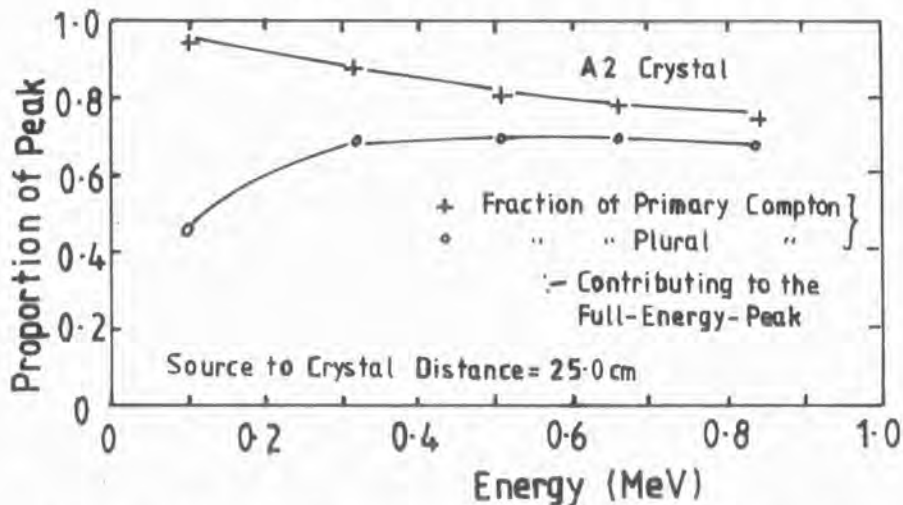


Figure 4.29 Fraction of photon histories which undergo (a) primary Compton scattering and (b) multiple (i.e. >1) Compton scattering, that contributes to the full-energy-peak, as a function of energy for the A2 shield crystal.

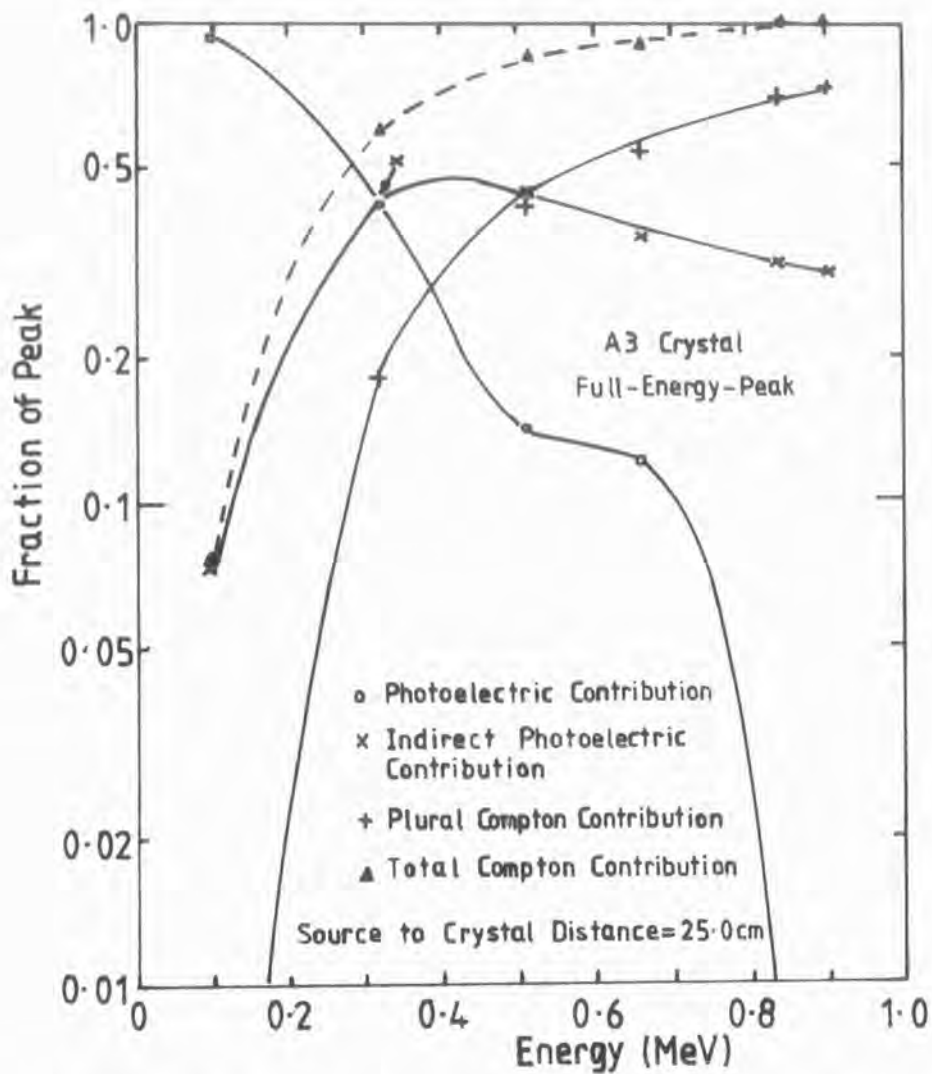


Figure 4.30 Composition of the full-energy-peak as a function of energy (monoenergetic, isotropic, point sources) for the A3 shield crystal.

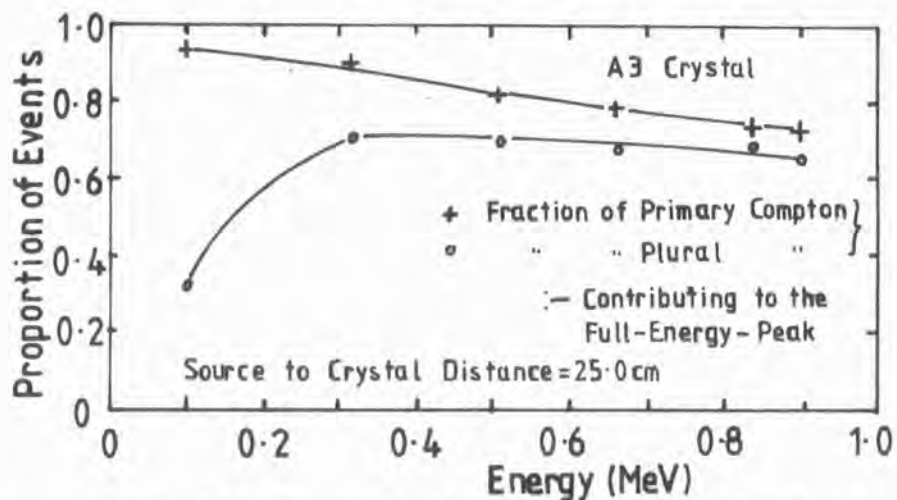


Figure 4.31 Fraction of photon histories which undergo (a) primary Compton scattering and (b) multiple (i.e. >1) Compton scattering, that contributes to the full-energy-peak as a function of energy for the A3 shield crystal.

~ 64% and ~ 20% of primary Compton events produce secondary photons which escape from the Ge and A2 crystals respectively. Additionally the same three figures show, as a function of source energy, the fraction of events undergoing multiple Compton scattering which contribute to the full-energy-peak and again from the complements it can be seen that, for instance at 0.511 MeV, ~ 75% and ~ 30% of these events eventually escape from Ge and A2.

The curves shown in figures 4.32, 4.33 and 4.34 illustrate the variation of efficiency and peak to total ratio, as obtained from the Monte-Carlo simulations, for the Ge crystal as a point source is moved along the central axis. Crisler et al. (1971) reports a relationship which permits calculation of the efficiency at any source distance from a knowledge of the value at a single distance together with the effective interaction depth of the crystal. Effective interaction depth d_{eff} is defined as that distance below the surface of the outside detector mounting-can at which a gamma-ray of a particular energy appears to interact. Crisler gives:

$$\frac{\epsilon(r_1)}{\epsilon(r_2)} = \left\{ \frac{(r_2 + d_{\text{eff}})^2}{(r_1 + d_{\text{eff}})^2} \right\} \quad (4.44)$$

where ϵ is the absolute full-energy peak efficiency which represents the probability of total absorption of any photon emitted by the source, and r_1 and r_2 are the two relevant source to mounting-can distances. This relationship may be adapted to the intrinsic full-energy-peak efficiency ϵ_p through the use of the Geometrical factor $G(r)$ where:

$$G(r) = \frac{\epsilon(r)}{\epsilon_p(r)} \quad (4.45)$$

Hence equation 4.42 may be restated in the form:

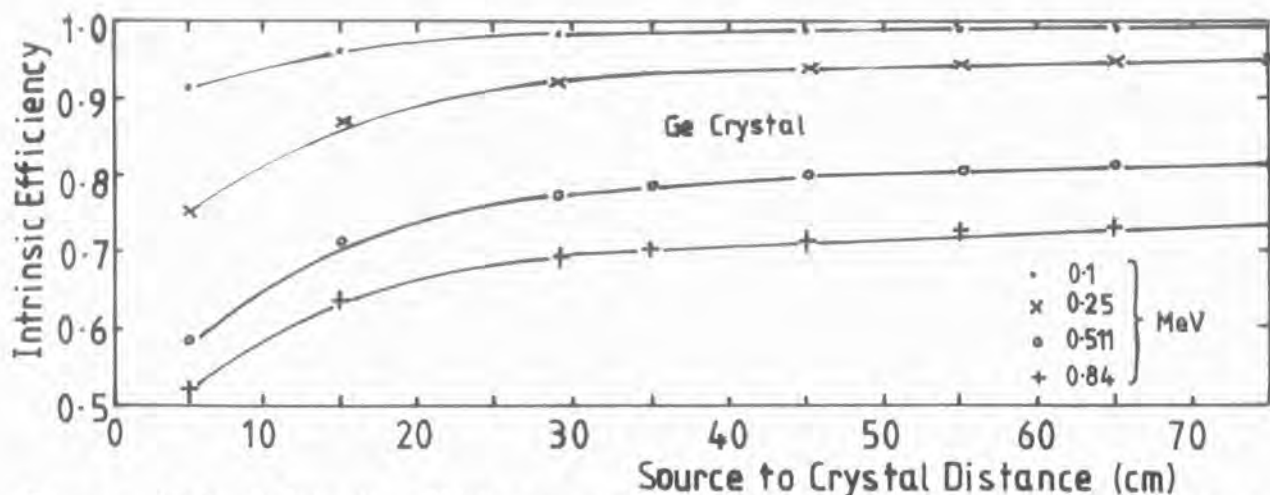


Figure 4.32 Intrinsic efficiency vs source-crystal distance at various energies from monoenergetic, isotropic, point sources on the central axis of the Durham gamma-ray spectrometer Ge crystal.

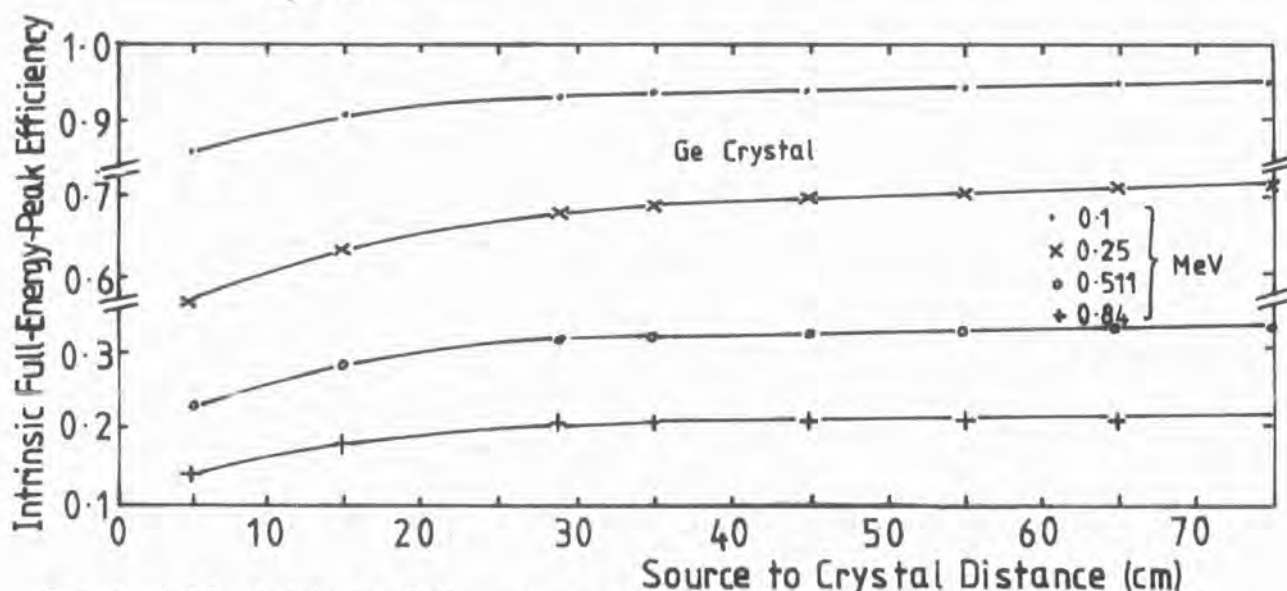


Figure 4.33 Intrinsic full-energy-peak efficiency vs source-crystal distance at various energies from monoenergetic, isotropic, point sources on the central axis of the Durham spect. Ge crystal.

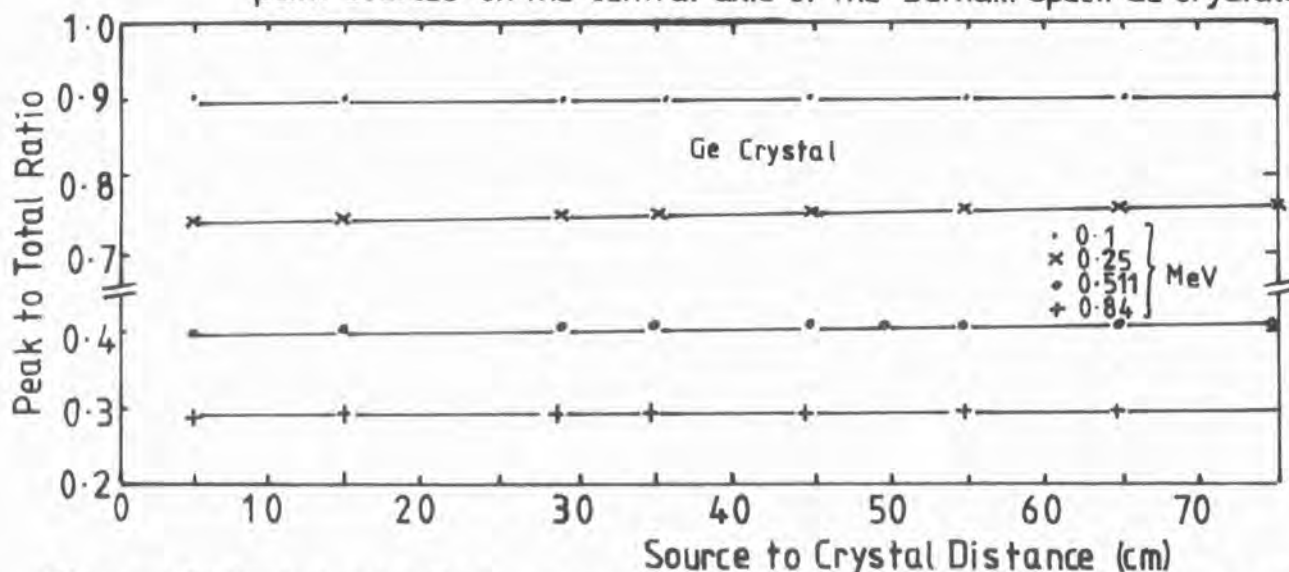


Figure 4.34 Peak-total ratio vs source-crystal distance at various energies from monoenergetic, isotropic, point sources on the central axis of the Durham gamma-ray spectrometer Ge crystal.

$$\frac{\epsilon_p(r_1)}{\epsilon_p(r_2)} = \frac{G(r_2)}{G(r_1)} \left\{ \frac{r_2 + d_{\text{eff}}}{r_1 + d_{\text{eff}}} \right\}^2 \quad (4.46)$$

A further Monte-Carlo calculation has been used to produce values of the interaction depth as a function of source to crystal distance for various source energies and these are plotted in figure 4.35 (where interaction depth is that distance below the top surface of the crystal at which a source gamma-ray interacts). To obtain the effective interaction depth the mean of the values in figure 4.35 is taken for each energy (these have been plotted in figure 4.36 and the distance between the top surface of the Ge crystal and the can (= 4mm) is added in each case. Using the Monte-Carlo values of intrinsic full-energy-peak efficiency shown in figure 4.20 for a source to crystal distance of 29.2 cm, as $\epsilon_p(r_1)$, equation 4.46 produces values for $\epsilon_p(r_2)$ which are in reasonable agreement with the Monte-Carlo values given in figure 4.33.

Monte-Carlo calculations have also been carried out for the polarimeter (P1 to P4 and Ge). In this case polarised photons enter the Ge detector and those producing Compton secondary photons which scatter into one of the polarimeter quadrants and interact within it, are recorded. Figure 4.37 shows the results obtained; this is a plot of the ratio of counts in two neighbouring quadrants as a function of incident photon energy. The source photons are 100% polarised with their electric vector normal to one of the quadrants. From such polarisation, quadrant number 2 is expected to show enhanced counts, indicated by the ratio C1/C2 being greater than 1.0 which is the value for zero polarisation.

The Ge detector energy resolution has been measured in the laboratory using the pulse-height spectra for standard radioactive isotopes placed on the central axis of the spectrometer above the collimator (A1) and figure 4.38 is a plot of the results. Also given here is a plot of the

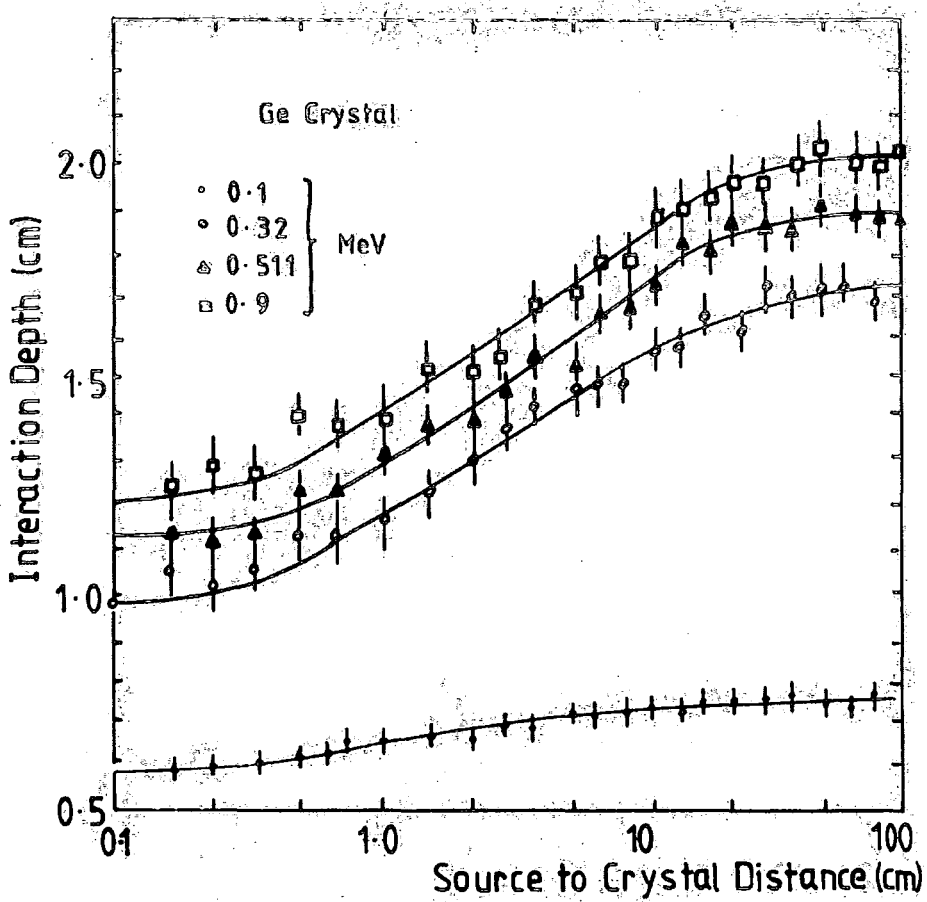


Figure 4.35 Interaction depth vs source to crystal distance at various source energies for the Ge crystal of the Durham gamma-ray spectrometer.

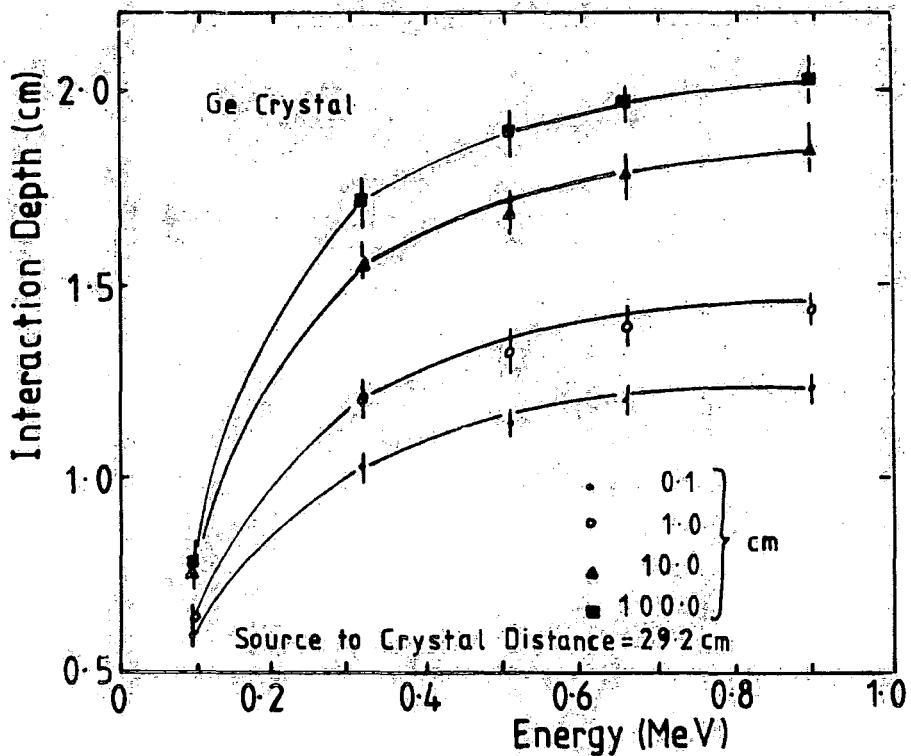


Figure 4.36 Interaction depth vs energy at various source to crystal distances for the Ge crystal of the Durham gamma-ray spectrometer.

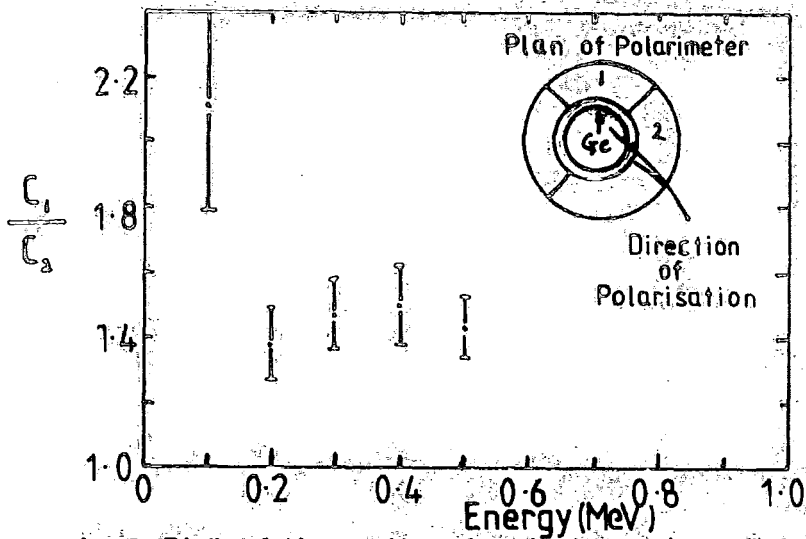


Figure 4.37 Plot of the ratio of counts in two neighbouring quadrants of the polarimeter for 100% polarised, incident photons vs energy.

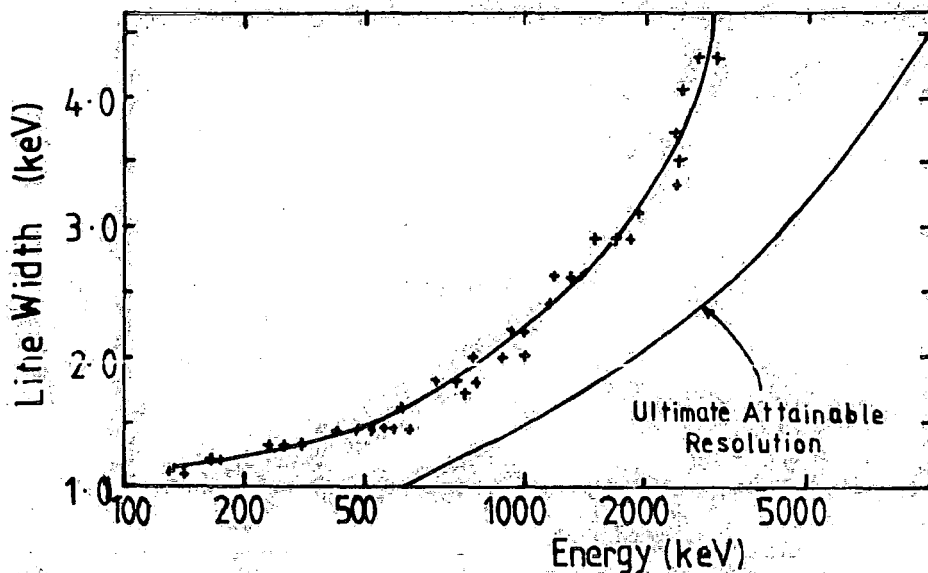


Figure 4.38 The Germanium energy resolution vs energy.

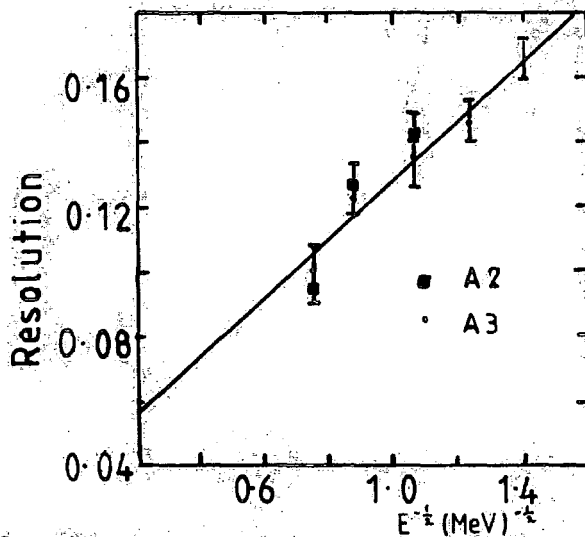


Figure 4.39 The energy resolution of the A2 and A3 shield crystals vs $(\text{Energy})^{-1/2}$.

ultimate achievable resolution for this detector which would be obtained if an ideal preamplifier could be used and assuming a Fano factor of 0.13 for the detector. The measured resolution is a result of two contributions (a) the intrinsic resolution of the detector itself σ_D and (b) the preamplifier resolution σ_p :

$$(a) \quad \sigma_D^2 = E_o F W \quad (4.47)$$

$$(b) \quad \sigma_p^2 = W^2 \left\{ \frac{2I_D \tau}{e} + QN^2 \right\} \quad (4.48)$$

at energy E_o and where W is the electron-hole pair creation energy (2.98 eV for cooled Ge), F is the Fano factor, QN and τ are the equivalent noise charge and time constant of the preamplifier respectively and I_D is the detector leakage current. The resulting detector line width is then:

$$\text{FWHM(keV)} = 2.35 \sqrt{\sigma_D^2 + \sigma_p^2} \quad (4.49)$$

Measurements of the A2 and A3 shield crystal resolutions are shown in figure 4.39. In these cases the summed output signal from the four and three associated photomultiplier tubes respectively were used for the measurements. This summation signal removes pulse-height variation arising from the location of the interacting photons and improves resolution by a factor equal to the square root of the number of tubes.

Owing to the construction format of the A1 collimator the resulting pulse-height spectrum does not exhibit any features from which resolution measurements could be obtained.

At gamma-ray energies the aperture of the spectrometer varies with energy owing to the increasing penetrability of the photons with increasing energy. Thus the geometrical aperture, defined by the physical

boundaries of the collimator, does not represent the true aperture. The energy dependence of the Durham spectrometer aperture has been measured using the laboratory radioactive sources as follows. One of the sources was placed above the spectrometer and moved in one centimetre steps along a diammetrical line. At each position a pulse-height spectrum was collected and the area under the peak (background subtracted) recorded. The areas were plotted as a function of position as shown in figure 4.40 for the 0.847 MeV source, and the FWHM was taken as the angular aperture at that energy. The process was repeated for a range of source energies and the angular aperture plotted as a function of energy (figure 4.41). It can be seen that the FWHM varies by $\sim 1^\circ$ between energies 0.847 and 3.25 MeV. A stronger energy dependence would be expected for a NaI(Tl) collimator due to increased leakage through the edges as compared to the lead (Pb) used here.

These measurements may only be used to study the energy variation of the geometrical factor of the spectrometer since the angular response to a distant, celestial, point source is quite different depending not only on energy but also on the relative angular position of the source trajectory with respect to the aperture centre. This is shown in figure 4.42.

4.4 GAMMA-RAY LINE DETECTABILITY

In the presence of a specific background flux the minimum detectable flux from a gamma-ray line after a particular source and background observation time is given as follows. At energy E_o , if the line flux is F_L photons $\text{cm}^{-2}\text{s}^{-1}$ then the observed detector counting rate R_L^1 , where the flux passes through absorptive material of transmission α , is:

$$R_L^1 = F_L \alpha \epsilon A \text{ counts s}^{-1} \quad (4.50)$$

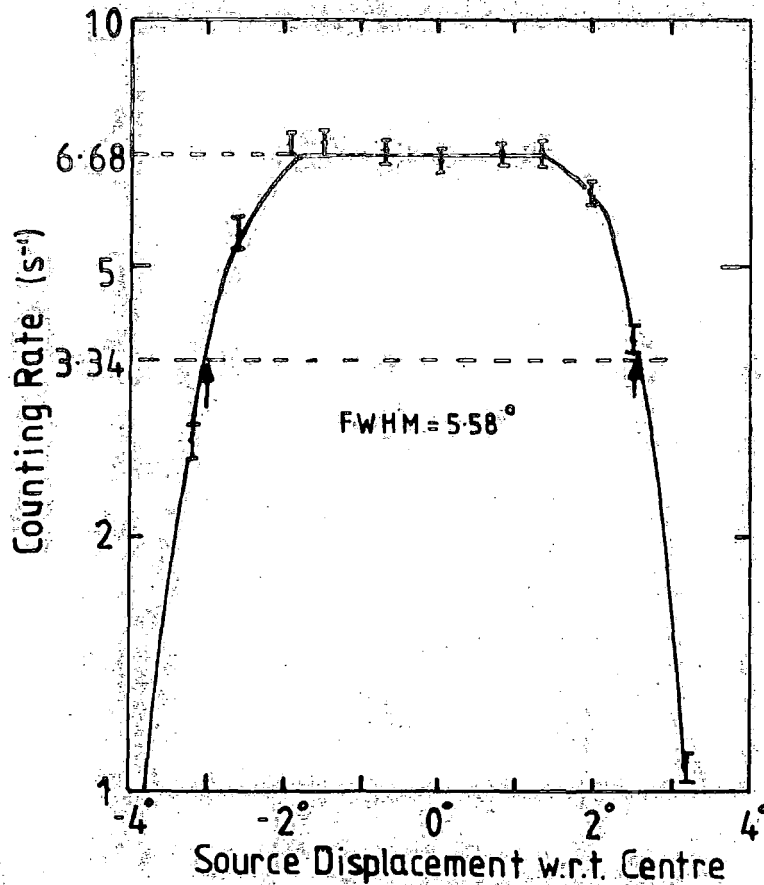


Figure 4.40 Area under the 0.847 MeV peak as a function of source position along a diammetrical line.

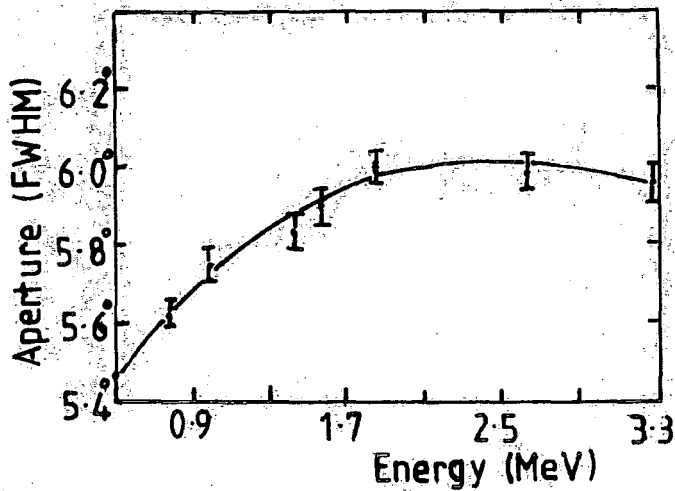


Figure 4.41 Aperture of the Durham gamma-ray spectrometer vs energy.

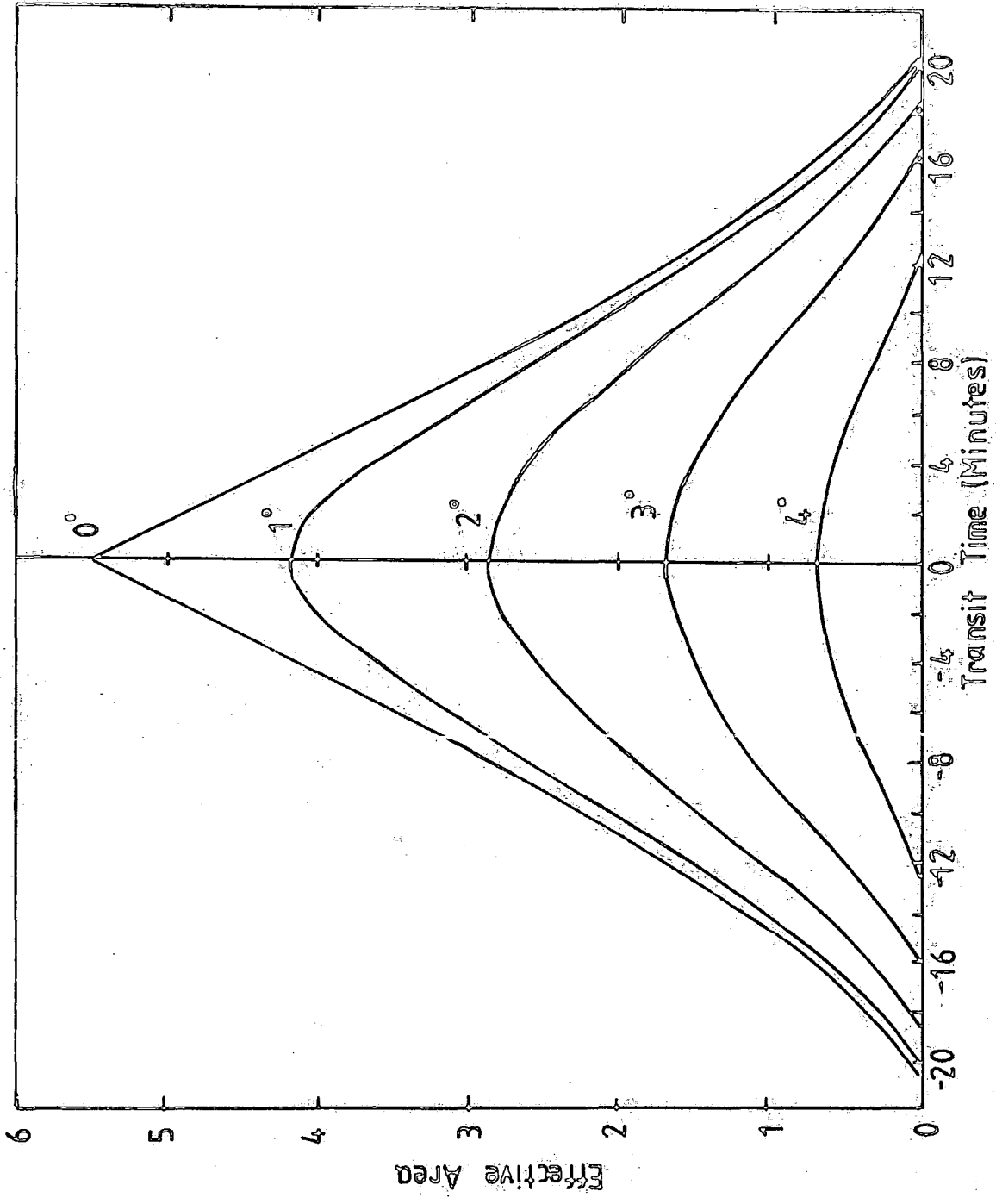


Figure 4.42 Variation of sensitive area as a point source passes over the detector's field of view. Curves are shown for both on and off axis transits.

where ϵA is the full-energy-peak detection effective area. Then, for a channel of $\Delta E(E_0)$ centred at E_0 the measured counting rate in the channel after Gaussian resolution spreading is:

$$R_L = \frac{\alpha \epsilon A F_L}{\sqrt{2\pi} \sigma} \int_{E_0 - \frac{1}{2}\Delta E}^{E_0 + \frac{1}{2}\Delta E} \exp \left\{ -\frac{(E^1 - E_0)^2}{2\sigma^2} \right\} dE^1 \quad (4.51)$$

and substitution of the expression:

$$G(x) = \frac{1}{\sqrt{2\pi}} \int_{-x}^x \exp(-\frac{1}{2}t^2) dt \quad (4.52)$$

yields:

$$R_L = \alpha \epsilon A F_L G \left(\frac{\Delta E}{2\sigma} \right) \text{ counts s}^{-1} \quad (4.53)$$

If the line is to be seen then the flux must be n standard deviations greater than the background rate R_B , and since the variance in background subtraction is:

$$\sigma_L^2 = \frac{\alpha \epsilon A F_L G + R_B \Delta E}{T_L} + \frac{R_B \Delta E}{T} \quad (4.54)$$

where T and T_L are the respective background and source observing times, then for $n\sigma_L$ detection significance:

$$R_L = \alpha \epsilon A F_L G = n\sigma_L \quad (4.55)$$

Solving for F_L produces the expression for the minimum detectable line flux:

$$F_L = \frac{n}{2\alpha \epsilon A G} \left\{ \frac{n}{T_L} + \left[\left(\frac{n}{T_L} \right)^2 + 4R_B \Delta E \left(\frac{1}{T_L} + \frac{1}{T} \right) \right]^{\frac{1}{2}} \right\} \quad (4.56)$$

Historically the parameter n has been taken as 3 but it is recommended that a value of 5 should be used.

Increasing the observation time, detector area, detector efficiency and photon transmission into the detector and decreasing the detector FWHM and background all result in improved sensitivity.

CHAPTER 5

THE DURHAM GAMMA-RAY SPECTROMETER BALLOON FLIGHT

5.1 INTRODUCTION

As the terrestrial atmosphere prevents celestial gamma-ray emission from reaching sea level and since it also generates secondary gamma radiation from cosmic-ray particle interactions, then in order to obtain meaningful data from celestial sources at gamma-ray energies it is necessary to establish an observation platform either above or as close to the 'top' of the atmosphere as is practicable. To this end, arrangements were made for a high altitude balloon flight of the Durham gamma-ray spectrometer, to be launched during August 1979 from Palestine, Texas, U.S.A., under the auspices of the National Scientific Balloon Facility (NSBF) of the National Centre for Atmospheric Research (NCAR). A precise date for the balloon flight could not be fixed in advance as this would be very much dependent upon the local weather conditions around the launch site, to the extent that a flight could be postponed at any time up to the commencement of balloon inflation, i.e. approximately thirty minutes prior to launch. However, during August the average delay at Palestine for an evening launch is three to four days and this is reduced to approximately 24 hours for a morning launch.

Although the primary aim of this flight was to be the evaluation of the system performance under real observing conditions, it was believed judicious to prepare for the execution of source observations should circumstances prove favourable. Consequently calculations were performed for several discrete gamma-ray sources, to resolve the times between which each one would lie at a Zenith Angle of less than 50° as seen from Palestine (latitude 32° North, longitude 96° West) during August 1979. The maximum zenith angle of 50° was chosen as owing to the configuration of the apparatus it was considered unwise to use the zenith

drive beyond this angle. Figure 5.1 indicates graphically the results of the calculations and since on this occasion each of the sources would be of equal interest it is clear from figure 5.1 that the uncertainty in the launch date and time would not be at all detrimental from the observational viewpoint.

In spite of a lack of foreknowledge of the precise timing of the flight's commencement it was possible to construct provisional 'order of observation' schedules in advance and this was done, based on the information from figure 5.1, for flights beginning with (a) an evening launch and (b) a morning launch. Common to both schedules were: (i) the ascent phase of approximately three hours during which time the atmospheric gamma-ray spectrum and counting rates would be monitored and (ii) an initial period at float altitude of systems checking and background measurement. Source observations would then begin, employing a 'nodding' technique, i.e. alternation between background only and source plus background, on a time scale of the order of minutes, over a period of three to four hours for each source. The arrangement would be:-

- Schedule (a) Evening launch : (1) N.G.C. 1275 (Seyfert Galaxy)
(2) M1 (Crab Nebula : Supernova remnant containing a pulsar)
(3) N.G.C. 4151 (Seyfert galaxy).

- Schedule (b) Morning launch : (1) N.G.C. 4151 (2) Hercules X-1
(3) Cygnus X-1.

Upon completion of these observations the flight would be terminated.

Computer programmes were constructed in BASIC for use with a Tektronix 4051 minicomputer, to facilitate rapid calculation of source positions (Zenith Angle and Azimuth) during the flight which could then be telemetered to the payload.

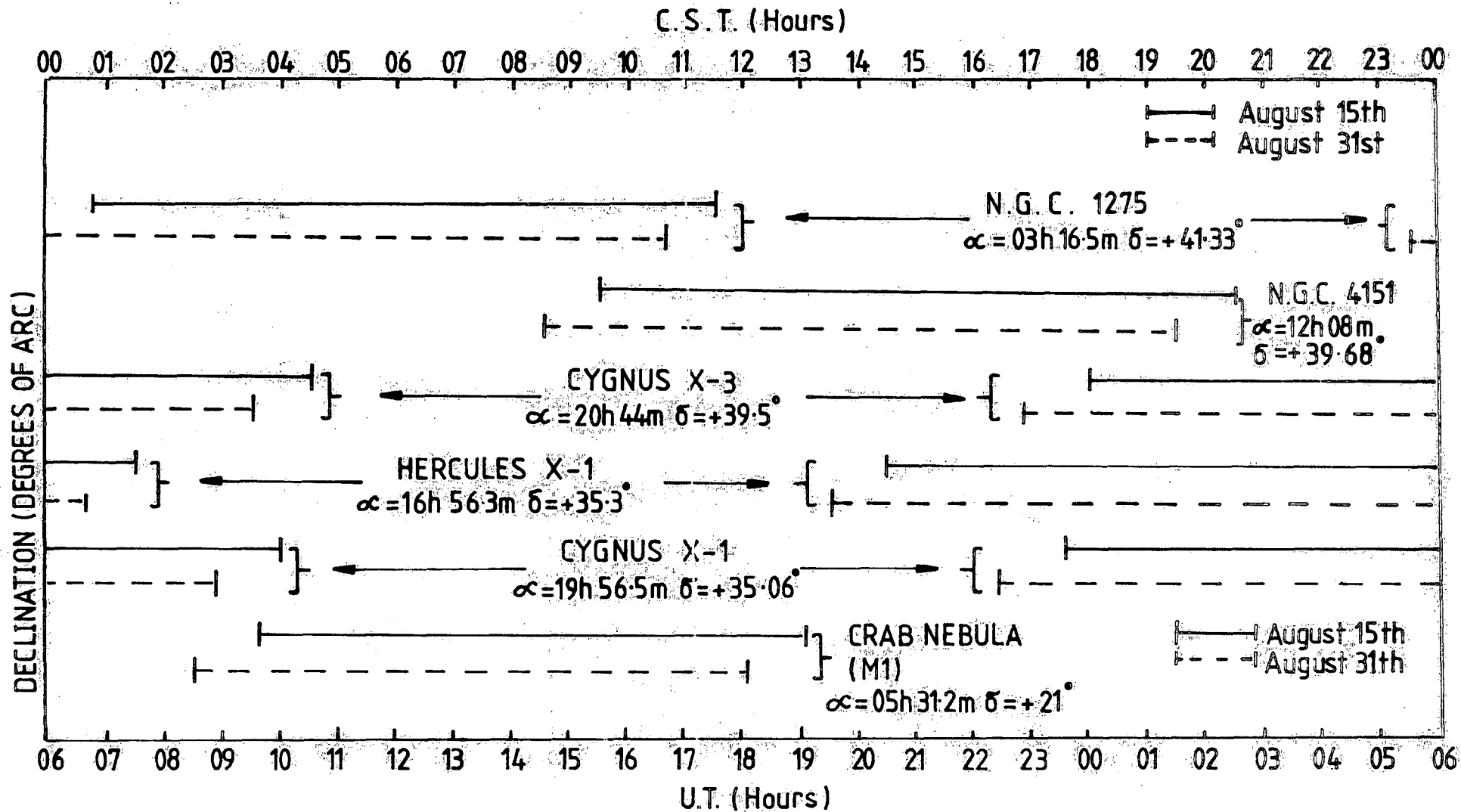


Figure 5-1 Times and periods for which possible, discrete, celestial, gamma-ray sources lie at a zenith angle $< 50^\circ$ as observed from Palestine during late August. (The Declination axis is not to scale).

5.2 THE FLIGHT

During the course of pre-flight systems testing at Palestine NSBF the azimuth motor's gearbox ceased to function thus preventing any use being made of the azimuth steering system and development of a fault in the zenith autosystem necessitated a last minute alteration to permit manual control of the zenith drive. A decision was taken to proceed with the flight in spite of the reduced steering capability since the original flight proposal simply called for monitoring of background counting rates and spectra which could still be achieved even with the apparatus in its then current condition. It may even have proved possible to carry out discrete source observation in a limited manner.

During the hour immediately prior to launch the spectrometer and telemetry system were given a final testing and a calibration test tape was recorded. As had been foreseen a delay in the launch was encountered due to adverse weather conditions, however launch into clear skies was finally achieved on the morning of 28th August 1979 at 14.00:55 U.T. Surface winds were calm at launch, the temperature was 26°C and the average ascent rate was 4.28 m s^{-1} , reaching a mean float altitude of 4.33 g cm^{-2} . Further flight and payload parameters are given in tables 5.1 and 5.2.

It was noted in real time that the pressure vessel did not maintain the payload internal pressure as required and this attained an equilibrium value of 33 Mbs at float altitude. Thus when the anticoincidence shield E.H.T. set became increasingly unstable, finally ceasing to operate altogether at 15.45 U.T., the cause was attributed to corona discharge in the set as a direct result of the reduced pressure. Since the active element of the shielding array was now non-operational but the Ge detector was apparently unaffected it was still considered

TABLE 5.1 Balloon and payload weight data for the Durham Gamma-Ray Spectrometer balloon flight of 28th August 1979.

BALLOON AND PAYLOAD WEIGHT DATA	
Description	Weight (kg)
Balloon : Winzen 12.70 Micron Stratofilm 328,477 m ³	542.0
Parachute : 24.1 m	106.1
Payload Including Consolidated Instrumentation Package	662.3
Ballast : Glass	136.1
Safety Cables, Crash Padding & Ballast Hopper	10.9
Control Instruments	12.7
Gross Weight	1470.1
Gross Lift	1646.5
Free Lift 12%	176.4

TABLE 5.2 Parameters for the Durham Gamma-ray Spectrometer balloon flight of August 28th 1979

	Time (U.T.)	Pressure (Mb)	Air Mass (g cm ⁻²)	Latitude (Deg. N)	Longitude (Deg. W)
Launch :	1400.9	999	1020.68	31.78	95.7
	1421.7	465.63	476.55	31.82	95.68
	1441.8	187.54	192.33	31.83	95.48
	1503.9	71.72	73.71	31.85	95.37
	1528.0	27.61	28.44	31.85	95.52
	1553.8	10.9	11.25	31.82	95.77
	1603.0	6.92	7.15	31.85	95.87
	1618.0	4.46	4.61	31.83	96.07
	1628.0	3.92	4.06	31.82	96.23
	1700.0	3.96	4.09	31.7	96.72
	1730.0	3.96	4.09	31.6	97.2
	1800.0	4.03	4.16	31.52	97.63
	1830.0	4.1	4.24	31.5	97.92
	1900.0	4.31	4.46	31.32	98.5
	1930.0	4.33	4.48	31.28	98.95
	2000.0	4.33	4.48	31.17	99.5
	2030.0	4.42	4.58	31.12	100.1
Termination :	2101.0	4.29	4.44	31.08	100.6
Impact:	2144.2	935.25	955.69	31.03	100.62

worthwhile to continue data collection using the remaining passive element of the shielding only.

A further problem occurred at 17.03 U.T. when the zenith steering system apparently failed to operate on command, as indicated by the real time pendulum data display continuing to show a Zenith Angle setting of 0° . Thus after 4.6 hours at float altitude with the spectrometer having been orientated at constant Z.A. = 0° , hence indeterminate azimuth {i.e. constant declination = 31.5° and $7\text{h } 30\text{m} \leq \text{R.A.} \leq 12\text{h}$ (figure 5.2)}, the flight was terminated and the payload landed safely at 21.44 U.T., 23 nautical miles south of San Angelo, Texas. The payload was found by the ground recovery crew to be in good condition apart from expected superficial damage to the gondola.

Post flight analysis of the instrumentation was performed on return to Durham. Concerning the zenith drive system failure, it was believed that at a temperature of $\sim -40^\circ\text{C}$ the gearbox froze and this freezing had resulted in the stripping of the gears by the motor which had continued to turn. The remedy for this problem in a future system should be a slacker and cleaner gearbox.

The anticoincidence shield's E.H.T. problem was found to have occurred as a consequence of interference on the common electrical supply-rail to the E.H.T. sets of the Ge crystal and shield, resulting from corona discharge of the Ge E.H.T. unit. This latter device was seen during vacuum tests to discharge at ~ 750 Mbs pressure and the consequent supply-rail interference caused the supply voltage to undergo a ± 4 Volt variation, in turn causing an inhibit control on the shield E.H.T. set to switch this unit off. Potting of the E.H.T. connections for subsequent flights should prevent a recurrence of this problem.

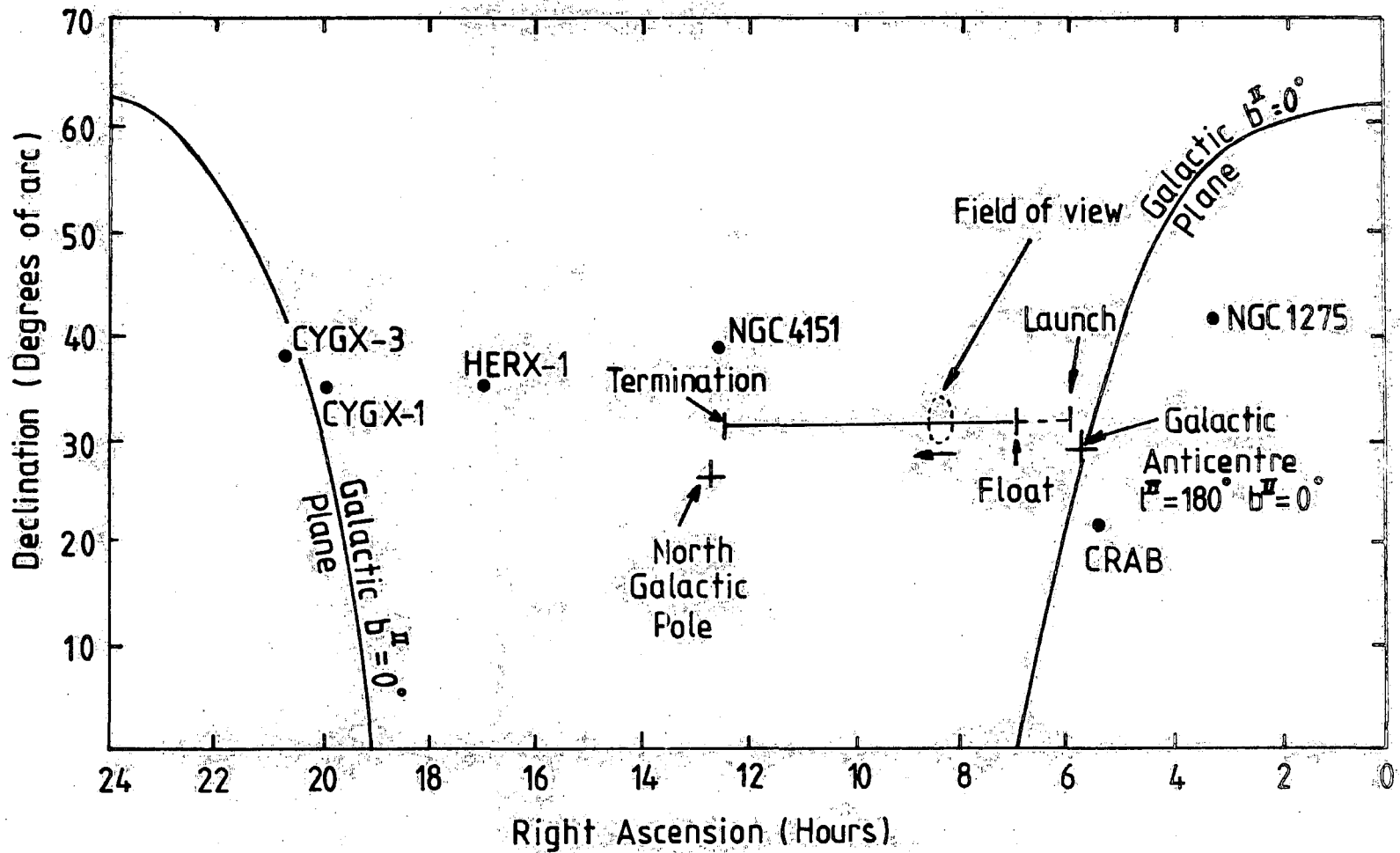


Figure 5-2. Pointing direction of the Durham gamma-ray spectrometer during the balloon flight of 1979 August 28th.

CHAPTER 6

EVALUATION OF THE FLIGHT DATA

6.1 INTRODUCTION

A total of 12 magnetic tapes were used to record the data from the 1979 August 28th flight of the Durham spectrometer. This constituted approximately 115,000 data records, where a record is composed of one complete telemetry cycle of 250 ms duration, (i.e. 32 telemetry frames, each containing 30 two-byte, binary data words), plus one ground frame of 16, two-byte, ASC II words (figure 3.20). Thus, each tape contains an average of 9500 records.

Analysis of the data was performed employing purpose written FORTRAN programmes for use with the IBM 370/168 machine of the Northumbrian Universities Multiple Access Computer (NUMAC). Each of the analysis programmes is designed to primarily extract from the raw data tapes only those words from a specified number of records which are connected with one particular aspect of the experiment (i.e. pulse-height spectra, individual detector counting rates, housekeeping, system orientation) and then appropriately process that information. In all cases the data words are composed of two bytes though only 10 bits of useful information are encoded therein (figure 3.19) so each programme contains a routine for the truncation of the useless bits prior to processing. An additional complication arises for the analysis of the main ADC spectra since not only is the relevant information for two pulse-heights distributed over several data words but also, contained within each of these words there is latch, paralysis and busy bit information (figure 3.19). Hence the main ADC pulse-height analysis programme has to perform the additional task of decoding these bits before analysis.

Because of the malfunctions mentioned previously and a problem in the ADC concerned with unmistakable excesses in particular channels, spectral information obtained from this flight is limited to that from the background for the ascending phase only and is restricted to the energy range 0.09 to 0.8 MeV.

6.2 HOUSEKEEPING AND SYSTEM ORIENTATION

Shown in figure 6.1 are the in-flight time profiles of (a) the system internal pressure, derived from the pressure transducer mounted inside the domes, and (b) the external atmospheric pressure, obtained from the Rosemount altimeter provided in the C.I.P. by NSBF. The obvious fall of the internal pressure from the time of launch is indicative of unsuccessful sealing of the pressure vessel prior to launch, however, the leak appears to have been only slight at first since the fall rate of the internal pressure is lower than that of the external pressure. This is more easily understood from the plot given in figure 6.2 which shows the Internal/External pressure difference to rise during the initial ~ 20 minutes of the flight. However, after this period the pressure difference becomes sufficiently large to increase the severity of the leak. The internal pressure's rate of fall now exceeds that of the atmospheric pressure as indicated by the reduction in the pressure difference shown in figure 6.2. After approximately 120 minutes of flight time it apparently becomes small enough to allow the leak to re-seal since the internal pressure attains an equilibrium value of ~ 33 Mb after this time rather than continuing to fall towards the float altitude atmospheric pressure value of 4.25 Mb.

Such a profile would seem to be consistent with the hypothesis that the leakage occurred around the domes' rubber sealing gaskets since the rubber would have the capability to re-adjust on reduction of the pressure difference. This emphasises the importance of adopting a

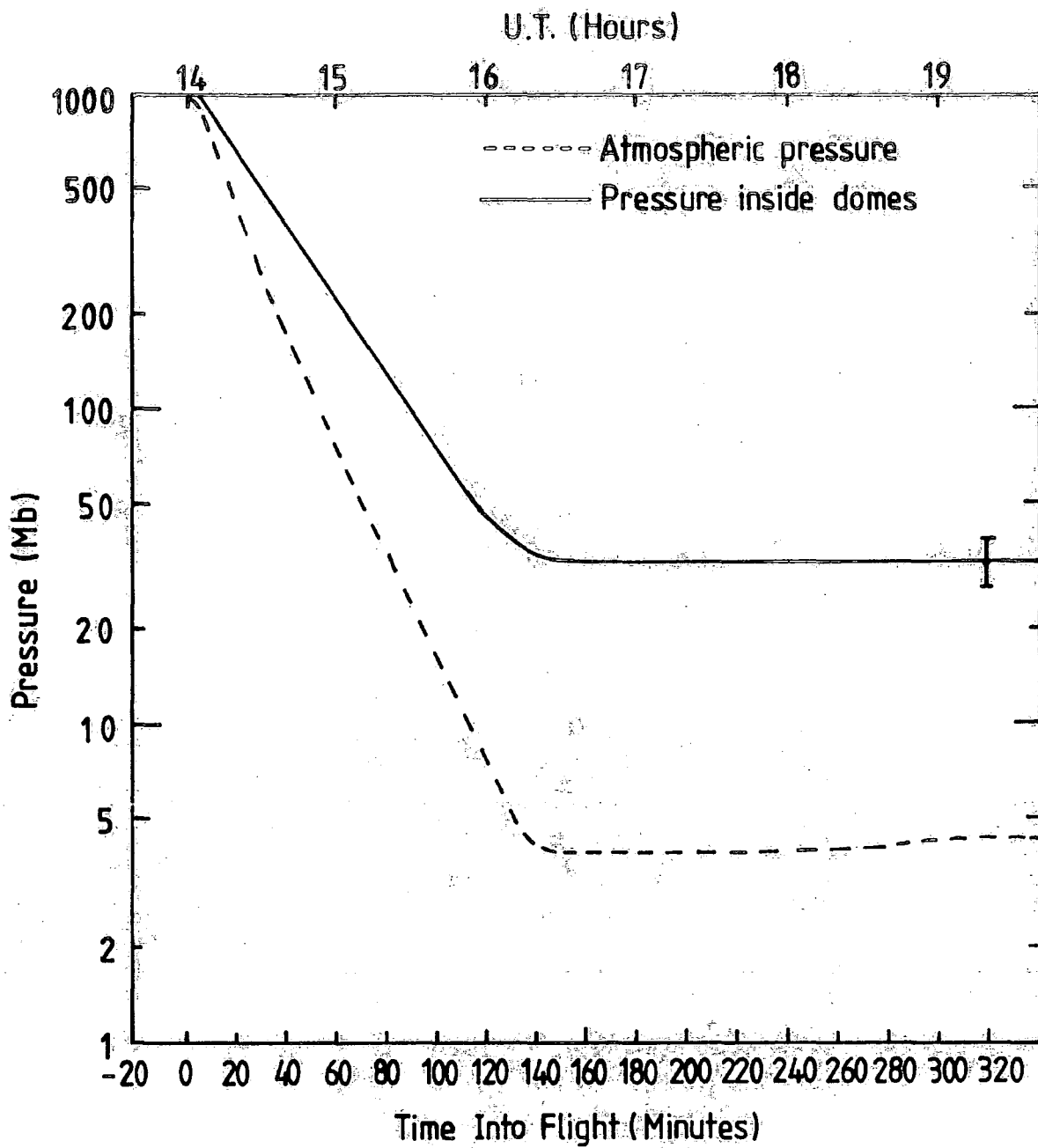


Figure 6.1 Pressure / time profiles.

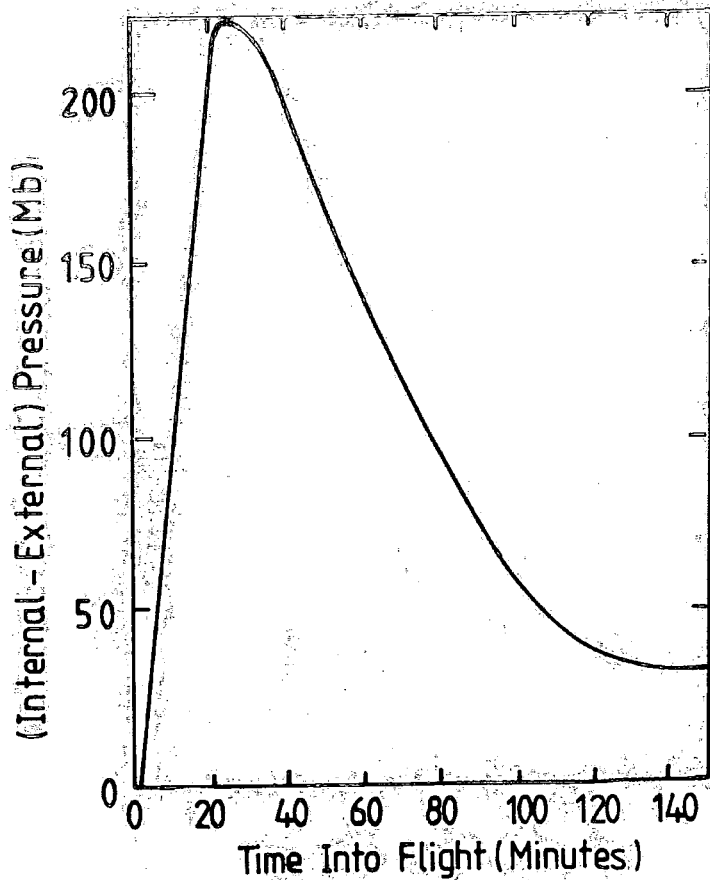


Figure 6-2 The difference between the pressure inside the domes and the external atmospheric pressure as a function of time into the flight.

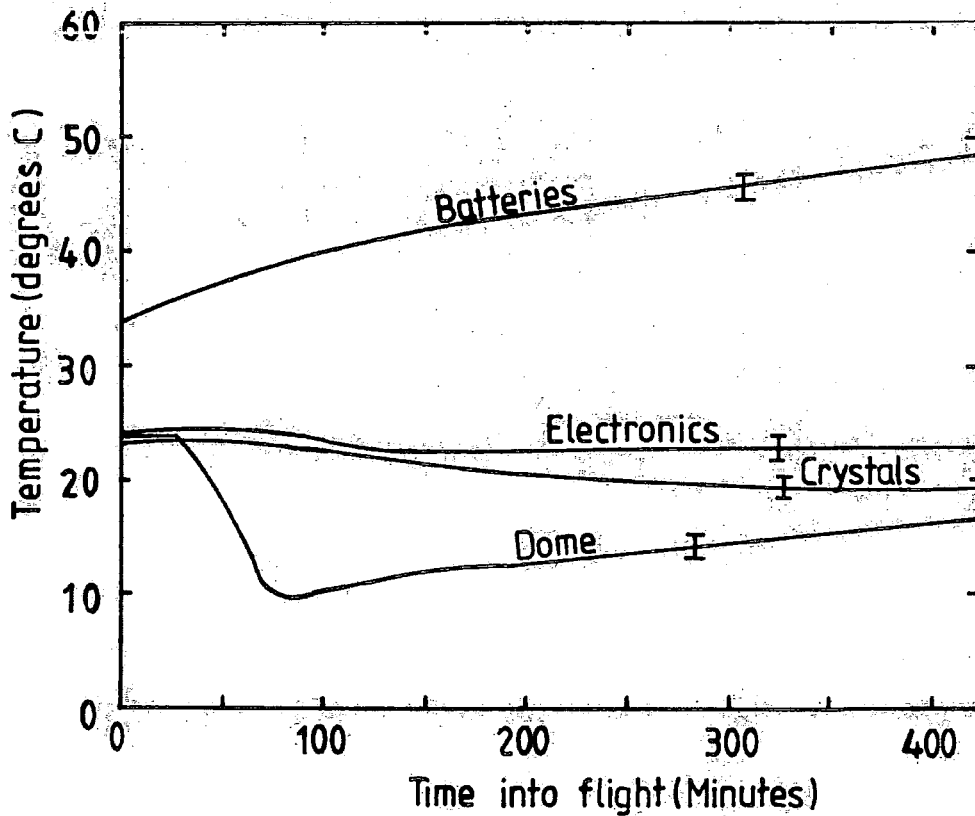


Figure 6-3 Recorded temperatures during the flight.

more systematic approach to the bolting down of the domes prior to any future flight of the apparatus.

Figure 6.3 illustrates the profiles for the various temperatures measured during the flight and since the crystals and electronics were maintained at $\sim 23^{\circ}\text{C}$ throughout, data corrections due to temperature variations have not been necessary.

As mentioned in Chapter 5 after reaching float altitude the zenith drive failed to operate and therefore the spectrometer viewing aperture remained centred upon the zenith. Thus the orientation in celestial Declination of the field centre simply varied as the latitude of the spectrometer (table 5.3) i.e. $+31.78^{\circ} \geq \delta \geq +31.03^{\circ}$. However, in this attitude over the flight period the celestial Right Ascension changed constantly over the range $7\text{h } 30\text{m} < \alpha < 12\text{h } 00\text{m}$. In the Galactic coordinate system the overall orientation corresponds to a movement of the field of view from the Galactic anticentre to approximately the north Galactic pole, spanning 10° in galactic longitude; specifically $180^{\circ} < l^{\text{II}} < 190^{\circ}$. None of the sources we had hoped to observe passed through the field of view (figure 5.2) and the same applies to all other known gamma-ray sources.

Integral counting rates, for energies above the discrimination threshold, from each of the elements in the anticoincidence shield array are presented in figure 6.4 as a function of time into the flight; up to 100 minutes ($\sim 10 \text{ g cm}^{-2}$), after which the malfunction in the E.H.T. unit occurred. The shapes of the curves agree well with those obtained by Ling et al. (1974) and show an expected maximum at an atmospheric depth of 100 g cm^{-2} (the Pfozter maximum).

The integral photon counting rates from the Ge detector, shown as a function of time in figure 6.5, are taken from the secondary ADC over the energy range 0.09 to 8.8 MeV. (i) The lower set of points are the

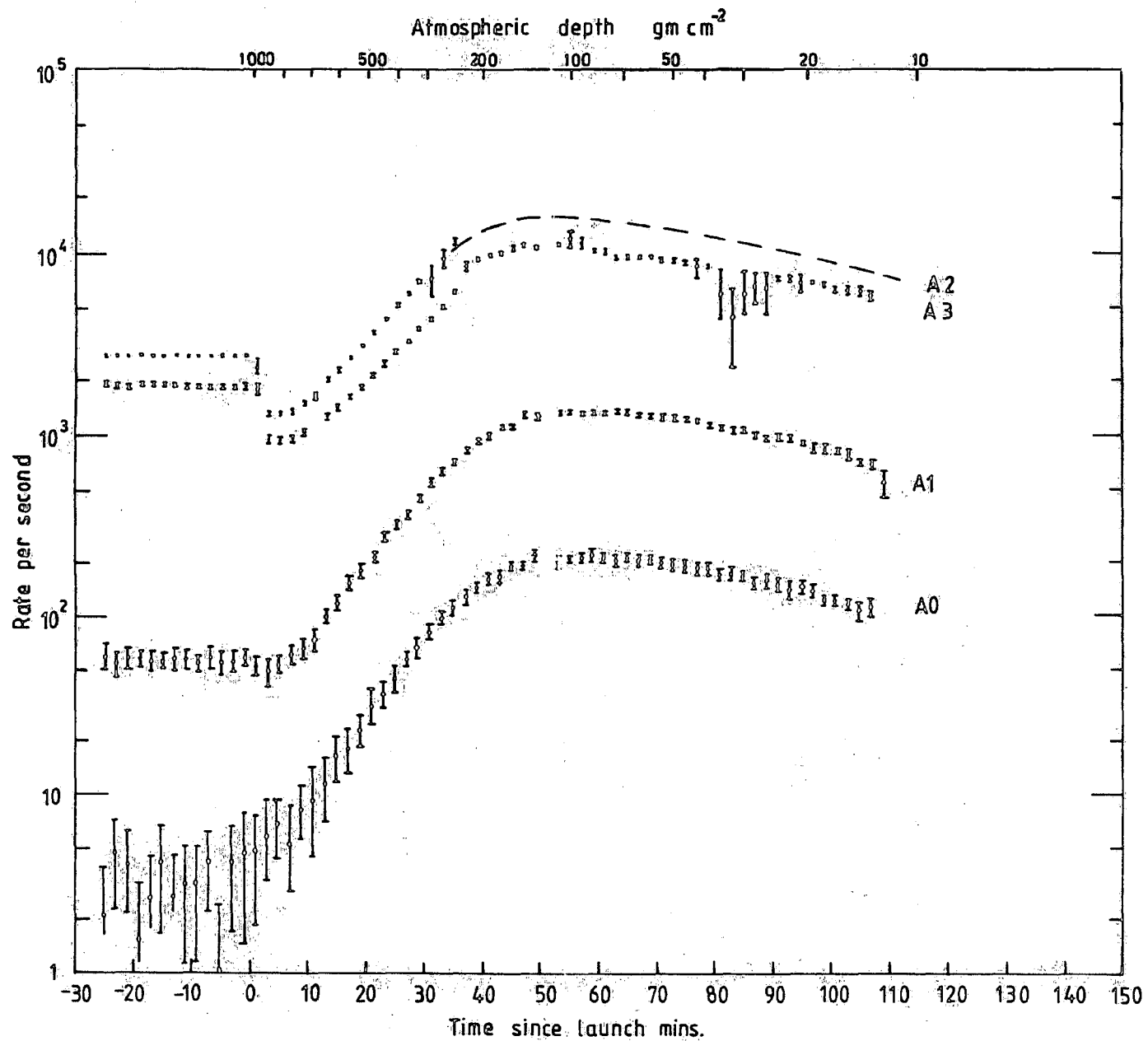


Figure 6.4 The counting rate of the anticoincidence shield elements as a function of time and atmospheric depth.

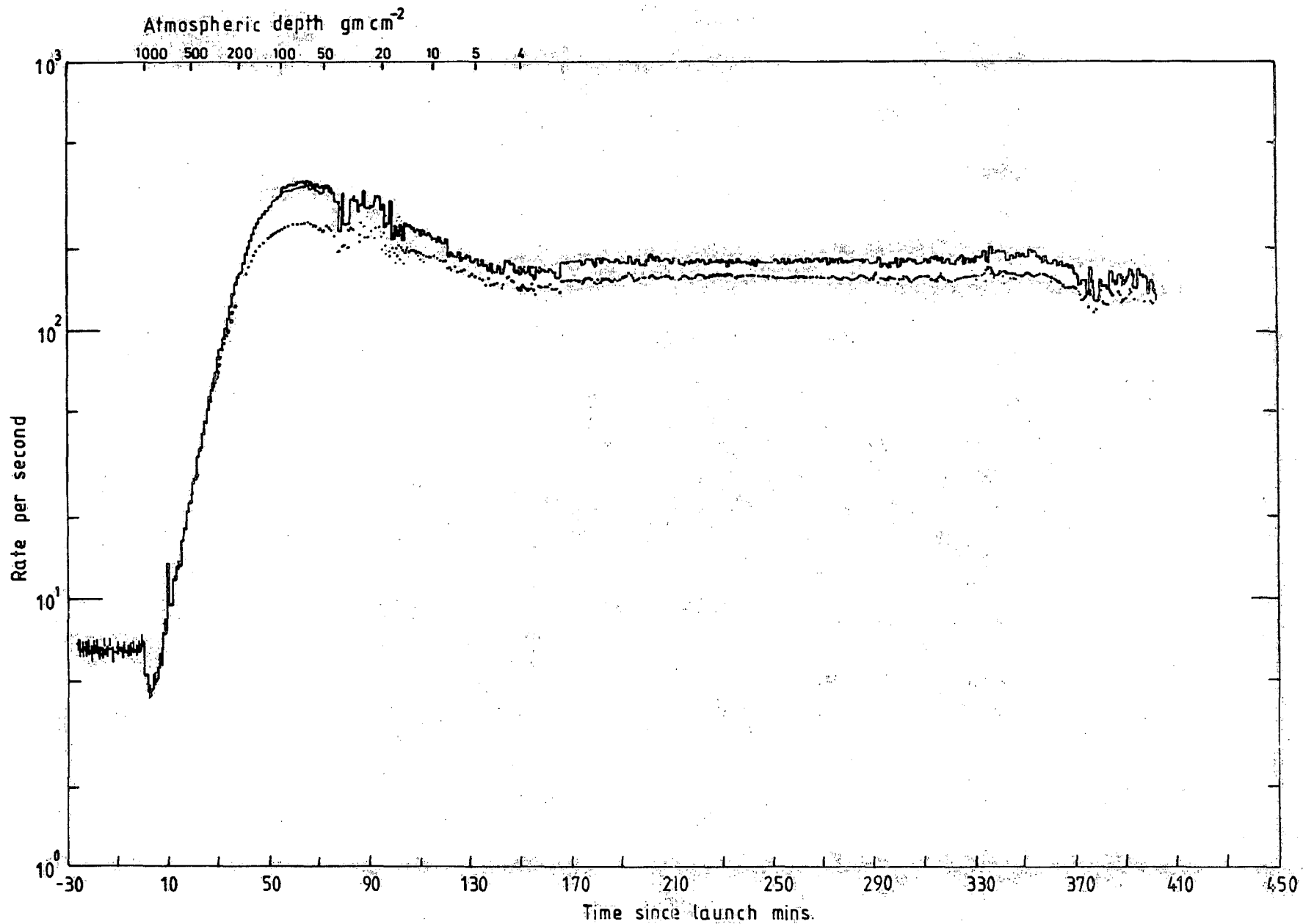


Figure 6.5 The unvetoes counting rate of the Germanium detector as a function of time since launch and atmospheric depth.

event recording rates in the secondary ADC and (ii) the upper set of points are the true rates which are calculated from an interval distribution to the events in (i). (iii) the histogram represents the event recording rate corrected for system dead time, which for the secondary ADC is $\sim 16\%$ and for the main ADC the value is $\sim 60\%$. Again the expected maximum is seen at atmospheric depth 100 g cm^{-2} .

6.3 PULSE-HEIGHT SPECTRA

Atmospheric background spectra have been obtained for various altitudes throughout the balloon ascent and figure 6.6, which is a summation over ~ 60 minutes, is a representative example. Both unvetoes and vetoed Ge spectra are shown and the necessity for the application of active shielding to a system searching for gamma-ray lines is clear since the lines at 139 keV and 198 keV are only discernible in the vetoed spectrum. After correcting for chance coincidences the spectrum of the vetoed gamma-rays is $\sim 10\%$ of the unvetoes spectrum.

The above stated background lines are the result of atmospheric neutron interactions with the Ge detector, namely: ${}^{74}\text{Ge}(n,\gamma){}^{75}\text{Ge}^m [T_{1/2}=48\text{s}]$ and ${}^{70}\text{Ge}(n,\gamma){}^{71}\text{Ge}^m [T_{1/2}=20\text{ms}]$ respectively, though the existence within a natural Ge crystal of five different stable isotopes of Ge complicates the matter. Fifty-six per cent of the observed 139 keV line counting rate $[(0.13 \pm 0.04) \text{ counts s}^{-1} \text{ at } (280^{+360}_{-170}) \text{ g cm}^{-2} \text{ atmospheric depth}]$ is accounted for from the resonant absorption of $\sim 104 \text{ eV}$ neutrons by ${}^{74}\text{Ge}$ and the remainder is believed to be caused by reactions (a) ${}^{76}\text{Ge}(n,2n){}^{75}\text{Ge}^m$ and (b) ${}^{76}\text{Ge}(p,pn){}^{75}\text{Ge}^m$.

The counting rate for the 198 keV line at the same atmospheric depth is $(0.34 \pm 0.04) \text{ counts s}^{-1}$ and in both cases the observed rates agree with those reported by Mahoney et al. (1978) and Womack and

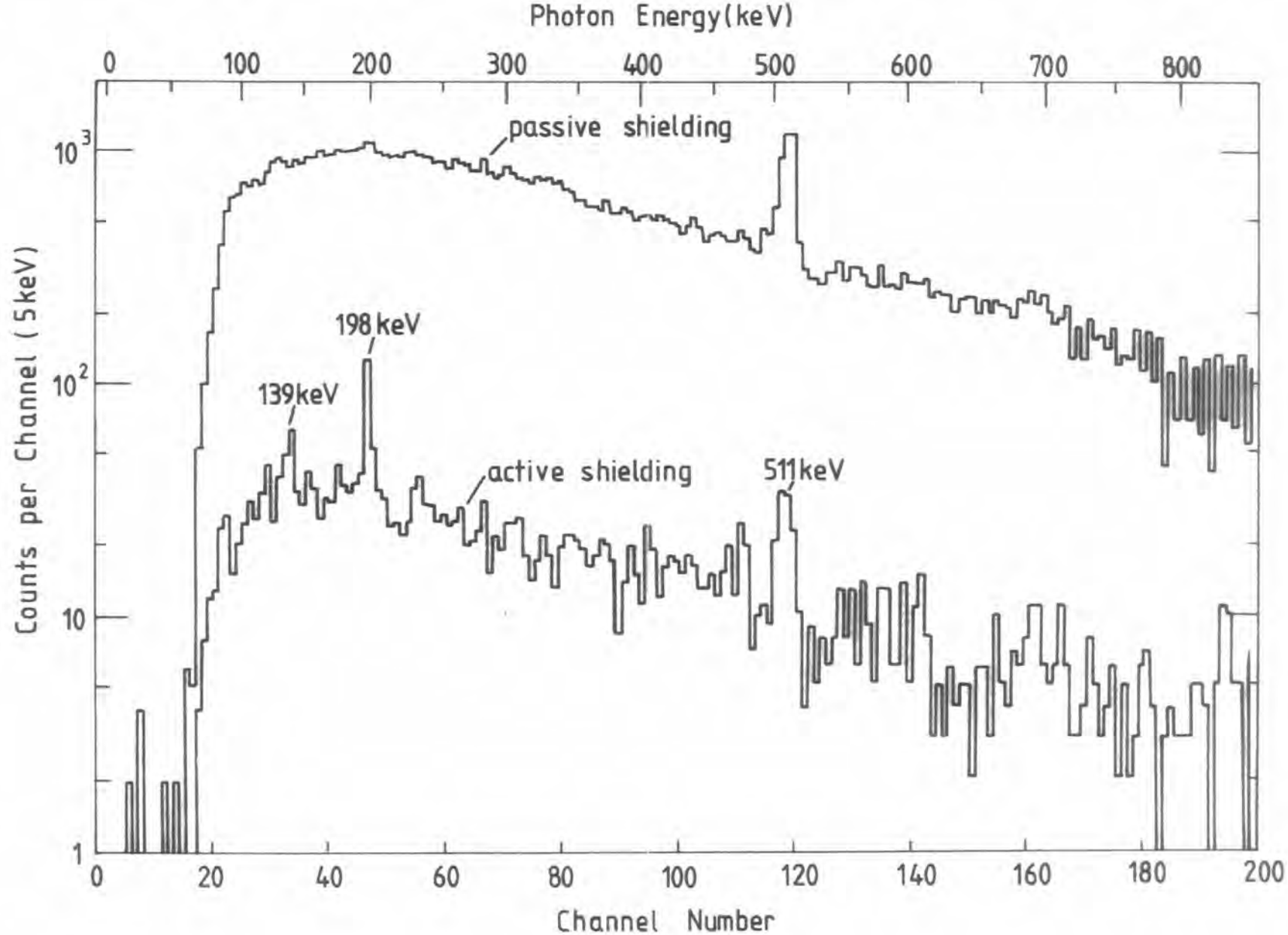


Figure 6-6 Atmospheric background spectrum not corrected for apparatus dead time.

Overbeck (1970) though for each of these reports the atmospheric depths were widely different from that of the present investigation. Figure 6.7 shows the measured variation of the intensities of the 138 keV and 198 keV lines with atmospheric depth.

Background lines other than those discussed, though not seen on this occasion, are expected to arise from the Ge crystal by similar processes, e.g. 175 keV, 595 keV, and 691 keV. Also, weaker lines could be produced from some of the other materials in the apparatus.

Figure 6.6 reveals the 511 keV line as the dominant feature, to the extent that this line is seen even in the unvetoes spectra. In the vetoed spectra the line is contributed to by three components, (a) atmospheric 511 keV photons entering through the aperture, (b) atmospheric 511 keV photons which pass through the shield without interacting and (c) β^+ decay of radioactive nuclei produced in the Ge crystal and its assembly, (β^+ annihilation yields two 511 keV photons, one of which is absorbed by the crystal and the other escapes without interacting in the shields). Each of these components of the counting rate are plotted as a function of atmospheric depth together with the observed rate in figure 6.8. This figure shows that the most significant contributions to the observed rate arise from components (b) and (c).

Component (a) is estimated using the semi-empirical model [Ling et al. (1977)]. Fluxes of upward and downward moving photons have been calculated as a function of depth by Ling et al. (1977) from measurements, over Palestine, of the 511 keV photon flux taken from uncollimated detectors [Peterson et al. (1973), Boclet et al. (1963) and Chupp et al. (1967), (1970)]. The mean effective thickness of the Durham spectrometer shields is estimated using a Monte-Carlo simulation [Bhat and Thompson (1981)]. From these results atmospheric 511 keV

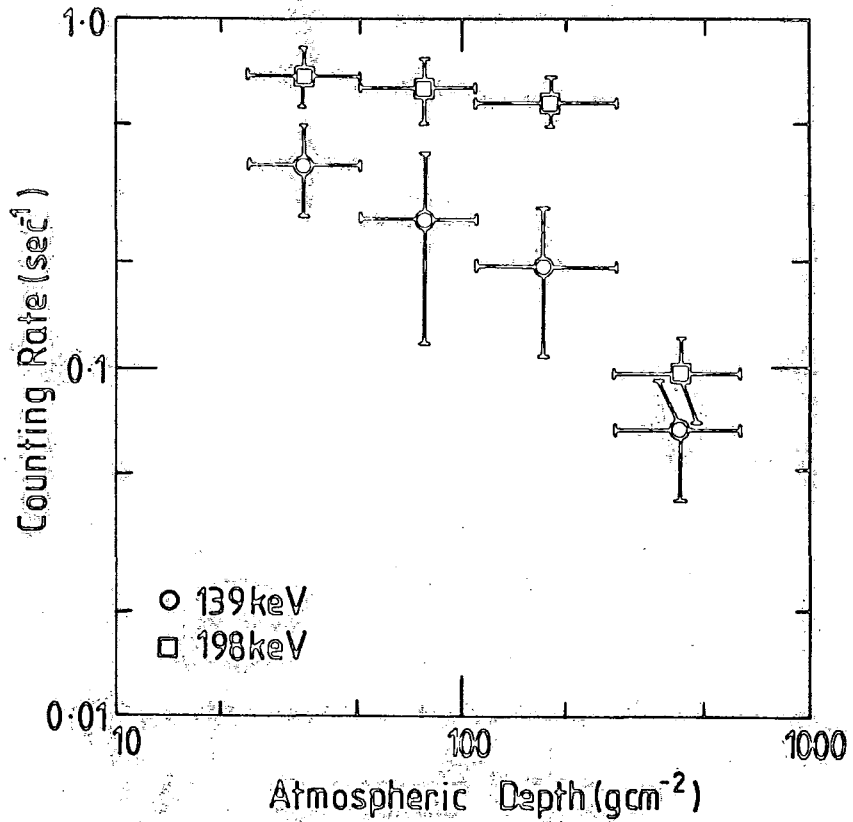


Figure 6.7 The 139 and 198 keV line intensities as a function of atmospheric depth.

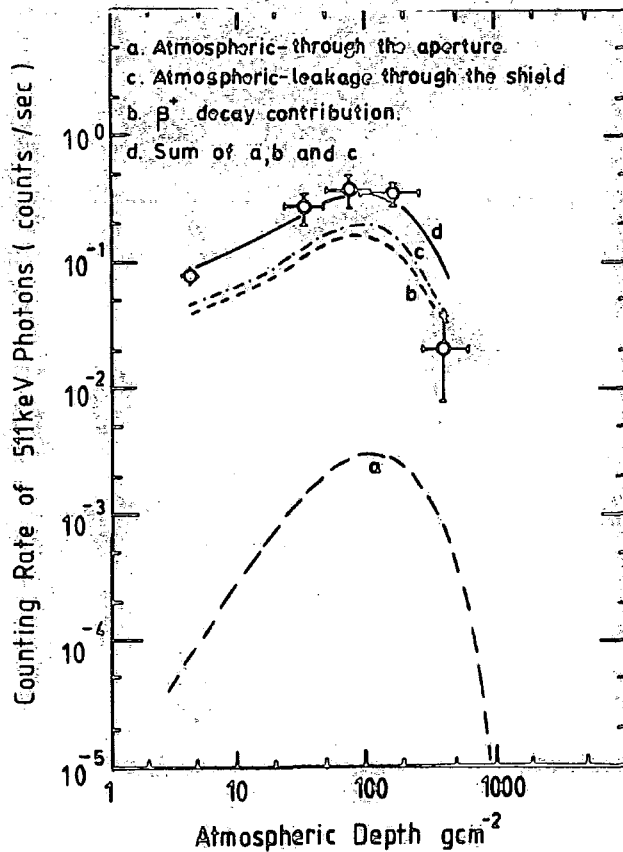


Figure 6.8 The components (a,b,c) and the observed, vetoed (d) counting rates of the 511keV photons as a function of atmospheric depth.

photon counting rates due to component (b) are calculated as a function of depth. At depths $\lesssim 100 \text{ g cm}^{-2}$ the bulk of the leakage comes from the upward flux since above the Pfozter maximum the downward flux decreases more rapidly than the upward flux.

Since an external 511 keV photon cannot interact in the shield and also contribute to the 511 keV peak then the counting rate of annihilation photons due to locally induced radioactivity is given by: $[1/(1-p)](r_v - r_u)$, where r_v and r_u are the counting rates with and without veto respectively and p is the shield survival probability of 511 keV photons, calculated, from the computed mean path lengths in the shield, to be $\sim 4\%$. Hence a 511 keV event with a simultaneous shield trigger must be the result of internal β^+ annihilation. Possible contributions to local production of β^+ have been suggested by Ling et al. (1977), e.g. the following processes $\text{Cu}^{63}(n,2n)\text{Cu}^{62}$, $\text{Cu}^{63}(p,n)\text{Zn}^{63}$, $\text{Cr}^{52}(p,n)\text{Mn}^{52}$, $\text{Ge}^{70}(p,n)\text{As}^{70}$, $\text{Al}(p,n)\text{Si}^{27}$.

Table 6.1 summarises the 511 keV counting rates measured at various depths during the flight for both vetoed and unvetoed cases. The figures given in the table for float altitude are indirectly derived from the observed variation of the ratio of counting rates with and without veto and the calculated chance coincidence correction; they are therefore subject to systematic errors of $\lesssim 50\%$.

From the observed background spectra the differential Ge counting rate at float altitude (4.3 g cm^{-2}) is obtained and is shown in figure 6.9. The integral counting rate, derived by integrating the sum distribution, is $19.5 \text{ counts s}^{-1}$. A plot of the 3 σ minimum detectable line flux from a point source derived from the float differential counting rate is given in figure 6.10 for active and passive shielding. A factor of \sim three improvement in the spectrometer's sensitivity is gained by the use of active shielding as can be seen from the minima

TABLE 6.1 Summary of the measured 511 keV counting rates

Atmospheric depth (g cm ⁻²)	511 keV photon counting rate in Ge crystal (sec ⁻¹)		
	vetoed	unvetoed	local production
430 + 210 - 150	(2.2 ± 1.4) × 10 ⁻²	0.97 ± 0.05	0.99 ± 0.05
172 + 108 - 62	0.36 ± 0.07	3.57 ± 0.11	3.34 ± 0.14
78 + 32 - 27	0.38 ± 0.11	4.16 ± 0.13	3.93 ± 0.18
35 + 16 - 11	0.27 ± 0.08	3.16 ± 0.12	3.01 ± 0.15
4.3 ± 0.2	0.079 ± 0.003	1.08 ± 0.03	1.04 ± 0.03

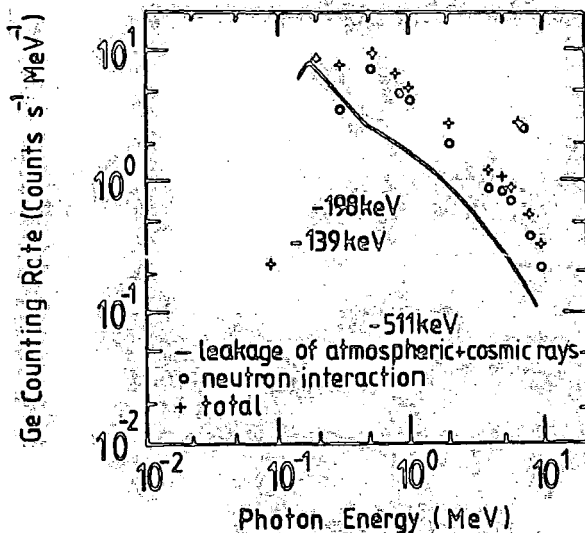


Figure 6-9 Differential counting rate of the Ge crystal actively vetoed by the shields at float altitude (4.3 g cm⁻²).

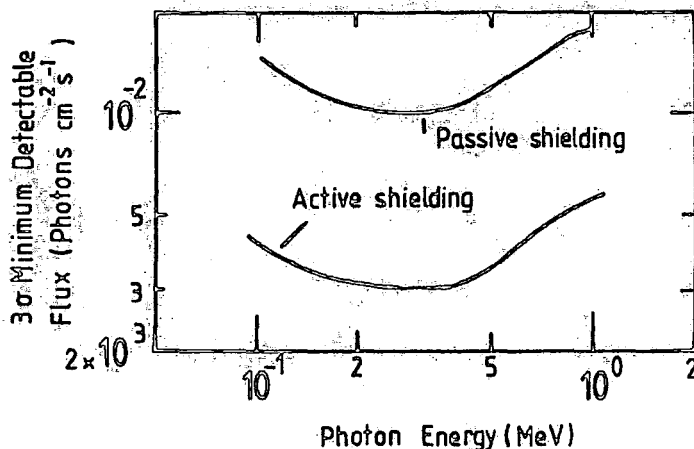


Figure 6-10 3σ minimum detectable flux from a point source as a function of photon energy in the range 0.1 to 1.0 MeV.

of the active and passive curves at 3×10^{-3} and 10^{-2} photons $\text{cm}^{-2} \text{s}^{-1}$ respectively.

CHAPTER SEVEN

THE FUTURE OF EXPERIMENTAL GAMMA-RAY ASTRONOMY

In relation to the immediate future a new gamma-ray spectrometer is proposed for the Durham group which is expected to have a line sensitivity of approximately 2×10^{-4} photons $\text{cm}^{-2} \text{s}^{-1}$ and energy resolution of 2 keV at 1 MeV.

This instrument is again to be based on the active shielding principle and is to incorporate a nine headed Ge detector, presenting a total detection area of 220 cm^2 , which is contained in a single aluminium vacuum cryostat. As mentioned in Chapter 3 current technology precludes the fabrication of large solid state devices and therefore in order to achieve the same result multi-headed arrays of crystals close to the maximum size presently available are employed. The proposed shielding is based on an activated five segment NaI(Tl) array and from the calculations of Bhat and Thompson (1981) the optimum thickness is believed to be $(8.5 \pm 2) \text{ cm}$; the error being due to uncertainty in the relevant cross sections for the incident neutron spectrum. Collimation is to be provided by a passive Tungsten lattice.

Turning to the more general aspect then, for the full development of the potential contained in the gamma-ray astronomy field there is a requirement for both better instruments and improved vehicles to support them. If the true nature of gamma-ray sources is to be discerned, information on their long term variability must be obtained and this will necessitate extended observation times of the order of days or even weeks. Additionally access to the whole celestial sphere is required to facilitate a comprehensive study of the cosmic gamma-ray background. Experiments containing detectors of area \sim one square metre would reduce the presently encountered random errors by a factor

of approximately ten. The proposed earth orbiting Gamma-Ray Observatory satellite (G.R.O.) will go some way towards achieving these ends, however there should still be a need for an enthusiastically pursued programme of balloon-borne experiments.

Of prime concern is the improvement of instrument sensitivity to $\sim 10^{-4}$ photons $\text{cm}^{-2} \text{s}^{-1}$ from the current figure of $\sim 10^{-3}$ photons $\text{cm}^{-2} \text{s}^{-1}$ as it will only be from this level that the wealth of spectral lines emanating from even those sources already discovered may be realised. Angular resolution should be improved to better than one degree of arc since, based on the knowledge of discrete X-ray source separation, it is not unlikely that gamma-ray sources are spaced about this much apart.

New innovative approaches to the field are also required for not only the improvement of sensitivity but in addition, to eliminate systematic errors including offset background pointing and induced radioactivity. For the measurement of cosmic sources with actively shielded apparatus an accompanying background measurement must be made which requires re-orientation of the system but the celestial gamma-ray flux is directionally dependent so there is the inherent problem of where to point for the measurement. Also this background determination should be made simultaneously with the source observation because of the induced radioactivity problem and such cannot be achieved with instruments currently in use. One unconventional concept which goes a good way towards solving these problems is the gamma-ray "correlation" system which comprises many independent gamma-ray detectors, some of which are pointed non skyward. Such a device synthesises the absolute energy spectrum via correlation of the energy deposition spectra from the several elements and this process rejects much of the background from the instrument itself while the remainder has the advantage of having

been simultaneously collected with the source spectrum.

If the G.R.O. is launched then it will be in connection with balloon work that the new techniques will be required, for there is little doubt that there is a future for ballooning if for no other reason than its ability to provide a fast reaction capability to the development of new and unexpected phenomena.

ACKNOWLEDGEMENTS

The author is grateful to his supervisor, Dr. M.G. Thompson, for the opportunity of studying with the Experimental Gamma-ray Astronomy Group and to the University of Durham for the provision of a studentship. Dr. C.A. Ayre, Dr. P.N. Bhat, Mr. A. Owens and all members of the group are thanked for their friendship and assistance. Special thanks are extended to Mr. K. Tindale for his unfailing assistance with all aspects of the practical work and to Mrs. P.A. Russell for her help throughout and for drawing the diagrams.

All members of the Physics department workshops' staff are thanked for their contributions to the project as a whole and the staff of N.C.A.R., Palestine, Texas are acknowledged for their efforts during the flight campaign.

Finally, I am extremely grateful to Mrs. M.A. Chipchase for the typing of this thesis.

REFERENCES

- Albernhe, F., Boclet, D., Chabaud, J.P., Claisse, J., Durouchoux, P., Olivier, E., Dacosta, J.M., Pagnier, P., Rocchia, R., Vedrenne, G.: 1978, Nucl. Instr. and Methods, 155, 171.
- Albernhe, F., Leborghne, J.F., Vedrenne, G., Boclet, D., Durouchoux, P. and da Costa, J.M. : 1981 Astron. and Astrophys. 94, 214.
- Albernhe, F., Vedrenne, G., : 1976, J. Geophys. Res., 8, 2433.
- Anderson, K.A. : 1981, Phys. Rev. 123, 1435.
- Apparao, M., Krishna, V., Daniel, R.R., Vijayalakshimi, B., Batt, V.L. : 1966, J. Geophys. Res. 71, 1781.
- Arnett, W.D. : 1978, NASA Tech. Mem. 79619.
- Arnold, J.R., Metzger, A.E., Anderson, E.C. and Van Dilla M.A. : 1962, J. Geophys. Res. 67, 4878.
- Auriemma, G., Angeloni, L., Belli, B.M., Bernardi, A., Cardini, D., Costa, E., Emanuele, A., Giovanelli, R. and Ubertini, P. : 1978 Astrophys. J., 221, L7.
- Baker, R.D., Lovett, R.R., Orford, K.J. and Ramsden, D. : 1973, Nature, Phys. Sci., 245, 18.
- Becker, R.H., Boldt, E.A., Holt, S.S., Praydo, S.H., Rothschild, R.E., Serlemitsos, P.J., Smith, B.W. and Swank, J.H. : 1977, Astrophys. J., 214, 879.
- Beuermann, K.P. : 1971, J. Geophys. Res. 76, 4291.
- Bhat, P.N. and Thompson, M.G. : 1981, Proc. 17th I.C.R.C., Paris, 8, 15.
- Bignami, G.F., Fichtel, C.E., Kniffen, D.A. and Thompson, D.J. : 1975, Astrophys. J., 199, 54.
- Boclet, D., et al. : 1963, Proc. 8th I.C.R.C., Jaipur, 3, 194.
- Carlson, A.G., Hooper, J.E. and King, D.T. : 1950, Phil. Mag. 41, 701.
- Carlson, B. : 1953, The Monte Carlo method applied to a problem in γ -ray diffusion, Los Alamos Scientific Lab. Report AECU-2857.
- Carpenter, G.F., Coe, M.J. and Engel, A.R. : 1976, Nature, 259, 99.
- Chambon, G., Hurley, K., Niel, M., Talon, R. and Vedrenne, G. : 1978, NASA Tech. Mem. 79619.
- Chupp, E.L. : 1977, Gamma-Ray Astronomy, Reidel Publishing Company, Dordrecht, Holland.
- Chupp, E.L., Sarkady, A.A. and Gilman, H.P. : 1967, Planet, Space Sci., 18, 939.

- Chupp, E.L., Forrest, D.J., Higbie, P.R., Suri, A.N., Tsai, C., Dunphy, P.P. : 1973, Nature, 241, 333.
- Chupp, E.L., Forrest, D.J., Ryan, J.M. and Cherry, M.L. : 1981, Astrophys. J. (Letters), 244, L171.
- Chupp, E.L., Forrest, D.J., Sarkady, A.A. and Lavakare, P.J. : 1970, Planet Space Sci., 18, 939.
- Chupp, E.L., Forrest, D.J. and Suri, A.N. : 1975, I.A.U. Symposium No. 68, D. Reidel Publishing Company, Dordrecht, Holland.
- Clayton, D.D., Colgate, S.A. and Fishman, G.J. : 1969, Astrophys. J., 155, 75.
- Clayton, D.D. and Hoyle, F. : 1974, Astrophys. J. (Letters), 187, L101.
- Clayton, D.D. and Silk, J. : 1969, Astrophys. J. (Letters), 158, L43.
- Cline, T.L. : 1961, Phys. Rev. Letters, 7, 109.
- Coe, M.J., Engel, A.R., Quenby, J.J. and Dyer, C.S. : 1977, Nature, 268, 508.
- Cohen, J., : 1971, Concepts of Nuclear Physics, McGraw-Hill Book Company, New York.
- Crisler, D.F., Jarmer, J.J. and Eldridge, H.B. : 1971, Nucl. Instr. and Method, 94, 285.
- Critchfield, C.L., Ney, E.P. and Oleksa, S. : 1952 Phys. Rev. 85, 461.
- Daniel, R.R., Joseph, G., Lavakare, P.J. and Sunderrajan, R. : 1967, Nature 213, 21.
- Daniel, R.R. and Lavakare, P.J. : 1975, Proc. 14th I.C.R.C. 1, 23.
- Daniel, R.R. and Stephens, S.A. : 1974, Revs. of Geophys. and Space Phys., 12, 233.
- Davison, P.J.N. and Fabian, A.G. : 1977, M.N.R.A.S. 178, 1P.
- Davison, C.M., : 1966, in K. Seigbahn (ed.), Alpha-, Beta-, and Gamma-Ray Spectroscopy, Vol. 1, North Holland Publishing Company, Amsterdam, p.37.
- De Castro Faria, N.V. and Levesque, R.J.A. : 1967, Nucl. Instr. and Methods 46, 325.
- Dennis, B.R., Maurer, G.S., Cutler, E.P., Cranwell, C.J., Dolan, J.F., Frost, K.J. and Orwig, L.E. : 1978, NASA Tech. Mem. 79619.
- Di Cocco, G., Boella, G., Perotti, F., Stiglitz, R., Villa, G., Baker, R.E., Butler, R.C., Dean, A.J., Martin, S.J. and Ramsden, D. : 1977, Nature, 270, 319.
- Dolan, J.F., Cranwell, C.J., Dennis, B.R., Frost, K.J., Maurer, G.S. and Orwig, L.E. : 1977, Astrophys. J., 217, 809.

- Duthie, J.G., Hafner, E.M., Kaplan, M.F. and Fazio, G.G. : 1963, Phys. Rev. Letters, 10, 364.
- Eisberg, R. and Resnick, R. : 1974, 'Quantum Physics, of Atoms, Molecules, Solids, Nuclei and Particles', John Wiley and Sons, New York, p3.
- Fabian, A.C. and Sanford, P.W. : 1971, Nature Phys. Sci., 231, 52.
- Fazio, G.G. in L. Goldberg (ed.) : 1967, Ann. Rev. of Astron. and Astrophys. Vol. 5, Annual Reviews, Inc., Palo Alto, California, P481.
- Felten, J.E. and Morrison, P. : 1966, Astrophys. J., 146, 686.
- Fichtel, C.E., Kniffen, D.A., Thompson, D.J. : 1977, Proc. of the 12th ESLAB Symposium, ESA SP-124, 95.
- Forrest, D.J., Higbie, P.R., Orwig, L.E. and Chupp, E.L. : 1972, Nucl. Instr. and Methods, 101, 567.
- Frost, K.J. and Orwig, L.E. : 1978, NASA Tech. Mem. 79619.
- Frost, K.J. Rothe, E.D., Peterson, L.E. : 1966, J. Geophys. Res., 71, 4079.
- Fukada, Y., Hayakawa, S., Kasahara, I., Makina, F., Tanaka, Y. and Sreekantan, B.V. : 1975, Nature, 254, 398.
- Gnedin, Yu. N. and Sunyaev, R.A. : 1974, Astr. Ap. 36, 379.
- Graml, F., Penningsfeld, F.P. and Schönfelder, V. : 1977, Recent Advances in Gamma-Ray Astronomy, Proc. 12th ESLAB Symp. (ESA SP-124).
- Graml, F., Penningsfeld, F.P. and Schönfelder, V. : 1978 NASA Tech. Mem. 79619.
- Graser, U. and Schönfelder, V. : 1977, Astrophys. J., 217, 306.
- Green, R.M. and Finn, R.J. : 1965, Nucl. Instr. and Meths. 34, 72.
- Grindlay, J.E. : 1978, Nature, 273, 211.
- Gruber, D.E. and Ling, J.C. : 1977, Astrophys. J., 213, 802.
- Gunnink, R. and Stoner, A.W. : 1961, Anal. Chem. 33, 1311.
- Hall, R.D., Meegan, C.A., Walraven, G.D., Djuth, F.T., and Haymes, R.C., : 1976, Astrophys. J., 210, 631.
- Haymes, R.C. : 1973, Astrophys. J., 184, 103.
- Haymes, R.C., Ellis, D.V., Fishmann, G.J., Kurfess, J.D. and Tucker, W.H. : 1968, Astrophys. J. (Letters), 151, L9.
- Haymes, R.C., Glenn, S.W., Fishman, G.J. and Harnden, F.R., Jr., : 1969, J. Geophys. Res. 74, 5792.
- Haymes, R.C., Walraven, G.D., Meegan, C.A., Hall, R.D., Djuth, F.G. and Shelton, G.H. : 1975, Astrophys. J. 201, 593.

- Heath, R. : 1957, IOD-16408.
- Heitler, W. : 1954, The Quantum Theory of Radiation, Oxford Univ. Press, London.
- Herzo, D., Koga, R., Millard, W.A., Moon, S., Ryan, J., Wilson, R., Zych, A.D. and White, R.S. : 1975, Nucl. Instr. and Methods, 123, 583.
- Higbie, P.R., Chupp, E.L., Forrest, D.J. and Gleske, I.U. : 1972, I.E.E.E. Trans. Nucl. Sci. NS-19, No. 1, 606.
- Hirasima, Y., Okudaira, K., and Yamagami, T. : 1969, Acta Phys. Hungarian (Suppl. 2) 29, 683.
- Hudson, H.S., Bai, T., Gruber, D.E., Matteson, J.L., Nolan, P.L. and Peterson, L.E. : 1980, Astrophys. J. (Letts), 236, L91.
- Jackson, J.D. : 1962, Classical Electrodynamics, John Wiley and Sons, Inc., New York.
- Jacobson, A.S., Bishop, R.J., Culp, G.E., Jung, L., Mahoney, W.A. and Willett, J.B. : 1975, Nucl. Instr. and Meths, 127, 115.
- Jacobson, A.S., Ling, J.C., Mahoney, W.A. and Willett, J.B. : 1978, NASA Tech. Mem. 79619.
- Johnson, W.N., Harnden, F.R. and Haymes, R.C. : 1972, Astrophys. J. (Letts.), 172, L1.
- Johnson, W.N. and Haymes, R.C. : 1973, Astrophys. J., 184, 103.
- Jones, F.C. : 1965, Phys. Rev., 137, B1306.
- Kasturirangan, K., Rao, U.R. and Bhaysar, P.D. : 1972, Planet Space Sci., 20.
- Kellerman, K.I. : 1974, Astrophys. J. (Letts.), 194, L135.
- Kinzer, R.L., Share, G.H. and Seeman, N. : 1974, J. Geophys. Res., 79, 4567.
- Kondo, I. and Nagase, F. : 1969, 'Solar Flares and Space Research', North Holland Publishing Co., Amsterdam, P.314.
- Kreger, W.E. and Mather, R.L. : 1967, in Shafroth, S.M. (ed), Scintillation Spectroscopy of Gamma Radiation, Vol. I, Gordon and Breach Publishers, London, P.33.
- Kurfess, J.P. : 1978, NASA Tech. Mem. 79619.
- Lederer, C.M., Hollander, J.M. and Perlmann, I. : 1968, Table of Isotopes, 6th edition, John Wiley and Sons, New York (corrected printing).
- Leventhal, M., MacCallum, C.J., Hutters, A.F. and Stang, P.D. : 1980, Astrophys. J. 240, 338.



- Leventhal, M., MacCallum, C.J., and Stang P.D. : 1978, NASA Tech. Mem. 79619.
- Leventhal, M., MacCallum, C.J. and Watts, A.C. : 1977, Nature, 266, 696.
- Ling, J.C. : 1974, Doctoral Thesis, UCSD, La Jolla, Calif.
- Ling, J.C. : 1975, J. Geophys. Res. (Space Phys.), 80, 3241.
- Ling, J.C. and Gruber, D.E. : 1977, J. Geophys. Res., 82, No. 7, 1211.
- Ling, J.C., Mahoney, W.A., Willett, J.B. and Jacobson, A.S., : 1977, J. Astrophys. Res., 82, 1463.
- Ling, J.C., Mahoney, W.A., Willett, J.B. and Jacobson, A.S. : 1979, July 15th edition of Astrophys. J.
- Lingenfelter, R.E. and Ramaty, R. : 1967, High Energy Nuclear Reactions in Astrophysics, W.A. Benjamin, New York, P.99.
- Lingenfelter, R.E. and Ramaty, R. : 1978, NASA Tech. Mem. 79619.
- Mahoney, W.A., Ling, J.C., Jacobson, A.S. and Tapphorn, R. : 1960, Nucl. Instr. and Meths. 178, 363.
- Mahoney, W.A., Ling, J.C., Willett, J.B. and Jacobson, A.S. : 1978, NASA Tech. Mem. 79619.
- Manchanda, R.K. : 1977, Astrophys. and Space Sci., 50, 179.
- Matteson, J.L. : 1978, Proc. A.I.A.A., 16th Aerospace Sci. Meeting.
- Mazette, E.P., Golenetskii, S.V., Il'inski, V.N., Guryan, Yu. A. and Kharitonova, T.V. : 1975, Ap. Space Sci., 33, 347.
- Meegan, C.A. : 1978, NASA Tech. Mem. 79619.
- Meegan, C.A. and Haymes, R.C. : 1979, Astrophys. J., 233, 510.
- Meneguzzi, M. and Reeves, H. : 1975, Astron. and Astrophys., 40, 91.
- Metzger, A.E., Anderson, E.C., Van Dilla, M.A. and Arnold, J.R. : 1964, Nature, 204, 766.
- Morrison, P. : 1958, Nuovo Cimento 7, 858.
- Nakagawa, S., Tsukada, M., Okudaira, K., Hirasima, Y., Yoshimori, M., Yamagami, T., Murakami, H., Iwama, S. : 1971, Proc. 12th I.C.C.R., Vol. 1, Hobart, Tasmania, P.77.
- Perlow, G.J. and Kissinger, C.W. : 1951, Phys. Rev., 81, 4.
- Peterson, L.E. : 1963, J. Geophys. Res., 68, 979.
- Peterson, L.E., Schwartz, D.A. and Ling, J.C. : 1973, J. Geophys. Res., 78, 7942.

- Pollack, J.B. and Fazio, G.G. : 1963, Phys. Rev., 131, 2684.
- Ramaty, R., Borner, G. and Cohen, J.M. : 1973, Astrophys. J., 181, 891.
- Ramaty, R., Kozlovsky, B. and Lingenfelter, R.E. : 1979, Astrophys. J. Suppl., 40, 487.
- Ramaty, R. and Lingenfelter, R.E. : 1973, High Energy Phenomena On the Sun, (R. Ramaty and R.G. Stone Eds). NASA SP-342.
- Ramaty, R. and Lingenfelter, R.E. : 1981, Phil. Trans. R. Soc., London.
- Rocchia, R., Ducros, R. and Gaffet, B. : 1976, Astrophys. J. 209, 350.
- Rocchia, R., Labyrie, J., Ducros, G. and Boclet, D. : 1965, Proc. I.C.C.R., London, P:423.
- Rossi, B. and Hulsizer, R.I. : 1949, Phys. Rev. 73, 1402.
- Ryan, J.M., Moon, S.H., Wilson, R.B., Zych, A.D., White, R.S. and Drayton, B. : 1977, J. Geophys. Res., 82, 3593.
- Schönfelder, V. : 1978, Nature 274, 344.
- Schönfelder, V., Graser, U. and Daugherty, J. : 1977, Astrophys. J., 217, 306.
- Schönfelder, V., Hirner, A., and Schneider, K. : 1973, Nucl. Instr. and Methods 107, 385.
- Schwartz, D.A. : 1970, Astrophys. J. 162, 439.
- Schwinger, J. : 1949, Phys. Rev. 75, 1912.
- Staib, J.A., Frye, G.M. Jr. and Zych, A.D. : 1974, J. Geophys. Res., 79, 929.
- Stecker, F.W. : 1969, Nature 211, 1229.
- Stecker, F.W. : 1970, Astrophys. Space Sci. 6, 377.
- Stecker, F.W. : 1971, Cosmic Gamma-Rays, NASA, SP-249 and Mono-book Co., Baltimore, Md.
- Stecker, F.W. : 1973, Astrophys. J. 185, 499.
- Stecker, F.W., Morgan, D.L., Jr. and Bredekamp, J. : 1971a, Phys. Rev. Letts, 27, 1469.
- Stecker, F.W., Morgan, D.L., Jr. and Bredekamp, J. : 1971b, Cosmic Matter-Antimatter Annihilation and the Gamma-ray Background Spectrum GSFC X-647-71-237, Goddard Space Flight Center, Greenbelt, Md.
- Sturrock, P. : 1971, Astrophys. J., 164, 529.
- Svensson, G. : 1958, Arkiv. Fysik., 13, 347.
- Toor, A. and Seward, F.D. : 1974, Astro. J. 74, 995.

- Trombka, J.I., Dyer, C.S., Evans, L.G., Bielefeld, M.J., Seltzer, S.M. and Metzger, A.E. : 1977, *Astrophys. J.* 212, 925.
- Trümper, J. : 1978, *NASA Tech. Mem.* 79619.
- Trümper, J., Pietsch, W., Reppin, C. and Voges, W. : 1978, *Astrophys. J. (Letts.)*, 219, L105.
- Trümper, J. Pietsch, W., Reppin, C., Sacco, B., Kendziorra, E. and Staubert, A. : 1977, *Proc. 8th Texas Symposium*, 538.
- Truran, J.W., Starrfield, S.G. and Sparks, W.M. : 1978, *NASA Tech. Mem.* 79619.
- Unsöld, A. : 1969, *The New Cosmos*, The English Universities Press Ltd., London, P.100.
- Van Lieshout, R., Wapstra, A.H., Ricci, R.A. and Girgis, R.K. : 1966, in K. Siegbahn (ed.), *Alpha, Beta and Gamma-ray Spectroscopy*, Vol. I, North Holland Publishing Co., Amsterdam, Holland, P.518.
- Vette, J.I. : 1962, *J. Geophys. Res.*, 67, 1731.
- Wainio, K.M. and Knoll, G.F. : 1966, *Nucl. Instr. and Methods*, 44, 213.
- Walraven, G.D., Hall, R.D., Meegan, C.A., Coleman, P.L., Shelton, D.H. and Haymes, R.C. : 1975, *Astrophys. J.* 202, 502.
- Weekes, T.C. : 1969, *High Energy Astrophysics*, Chapman and Hall, London.
- Weitkamp, C. : 1963, *Nucl. Instr. and Methods*, 23, 13.
- White, R.S., Dayton, B., Gibbons, R., Long, J.L., Zanrosso, E.M., and Zych, A.D. : 1980, *Nature, (Letts.)*, 284, 608.
- White, R.S., Dayton, B., Moon, S.H., Ryan, J.M., Wilson, R.B., and Zych, A.D. : 1977, *Astrophys. J.* 218, 920.
- White, R.S., Ryan, J.M., Wilson, R.B. and Zych, A.D. : 1978, *NASA Tech. Mem.* 79619.
- Willett, J.B., Ling, J.C., Mahoney, W.A. and Jacobson, A.S., : 1979, *Astrophys. J.*, 234, 753.
- Wolfendale, A.W. : 1982, *Journal of the British Astronomical Association*, 92, 3.
- Womack, E.A. and Overbeck, J.W. : 1970, *J. Geophys. Res.* 75, 1811.
- Zerby, C.D. and Moran, H.S. : 1961, *Nucl. Instr. and Methods* 14, 115.